Universidade de São Paulo
Instituto de Astronomia, Geofísica e Ciências Atmosféricas
Departamento de Astronomia

Juan Carlos Basto Pineda

Dark and Baryonic Matter in Spiral Galaxies: A Joint Analysis of Observations and Numerical Simulations

Matéria escura e bariônica em galáxias espirais: Uma análise conjunta de observações e simulações numéricas

São Paulo
2016

Juan Carlos Basto Pineda

Dark and Baryonic Matter in Spiral Galaxies: A Joint Analysis of Observations and Numerical Simulations

Matéria escura e bariônica em galáxias espirais: Uma análise conjunta de observações e simulações numéricas

Thesis presented to the Astronomy Department at Instituto de Astronomia, Geofísica e Ciências Atmosféricas da Universidade de São Paulo as a partial requisite for obtaining a PhD in Sciences.

Research Field: Astronomy
Advisor: Professor Claudia Mendes de Oliveira, PhD.

This is a corrected version; the original one is available at the Astronomy Department.

São Paulo
2016

A mi familia.

Acknowledgements

I would like to thank,

My supervisor, Dra. Claudia Mendes de Oliveira, for her priceless support and kindness;

Scientific Collaborators Dr.Volker Springel, Dr. Chris Hayward, and Dr. Philippe Amram, for their important contributions to this work and their inspiring love for science;

Fundação de Amparo à Pesquisa do Estado de São Paulo, FAPESP, for financial support through fellowships 2011/21678-0 and 2012/21375-0, which was vital for the fulfilment of this work;

Scientific Institutions IAG/USP and Heidelberg Institute for Theoretical Studies, HITS, which became my home away from home;

The staff and scientific colleagues of IAG and HITS for their warming heart and sincere support during all the adventures we faced together;

My Family, to which every page of this thesis truly belongs;

Finally, I would also like to acknowledge the support and honest friendship of the rest of the crew, those special people who shared this adventure side by side and so many times helped me to carry on; particularly, I sincerely thank Miguel Andrés Páez, Carlos Eduardo Barbosa, Federico Marinacci, Valentin Perret, Denis Yurin, Andreas Bauer, Maria Luiza Dantas, Thiago Kater Pinto, Silvio Fiorentin, and Daniel May for their incalculable support.

Esta tese/dissertação foi escrita em LaTeX com a classe IAGTESE, para teses e dissertações do IAG.

“*Highway, mi amor,*
encendiste la máquina de hacer los días y no sé como pararla.
Highway, mi amor,
prefiero las máquinas de hacer pájaros.”

Rafael Chaparro Madiedo en *Opio en las nubes.*

Resumo

A estrutura interna dos halos de matéria escura de galáxias é uma questão amplamente debatida. Enquanto as simulações cosmológicas ΛCDM predizem perfis de densidade crescendo abruptamente em direção ao centro (*cusps*), as curvas de rotação das galáxias sugerem a presença de núcleos de matéria escura de densidade constante (*cores*). Entender a origem desta contradição *cuspy-core* é importante para restringir cenários cosmológicos e modelos de formação de galáxias. Nesta tese, apresento um conjunto de experimentos controlados com simulações de N-corpos+hidrodinâmicas de galáxias e observações simuladas para testar a precisão dos métodos observacionais na caracterização dos halos de matéria escura. Partindo de galáxias anãs em halos de matéria escura do tipo *cuspy*, foram encontradas curvas de rotação mais compatíveis com a forma esperada para núcleos *cored*, oferecendo assim evidência enganosa sobre a verdadeira natureza de seus halos. A principal razão para isto é a pressurização do meio interestelar pelo *feedback* estelar, o que reduz a velocidade circular do gás em $\sim$5 km s^{-1} no kiloparsec central. Os experimentos sugerem que, mesmo com os dados de maior qualidade dos estudos atuais do problema *cusp-core*, é extremamente dificil corrigir esse efeito. Dado que as análises das curvas de rotação simuladas são muito consistentes com as observações, segue-se que os estudos observacionais dessas curvas podem não ser uma evidência conclusiva contra os halos de matéria escura *cuspy*. Outros fatos adicionais são examinados em detalhes, cuja maioria aponta na mesma direção. Na parte final desta tese, simulações de galáxias espirais mais massivas são utilizadas para introduzir uma metodologia para testar os metodos de determinação da distribuição de massa estelar a partir de dados fotométricos, e alguns resultados preliminares são apresentados. Globalmente, este estudo representa uma abordagem muito detalhada e inovadora para estudar a precisão na recuperação das distribuições radiais da matéria escura e bariônica a partir de observações fotométricas e cinemáticas.

Abstract

The inner structure of galactic dark matter haloes is a long-standing matter of debate. While ΛCDM cosmological simulations predict cuspy density profiles (i.e steeply growing towards the center), rotation curves of galaxies seem to indicate the presence of constant-density dark matter cores. Understanding the origin of this cusp-core contradiction is important to constrain cosmological scenarios and galaxy formation models. In this thesis I present a set of controlled experiments to test the ability of observational methods in recognizing cuspy dark matter haloes. For this purpose, I use N-body+hydrodynamical simulations of late-type galaxies representative on the local Universe and realistic mock observations. Starting with dwarf galaxies in cuspy dark matter haloes, I found their mock rotation curves more compatible with the shape expected for dark matter cores, thus offering misleading evidence about the true nature of their haloes. The main reason for this is the pressurization of the interstellar medium by the stellar feedback, which lowers the gas circular speed by $\sim$5 km s^{-1} in the central kiloparsec. The experiments suggest that even with the highest-quality data from current cusp-core studies it is extremely challenging –if not impossible– to effectively correct this effect. Given that the analyses from the mock rotation curves are pretty consistent with those from observations, it follows that rotation curve studies may not be a conclusive evidence against cuspy dark matter haloes. Additional facts are examined in detail, most of which point in the same direction. In the final part of this thesis I use simulations of more massive spirals to I introduce a framework for testing the accuracy in the estimation of the stellar mass distribution from photometric data, along with some preliminar results. Overall, this study represents a very detailed and innovative approach to estimate the accuracy in the recovery of the radial distributions of the dark and baryonic matter from photometric and kinematic observations.

List of Figures

List of Tables

Contents

Chapter 1

Introduction

This thesis deals with the possibility of measuring the amount and distribution of dark and baryonic matter in late-type galaxies. Galaxies are the building blocks of the large-scale structure of the Universe and the ultimate product of ∼13.7 billion years of evolution since the Big Bang. The population of galaxies is estimated to reach several hundreds of billions in the observable Universe, but despite such *astronomical* number, we have found so far many more intriguing questions than answers regarding the complex physical processes driving their formation and evolution over cosmic time scales. The study of galaxies is a fascinating and active matter of research in itself, which also provides key insights into the cosmological history of the Universe.

In the first part of this introduction I present an overview of the current leading paradigm of cosmology and galaxy formation. In the second part I describe how the dark and baryonic matter distributions in rotating disc galaxies may be inferred from observational data. Basicaly, this is achieved by modelling a galaxy as an ensemble of mass components with a simplified geometry, which consistently resembles the observed baryonic configuration and explains the observed internal kinematics. Such kind of procedure is sometimes called *mass modelling of galaxies*, and I will refer to it in these terms.

1.1 The formation of structures and galaxies in a ΛCDM Universe

In order to understand how galaxies formed in the Universe, one can ask oneself where everything came from. This question directly points to cosmology, the research area which aims at describing the whole Universe, its beginning, and evolution. I shall now describe some basic features of the cosmological standard model to discuss how structure formation happened.

The standard cosmological model is primarily based on the Big Bang scenario. The Big Bang refers to an Universe dense and hot in the past, whereas it is firmly established in three cosmological observables and one theory. The theory is General Relativity, the best theory describing gravity, the dominant force on large scales, so far. The first observable is the expansion of the Universe, first detected by Hubble in 1929 (Hubble, 1929). Basically speaking, Hubble detected that the farther a galaxy is away from us, the faster this galaxy is receding from us, regardless the direction on the sky we look at. As the phenomenon is isotropic and we are “typical” observers (the Copernican Principle), we interpret the recession as the expansion of the space between us and the galaxies. If we move in time backwards, this means that eventually all the points in space were much closer, thus generating hotter and denser regions, up to a point of infinity density and temperature, which is called the Big Bang[1].

The second observable is the abundance of light elements in the Universe. With a very hot and dense environment, atom nuclei other than ^{1}H were not able to form. As the temperature dropped due to the expansion, a point was reached where hydrogen, helium and lithium were formed. Heavier elements could not be formed due to the fast expansion of the Universe, so they were formed mostly in stars. This prediction was first put forward in the 1940’s (Alpher et al., 1948), although the first measurements took place in the 1960’s.

The third observable is the cosmic microwave background (CMB). In the hot and dense early Universe, the radiation was entangled to baryons through the Compton scattering. This coupling between the two components resulted in a black body spectrum for the radiation. When the temperature dropped below $\sim 3,000$K, photons no longer were able to ionize the hydrogen atoms, making the Universe transparent. This period is known as decoupling, or recombination, and represents the time when the first atoms formed. This radiation continued to decrease its temperature due to the expansion, where its emission peak today is at the microwave range of the electromagnetic spectrum, therefore called the cosmic microwave background. It was first predicted by Gamow and collaborators (Alpher

---

[1] It is important to stress that this extrapolation back in time is only valid up to the Planck era ($\sim 10^{-43}$s), before this time it is necessary to use a quantum gravity theory, but there is no successful one until now.

and Herman, 1948) and detected by Penzias and Wilson in 1965 (Penzias and Wilson, 1965).

On top of the Big Bang scenario one has to introduce the inflationary paradigm. The temperature fluctuations observed at the CMB today are of the order of 10^{-5} and isotropic. The Big Bang is not able to explain why the CMB is so smooth and isotropic, since light did not have time to interact and thermalize. In order to solve this issue (along with the so-called monopole and flatness problems, which are not discusse here), Guth (1981) proposed a mechanism where the Universe expanded in an accelerated way just after the Planck era, thereby smoothing the density contrast of the material components of the Universe. This acceleration was driven by the inflaton field, whose quantum fluctuations were stretched by the accelerated expansion, providing the seeds for the posterior formation of structures in the Universe.

Now I shall describe the components of the standard cosmological model. The two dominant components today, in terms of their current energy density, are the cosmological constant Λ and the cold dark matter (CDM). These two components give the name of the model, known as the ΛCDM model. The cold dark matter existence was first inferred by Zwicky in the 1930's by analyzing the dynamics of galaxy clusters, where he saw that the luminous matter was not able to match the mass calculated from the virial theorem. However, CDM was more strongly accepted through the measurements of galaxy rotation curves in the 1970's by Vera Rubin and others (more on this topic in Section 1.3 and in the remaining of the present thesis work). Basically, CDM is composed by a type of matter which does not interact electromagnetically, so we can only infer its existence through its gravitational interaction. It is cold because it has a low velocity dispersion, what is necessary to explain the structure formation. On the other hand, the cosmological constant was widely accepted only in 1998, when two type-Ia supernovae (SNe Ia) teams announced that the expansion of the Universe is accelerating (Riess et al., 1998; Perlmutter et al., 1999). They drew this conclusion by measuring the distances to high-redshift SNe Ia, which can be calibrated into standard candles, and showed that they were much farther than in a universe composed only by radiation and matter. The simplest way to explain the data was to consider that an extra component in the Universe, known as the cosmological constant, was providing the repulsive character to accelerate the expansion. This component is often associated with the vacuum energy.

These two components, Λ and CDM, have respectively approximately 69% and 26% of the energy budget of the Universe. The other 5% is mainly baryons, with fractions much smaller than 1% for radiation and neutrinos. These fractions represent the compilation from several observations (e.g. Planck Collaboration et al., 2014, 2015, and references therein).

The ΛCDM model has been extremely successful at explaining a myriad of observations. For instance, they involve measurements of the fluctuations of the CMB by the Planck satellite (Planck Collaboration et al., 2015), distances inferred from SNe Ia (Betoule et al., 2014), the baryon acoustic oscillations imprinted on the distribution of galaxies used as a standard ruler (Blake et al., 2011), and so on. This is the model considered in this thesis. Let me now briefly describe how the structures we see today were formed.

As it was said before, the seeds for structure formation were generated during the inflationary period, where the quantum fluctuations of the inflaton were extremely amplified. At the end of inflation the field oscillated and decayed into the matter. The inflation was followed by a period dominated by radiation. During this time it was not possible for structures to grow. As the time passed and the temperature dropped, eventually the Universe entered in the matter era. In this period the baryons were coupled to photons so they could not agglomerate, but the CDM started to collapse and create the potential wells where baryons fell later on. This process happened forming first the small objects, followed by the bigger ones in a series of mergers, and is called the hierarchical scenario of structure formation.

As the density contrasts were very small, a great part of the evolution of clustering can be studied using linear perturbation theory, one example being the study of the CMB. However, structures can grow above a point where the linear theory ceases to be valid. In spite of theories describing the non-linear collapse, e.g. the Zel'dovich approximation, they generally are not able to describe fully the physical phenomenon, and one has to resort to cosmological simulations.

Cosmological simulations of galaxy formation represent a challenge both from a numerical point of view and from a physical modelling point of view, given the tremendous range in spatial scales that have to be simultaneously modelled to simulate the process of structure formation. Notwithstanding that, they are the best tool at our disposal to gain a better theoretical understanding of the complex and non-linear evolution of the Universe.

Indeed, they now have reached a sufficient degree of maturity and reliability and are now able to explain evolution of the structures in the Universe that we see from galaxy surveys, as galaxy clusters, filaments and voids (Vogelsberger et al., 2014; Schaye et al., 2015a). However, they are still affected by the uncertainties especially in the modelling of the so-called baryonic physics. Although they are only a tiny fraction (5%) of the total energy budget of the Universe, baryons are extremely important because it is through them, and in particular through the electromagnetic radiation they emit, that we gather information about the physical conditions of the Universe. Therefore a proper description of the main physical processes governing their evolution is fundamental to completely describe the evolution of the structures in the Universe.

The main goal of cosmological simulations is to model what happens after structure growth goes beyond the linear theory, and in particular to describe what happens to the gas after it falls into the potential wells formed by the dark matter (the so-called haloes). Put in very simple terms, the gas now more dense can cool efficiently via emission of radiation, reaching higher and higher densities where the necessary instabilities for self-gravitating clouds finally develop. In the case of massive-enough structures, the gravitational collapse ended up igniting the atomic fusion engine that pushed the gas against gravitational collapse, thus forming stars. As star formation proceeds galaxies are born which subsequently evolve in the structures that we can observe nowadays in the Universe. This evolution is very complex because many physical processes come into play. For instance gas infall, deposition of energy in the interstellar medium by supernova explosions and stellar winds, the eventual formation of central black holes and the associated feedback onto the accreting gas, stellar evolution, metal enrichment, etc (see e.g. Vogelsberger et al., 2013). Morevoer, all these physical processes are strongly coupled in a non-linear fashion, and much of the theoretical work in simulations is trying to clarify the role of each process and its interrelation to the in the global galaxy formation picture.

Recently much attention has been drawn to the effects that feedback loops, and in particular supernova explosions, can have on the dark matter distribution in the central regions of galaxies (e.g. Pontzen and Governato, 2012). This thesis will focus on the connection between dark matter and baryonic matter in spiral galaxies of several masses by studying them at the small scales (< 1 kpc), where tensions between the standard ΛCDM and the observations have been reported.

1.2 Dark matter on galactic scales

The necessity for a dark matter component was first proposed by Zwicky (1933), based on his studies of the Coma galaxy cluster. Nevertheless, it was only during the 80's that this hypothesis became popular, when the systematic study of extended galactic rotation curves showed that in many cases they tended to remain flat well beyond the optical radius, suggesting the presence of an invisible matter component with cumulative mass growing linearly with radius (Roberts and Whitehurst, 1975; Rubin et al., 1978). Even though there are some alternative theories of gravity which could explain this observation without dark matter (Milgrom, 1983), they are unable to reconcile different observations at the same time, like the gravitational lensing observations of the Bullet galaxy cluster (Bradač B. and Bullet Cluster Collaboration, 2008; Ferreras et al., 2008), for instance. Additionally, nowadays the ΛCDM cosmologic paradigm, which implies a considerable amount of dark matter filling the Universe has succeeded in explaining many observations, from the power spectrum of the cosmic microwave background (Komatsu et al., 2011) to the luminosity curve of type-Ia supernovae (Perlmutter et al., 1999). In spite of that fact, we still do not know much about the nature of this dark matter, and only its kinematic effects are observed. In that regard, some clues may come from the inner part of late-type galaxies, as I describe in the following.

1.3 The cusp-core problem

On galactic scales, mainly two methods have been used to infer the concentration and shape of the dark matter halos: rotation curve fitting[2] and numerical simulations.

The first attempts to determine the dark matter profiles in spiral galaxies were done in 1985 (Carignan and Freeman, 1985a; van Albada et al., 1985a), and essentially the same principles are applied to interpret observational data today. Basically, the idea is to consider a galaxy as a sum of simplified building blocks: a stellar disk, a stellar bulge, a gaseous disk, and a dark matter halo. All these components are assumed to be axysymmetric and to share the same center and orientation. Then, using a given mass-

---

[2] In smaller systems, i.e. dwarf spheroidal galaxies, the total mass is constrained using stellar velocity dispersions instead of rotation curves. I remind the reader that this thesis is limited to disk-like galaxies (e.g. spirals and dwarf irregulars), and that is why it is only concerned about rotation curves

to-light ratio one can translate images and HI maps into baryonic mass distributions, and finally infer the amount of dark matter necessary to account for the observed rotation curve, assuming that the system is in dynamical equilibrium and therefore the centrifugal forces exactly balance the gravitational pull. A detailed description of this type of studies is given in Sec. 1.4

Using this kind of approach it has been claimed that several galaxies exhibit nearly constant dark matter density profiles at their centres, i.e. *cores* following $\rho_{\mathrm{dm}_{\mathrm{inner}}} \sim r^0$, a fact that contradicts the much steeper distribution expected from ΛCDM numerical simulations, which anticipate *cusps* following $\rho_{\mathrm{dm}_{\mathrm{inner}}} \sim r^{-1}$ (Navarro et al., 1996a). This fact is known as the cusp-core problem and remains one of the biggest problems for small scale cosmology (for a recent review see de Blok, 2010).

Several hypotheses have been proposed to explain the CUSP/CORE controversy. Initially, the low resolution of the HI kinematic data and systematic errors related to the long-slit spectroscopy technique used to build the rotation curves, as well as the presence of non-circular motions and projection effects were pointed out as possible sources of uncertainty masking cusps into cores (de Blok et al., 1996). Most of these problems have been overcome in the last decade with the use of high resolution 2D velocity maps, nevertheless, most observational studies still favour flat dark matter distributions in the center of galactic halos (Oh et al., 2011a)(Kuzio de Naray et al., 2009a), and it has been claimed that if a cusp would really exist it should be possible to detect it (Kuzio de Naray et al., 2008a).

Even though it seems that the existence of cored central dark matter distributions in galactic halos is a well-stablished fact, there are several assumptions made in this approach that may influence the results in unknown ways. For example, the baryonic components are being modeled as axisymmetric, while it is definitively not the case for most galaxies, with bars and spiral arms being the most obvious counterexamples. Secondly, the galaxies are assumed to be in pure rotation; in some cases random non-circular motions are corrected (Oh et al., 2008a), but there is no prescription about how to handle streaming motions by bars and spiral arms. Additionally, there are several ways for translating a data cube into a velocity map, and a velocity map into a final rotation curve. There are some attempts to compare those methods in the literature (Simon et al., 2003a)(de Blok et al., 2008a), but their overall impact on the cusp-core controversy is far from obvious.

The other way to study the properties of dark matter haloes is using numerical simulations of structure formation. From this approach, it was noticed that a cold dark matter cosmogony tended to produce halos with the same radial density profile over a wide range of masses, which can be well represented by the Navarro-Frenk-White formula (Navarro et al., 1996a), hereafter NFW. This formula implies inner density profiles growing steeply to the center, therefore in clear disagreement with the almost-flat distribution of the pseudoisothermal sphere model, the preferred formula to describe the cored profiles inferred from observations. Nevertheless, it is important to say that the universal cusp-like density profile was predicted by numerical simulations of dark matter only, and it has been shown recently that the effect of baryonic feedback during the process of galaxy formation may be able to change the shape of the hosting dark matter halos (Governato et al., 2010a). This possibility is being actively debated in the literature but can not be considered yet a definite answer about the real existence of DM cores in nature or about the way they form.

1.4 Mass modelling of galaxies

In this section I present an overview of the fundamentals on mass modelling of late-type galaxies (i.e. the estimation of their dark and baryonic matter distributions from observations) which is the backbone of this work. The solely intention of this summary is to serve as a quick reference handbook. It is necessarily incomplete, but several of the concepts reviewed here will be covered in more detail in the next chapters as necessary. I give special attention to the relevant aspects for the cusp-core problem, which was the main driver during the seminal stage of this thesis, and echoes through all this manuscript.

Finally, at the end of this section I summarize the main sources of systematic uncertainties that may affect the results of mass modelling studies, which is very important to understand their true robustness and limitations. Particularly, note that galaxies are in general very intricate systems in comparison with ideal geometrical models. This was the principal motivation for this thesis, which is devoted to perform a suit of controlled experiments with numerical simulations and mock observations of galaxies, in order to explore the reliability and possible biases of observational results.

1.4.1 Dark matter estimations from rotation curves

The nickname *dark matter* comes from the fact that this kind of matter does not produce, absorbe, or scatter electromagnetic radiation. For this reason, in general the amount of dark matter in astrophysical objects can be only investigated in indirect forms[3], for example through its gravitational effect on the surrounding baryonic material and on the geometry of space. Particularly, dark matter haloes of disc-like galaxies may be indirectly studied from their observed rotation curves. This is possible because, in dynamical equilibrium, the rotational motions are a reflection of the overall gravitational potential, from which one may try to discount the contribution of baryons using reasonable proxies and additional observations (see Section 1.4.2). This type of rotation curve analysis has been largely employed to probe the dark matter haloes of galaxies, and even though a number of details may vary from study to study, there is a general framework that I will try to synthesize in the following bullet points.

i. Consider a test particle in the equatorial plane of a mass structure with vertical and axial symmetries. If this particle rotates in equilibrium under only the effect of gravity, then its velocity relates to the encompassing gravitational potential as

$$\frac{V_{\mathrm{c}}^2}{r} = a_r = \nabla\Phi_{\mathrm{total}} = \frac{\mathrm{d}}{\mathrm{d}r}\Phi. \tag{1.1}$$

ii. Now let's assume that a disc galaxy can be modelled as an ensemble of axisymmetric components: a stellar disc, a gaseous disc, possibly a spherical stellar bulge, and a spherical dark matter halo. If it were possible to separate the components, equation (1.1) would hold for a test particle rotating in the gravitational potential of any of them, i.e.,

$$\begin{array}{ccc} \dfrac{V_{\mathrm{disc}_\star}^2}{r} = \dfrac{\mathrm{d}}{\mathrm{d}r}\Phi_{\mathrm{disc}_\star} & ; & \dfrac{V_{\mathrm{bulge}_\star}^2}{r} = \dfrac{\mathrm{d}}{\mathrm{d}r}\Phi_{\mathrm{bulge}_\star} \\ \dfrac{V_{\mathrm{gas}}^2}{r} = \dfrac{\mathrm{d}}{\mathrm{d}r}\Phi_{\mathrm{gas}} & ; & \dfrac{V_{\mathrm{dm}}^2}{r} = \dfrac{\mathrm{d}}{\mathrm{d}r}\Phi_{\mathrm{dm}}, \end{array} \tag{1.2}$$

where $V_{\mathrm{disc}_\star}$ represents the circular velocity of a test particle in the gravitational potential of the stellar disc, $V_{\mathrm{bulge}_\star}$ is the circular velocity of a test particle in the potential of the stellar bulge, and so on.

---

[3] Note that, even though several experiments on earth have tried to detect dark matter particles in a direct form, none of them have obtained convincing evidence of such detections yet.

iii. Considering the total gravitational potential,

$$\Phi_{\rm total} = \Phi_{{\rm disc}_\star} + \Phi_{{\rm bulge}_\star} + \Phi_{\rm gas} + \Phi_{\rm dm}, \tag{1.3}$$

one sees that, if and only if all the galaxy components share the same center and orientation, the set of equations (1.2) may be combined, demonstrating that the circular velocity of a test particle in the equatorial plane of the full model, $V_{\rm c}$, equates to the quadratic sum of the circular velocities associated to the individual components,

$$V_{\rm c}^2 = V_{{\rm disc}_\star}^2 + V_{{\rm bulge}_\star}^2 + V_{\rm gas}^2 + V_{\rm dm}^2. \tag{1.4}$$

iv. Assuming that the observed rotation curve is equivalent to the circular velocity profile $V_{\rm c}$, the strategy to assess the pure dark matter term in equation (1.4) is to find reasonable proxies for the mass distribution of the baryonic components, so one can estimate $V_{{\rm disc}_\star}$, $V_{{\rm bulge}_\star}$, and $V_{\rm gas}$. There are two main ways to accomplish this task, that I will present separately in **v.** and **vi.**.

v. Dwarf late-type and LSB galaxies are known to have very small baryonic fractions, and their dark haloes are expected to govern the dynamics at all radii. For this reason, these types of galaxies are often studied under the so-called *minimum disc approximation*, which consists in neglecting the baryonic terms in equation (1.4), approximating,

$$\frac{V_{\rm c}^2}{r} \approx \frac{V_{\rm dm}^2}{r} = \frac{\rm d}{{\rm d}r}\Phi_{\rm dm}. \tag{1.5}$$

Then the halo density profile can be explicitely computed using equation (1.5) in conjunction with Poisson's equation, which in the case of spherical symmetry is reduced to,

$$4\pi G\rho_{\rm dm} = \frac{1}{r^2}\frac{\rm d}{{\rm d}r}\left(r^2\frac{\rm d}{{\rm d}r}\Phi_{\rm dm}\right). \tag{1.6}$$

Incidentally, this also puts forward that spherical systems exhibit a one-to-one correspondence between any two terms of the triplet $(\rho, \Phi, V_{\rm c})$. Because it has played a capital role in the cusp-core debate, I will provide more information about the minimum disc approximation in Section 1.4.2.1.

vi. In normal spirals, on the other hand, the dynamical contribution of baryons in the inner region is not negligible, so it has to be estimated from observations. The distribution of stars is normally assessed from optical and/or near-infrared images, and that of the neutral gas is mapped through the 21-cm emission. This information is necessary to validate the approximation of the stellar and the gaseous aggregations as axisymmetric discs, as well as to calibrate their mass profiles. Once the contribution of baryons to the gravitational potential is estimated, one can infer the unseen distribution of dark matter that is needed to explain the observed rotation curve. This kind of analysis is often referred to as *rotation curve decomposition*, a denomination that I will adopt in this text. In Fig. 1.1, I present a schematic diagram of this approach, and more details about the modelling of the baryonic mass structures from optical/NIR and radio observations are given in Section 1.4.2.

The bottom line of mass modelling studies is that rotation curves are fair, accurate tracers of the underlying gravitational potential, which should be also markedly symmetric. The mass modelling of galaxies has the advantage of relying in simple, straightforward theoretical principles, which at a first-order approximation look reasonable for non-perturbed, rotating disc galaxies. Nonetheless, several caveats to this idealised picture exist, of which I make a short list in Section 1.4.5. Particularly, note that if mass modelling is employed to distinguish cusps from cores, its ideal framework must be well suited up to the very center of galactic discs, where the cusp-core controversy is debated (quite often $r \leq 1$ kpc). Whether or not it is possible to accurately determine the inner density profiles of galactic haloes from rotation curve analyses is a long-standing matter of debate, to which I expect to contribute new evidences with this work.

1.4.2 Assessing the baryonic mass distribution

After introducing the concepts of mass modelling and rotation curve decomposition, in this section I review how the contribution of baryons to the overall potential may be inferred from observations, but first I present the special case of very dark matter dominated systems, for which the baryonic potential may be simply neglected to a first approximation.

1.4.2.1 The minimum disc approximation

Many observational investigations of the cusp-core problem have focused in low surface brightness galaxies and late-type dwarfs (e.g. de Blok and Bosma, 2002; Spekkens et al.,

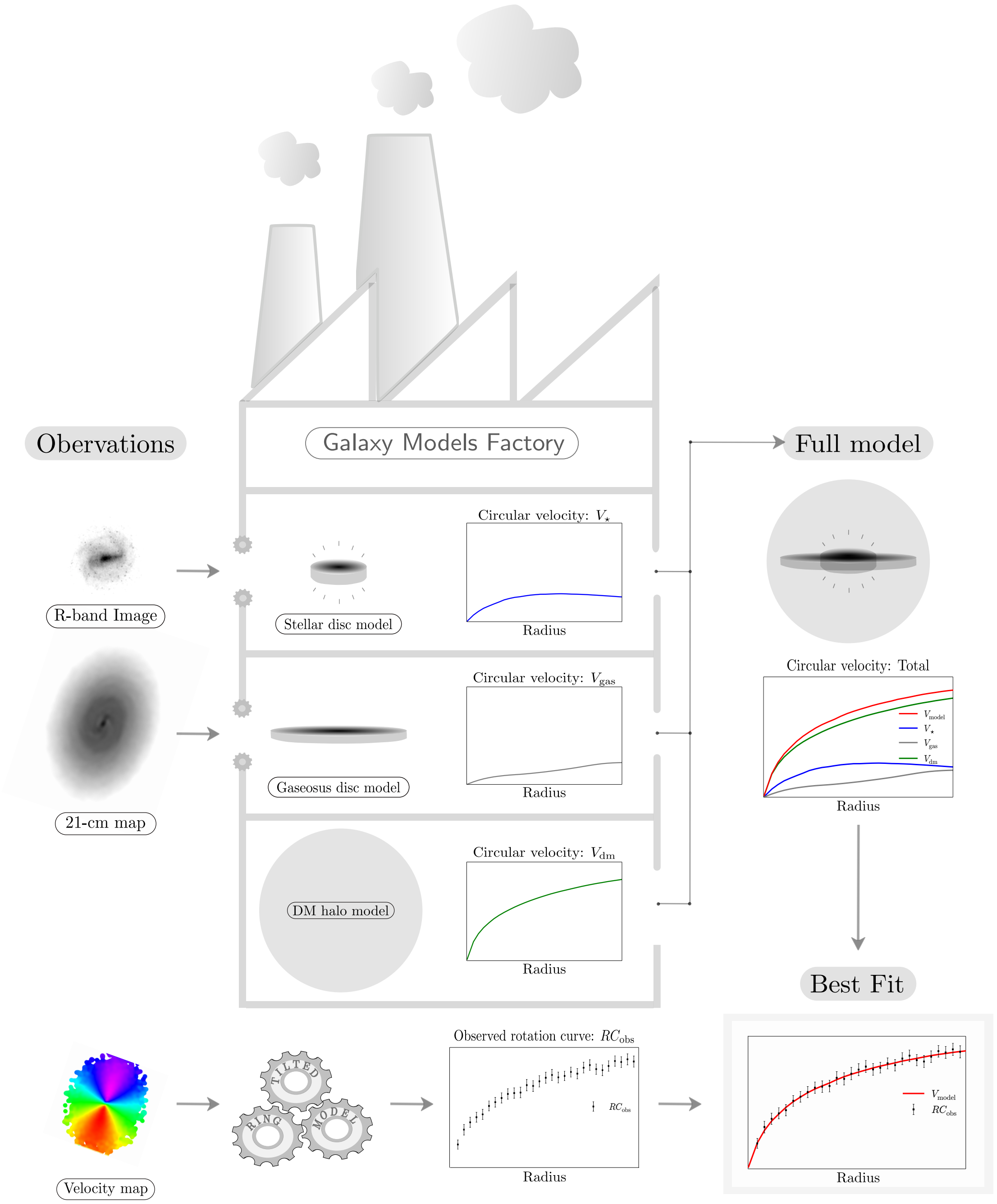

Figure 1.1: Illustrative scheme of the mass modelling of galaxies. In the column on the left I present the observables, which serve as input for the mass modelling analysis. From top to bottom I show the R-band image of a galaxy, its 21-cm emission map, and its velocity map. The first two serve to create axisymmetric models of the stellar and gaseous mass distributions, each one with an associated circular velocity profile. This is depicted in the upper levels of the *Galaxy models factory*. In this "factory" it is also created a spherical model for the dark matter halo, and the final product is an idealized geometrical representation of the galactic system, which I label as the "Full model" on the right. As explained in the main text, the circular velocity of a test particle in this ensemble can be estimated from the circular velocities associated to each component. In a parallel branch, the velocity map is analyzed and reduced to a rotation curve, which hopefully would represent the overall circular velocity of the system. Then the circular velocity of the model is compared against the observed rotation curve, and the model is refined iteratively until the best model, i.e. the one providing the best fit to the kinematic data, is found. In this schematic example, the "data" comes from one of the simulations that I will describe in Chapter 2.

2005; Adams et al., 2014; Oh et al., 2015). The reason for this is their comparatively low amount of baryonic matter, which minimizes the concerns about the uncertainty in the baryonic contribution to the observed rotation curve, and even endorse the assessment of the dark matter distribution directly from the observed rotation curve, by assuming $V_{\rm dm} \approx V_{\rm c}$. Neglecting the baryons has the advantage of allowing a much simpler analysis, which still seems to be meaningful to study the internal structure of the invisible dark matter haloes in these systems. As already mentioned in Section 1.4.1, this is known as the minimum disc approximation (e.g. de Blok and McGaugh, 1997; de Blok et al., 2001). Besides the dominance of the dark matter component, there are additional reasons to favour the study of low surface brightness galaxies. For instance, LSBs exhibit young stellar populations, low interstellar medium metallicities, large gas fractions, and very small or inexistent bulges; these observations support a quiescent evolution of the low surface brightness discs, implying a smaller probability that the baryonic feedback effects may have modified the dark matter distribution (e.g. Schombert et al., 1992; McGaugh and Bothun, 1994; McGaugh, 1994; de Blok et al., 1995; Impey and Bothun, 1997; Schombert et al., 2001; Du et al., 2015). In other words, low surface brightness galaxies are better suited than normal spirals to study the pristine shape, acquired at formation, by dark matter haloes, which makes them specially interesting for cosmological tests. Small bulges are also important to guarantee the dominance of the dark matter potential in the very center of the galaxy, both in low surface brightness galaxies as well as in late-type dwarfs.

The popularity of the minimum disc approximation raised considerably after the work of de Blok and McGaugh (1997), where a sample of 19 LSBs was studied and the authors concluded that the inferred structure of the dark matter haloes was barely dependent on the assumed mass-to-light ratios, i.e., on the conversion factor used to calibrate the stellar disc masses from their measured luminosities (see Section 1.4.2.2). Later in de Blok et al. (2001) the inner logarithmic slopes of the halo density profiles inferred from the minimum disc approximation, using an enlarged sample, were compared against the results obtained by first subtracting the dynamical contribution of the baryons to the rotation curve, and it was found that taking the baryons into account made the haloes appear shallower. In consequence, many authors since then have assumed that the minimum disc approximation serves to impose upper limits to how steep the halo density profiles are (e.g. Swaters et al., 2003; Spekkens et al., 2005), an idea that results very attractive as some of them have inferred shallow central dark matter distributions in this way (e.g. de Blok and Bosma, 2002; Marchesini et al., 2002; Kuzio de Naray et al., 2006). This was interpreted as a capital proof of the factual existence of dark matter cores at a time when the uncertainty in the baryonic contribution to the rotation curves was the most stringent limitation to study the properties of the dark matter haloes. The minimum disc approximation has played a preponderant role in the history of the cusp-core problem and, because of that, I will dedicate Chapters 2 and 3 of this thesis to study the robustness of cusp-core inferences in this limit using controlled experiments.

In the case of normal spirals, which exhibit larger baryonic contents in the central region than late-type dwarfs and LSBs, the minimum disc approximation is not applicable, and rotation curve decompositions demand the assessment of the baryonic mass distribution from auxiliary observations. In the following sections I introduce the more popular methods used in the cusp-core literature to deal with this task, and in Chapter 4 I will propose some experiments to evaluate their performance using mock photometric observations, along with some preliminar results.

1.4.2.2 The stellar component

One of the most challenging steps in rotation curves analyses is to correctly account for the gravitational potential of the stars (e.g. van Albada et al., 1985b; Bell and de Jong, 2001; Bershady et al., 2010). In general, it is assumed that the stellar mass distribution follows the observed luminous distribution, such that they are linked through a constant of proportionality known as the mass-to-light ratio (M/L). In posession of spectroscopic data, nowadays this quantity would be likely estimated from forefront stellar population synthesis (SPS) models as those discussed by Noll et al. (e.g. 2009); Conroy and Gunn (e.g. 2010); Maraston and Strömbäck (e.g. 2011). Nevertheless, this is not usually the case, and virtually all rotation curve studies which attempted to model the stellar mass distribution relied on photometric data in a few bands. In the lack of adequate constraints, early works used dynamical arguments to, for example, put an upper limit to the mass-to-light ratio (e.g. Carignan and Freeman, 1985b; van Albada et al., 1985b), or treated this quantity as a free parameter to be tuned along with the dark matter halo in order to accomodate the best fit to the observed rotation curve (e.g. Côté et al., 2000; Barnes et al., 2004). Unfortunately, as those approximations are built over physical models of the stellar components or of galaxy evolution, whether the inferred mass-to-light ratios were consistent or not with the true stellar populations in the disc was always uncertain. A decisive leap forward was possible after the work of Bell and de Jong (2001), which established that the mass-to-light ratios of disc galaxies correlate with their colors, and provided a number of conversion factors for different colors and bands. This was done by simulating the spectro-photometric evolution of a large number of disc galaxy models, i.e., using an early version of the SPS algorithms and models available today. A corollary of the work by Bell and de Jong is that the mass-to-light ratios are better constrained towards redder bands. This is a result of extinction effects being less important here and the fact that old stellar populations, which contribute more to the mass than the young population dominate the emission in this part of the spectrum. Additionally, according to Bell and de Jong (2001), the variation of the mass-to-light ratio as a function of a given color is smaller in redder bands, making the effect of possible color gradients less important and allowing the use of a single mass-to-light ratio for the whole disc. For that reason, images in the I/R bands are typically preferred to constraint the stellar mass, and they are by far the dominant source of photometric data in the cusp-core literature (e.g. Côté et al., 2000; Marchesini et al., 2002; Gentile et al., 2004). Alternatively, some authors go for the use of near-infrared data, including images in the K-band (2.19 μm) (e.g. Bolatto et al., 2002) and in the more recently available 3.6μm band from SPITZER (e.g. Oh et al., 2015), because the effects of dust extinction at these wavelengths are virtually null (e.g. Walter et al., 2007). However, note that the emission in these bands may be contaminated by polycyclic aromatic hydrocarbons (PAH), organic compounds present in the interstellar medium which radiate through a prominent emission line centered at 3.3 μm (e.g. Meidt et al., 2014).

After assessing the mass-to-light ratio, one has to recall that knowing the total mass in the form of stars is not enough for rotation curve decomposition; in order to compute the circular velocity profile of the stellar component, its spatial 3D gravitational potential must be fully resolved, so one can estimate the circular velocity profile $V_{\mathrm{disc}_\star}$ using equation (1.2).

This is relatively straightforward in the case of spiral galaxies, as observations support the view of these systems as flattened, rotating discs, many of which are highly axisymmetric. This is evidenced, for instance, by the isophotal contours of some canonical discs like

UGC7045 (Fig. 1.2, left), which closely resemble concentric, parallel ellipses. Note that a natural explanation for this apparent ellipticity is offered by the projection effects due to the inclination of the disc in the sky, as ideal circular discs should exhibit intrinsically round isophotes. This is schematically represented in Fig. 1.2 (right).

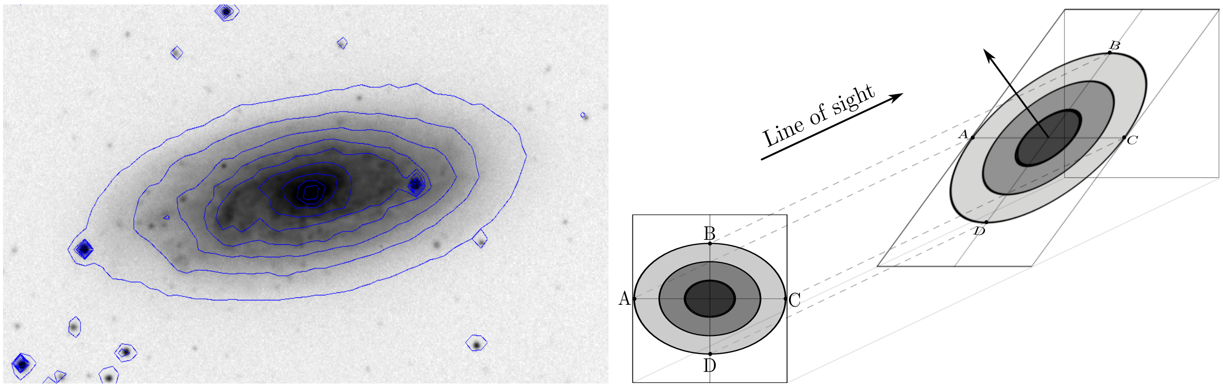

Figure 1.2: Left: R-band image of the disc galaxy UGC7045 with isophotal contours overplotted to it (Image source: Barbosa, 2016). Right: Schematic representation of a disc galaxy and its projected geometry in the plane of the sky.

Because of the simple geometry of galactic discs, they are commonly characterized by fitting constant-brightness ellipses to the galaxy image, in order to ascertain its intrinsic surface brightness as a function of radius (e.g. Jedrzejewski, 1987). This 1-dimentional surface brightness profile (SBP) can then be used to quantify some galaxy properties like the disc extent or the concentration of its light in the central region. Additionally, by averaging values azimutally over the ellipses one obtains more meaningful information on the global light distribution.

Once the surface brightness profile is determined, one can multiply it by the mass-to-light ratio to define a proxy for the stellar surface mass density profile. In the list below I present some of the more common approximations for the mass-to-light ratio that can be found in the literature:

- The mass-to-light ratio can be assumed constant across the disc and calculated from the relations of Bell and de Jong (2001) and Bell et al. (2003) using the colours of the whole disc. This is by far the most accepted prescription in the recent literature, and it is virtually always employed if the necessary data are available (e.g. Kassin et al., 2006; Simon et al., 2005). Extrapolations of the Bell and de Jong relations for additional bands have been also discussed; see for example de Blok et al. (2008a) for an empirical derivation of the mass-to-light ratio in the 3.6μm band of SPITZER.

- Eventually the color gradients in the disc are taken into account through a radially-dependent mass-to-light ratio (e.g. Kassin et al., 2006).

- In the lack of a reasonable proxy, some times the (M/L) coefficient is let as a free parameter during the fit of the mass model to the observed rotation curve (e.g. Spano et al., 2008). Note that this is a purely dynamical argument and it may in principle lead to unrealistic or simply unfaithful values of the stellar masses, not compatible with the actual stellar populations in the disc.

- An upper limit to (M/L) can be also estimated from the so-called *maximum disc approximation*, by scaling $V_{\mathrm{disc}_\star}$ to the maximum normalization that does not overshoot the observed rotation curve. This approach was popular in the past as an indirect way to put a lower limit to the dark matter content of spiral galaxies (e.g. van Albada et al., 1985a; van Albada and Sancisi, 1986).

After evaluating the surface brightness profile, and choosing a prescription for the mass-to-light ratio, the only missing ingredient to complete the 3D model of the stellar disc is its vertical density profile. In this regard, there is a general agreement in using the model of a locally isothermal sheet, $sech^2(\frac{z}{z_0})$, which has been found to describe well the vertical luminosity profile of edge-on galaxies with a scale height z_0 effectively independent of radius (e.g. van der Kruit and Searle, 1981).

Using these approximations, the structure of the stellar disc model can be parametrised as,

$$\rho_\star\left(r,z\right) = \frac{1}{2z_0}\left(\frac{M}{L}\right)\ \Sigma_\star\left(r\right)\ sech^2\left(\frac{z}{z_0}\right), \tag{1.7}$$

where $\Sigma_\star$ represents the radial surface brightness profile, and the extra factor $2z_0$ in the denominator sets the normalization to guarantee the following identity at all radii,

$$\int_{-\infty}^{\infty} \rho_\star\left(r,z\right)\mathrm{d}z = \left(\frac{M}{L}\right)\ \Sigma\left(r\right). \tag{1.8}$$

After defining the 3D density field, one needs to compute its gravitational potential, in order to assess the circular velocity profile of a test particle in the potential of the disc using equation (1.2). This is not a trivial step, but in principle it is achievable by solving the integral,

$$\Phi\left(r,\varphi=0,z=0\right) = \iiint\limits_{\text{All space}} \frac{G\rho\left(r',\varphi',z'\right)}{\sqrt{z'^2+r'^2+r^2-2rr'\cos\left(\varphi'\right)}}\mathrm{d}V', \tag{1.9}$$

where the square root in the denominator represents the distance between the point where the potential is being evaluated ($r, \varphi = 0, z = 0$), and the differential volume element at (r', φ', z'). For some parametrizations of $\Sigma_\star$ this integral may be solved analytically, as in the case of a thin exponential disc (Binney and Tremaine, 2008), but this is often not feasible and a numerical evaluation of the potential is preferable because it can deal with arbitrary shapes of the SBP (e.g. Barnes et al., 2004). However, it is worth noting that according to the implementation and to the desired accuracy, the numerical integration may demand considerable computer time on a regular desktop machine, which is a serious concern for the analysis of large data sets. I learned this through experience after solving equation (1.9) in PYTHON for a sample of galaxies from the GHASP survey at the beginning of this investigation. An interesting alternative emerged during my work with the numerical simulations, as it became clear that one can use an optimized N-body calculator to measure the gravitational field of any target matter distribution, it suffices to sample the density field with a large number of particles and pass their positions and masses to the N-body code in the appropriate format. Ever since I realized this fact, I calculated the radial accelerations (i.e. the circular velocities) of all the mass models in this work using GADGET (Springel, 2005), taking advantage of its optimized capabilities to speed up the accurate computation of the gravitational forces using multiple CPUs in parallel. As to my knowledge, this is the first time that the circular velocities of the model galactic components for rotation curve decompositions are computed in this fast-and-efficient way.

In the sake of completeness, it is important to say that the stellar discs of late-type galaxies have been found to be well represented by exponential light profiles of the form,

$$\Sigma_\star(r) = \Sigma_0 \; e^{-r/h}, \tag{1.10}$$

where Σ_0 represents the central surface brightness and h denotes the disc scale length (e.g. van der Kruit and Freeman, 2011). When this model is adopted, often the vertical scale height is taken to be a certain fraction of the radial scale length, e.g., $z_0 = h/5$. Even though this is supported by some observations (e.g. Edvardsson et al., 1993), it is an intense matter of debate (e.g. van der Kruit and Freeman, 2011).

Galaxies of earlier morphological types, on the other hand, exhibit light profiles that deviate from pure exponential discs and are commonly parametrized through the Sérsic profile of equation (1.11), governed by the parameter n which is known as the Sérsic index and controles the curvature of the light profile (e.g. Sersic, 1968),

$$\Sigma_\star(r) = \Sigma_0 \; e^{-k \; r^{\left(\frac{1}{n}\right)}} . \tag{1.11}$$

Alternatively, a combined analysis of the images and the shape of the SBP may suggest the existence of an underlying exponential disc with a second component on top, often a central stellar bulge that may be still parametrised via the Sérsic profile (e.g. Barbosa et al., 2015a). In those cases, the bulge must be included in the mass model of the galaxy as an additional spherical component with its own mass-to-light ratio.

So far I have discussed the case of ideal axisymmetric discs, in spite of the fact that all real systems deviate from this scenario by different amounts. Yet, it is interesting to note that for most non-ideal galaxies the elliptical isophotal analysis remain useful to understand the main features of the light distribution, and it is often employed to study even irregular galaxies or discs with substructures such as bars or strong spiral arms. In those cases, the best-fit ellipses are chosen to follow the true light distribution on the image without forcing them to be strictly parallel and concentric. This means that one may let the geometrical parameters: ellipticity (ε), position angle (PA), and central position (x_0, y_0), free to vary from ellipse to ellipse in order to get the best fit, and then the radial trends of these parameters may be investigated to better understand the patterns on the 2D light distribution. I show an example of the ellipse fitting to UGC1913 with all the geometrical parameters free to vary in Fig. 1.3.

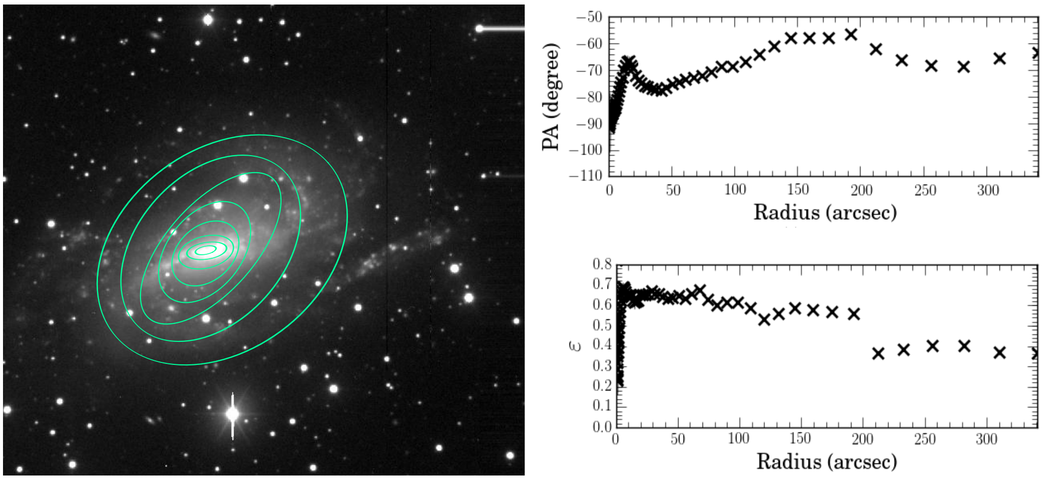

Figure 1.3: Example of an isophotal ellipse fitting model with the geometrical parameters free. Left: image of UGC1913 with the best-fit elliptical contours on top. Right: radial variation of the elipticity and position angle of the ellipses. Source of the image Barbosa (2016).

When it comes to rotation curve decompositions, the specific implementation of the isophotal-fit modelling of the disc is not homogeneous. According to the visible features in the image, some authors prefer to fit the isophotal ellipses with all the geometrical parameters fixed (e.g. Simon et al., 2005), while others fix the center but allow the geometrical parameters (ε, PA) to vary as a function of radius (e.g. de Blok et al., 2008a). The problem with the latter approach is that, even if the 2D luminous structure is well explained, the fundamental assumptions behind the simplified disc model of Fig. 1.2 can no longer be assumed. In the lack of a highly axisymmetric mass ensemble with a well defined center and orientation, the basis of the mass modelling algorithm described in Section 1.4.1 is put into question, and it is hard to anticipate what the impact of this treatment in the inferred dark matter density profiles could be.

1.4.2.3 The gaseous component

If one also wants to account for the gravitational potential of the gas, surface density maps of the neutral HI are needed. The procedure is similar to the one described for the stars, as the gaseous phase does also form axisymmetric discs, though they tend to be thinner and much more extended than their stellar counterparts. Once the radial surface brightness profile is obtained, the conversion from light to mass is straightforward because the probability of a spontaneous spin flip which gives origin to the 21-cm emission, as well as the energy of the emitted photon, can be calculated exactly from the quantum physics of the hydrogen atom. Not uncommonly, the inferred masses are also multiplied by a factor of about $\sim$1.25 to account for metals, as the mass in the form of heavier species is much harder to be traced. In general the gaseous component is found to be dynamically subdominant, and therefore it is often neglected by authors when HI data are not available.

1.4.3 Differentiating cusps from cores

As shown in Section 1.4.1, spherically symmetric haloes display an exact correspondence between $\rho_{\rm dm}$ and $V_{\rm dm}$. Exploiting this fact, there are two major approaches to infer the intrinsic cuspyness of a dark matter halo: fitting diagnostic analytic models to the inferred $V_{\rm dm}$, or inverting this curve to explicitely approximate the density profile $\rho_{\rm dm}$. In the following paragraphs I will synthesise the *modus operandi* of these methods, and in the next chapters I will thoroughly investigate their ability to recognize dark matter cusps as such using mock observations of realistic simulated galaxies.

1.4.3.1 Rotation curve fitting

This method consists in comparing the best fits to $V_{\rm dm}$ from a set of analytic models, associated to cuspy and cored density profiles, by means of the reduced χ^2_ν. This is especially interesting when there is available information beyond the central kiloparsecs, as it allows to constrain the full halo density profile which may carry additional signatures of the cosmology beyond the inner logarithmic slope (e.g McGaugh et al., 2007). The more standard functional forms employed in this task are the Navarro-Frenk-White profile and the pseudo-isothermal sphere model (hereafter ISO), whose analytic density profiles are presented in equations (1.12) and (1.13). The NFW model is very representative of the haloes traditionally formed in cosmological numerical simulations (e.g Navarro et al., 1996a; Klypin et al., 2001; Vogelsberger et al., 2014), except for some recent, purpose-specific implementations resorting to customized, violent stellar feedback models as a way to induce the transformation of cusps into cores in the haloes of dwarf galaxies (e.g. Governato et al., 2010b). As for the ISO model, more than being motivated by physical models of the dark matter dynamics, it was empirically found to provide good fits to a number of observed rotation curves,

$$\rho_{\rm NFW}(r) = \frac{\rho_0}{(r/R_s)[1+(r/R_s)]^2}, \tag{1.12}$$

$$\rho_{\rm ISO}(r) = \frac{\rho_0}{1+(r/R_c)^2}. \tag{1.13}$$

In both cases ρ_0 is a representative density of the central region. More especifically, it is the central density in the ISO model, and the density at $\sim 0.46 \times R_s$ in the NFW case. R_c and R_s represent the transition radii between the inner and the outer parts of the density profiles, where they exhibit different asymptotic behaviours. The equivalent circular velocity profiles can be obtained by integration, as for spherical matter distributions, the circular velocity in equation (1.1) can be expressed in terms of the enclosed mass as a function of radius via,

$$V_{\rm c} = \sqrt{G\frac{M(<r)}{r}}, \tag{1.14}$$

where

$$M(<r) = \int_0^R 4\pi r^2 \rho(r) {\rm d}r. \tag{1.15}$$

An inspection of equation (1.12) reveals that the inner region of the NFW profile increases steeply towards the center as $\rho_{\text{inner}} \sim r^{-1}$, which corresponds to the classical definition of a dark matter cusp. The ISO model, on the other hand, has a central constant-density core, $\rho_{\text{inner}} \sim r^{0}$, its size can be roughly approximated by R_c. Combining these results with equations (1.14) and (1.15) one sees that the inner velocity profile of the ISO model grows linearly as $V_{\text{inner}} \sim r$, which matches that of a solid-body rotating model. As for the NFW profile, a similar analysis yields $V_{\text{inner}} \sim \sqrt{r}$, granting the central velocity profile with a curved shape.

At very large radii these models differ. The NFW profile goes like $\rho_{\text{outer}} \sim r^{-3}$, while the ISO one follows a $\rho_{\text{outer}} \sim r^{-2}$ dependence. This implies that, at some point, the NFW circular velocity profile starts to decrease, as it is expected for any finite matter distribution. However, this behaviour presumably occurs at a radial range that is not covered by observations, as dark matter haloes are much more extended than their baryonic discs. In fact, it does not play a role in the rotation curve fitting because the NFW model is able to follow the flat part of observed rotation curves over their whole extent. As for the ISO density model, its asymptotic behaviour would force the circular velocity profiles to remain artificially flat to infinite, confirming that this model is an useful mathematical tool to describe galactic rotation curves but it can not represent a plausible physical scenario at large radii. All in all, as there are no sensible differences in the ability of both models to fit the outer parts of rotation curves, they should, in principle, be well-suited for differentiating cusps and cores in the central matter distribution.

The NFW velocity profile obtained from equations (1.12), (1.14) and (1.15) is commonly expressed in an alternative parametrization to (ρ_0, R_s), which provides more insights into the overall physical structure of the halo, namely,

$$v_{\text{NFW}}(r) = v_{200}\sqrt{\frac{\log(1+cx) - cx/(1+cx)}{x[\log(1+c) - c/(1+c)]}}, \tag{1.16}$$

where r_{200} represents the radius at which the mean density of the enclosed dark matter drops to 200 times the critical density for closure ρ_c, and it is an indicator of the halo size; v_{200} is the circular velocity at r_{200}, and it is also an indirect measurement of the halo mass through $M_{200} = \frac{v_{200}^3}{10GH_0}$; the concentration parameter, $c = r_{200}/R_s$, measures how centrally packed the dark matter is; and $x = r/r_{200}$ is simply a rescaled version of the radial coordinate.

As for the ISO model, its circular velocity profile computed from $M(< R)$ can be expressed as,

$$V_{\text{P-ISO}}(r) = \sqrt{\frac{4\pi G \rho_0 R_c^3}{r} \left[\frac{r}{R_c} - \tan^{-1}\left(\frac{r}{R_c} \right) \right]}. \tag{1.17}$$

The fit with the analytic prescriptions must be performed after subtracting the contribution of the baryonic components to the gravitational potential, i.e., the fit is done to $V_{\rm dm}$ and not to the observed rotation curve, unless the minimum disc approach is to be invoked. Yet another possibility arises when the mass-to-light ratio, which controls the amplitude of $V_{\rm disc_\star}$, is expected to be non-negligible, but it can not be assessed. In this cases some authors treat it as a free parameter to be fit simultaneously with the halo model in order to recover the full observed rotation curve (e.g. Barnes et al., 2004).

An example of the rotation curve fitting procedure is shown in figure (1.4). By means of this kind of analysis, several authors have found the pseudo-isothermal sphere formula to provide better fits to the data, mainly because the NFW profile tends to overestimate the circular velocities in the inner region of the rotation curves, where they look more like solid-body rotators. This has been traditionally interpreted as an evidence of the shallower central dark matter density profiles of real haloes with respect to those predicted by traditional ΛCDM simulations. Nevertheless, the robustness of this conclusion has been put into question by some authors, specially when the effect of systematic errors is taken into account (e.g. Swaters et al., 2003). I will dedicate Chapter 2 of this thesis to study the performance of the rotation curve fitting methods.

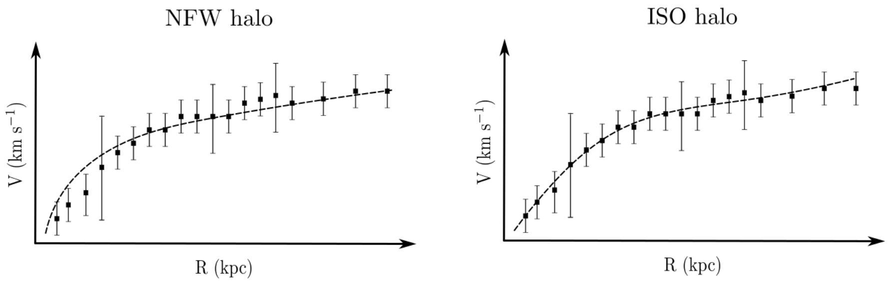

Figure 1.4: Example of a typical rotation curve fitting to differentiate cusps from cores.

1.4.3.2 Rotation curve inversion

Due to the low baryonic content of LSB galaxies and dwarf spirals, dynamical analyses of these objects often rely on the minimum disc approximation, according to which the contribution of baryons to the total gravitational potential may be treated as negligible at all radii, i.e., assuming $V_{\rm dm} \approx V_{\rm rot}$. Resorting to the assumption of spherical symmetry, this approximation motivated the use of Poisson's equation to estimate the dark matter density profile from the inversion of the observed rotation curve. Combining equations (1.5) and (1.6) the inversion relation reads (see Section 1.4.1),

$$4\pi G\rho_{\rm dm} \approx 2\,\frac{V_{\rm c}}{r}\,\frac{\rm d}{{\rm d}r}\,(V_{\rm c}) + \left(\frac{V_{\rm c}}{r}\right)^2 \tag{1.18}$$

This technique has been regularly used in the cusp-core literature after the works of de Blok et al. (2001) and de Blok and Bosma (2002), who used it to derive the density profiles of a sample of LSBs and explicitely measure their inner logarithmic slopes. Assuming an asymptotic behaviour, $\rho_{\rm inner} \sim r^{-\alpha}$, α can be assessed from a linear fit to the inner region of the density profile in the $\log(\rho)$-$\log(r)$ plane. These authors also plotted the inferred slopes as a function of the innermost velocity measurement, roughly equivalent to the spatial resolution of the observations, in order to compare them with the expectations from the Navarro-Frenk-White and the pseudo-isothermal sphere models. Typifying the slopes as a function of the position where they were measured is crucial, as the quoted models anticipate a radial dependence for this parameter. In Fig. 1.5, I present an illustrative example of the procedure just described.

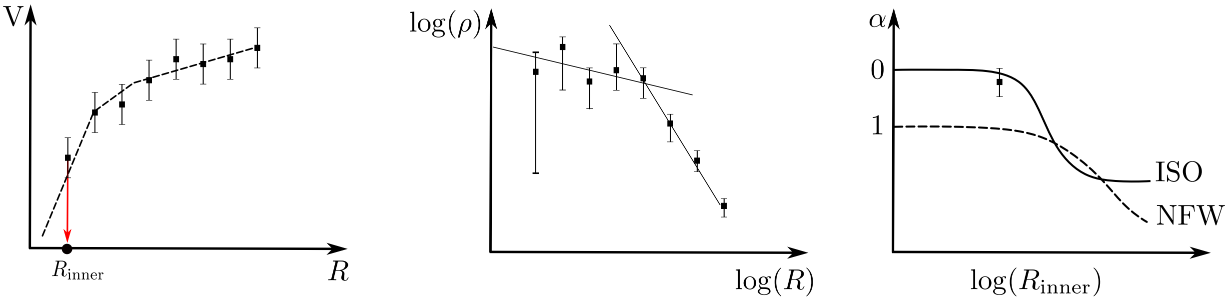

Figure 1.5: Schematic example of the rotation curve inversion method to determine the cuspyness of the dark matter halo. Left: mock rotation curve of a simulated galaxy. Middle: density profile obtained by the inversion of the rotation curve using equation (1.18), plotted in logarithmic scale. The linear fit to the first points serves to determine the inner slope α. Right: Logarithmic dark matter density slope as a function of spatial resolution, compared to typical expectations from the NFW and ISO models.

The seminal works of de Blok et al. (2001) and de Blok and Bosma (2002) inspired a number of subsequent studies, as their framework was considered a straightforward way to impose an upper limit to the true logarithmic slopes of the inner dark matter density profiles. Along similar lines several authors have alleged the existence of cores in the dark matter haloes of a multitude of dwarf spirals and LSB galaxies (e.g. de Blok et al., 2001; Kuzio de Naray et al., 2006), posing an enormous challenge for ΛCDM cosmological simulations of structure formation. For this reason, I will dedicate Chapter 3 of this manuscript to thoroughly test the ability of rotation curve inversion methods to efficiently recognize the steep density slope of dark matter cusps in realistic models of dwarfs and LSB galaxies.

1.4.4 Kinematic observations and rotation curves for cusp-core studies

The neutral hydrogen in disc galaxies is a cold dynamical component and therefore it is expected to settle down forming a thin, extended disc, which steadily rotates at the circular speed of the total gravitational potential, and rotation curves extracted from radio observations of the HI 21-cm emission have been used for decades to study the dynamics of spiral galaxies, even playing a fundamental role in the formulation of the dark matter hypothesis (e.g. Sofue and Rubin, 2001). In spite of that fact, most of the available HI data are not well suited to probe the inner region of galactic haloes because of the so-called *beam smearing* effect, which artificially smoothes out the velocity gradients in the rising part of the rotation curves, biasing their inferred shapes towards the linear solid-body rotation expected from dark matter cores. The beam smearing effect is caused by the low spatial resolution of HI observations, which 20 years ago was of the order of ~ 30 arcsec (the size of the beam), as every velocity measurement is in reality an average from all the gas under the finite area of the beam (e.g. van den Bosch et al., 2000).

Soon after beam smearing was demonstrated to be a problem for cusp-core studies (e.g. Swaters et al., 2000), HI observations were systematically replaced by optical Hα rotation curves with typical resolutions of ~ 2 arcsec (seeing limited) (e.g. Swaters et al., 2003). The enhancement in spatial resolution is remarkable but it comes at the cost of probing reduced radial extents, as the ionising radiation is confined to the stellar disc. For this reason, whenever kinematic information from both the neutral and the ionised gas phases exist, the best solution is to join them into the so-called *hybrid rotation curve*, which is simply an aggregation of the Hα data in the inner region and the HI data in the outer part (e.g. Spano et al., 2008). In this way, one keeps the best available resolution in the rising part of the rotation curve, minimising concerns about beam smearing, while hopefully reaching the flat part of the rotation curve with the radio data, which may allow imposing better constraints on the global shape of the dark matter halo. Nonetheless, as for many objects with optical rotation curves there is no HI available data, many cusp-core dynamical studies have been carried out using Hα data alone. Even though this seems acceptable for the rotation curve inversion method, it is less robust when it comes to the rotation curve fitting method, as Hα datasets frequently cover only the rising part of the rotation curves.

Early Hα rotation curves were derived from optical spectra observed through a long-slit placed along the major axis of the galaxy, where the line-of-sight component of the rotational motions is maximized. Then in 2001 the first few high-resolution velocity maps became available (Blais-Ouellette et al., 2001). 2D velocity fields are preferable over long-slit data because concerns related to possible missalignements or misscenterings of the slit disappear and, simultaneously, the enhanced spatial coverage leads to more robust estimations of the rotation curve and allows the assessment of possible systematic errors related to non-circular motions, loopsidedness, and possible shifts between the photometric and the kinematic centers. More recently, high resolution HI velocity maps (6∼12 arcsec) have also been obtained (e.g. Begum et al., 2008; Walter et al., 2008; Ott et al., 2012, among others), and some of them have been used to study the dark matter haloes of very nearby galaxies (D < 10Mpc) in order to keep the beam smearing effects under control (de Blok et al., 2008a; Oh et al., 2011b),

After this brief summary on the more relevant characteristics of former and current kinematic observations, I dedicate a few words to the way in which the "observed" rotation curve is finally defined. Basically, the two-dimensional velocity map has to be resumed into a 1D rotation curve, in close analogy to the reduction of 2D images and gas emission maps into 1D surface brigthness profiles described in Section 1.4.2.2. This can be done by resorting to a kinematic version of the tilted-ring method. Notwithstanding, note that because we are observing the line-of-sight component of the velocities instead of the true circular motions in the plane of the disc, ellipses representing points that lie at the same physical radius in the disc will not correspond with the iso-velocity contours at all. Instead of that, the velocities measured along the ellipses will resemble a sinusoidal behaviour as a function of the angular position. To better understand this fact, consider a point at a radius r in the disc that moves with velocity components $(V_r, V_{\rm rot}, V_z)$ in the (r, ϕ, z) directions; because of the projection geometry, the line-of-sight velocity that one would observe can be expressed as,

$$V_{\rm los} = V_{\rm rot} \sin(i) \cos(\theta) + V_r \sin(i) \sin(\theta) + V_z \cos(i), \tag{1.19}$$

where i represents the inclination of the disc relative to the plane of the sky (which is perpendicular to the line of sight) and θ is the azimuthal angle with respect to the major axis in the plane of the sky. After approximating a value for the inclination, one could simply assume that the disc is in perfect rotation and take the mean value of the de-projected velocities in order to partially cancel out random motions and non-circular components. Alternatively, one can apply a more robust technique like fitting a Fourier series to the measured projected velocities, including terms for the circular component, possible radial expansion motions, a constant term absorbing the systemic velocity of the galaxy and any coherent component in the z direction, and high order terms which account for the residuals. As in the case of the photometric analyses introduced in Section 1.4.2.2, the ellipticity of the rings and their positions angles may be treated as constant at all radii (e.g. Spano et al., 2008; Simon et al., 2005) or may be let free to vary from ellipse to ellipse (e.g. de Blok et al., 2008a; Oh et al., 2011b). A common methodology is to build the tilted-ring model in an iterative way, letting all parameters free to vary at the beginning, and fixing them one by one after each iteration. Sometimes the iterations are not used to fix the parameters, but to refine them until they exhibit only smooth changes as a function of radius. It is uncertain which of these approaches is more accurate and whether they might introduce systematic errors in the interpretation of the rotation curves as tracers of the underlying gravitational potential in the very inner region. This question points in the same direction of the use of the fixed/free geometrical parameters in the isophotal-fit modelling, which I will go back to in Chapter 4.

1.4.5 Potential sources of systematics

After having stated the most common procedures and methods in the cusp-core literature, it is worth mentioning that several sources of possible errors exist at different layers of the analysis, which may affect the conclusions about the shape of dark matter haloes. Below I present a list of some of the more important points, some of which will be addressed in the next chapters.

Deviations from symmetry

The mass modelling method relies on the assumption that a galaxy can be modelled as a set of perfectly symmetric components, which must also share the same center and orientation. This is of course an idealised scenario, and real systems deviate from it by different extents. In general, galaxies which are evidently far from equilibrium are avoided in the samples studied in the literature, while less dramatic asymmetries such as sizable spiral arms and soft bars are sometimes admitted (e.g. de Blok et al., 2008b). Irregular dwarfs are also extensively used for cusp-core studies in the minimum disc limit given that they are very dark-matter dominated systems (e.g. Oh et al., 2011). Nevertheless, as the α slope is often estimated from very few points close to the galactic center, it is not obvious that the effect of baryonic asymmetries in the measured velocities can be ignored. Deviations from symmetry are also manifested in the tilted ring modelling of the stellar discs, appearing as twists, shifts, or changes in the ellipticity of the fitting ellipses as a function of radius. These radial trends are almost ubiquitous and different works treat them in different manners. While some authors only consider galaxies where all geometrical parameters can be approximated as constant with radius (e.g. Simon et al., 2003a), in most cases these parameteres are let unconstrained (e.g. Oh et al., 2011), in spite of the fact that such a treatment can not be formally reconciled with the idea of simplified axisymmetric components that lie in the heart of the mass modelling technique. The same comments are valid for the reduction of a 2D velocity map into a 1D rotation curve. In fact, an ideal disc model should be well fit using the same constant value of each geometrical parameter for the tilted-ring model of the photometry, of the gas intensity map, and that of the kinematics, a constraint that is virtually never imposed and is only sometimes checked out for consistency.

Pressure support and non-circular motions

When it comes to dynamical analyses, it is worth noting that observed rotation curves may deviate from the circular velocity profile of the gravitational potential for several reasons. In first place, observations often target gaseous tracers which are subject to hydrodynamical forces in addition to the gravitational ones. Particularly, pressure gradients may offer partial support against the gravitational collapse of the gaseous disc, reducing the necessary rotational velocity for centrifugal equilibrium (e.g. Dalcanton and Stilp, 2010). This so-called *pressure support* effect is usually neglected in rotation curve studies, as some observational analyses suggest that it is generally very small (e.g. de Blok and Bosma, 2002). Nevertheless, considering that observations are always biased at some extent because they target a specific gas phase (neutral or ionised, for instance), and that they may be affected by additional instrumental effects, I revisit the question of whether or not pressure support can be accurately diagnosed and corrected in the central part of gas-rich galaxies in Chapter 2.

Non-circular motions related to streaming velocities and random components injected by, for example, super novae explosions, are also a concern. Even though the amount of non-circular motions can be quantified from 2D velocity maps, this only serves to check if they are low enough as to not interfere with the mass modelling approximation, but their true effect on dynamical studies can not be modelled from first principles. This is particularly concerning in the inner regions, where there are very few measurements per elliptical ring and the stochasticity introduced by non circular motions may bias the final rotation curve. The same is true for long-slit data, but in that case deviations may occur at all radii, causing the noisy appearance and wiggles often present in long slit rotation curves.

Beam smearing, distance, and inclination

Beam smearing is also a concern for optical data, in spite of the enhanced spatial resolution of optical data with respect to early radio observations. This is because the *physical* spatial resolution is not only given by the *angular* resolution of the instrument, but also by the galaxy distance. Therefore, even in Hα, beam smearing may play a role for the observations of distant galaxies (Swaters et al., 2003). However, there are many examples of samples of galaxies more distant than 10 Mpc. Fig. 2 of Spekkens et al. (2005), for instance, presents a sample including galaxies which are quite distant and were used for the study of the cusp-core problem. It shows that there is only one galaxy closer than 10 Mpc, seven galaxies inside 20 Mpc, and about 75% of the sample is beyond 50 Mpc, with a few galaxies as far as 200 Mpc. This is not an isolated case. Many of these galaxies came from Mathewson et al. (1992), whose data was later reprocessed by Persic and Salucci (1995), and served for a number of cusp-core studies (e.g. Salucci and Burkert, 2000; Salucci, 2001). To avoid this complication, recent papers like Oh et al. (2011b) have focused on very nearby galaxies ($D < 5$ Mpc), earning excellent spatial resolution at the cost of keeping much smaller samples (~ 10 galaxies). The beam smearing effect is also exacerbated by projection effects due to inclination. Strikingly, the corresponding histogram in Fig. 2. of Spekkens et al. (2005) shows that around 75% of their sample galaxies are more inclined than 70°. This paper is mentioned here again just because the quoted histograms allow a quick-view assessment of the point in debate, but several other cusp-core works included some highly inclined galaxies in their samples as well. This might have unfairly increased the fame of the cusp-core problem.

Mass-to-light ratios and stellar bulges

Regarding the mass-to-light relations from Bell and de Jong (2001), which became a standard tool in cusp-core studies, it is very important to raise awareness on several facts that may limit their applicability in certain situations. For example note that they were derived for late-type disc galaxies without bulges, and the authors explicitely mention that their models are not expected to be useful to study galaxies of earlier morphological types. Bell and de Jong also stated that their firmer constraint was given by the slope of the correlations between mass-to-light ratios and the colours of the galaxy; the zero point of these correlations was calibrated independently, studying rotation curves observations of a sample of galaxies in the Ursa Major cluster under the maximum disc approximation. As several authors suggest that submaximal discs are very common in the local Universe (e.g. Martinsson et al., 2013), this implies that the masses assessed through the Bell and de Jong relations are likely upper limits rather than exact indicators of their true values (de Jong and Bell, 2007). Other concerns have to do with the models of spectrophotometrical evolution of galaxies and the libraries of stellar population SEDs, which may lack sensible ingredients even today. For example Meidt et al. (2014), who aim to draw accurate stellar mass maps using SPITZER data, discuss the fundamental necessity of subtracting the light contamination from PAHs, hot dust, and stars from the assymptotic giant branch (AGB) and red supergiants (RSG), which have a small contribution to the mass but emit considerable amounts of light, biasing the inferred mass-to-light ratios in infrared bands towards higher values. Uncertainties in the mass-to-light ratios are actively debated in the literature without a strong consensus (see e.g. McGaugh and Schombert, 2014).

Regarding the mass modelling of galaxies with bulges, the problem is that they add a layer of uncertainty to the inferred cuspyness of the dark matter haloes, mainly as a result of the uncertain mass-to-light ratio of this component which strongly influences the dynamics of the central region. Bulges also make the interpretation of the mass distribution more uncertain because they force the analyses to assume that the exponential disc continues all the way to the center of the galaxy, a fact that has been put into question.

Finally I would like to highlight that, in spite of the fact that many authors defend the authentic existence of cored galactic haloes based on mass modelling studies, a considerable number of studies find the observational data to be consistent with cuspy haloes as well, particularly when the sources of systematic errors are take into account (e.g. van den Bosch et al., 2000; Swaters et al., 2003; Barnes et al., 2004; Rhee et al., 2004; Spekkens et al., 2005), and some works do also find intermediate slopes, e.g. $\alpha \sim 0.7$ (e.g. Simon et al., 2005; Adams et al., 2014). For unclear reasons these conclusions have received much less attention, and a large fraction of the astronomical community assumes that the existence and prevalence of galactic dark matter cores is an unquestionable fact. Also note that, given the number of potential errors related to distance, inclination, lack of symmetry, etc., it is naive to expect that samples of hundreds of galaxies which can be modelled as ideal even in the very center and for which the data is of sufficient resolution etc., can be found. For these reason, I would say that those studies using massive samples such as Spekkens et al. (2005) should be revisited carefully, as well as those which were based on low-resolution HI data and long-slit observations, which are subject to even more sources of problematic errors. Taking that into account, the number of studies and the number of galaxies suitable to be considered as very robust for cusp-core studies, reduce dramatically.

1.5 This thesis

This project intends to gain new insights into the dynamics of galaxies by jointly using numerical simulations and observational data. It tries to look for the best way to fairly compare these two approaches, incorporating up-to-date models and techniques from both fields.

As I described in the former sections, even though the mass modelling of galaxies is a very interesting and useful approach, there are a large number of possible systematic errors which may affect observational studies, especially in the case of the cusp-core problem. Incidentally, some preliminary experiments that I performed at an early stage of my PhD, modelling a small sample of galaxies for which CCD images and velocity maps were available, show me how intricate real systems are in comparison with simple geometrical models (see Appendix A). As a side effect, these tests brought me some doubts about the suitability of mass modelling approaches to faithfully uncover the very inner structure of the dark matter haloes of galaxies.

This was the paramount motivation for the main component of my PhD research investigation, which consists in a set of thorough controlled experiments, carefully designed to validate the accuracy of mass modelling techniques using forefront, self-consistent numerical simulations of isolated galaxies and radiative transfer models.

The structure of this thesis is the following.

In Chapter 2 I present part of my work with numerical simulations. There I present an extensive, thorough study of the dynamics of 6 simulated dwarf galaxies for which I created mock realistic kinematic observations of the gaseous component, that were later analysed in the very same way as it is done with real data in the cusp-core context. Dwarf spirals and low surface brightness galaxies have played a fundamental role in the the cusp-core controversy because of their low baryonic content, which should in principle make the measurement of their dark matter haloes structure more straightforward. The main aim of Chapter 2 is to determine the accuracy of the rotation curve fitting methods to recognize the signature of a cuspy dark matter halo, both from ideal theoretical measurements as well as from mock realistic kinematic observations.

In Chapter 3 I present further theoretical analyses of the data set introduced in Chapter 2. There I focus on the determination of the ability of rotation curve inversion methods to determine the real logarithmic slope of a dark matter halo from the inner part of a velocity profile, and on the possibility of correcting for pressure support effects from observationally accessible information. Several methods employed in influential works of the cusp-core literature are studied in order to determine their strengths and drawbacks.

In Chapter 4 I present numerical simulations of more massive spiral galaxies, for which the minimum disc approximation is not suitable. The final goal of the work initiated in Chapter 4 is to investigate if the radial distribution of the stellar component may be truly estimated from multi-band images. For this I resort to forefront radiative transfer models, which allow the creation of realistic images from simulated galaxies. The general framework is introduced and I present some preliminary results.

Finally in chapter 5 I present a summary of this investigation, my conclusions, and some perspectives of the future work that may be done in order to give continuity to this line of research.

Chapter 2

May cusps be disguised as cores?

As discussed in the introduction, the mass modelling of galaxies is a very useful approach, but there are a number of difficulties that may prevent its application in real systems. Unfortunately, in general the factual effect of deviations from ideal models can not be determined theoretically, and even the study of non-perturbed galaxies with high-quality observations has a considerable degree of uncertainty. The question is then: what observations and methods have to be used in order to differentiate cusps from cores? An interesting way of approaching this problem is by means of numerical simulations, as this is the closest we will ever be of fabricating a galaxy in a laboratory. So, in order to learn more about the true performance of rotation curves studies I run a set of controlled experiments using mock observations of simulated galaxies. The results described here and in the following chapter are focused in the minimum disc approximation, because it has played a major role in the history of the cusp-core problem and because it dismisses the estimation of the baryonic mass distributions, which is known to be a problematic source of uncertainties. In this way, i.e. by starting from a scenario which is known to be the least affected by errors, a comprehensive analysis disentangling individual effects is more suitable. This chapter includes the largest body of interesting, original results obtained during this thesis. They have been already put into a paper in collaboration with Dr. Volker Springel, Dr. Chris Hayward, and Dr. Claudia Mendes de Oliveira, which has been already accepted for publication (Pineda et al., 2016). Here I reproduce the text of the paper –before the final editing by the MNRAS editorial team–, with the exception of one section which fits better in the next chapter of this thesis. Some stylistic differences exist in the text from the paper and the rest of the thesis, but I keep them in order to ensure full consistency with the published work.

MNRAS (2016) Preprint 9 November 2016 Compiled using MNRAS LaTeX style file v3.0

Rotation curve fitting and its fatal attraction to cores in realistically simulated galaxy observations

Juan C.B. Pineda[1]*, Christopher C. Hayward[2,3,4], Volker Springel[5,6] and Claudia Mendes de Oliveira[1]

[1] *Instituto de Astronomia, Geofísica e Ciências Atmosféricas, Universidade de São Paulo, R. do Matão 1226, 05508-090 São Paulo, Brazil*

[2] *Center for Computational Astrophysics, 160 Fifth Avenue, New York, NY 10010, USA*

[3] *TAPIR 350-17, California Institute of Technology, 1200 E. California Boulevard, Pasadena, CA 91125, USA*

[4] *Harvard–Smithsonian Center for Astrophysics, 60 Garden Street, Cambridge, MA 02138, USA*

[5] *Heidelberger Institut für Theoretische Studien, Schloss–Wolfsbrunnenweg 35, 69118 Heidelberg, Germany*

[6] *Zentrum für Astronomie der Universität Heidelberg, Astronomisches Recheninstitut, Mönchhofstr. 12-14, 69120 Heidelberg, Germany*

Submitted to MNRAS

ABSTRACT

We study the role of systematic effects in observational studies of the core/cusp problem under the minimum disc approximation using a suite of high-resolution (25-pc softening length) hydrodynamical simulations of dwarf galaxies. We mimic realistic kinematic observations and fit the mock rotation curves with two analytic models commonly used to differentiate cores from cusps in the dark matter distribution. We find that the cored pseudo-isothermal sphere (ISO) model is strongly favoured by the reduced χ^2_ν of the fits in spite of the fact that our simulations contain cuspy Navarro-Frenk-White profiles (NFW). We show that even idealized measurements of the gas circular motions can lead to the incorrect answer if velocity underestimates induced by pressure support, with a typical size of order $\sim$5 km s^{-1} in the central kiloparsec, are neglected. Increasing the spatial resolution of the mock observations leads to more misleading results because the inner region, where the effect of pressure support is most significant, is better sampled. Fits to observations with a spatial resolution of 100 pc (2 arcsec at 10 Mpc) favour the ISO model in 78-90 per cent of the cases, while at 800-pc resolution, 40-78 per cent of the galaxies indicate the fictitious presence of a dark matter core. The coefficients of our best-fit models agree well with those reported in observational studies; therefore, we conclude that NFW haloes can not be ruled out reliably from this type of analysis.

Key words: cosmology: theory – dark matter – galaxies: dwarf – galaxies: haloes – galaxies: kinematics and dynamics – galaxies: structure.

MNRAS Advance Access
Published: November 22, 2016

Downloaded from:
http://mnras.oxfordjournals.org/

---

* Contact e-mail: basto-pineda@usp.br

© 2016 The Authors

2.1 Introduction

In the last decades, cosmological numerical simulations based on the ΛCDM concordance model have substantially improved our understanding of the dynamical evolution of the Universe on large scales (Davis et al., 1985; Springel et al., 2005; Boylan-Kolchin et al., 2009; Angulo et al., 2012; Klypin et al., 2014). More recently, it has also become possible to include baryons in large cosmological volumes and directly follow galaxy formation, with very promising results (Vogelsberger et al., 2014; Schaye et al., 2015a). However, a number of well documented small-scale discrepancies between ΛCDM and observations still remain to be understood, including the so-called *cusp-core* problem concerning the inner structure of galactic dark matter haloes (Flores and Primack, 1994; Moore, 1994). On one hand, dark matter (DM) haloes assembled in cosmological simulations exhibit *cuspy* radial density profiles which steeply increase towards the center (Navarro et al., 1996b, 1997; Moore et al., 1999; Klypin et al., 2001; Navarro et al., 2004; Diemand et al., 2005; Stadel et al., 2009). They are fairly well represented by the Navarro, Frenk e White (1996b, hereafter NFW) fitting formula, with an asymptotic behaviour of $\rho_{\text{inner}} \propto r^{-1}$. On the other hand, kinematic observations of disc galaxies (via rotation curves) and dwarf spheroidals (via stellar velocity dispersions) often seem to be more compatible with core-like DM haloes ranging from $\rho_{\text{inner}} \propto r^{0}$ to $\rho_{\text{inner}} \propto r^{-0.3}$ (Flores and Primack, 1994; de Blok et al., 2001; Salucci, 2001; de Blok and Bosma, 2002; Kuzio de Naray et al., 2006; Spano et al., 2008; Oh et al., 2011b; Walker and Peñarrubia, 2011; Oh et al., 2015). A number of studies have also inferred intermediate slopes, which do not evidence constant-density cores but still are substantially shallower than canonical cusps from simulations (Simon et al., 2005; Adams et al., 2014).

Several physical mechanisms have been proposed to reconcile these findings and explain the origin of DM cores. The current leading picture invokes repetitive starburst episodes and the associated SNe feedback to blow out central baryons and induce rapid changes in the gravitational potential (Navarro et al., 1996b; Gelato and Sommer-Larsen, 1999; Read and Gilmore, 2005; Mashchenko et al., 2008; Governato et al., 2010a, 2012; Pontzen and Governato, 2014; Madau et al., 2014; Chan et al., 2015; Oñorbe et al., 2015). However, many feedback implementations do not form cores (Lia et al., 2000; Gnedin and Zhao, 2002; Ceverino and Klypin, 2009), which has not precluded the formation of realistic galaxies

(Sawala et al., 2010; Marinacci et al., 2014) as well as realistic populations of galaxies at $z = 0$ in fully cosmological runs (Vogelsberger et al., 2014; Schaller et al., 2015). Also, there are lingering doubts (Garrison-Kimmel et al., 2013) regarding whether the available supernova energy is actually sufficient to create cores of the alleged size.

From the observational point of view, a problematic issue of using rotation curves to probe the DM density profiles is to accurately account for the stellar gravitational potential, mainly because of the uncertain mass-to-light conversion factor (van Albada et al., 1985b; Bell and de Jong, 2001; Bershady et al., 2010). One way around this problem lies in studying dark matter-dominated systems, such as late-type dwarf irregulars and low surface brightness (LSB) galaxies. For these systems, it is acceptable to use the minimum disc approximation, i.e. to ignore the existence of baryons and use the observed rotation curves at face value to derive an indicative upper limit on the amount of DM (de Blok and McGaugh, 1997; de Blok et al., 2001; Spekkens et al., 2005; Kuzio de Naray et al., 2006). Furthermore, different observations suggest that LSBs are characterized by a comparatively quiescent evolution, which likely implies relatively unperturbed DM haloes, making them very interesting for cosmology (de Blok et al., 1995; Impey and Bothun, 1997; Du et al., 2015). Indeed, these kinds of galaxies have been a main target of observational studies and represent some of the most acute challenges for the ΛCDM cosmogony, as their rotation curves are interpreted by several authors as strong evidence for DM cores (de Blok et al., 2001; de Blok and Bosma, 2002; Simon et al., 2003b; Oh et al., 2011b, 2015). However, some studies find some dwarfs and some LSB galaxies to be compatible with CDM cusps or claim that available data simply does not allow to differentiate cusps from cores (e.g. van den Bosch et al., 2000; van den Bosch and Swaters, 2001; Swaters et al., 2003; Spekkens et al., 2005; Simon et al., 2005; Valenzuela et al., 2007). The systematic uncertainties involved in studying this problem are a matter of active debate in the literature.

A number of effects that may lower the inner rotation curves and potentially mask cusps and make them appear as cores have been investigated over the years. For instance, early H I rotation curves had poor spatial resolution and were considerably affected by beam smearing. This motivated the gathering of high-resolution optical data for which beam smearing is expected to no longer be a problem (Blais-Ouellette et al., 1999; Swaters et al., 2000), though it may still play a role in the very inner measurements, specially for distant galaxies (Swaters et al., 2003). More recently, some surveys of H I in very nearby galaxies, like THINGS (Walter et al., 2008) and LITTLE THINGS (Hunter et al., 2012) (amongst others, e.g., Begum et al., 2008; Ott et al., 2012), have also reached the necessary resolution to alleviate beam smearing concerns. The first H α rotation curves were obtained from long-slit spectroscopy, with the associated risk of missing the kinematic center of the galaxy or its major axis; fortunately, this is no longer an issue since high-resolution velocity fields have become available (Blais-Ouellette et al., 2001; Garrido et al., 2002). Other problems that can be assessed by means of 2D velocity maps are possible offsets between the photometric and kinematic centers and the presence of non-circular motions (Simon et al., 2005; Oh et al., 2008b). A detailed analysis of these effects for a sample of 19 galaxies from THINGS was presented by Trachternach et al. (2008), who concluded that these effects are rather small and the sample is hence suitable for the mass modeling studies presented in de Blok et al. (2008a).

Projection effects related to the thickness of gaseous discs are also potentially problematic because mixing of material along the line-of-sight tends to lower the inferred circular velocity (Rhee et al., 2004). Additionally, pressure exerted by the gas can effectively lower the gravitational radial acceleration, thus lowering the rotational velocity needed for support. With very few exceptions (e.g. Oh et al., 2011b), pressure support corrections are usually neglected because they are expected to be small (de Blok and Bosma, 2002). Halo triaxiality has also been considered as a possible explanation for the core-cusp discrepancy (Hayashi et al., 2007), but using both observations and numerical modelling, other authors have argued that this is not likely to be the case (Simon et al., 2005; Kuzio de Naray et al., 2009b; Kazantzidis et al., 2010; Kuzio de Naray and Kaufmann, 2011). Besides all the potential complications already mentioned, we note that galaxies are often irregular and present substructures such as bars, bulges, and spiral arms. In addition, rotation curves are often wiggled, warped, or lopsided. The interpretation of these features and their impact on the cusp-core problem is not clear and cannot be modelled from first principles.

A powerful approach to study these systematic effects is by means of controlled experiments with simulated data. The first attempts in this direction mimicked long-slit observations of analytic velocity fields, including some uncertainties. In this way, de Blok et al. (2003) concluded that it should be possible to recognize the real steepness of a DM halo from its measured rotation curve and that no single systematic effect can account for the cusp-core difference. However, following the same approach, Swaters et al. (2003)

concluded that systematic effects tend to erase the signature of cusp-like haloes and that rotation curve analyses cannot compellingly rule out the presence of cusps. Similarly, Spekkens et al. (2005) found cuspy DM haloes to be consistent with the observed distribution of slopes once systematic effects are taken into account. Dutton et al. (2005) pointed out that uncertainties inherent in mass modelling studies prevent them from setting firm constraints on the shape of DM haloes. Kuzio de Naray et al. (2009b) did not use analytic velocity fields but instead integrated orbits numerically. They mimicked 2D integral field unit (IFU) data using a reference sample of observations and concluded that if present at all, NFW haloes should be still recognizable. However, although these kinds of models provided useful insights into the problem, they were clearly oversimplifications. For instance, with the exception of Dutton et al. (2005), these studies assumed infinitely thin massless discs, and none included hydrodynamics.

Rhee et al. (2004) brought analyses of observations and simulations closer together. They performed N-body simulations of stellar discs inside cuspy haloes and *observed* them in a realistic manner, concluding that projection effects, small bulges, and bars can often lead to false detections of DM cores. Valenzuela et al. (2007) confirmed these results using simulated analogs of the dwarf galaxies NGC 3109 and NGC 6822. They also compared a pure N-body simulation with hydrodynamical runs and suggested that pressure support related to stellar and supernova feedback can also produce the illusion of cores. A different result from similar simulations was presented by Kuzio de Naray and Kaufmann (2011). They concluded that the signatures of cores, cusps, and triaxiality in DM haloes should be clearly detectable in observed velocity fields. In recent work, Oh et al. (2011) analysed mock observations of two dwarf galaxies formed in zoom-in cosmological simulations that undergo the supernovae-driven cusp-to-core transformation (Governato et al., 2010a) and compared them with a sample of dwarfs from the THINGS survey. Oh et al. (2011) found that their mock observations trace the true rotation curves and true surface density profiles of the simulated galaxies fairly well. They also state that their simulations are a good match to real galaxies regarding these quantities, but Oman et al. (2015) showed that the alleged agreement is only apparent in some cases. Moreover, Oman et al. (2015) demonstrated that the diversity of dwarf galaxy rotation curves is much greater than that of galaxies formed in cosmological simulations, posing a new challenge to any model trying to solve the cusp-core problem. Recently, Read et al. (2016) addressed this question using mock observations from a suit of very high-resolution (4 pc) simulations and indicate that at least part of the observed diversity can be explained from the starburst cycles of galaxies and their influence on the dynamical state of the galaxy.

Given the body of in part contradictory conclusions in the literature, it is apparent that further investigations of potential systematic effects in observational inferences about the cusp-core problem are worthwhile. In this work, we carry out a comprehensive theoretical study of the kinematics of a set of simulated dwarf galaxies by carefully creating synthetic observations that are then analysed in exactly the same manner as real data. In this way, we can determine the effects of different sources of error in the context of the cusp-core problem and assess to what extent these errors can lead to misleading inferences about the structure of the analysed galaxies. Here we focus on the minimum disc approximation, exploting the fact that our models are dark matter dominated at all radii, and we only use rotation curve fitting to classify cusps and cores; a complementary analysis using rotation curve inversion methods will be presented in a separate paper, as they demand a different approach.

The outline of the paper is as follows. In Sec. 2.2 we present our simulated galaxy sample and summarize the simulation methodology. In Sec. 2.3 we introduce the methods we use to analyse the information from the snapshots. In Sec. 2.4 we present the dynamical evolution of the different components, the mock observed rotation curves, and the results from the rotation curve fitting methods that aim to distinguish cusps from cores. In Sec. 2.5 we discuss the systematic effects that influence these results, aiming to disentangle the effects of spatial resolution, inclination, pressure support, etc. Finally, in Sec. 2.6 we present our conclusions and a summary of our results.

2.2 Simulations

2.2.1 Physical characteristics of the simulated galaxies

We simulate six dwarf galaxies in isolation at high resolution using the N-body+smoothed-particle hydrodynamics (SPH) code GADGET-2 (Springel, 2005). Each simulation is composed of a dark matter halo plus an exponential disc of stars and gas, as summarised in Table 2.1. The methods for creating the numerical realizations of the initial conditions are essentially the same as described in Springel (2005) and Cox (2004). Here we hence focus on the motivation for choosing the physical parameters of the galaxies and only briefly mention the most relevant technical details.

Galaxy models 'Dwarf1' to 'Dwarf4' (or simply D1,..., D4) are representative of the bulk of the properties of observed dwarf spirals and LSBs (e.g. de Blok and Bosma, 2002; Spekkens et al., 2005; de Blok et al., 2008a; Kuzio de Naray et al., 2008b, 2009b; Stark et al., 2009; Oh et al., 2011b). These four galaxies are constructed to lie on the stellar and baryonic Tully-Fisher relations (TF) of Bell and de Jong (2001). Notice that if both TF relations are required to be satisfied simultaneously, this puts a constraint on the gas fraction as a function of the stellar mass. Using representative values from Bell and de Jong (2001), we define the following target relations:

$$\log(M_\star) = 0.83 + 4.34\log(V_{\rm flat}), \tag{2.1}$$

$$f_g = \frac{M_{\rm gas}}{M_{\rm gas}+M_\star} = 1 - \frac{M_\star^{0.21}}{170}, \tag{2.2}$$

where $M_\star$ and $M_{\rm gas}$ are the total masses of the stellar and the gaseous discs, f_g is the gas fraction, and $V_{\rm flat}$ is the maximum circular velocity. The radial stellar and gaseous distributions drop exponentially, with surface density profiles given by

$$\Sigma_\star(r) = \frac{M_\star}{2\pi h_0^2}e^{-r/h_0}, \tag{2.3}$$

$$\Sigma_{\rm gas}(r) = \frac{M_{\rm gas}}{2\pi h_{\rm gas}^2}e^{-r/h_{\rm gas}}. \tag{2.4}$$

The stellar scale lengths are chosen to be relatively large (but still realistic) in order to give our galaxies a low surface brightness. We make the gaseous discs three times more extended than the stellar ones as suggested by observations (Broeils and van Woerden, 1994).

The vertical structure of the stellar discs follows a typical $\text{sech}^2(z/z_0)$ model with the scale height z_0 equal to one fifth of the radial scale length h_0, so their 3D density fields read

$$\rho_\star(r,z) = \frac{M_\star}{4\pi h_0^2 z_0}e^{-r/h_0}\text{sech}^2(z/z_0). \tag{2.5}$$

For gaseous discs the vertical structure is self-consistently calculated considering the full gravitational potential and assuming hydrodynamic equilibrium under a given equation of state that we choose to be the multiphase model of Springel and Hernquist (2003).

Table 2.1 - Properties of the six simulated galaxies.

Model	$M_{\rm halo}$[a] ($\rm M_\odot$)	$N_{\rm halo}$[b] ($\times10^6$)	c[c]	$M_\star$[d] ($\rm M_\odot$)	$N_\star$[e] ($\times10^6$)	h_0[f] (kpc)	z_0[g] (kpc)	$M_{\rm gas}$[h] ($\rm M_\odot$)	$N_{\rm gas}$[i] ($\times10^6$)	$h_{\rm gas}$[j] (kpc)	f_g[k]	$V_{\rm flat}$[l] (km $\rm s^{-1}$)
Dwarf1	3.0×10^{10}	1.5	11	1.2×10^{8}	0.1	0.8	0.16	3.7×10^{8}	0.3	2.4	0.76	57
Dwarf2	7.0×10^{10}	3.5	11	6.0×10^{8}	0.5	1.7	0.34	1.1×10^{9}	0.9	5.1	0.65	78
Dwarf3	1.2×10^{11}	6.0	10	1.2×10^{9}	1.0	2.5	0.5	1.6×10^{9}	1.4	7.8	0.57	89
Dwarf4	2.6×10^{11}	6.5	10	6.0×10^{9}	1.2	3.0	0.6	3.4×10^{9}	0.7	9.0	0.36	119
G0	5.1×10^{10}	1.3	14	1.0×10^{9}	0.2	1.1	0.22	6.1×10^{8}	0.1	3.3	0.38	67
G1	2.0×10^{11}	5.0	12	5.0×10^{9}	0.3	1.5	0.3	2.0×10^{9}	0.1	4.5	0.29	103

Note: [a]Halo mass; [b]Number of particles in DM halo; [c]Halo concentration; [d]Stellar mass; [e]Number of stellar particles; [f]Stellar disc scale length; [g]Stellar disc scale height; [h]Gas mass; [i]Number of gas particles; [j]Gaseous disc scale length; [k]Gas fraction relative to baryonic mass; [l]Maximum rotation velocity.

Dark matter haloes are modelled with the cuspy NFW density profile (Navarro et al., 1996b). We did not simulate cored haloes because several mechanisms that might cause cusps to appear as cores have been proposed, but no mechanisms that can cause cores to appear as cusps are known. Moreover, to provide a potential solution to the cusp-core problem, it is only necessary to demonstrate that cusps can be mistaken for cores. The original NFW formulation is

$$\rho_{\text{NFW}}(r) = \frac{\rho_0}{(r/R_s)[1+(r/R_s)]^2}. \tag{2.6}$$

In equation (2.6), ρ_0 is a characteristic density and R_s represents a transition radius between an inner and an outer exponential law ($\rho_{\text{inner}} \sim r^{-1}$; $\rho_{\text{outer}} \sim r^{-3}$). An alternative parametrization that provides easier comprehension of the halo structure is obtained by casting the enclosed mass into a circular velocity profile,

$$v_{\text{NFW}}(r) = v_{200}\sqrt{\frac{\log(1+cx) - cx/(1+cx)}{x[\log(1+c) - c/(1+c)]}}, \tag{2.7}$$

with v_{200} representing the circular velocity at r_{200}, the radius at which the halo mean density is 200 times the critical density for closure[1]. The parameter $c \equiv r_{200}/R_s$ measures the central concentration of the mass distribution, and $x \equiv r/r_{200}$.

For each galaxy, the halo mass is chosen as a function of the stellar mass following the abundance matching relation of Guo et al. (2010). The concentrations are determined using the halo mass-concentration relation at redshift zero (Ludlow et al., 2014), which is a fundamental outcome of large cosmological simulations. Guo et al. (2010) used the Chabrier (2003) initial mass function (IMF), whereas Bell and de Jong (2001) used a scaled-down Salpeter (1955) IMF, giving rise to a systematic difference of 0.15 dex in stellar mass. For this reason, we add 0.15 dex to the actual stellar mass when we use equations (2.1) and (2.2) to define the target V_{flat} and f_g, respectively. Compared to the stellar masses at face value, this increment raises the target circular velocities by 8 per cent and the target gaseous masses by 10 to 25 per cent.

Once we have defined an initial configuration, we create the corresponding initial conditions file and check if V_{flat} actually satisfies the TF relations inside the expected scatter, slightly adjusting the halo parameters otherwise. As a side effect of this tuning, the less

---

[1] Notice that v_{200} encodes the halo mass through $M_{200} = v_{200}^3/(10GH_0)$; we use $H_0 = 70$ km s^{-1} Mpc^{-1}.

massive galaxies, D1 and D2, end up with DM haloes that are less massive than predictions from the abundance matching target relation. Nevertheless, through a comparison with different samples from the literature, Oh et al. (2011b) has noted that this is not at odds with observations of low-mass galaxies, for which the abundance matching relation of Guo et al. (2010) is not directly constrained but rather represents an extrapolation to smaller masses.

We also checked that our galaxies are consistent with the baryonic TF relation of Stark et al. (2009), which was calibrated specifically using small, gas-rich galaxies (mainly dwarf galaxies and LSBs). Additionally, we require V_{flat} to stay below 130 km s^{-1}, following the selection criterion of Spekkens et al. (2005) to characterize a galaxy as a dwarf. We note that galaxy models D1 to D4 retain well-behaved discs throughout the simulation. There are neither detectable signatures of central bulge-like mass concentrations nor formation of bars, spiral arms, or other baryonic substructures (see Figs. 2.1 and 2.2).

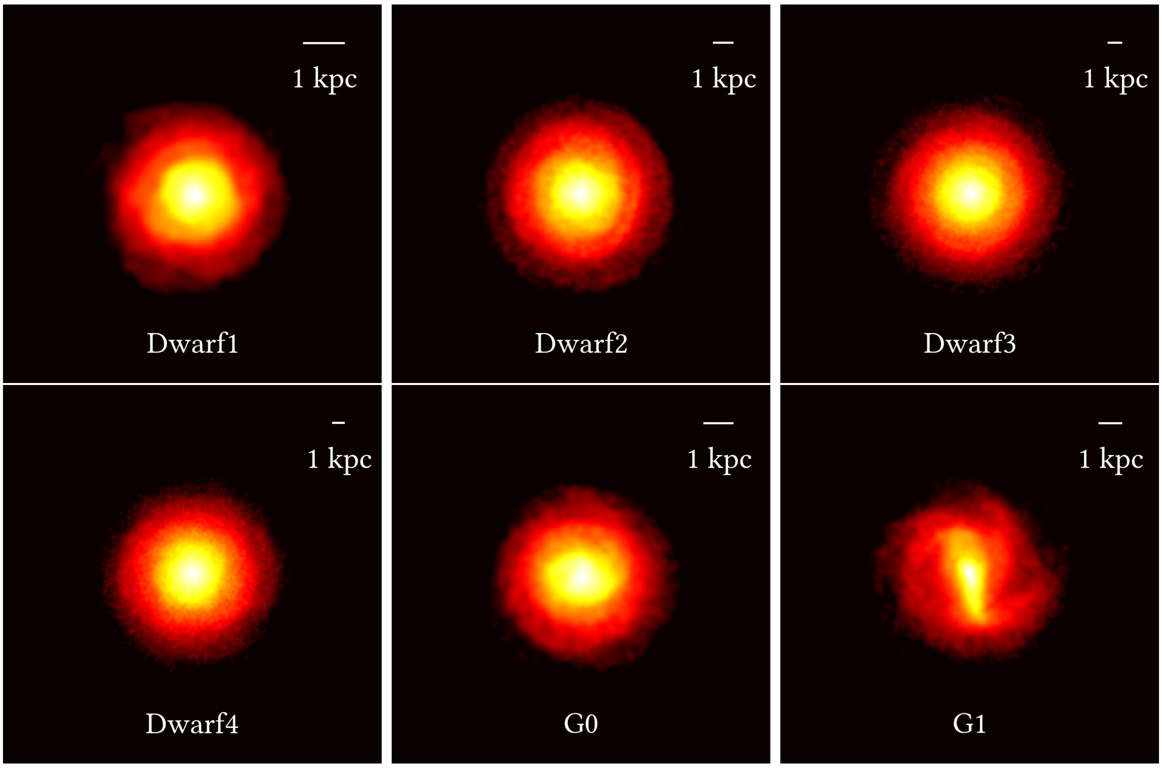

Figure 2.1: Face-on stellar density maps of our simulated galaxies at half the simulation time (3 Gyr). Note that with the exception of G1, the simulated galaxies do not exhibit non-axisymmetric structures such as spiral arms or bars.

We also re-simulated two galaxies from the sample of Cox (2004). These models are, by construction, representative of late-type galaxies in the local universe, as their main

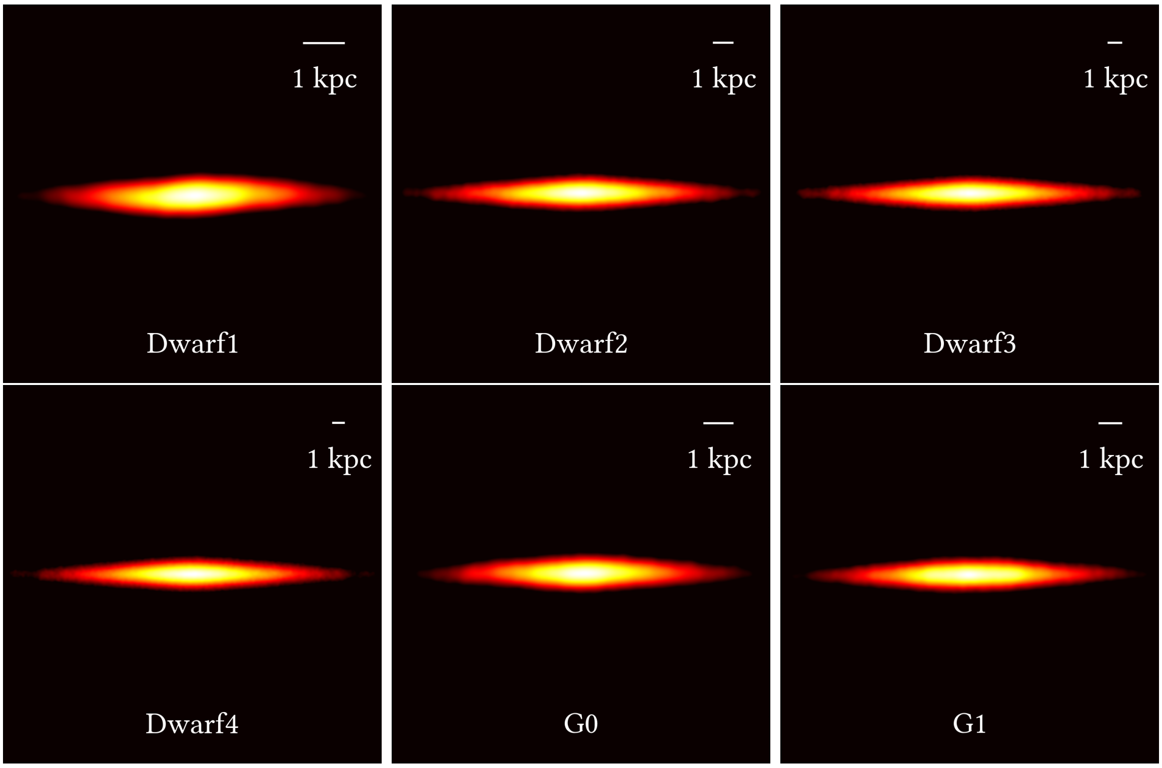

Figure 2.2: Edge-on stellar density maps after 3 Gyr of evolution. Our galaxies do not form bulge-like central concentrations of matter. This fact is confirmed by the lack of central peaks in the circular velocity profiles of the stellar component $V_\star$ in Fig. 2.5.

properties, such as disc size, dynamical mass, and gas fraction, are consistent with a large set of observations (Roberts and Haynes, 1994). From the sample of Cox (2004), we only included the systems with $V_{\mathrm{flat}} < 130$ km s^{-1}, G0 and G1. The DM haloes exhibit NFW density profiles with numerical parameters tuned to match the baryonic TF relation from Bell and de Jong (2001). We note that these parameters are quite consistent with the scheme we propose for Dwarfs 1 to 4 regarding the stellar mass-halo mass and halo mass-concentration relations. G0's halo mass is lower than the abundance matching prediction, but it is consistent with observed galaxies of similar mass, as already discussed for D1 and D2. A major difference between our models and Cox (2004) is that we omitted the bulge component in the initial set up. To minimize perturbations in the original target relations we redistribute the bulge mass into the disc, conserving the total stellar mass. Nevertheless, a central matter concentration builds up in the case of G1, resulting in the formation of a strong bar (see Fig. 2.1).

2.2.2 Simulation technique and numerical parameters

The specific version of GADGET-2 we use includes radiative cooling of the gas and a sub-resolution multiphase model for the interstellar medium that models the effects of star formation and stellar feedback (Springel and Hernquist, 2003). Neither black hole accretion nor AGN feedback is included because we want to study highly symmetric galaxies with non-perturbed kinematics, for which black hole growth is expected to be small.

Each galaxy is simulated for a period corresponding to six billion years, with snapshots (i.e. time slices) stored every one hundred million years, which is comparable to the orbital time for particles inside the first few kiloparsecs. This means that there is enough time between snapshots for the galaxy to undergo some small-scale morphological transformations, and therefore we expect our average results not to be strongly biased by odd individual cases with peculiar configurations. We exclude the first seven snapshots of each simulation in order to discard possible transient states during the initial relaxation towards a stable rotational configuration (this can arise because the initial conditions are not in perfect equilibrium); we then still have a large number of snapshots per galaxy ($\sim$54) in order to identify and explore global trends.

A key parameter in N-body simulations is the gravitational softening length, which is meant to keep two-body relaxation effects and orbital integration cost under control. Since gravitational forces are smoothed for particles approaching shorter distances than the softening length, the dynamics of structures smaller than this scale is artificially modified by this approximation. The spatial resolution of an N-body simulation is generally considered to be two to three times its softening length. Given that we want to investigate scales as small as 100 pc, we set the softening length to 25 pc in all our simulations. The baryonic particle (i.e. gaseous and stellar particles) masses are chosen to ensure at least 8 particles per softening volume within the central 2 kpc inside the disc. The DM particle mass is set to guarantee a minimum of 150 particles inside the inner 100 pc in order to have a relatively smooth DM distribution. Further, we impose an additional constraint, namely $\sqrt{GM_{\rm part}/\epsilon_{\rm soft}} \ll 16$ km s^{-1}, which ensures that perturbations induced by two-body encounters are below the typical velocity dispersion of a warm interstellar medium. The resulting baryonic particle masses in our simulations range from $1.2 \times 10^3 \mathrm{M}_\odot$ to $1.6 \times 10^4 \mathrm{M}_\odot$, and the DM particle masses range from $2 \times 10^4 \mathrm{M}_\odot$ to $4 \times 10^4 \mathrm{M}_\odot$ (see

Table 2.1).

GADGET-2 uses smoothed-particle hydrodynamics (SPH) to solve the hydrodynamic equations of the gas component. This computational method simulates fluids as collections of point-like elements. The SPH technique considers that each gas particle carries a certain amount of every gas property, which is smoothed over a finite volume according to a given kernel function. The value of a quantity at an arbitrary location is given by the sum of the smoothed contributions from all those particles enclosing that point inside their kernel volumes. The kernel employed by GADGET-2 is a spline function with one parameter, the smoothing length h, such that the value of every quantity outside a radius h is zero. The numerical approximations made in SPH have been shown to be sometimes inaccurate, especially for representing fluid instabilities such as the Kelvin-Helmholtz instability (e.g. Agertz et al., 2007). However, we do not expect that these hydrodynamical accuracy issues have a bearing on the questions studied in this paper, especially because Hayward et al. (2014) found that the results of GADGET-2 simulations of idealised isolated disc galaxies are very similar to simulations of the same galaxies performed with the state-of-the-art moving-mesh hydrodynamics code AREPO (Springel, 2010).

2.3 *Analysis methods*

To fully understand the systematic differences that can arise between the real circular velocity profile of the DM halo and the rotation curve that is actually inferred observationally, one has to go through a long chain of intermediate steps. In order to disentangle the impact of each approximation on the deduced cuspiness of the halo, our general strategy is to apply the same analysis methods to different circular velocity profiles, starting from the most ideal case and adding one layer of approximation at a time. Sorted by the degree of idealization involved, these circular velocity profiles are the following:

1. Dark-matter-only circular velocity ($V_{\rm dm}$)

2. Total-mass circular velocity ($V_{\rm tot}$)

3. True circular motions of the gas ($V_{\rm cir}$)

4. Observed rotation curve ($V_{\rm obs}$)

The quantity $V_{\rm dm}$ represents the circular velocity of a test particle under the gravitational potential of the dark matter halo alone. From a theoretical point of view, this velocity profile is the only one that traces the exact DM distribution. $V_{\rm tot}$ represents the circular velocity profile generated by the total gravitational potential (i.e. DM plus baryons) in the plane of the disc. With this definition at hand, the minimum disc approximation can be thought of as using $V_{\rm tot}$ instead of $V_{\rm dm}$ to directly estimate the cuspiness of the halo, thus neglecting the baryonic contribution to the potential. In both cases, $V_{\rm dm}$ and $V_{\rm tot}$ do not measure velocities but rather gravitational radial accelerations, as they translate into rotational velocities via $V_{\rm rot}(r) = \sqrt{a_r r}$.

In contrast, $V_{\rm cir}$ is a direct measure for the actual (circular) motions of the gas. Notice that $V_{\rm cir}$ can lie below $V_{\rm tot}$ if the hydrodynamical pressure pushes the gas outwards, thereby lowering the effective radial acceleration towards the center that needs to be balanced by centrifugal forces. Finally, $V_{\rm obs}$ refers to our mock observed rotation curves, which mimic several processes of real observations, such as projection effects and finite spatial resolution. This generic name comprises a large set of curves for each snapshot because we mimic two types of observations, long-slit rotation curves and 2D velocity fields, at five different inclinations and four different spatial resolutions (to mimick the effect of distance variations). It is worth emphasizing that $V_{\rm dm}$, $V_{\rm tot}$, and $V_{\rm cir}$ correspond to perfect theoretical measurements from the simulations, whereas $V_{\rm obs}$ accounts for the limitations of real data. However, we stress that because our simulations are constructed to be highly symmetric discs in perfect rotational equilibrium, even $V_{\rm obs}$ does not fully capture the difficulties inherent in inferring the DM profile shape from observations of real dwarf irregulars and LSB galaxies. Instead, the analysis that we present here should be considered a best-case scenario, at least given current observational limitations.

2.3.1 Snapshot preprocessing

Before we extract the relevant information from the snapshots, we process them to make sure that the center of the gravitational potential and the galactic disc orientation are robustly determined. This is very important because poorly constrained values can introduce harmful effects in the forthcoming analysis. For example, note that an error of 5° at low inclinations (∼15°) can propagate to an error as high as 50 per cent in the normalization of the observed rotation curves and that an incorrect determination of the center's position may lead to a spurious flattening of the inner part of a spherically averaged density profile.

We recenter the snapshots using an iterative version of the shrinking spheres method described in Power et al. (2003). We first calculate the center of mass inside a large sphere containing everything in the simulation and recenter all coordinates around this point. Next we shrink the sphere by 1 per cent in radius, find the new center of mass, and recenter the particles again. This is repeated until there are less than 10 particles in the sphere. We also rotate the frame of reference to make the net angular momentum of the gas component coincident with the z-axis.

2.3.2 Real density profiles

To determine the true DM density profiles and verify their steepness, we first measure the DM cumulative mass as a function of radius and then we compute

$$\rho = \frac{\frac{\mathrm{d}}{\mathrm{d}r} M_{\mathrm{dm}}(< r)}{4\pi r^2}. \tag{2.8}$$

We use spherical shells equally spaced in logarithmic radius and a central finite-differences scheme for the derivative. We test different steps, namely 0.05, 0.075, 0.1, 0.15, 0.2, and 0.3, and we adopt $\Delta \log(r) = 0.15$, where r is in kpc, which is the smallest interval that produces smooth profiles and is still largely affected by Poisson noise in the central region ($r < 150$ pc). We note that the measured cuspiness of the halo does not depend on this specific choice as variations in the density profiles are very subtle.

2.3.3 Theoretical circular velocity profiles

We refer to measurements that are calculated from detailed information in the snapshots as theoretical quantities, disregarding the issue of whether or not they can be actually assessed observationally. These quantities include the DM density profiles described earlier as well as a subset of the circular velocity profiles introduced at the beginning of Sec. 2.3, namely V_{dm}, V_{tot}, and V_{cir}.

(i) Dark-matter-only circular velocity, $\boldsymbol{V}_{\mathbf{dm}}$*:* Particles rotating at a constant speed satisfy $V_{\mathrm{rot}}(r) = \sqrt{a_r r}$, so it suffices to determine the mean radial acceleration attributed to the DM halo as a function of radius to determine its equivalent circular velocity profile. To do

this, we export all DM particles in the snapshot to a separate initial conditions file and run GADGET-2 for a single time-step to calculate the gravitational forces. Then, we measure the mean radial acceleration in thin spherical shells and compute

$$V_{\mathrm{dm}}(r) = \sqrt{\langle a_r(r) \rangle \, r}\,\Big|_{\mathrm{gravity,\ dm\ only}} . \tag{2.9}$$

(ii) Total-mass circular velocity, $\boldsymbol{V}_{\mathbf{tot}}$*:* This velocity profile is related to the gravitational potential of the whole system, i.e. dark matter plus baryons. It is interesting because a joint analysis with the DM-only circular velocity profile allows one to assess the validity of the minimum disc approximation without mixing in any other effect. Once again, we compute the mean radial accelerations due to gravity using GADGET-2. However, this time we cannot assume spherical but rather axial and vertical symmetries instead. Therefore, we compute the radial accelerations using thin cylindrical shells in the xy-plane ($|z| \leq 100$ pc) and then determine the circular velocity profile using

$$V_{\mathrm{tot}}(r) = \sqrt{\langle a_r(r) \rangle \, r}\,\Big|_{\mathrm{gravity,\ all\ particles}} . \tag{2.10}$$

(iii) True circular motions of the gas, $\boldsymbol{V}_{\mathbf{cir}}$*:* In this case, we select the gas particles in the equatorial plane ($|z| \leq 100$ pc) and measure their circular (tangential) velocities, taking the mean value in small radial bins:

$$V_{\mathrm{cir}}(r) = \langle V_\phi(r) \rangle |_{\mathrm{gas\ particles}} . \tag{2.11}$$

We emphasize that for axisymmetric systems in rotational equilibrium, any difference between V_{cir} and V_{tot} must be due to the fact that in addition to gravity, gaseous media also experience hydrodynamical forces. The above velocity profile is one step closer to reality because instruments do not detect gravitational potentials but rather velocities; thus, V_{cir} can be thought of as the rotation curve that a perfect instrument under perfect observational conditions would detect (neglecting projection effects).

Additionally, we calculate the circular velocity profiles associated with the gravitational potentials of the stellar and the gaseous components separately, using the same procedure as for V_{tot}. These curves are denoted as $V_\star$ and V_{gas} in the text. This complementary information is interesting for understanding the difference between V_{dm} and V_{tot}, as we have that

$$V_{\mathrm{tot}}^2 = V_{\mathrm{dm}}^2 + V_\star^2 + V_{\mathrm{gas}}^2 . \tag{2.12}$$

The theoretical rotation curves were calculated using shells of 100 pc width, linearly spaced every 100 pc, the first of which is centered at 125 pc in order to exclude particles inside 3 times the softening length. Except for when calculating $V_{\rm dm}$, we only consider particles in the midplane because the assumption of vertical symmetry breaks down as one moves above or below the equatorial plane, and this is likely to make particles rotate slower (Rhee et al., 2004). We check that there is a large enough number of particles in all bins, resulting in smooth velocity profiles without visible signs of shot noise. When we explore the effects of spatial resolution associated with the distance to the galaxies, we use re-sampled versions of the theoretical rotation curves matching the radial positions of the corresponding mock observations. The error bars on the theoretical rotation curves are fixed to 1 km s^{-1} where necessary.

2.3.4 Mock kinematic observations

We mimic different kinds of observations of the gas component, including optical long-slit rotation curves and 2D velocity maps. We consider two different cases, labeled as H I and H α, which represent some physical properties of the 21-cm and the H α emissions, respectively.

We *observe* each galaxy at five different inclinations from 15° to 75° in steps of 15°, the smallest one being the closest to a face-on view. We also try four different distances, namely 10, 20, 40, and 80 Mpc. Note that the truly important quantity is the spatial resolution of the observations, but because we use typical values for the instrumental angular resolutions, these distances are useful indicators. For our fiducial H α PSF of 2 arcsec, the corresponding spatial resolutions are ∼100, ∼200, ∼400, and ∼800 pc. Our H I resolution is six times poorer, but as we use the radio observations only in the outer part, the optical data is most important for differentiating cusps from cores. In the following, we first describe the basic concepts and common approximations employed to create our mock observations and then move on to more specific details as necessary.

We assume that some of the gas particles emit radiation through a spectrum composed of a single emission line with a gaussian profile. In the H I case, we consider all gas particles in the simulation to be radio emitters, and we make the amplitude of the 21-cm emission line proportional to the mass of the gas particle. The broadenings are given by the intrinsic velocity dispersions, σ, self-consistently calculated from the temperature of each particle as

$$\sigma = \sqrt{\frac{kT}{\mu m_H}}, \tag{2.13}$$

where k is the Boltzmann constant, T is the temperature of the gas particle, μ is the mean molecular weight, and m_H the mass of a hydrogen nucleus. For moving particles, we Doppler-shift the emission line without altering its width. This means that the intensity of the emission from a gas element with a mean velocity $\overline{v}_{\rm los}$ along the line of sight, detected at a different velocity (frequency) v, is given by

$$I_{\rm HI}(v) \propto \frac{M_{\rm part}}{\sigma}\, {\rm e}^{-\frac{(v-\overline{v}_{\rm los})^2}{2\,\sigma^2}}. \tag{2.14}$$

In the H α case, we only include gas particles with ongoing star formation activity, which is a good proxy for the spatial distribution of the ionized gas in H II regions, though it may miss the warm ionized gas pervading the rest of the ISM. The mock H α observations defined in this way have a smaller radial extent than our fiducial mock H I data, consistent with observations. Additionally, the disc of star-forming gas is thinner than our mock H I disc, which makes our choice conservative, as our mock H α data will be less affected by projection effects and will trace the disc kinematics more faithfully. Since H α emission depends on the mass of the ionized gas, we make the H α intensity proportional to the mass of the gas particles times their current star formation rate (SFR), which should roughly correlate with the amount of ionizing radiation available from young, massive stars. The H α intensity versus frequency is thus given by

$$I_{\rm H\alpha}(v) \propto {\rm SFR} \times \frac{M_{\rm part}}{\sigma}\, {\rm e}^{-\frac{(v-\overline{v}_{\rm los})^2}{2\,\sigma^2}}. \tag{2.15}$$

Regarding the observational process itself, we simplify it to a combination of a spatial and a spectral sampling of the emitted radiation field. The spatial sampling mimics the pixels of the detector. To be consistent with the SPH approximation, the radiation flux that a gas particle contributes to a certain pixel is inversely proportional to the projected distance between the particle and the center of the pixel, using the same kernel and smoothing lengths as in the SPH simulation. Adding contributions from all neighbouring particles, we obtain a resulting spectrum per pixel made up of individual shifted Gaussians. Then, we sample each spectrum in narrow velocity (frequency) channels to mimic the spectral resolution of a given instrument. At the end of this process, we obtain a datacube containing spatial and kinematic information about the gas component in the simulation box. Each slice of this datacube is an intensity map of the H α or H I radiation in a specific velocity channel. Finally, a 2D Gaussian convolution is implemented across each slice to mimic the effect of the optical seeing or the radio beam, and the cube is collapsed along the spectral axis by means of a simple intensity weighted mean (IWM) scheme to determine the observed line-of-sight velocity at each pixel,

$$\langle v \rangle = \frac{\sum_{\rm ch} I_{\rm ch} v_{\rm ch}}{\sum_{\rm ch} I_{\rm ch}} \tag{2.16}$$

For the 2D observations, mock intensity and velocity dispersion maps are also generated from the data cubes following Walter et al. (2008)

$$I = \sum_{\rm ch} I_{\rm ch} \tag{2.17}$$

$$\sigma = \sqrt{\frac{\sum_{\rm ch} I_{\rm ch} \times (v_{\rm ch} - \langle v \rangle)^2}{\sum_{\rm ch} I_{\rm ch}}}. \tag{2.18}$$

Interesting comparisons of the IWM algorithm with alternative ways of defining a velocity map from its parent data cube are discussed by de Blok et al. (2008a) and Oh et al. (2011b). They show that IWM velocities are potentially biased in the presence of non-circular motions as the emission lines become asymmetric or the spectrum may exhibit secondary peaks (i.e., additional velocity components). Notwithstanding, our galaxies are strongly dominated by rotational motions; thus, we find the IWM method good enough to trace the disc rotation (see Fig. 2.6). Moreover, we will show in Sec. 2.4 that for nearby galaxies, the final results obtained from our mock observations agree remarkably with those obtained from perfect theoretical measurements of the gas kinematics. Therefore, there is no need to employ more complex algorithms than the IWM. The same applies to more sophisticated schemes, as modelling the H I distribution and kinematics directly from from the datacubes (e.g. Bouché et al., 2015; Di Teodoro and Fraternali, 2015; Kamphuis et al., 2015). Even though a comparison of these methods through our mock data set would be interesting, it lies beyond the scope of this work.

We also address several numerical artifacts detected during the experiments. For example, we noticed that in low-intensity pixels, outliers moving at arbitrary velocities can dominate the velocity estimation and introduce spurious and sometimes enormous fluctuations in the final rotation curve. To avoid this effect, we define an arbitrary luminosity threshold of 10^{-4} times the maximum detected intensity, which works well in suppressing the fluctuations while filtering out just a few pixels. Another potentially harmful effect that we detected is a systematic underestimation of the velocity at the last measured points. We find the main cause of this to be related to the use of the SPH approach, as this implies that in principle, one can define velocities at points that are beyond all gas particles. To remove this artifact, we impose the maximum radius for velocity estimations to be the radius enclosing 99 per cent of the emitting particles. A further comparison between the mock observations and the theoretical rotation curves confirmed that imposing this maximum radius solved the problem. We only report rotation curves for radii beyond 75 pc plus the seeing/beam such that possible contamination from inner points affected by the softening is virtually absent even after the PSF/beam convolution. This places the first kinematic measurement at approximately 0.17, 0.27, 0.46, and 0.85 kpc for galaxies viewed at 10, 20, 40, and 80 Mpc, respectively.

2.3.4.1 H α long-slit rotation curves

In this case, we only consider pixels inside a virtual slit placed along the major axis of the disc. We use square pixels and enough spectral channels to sample the whole range of line-of-sight velocities. We choose instrumental parameters consistent with the majority of observational studies. The slit width is 1.4 arcsec, the pixel size is 0.7 arcsec, the FWHM of the PSF is 2 arcsec, and the spectral resolution is 47 km s^{-1}, equivalent to a 20 km s^{-1} channel separation. The spatial resolution corresponds to $\sim$ 100 pc at a distance of 10 Mpc, matching the size of the radial bins that we used to define the theoretical rotation curves. For mock observations at 20, 40, and 80 Mpc, the corresponding physical resolutions are $\sim$200, $\sim$400, and $\sim$800 pc, respectively. Given that the slit width is resolved into two pixels, we add them together before collapsing the cube to have a single velocity estimate at each position along the slit. Next, we fold the rotation curve to put the approaching and receding sides together, and we average both the radial and velocity information in bins of 1 arcsec ($\sim$ 50 pc at 10 Mpc), i.e. using 2 points per seeing, as is common practice for this kind of data. We adopt the standard deviation of individual velocity pixels in the bin as the error bar, and we check that this is perfectly consistent with taking the difference between the approaching and receding sides.

Similar to de Blok and Bosma (2002), we impose a minimum error of 2 km s^{-1} (they used 4 km s^{-1}). Finally, we de-project the observed line-of-sight velocities to get the actual rotation curve,

$$v_{\mathrm{rot}}(r) = \frac{v_{\mathrm{los}}(r)}{\sin(i)}, \tag{2.19}$$

where i represents the galaxy inclination. We use the true inclination and major axis of the gaseous disc, and we assume the galactic center to coincide with the center of the overall gravitational potential. In a forthcoming paper, we will present mock photometric data of these galaxies and demonstrate that classical photometric estimators can recover the center of the gravitational potential with an accuracy of 1 arcsec (half the spatial resolution) and the inclination and position angle with typical errors of less than 10°. As we commented in Sec. 2.3.1, small inclination errors can induce large differences in the normalization of the rotation curve for discs that are near to face-on. However, it is not clear whether such errors can cause the inferred cuspiness of the halo to be incorrect or they can be safely ignored; regardless, errors of this magnitude would certainly be considered acceptable in actual observational studies. In any case, in this work, we focus on the best case and do not include the effects of errors in the geometrical parameters.

2.3.4.2 H α velocity fields

To construct H α velocity fields, we map the entire H α emission across the galaxy. The instrumental parameters (pixel scale, seeing, and spectral resolution) are the same as above. The velocity field is computed using the IWM scheme defined in equation (2.16) and the rotation curves are extracted using the KINEMETRY software package (Krajnović et al., 2006). KINEMETRY performs a harmonic decomposition of the line-of-sight velocity field in elliptical rings as a function of the position angle θ, performing a least-squares minimization of

$$V_{\mathrm{los}}(\theta) = \sum_j A_j \sin(j\theta) + \sum_j B_j \cos(j\theta) \tag{2.20}$$

to find the best set of coefficients for each ring. In the case of pure circular motions, we have

$$V_{\mathrm{los}}(\theta) = V_{\mathrm{rot}} \sin(i) \cos(\theta). \tag{2.21}$$

Therefore, in the KINEMETRY expansion, the net amount of rotation would be proportional to the coefficient B_1, with all other components representing non-circular motions. We calculate the rotation curves in radial bins of 1 arcsec and adopt as final errors the formal

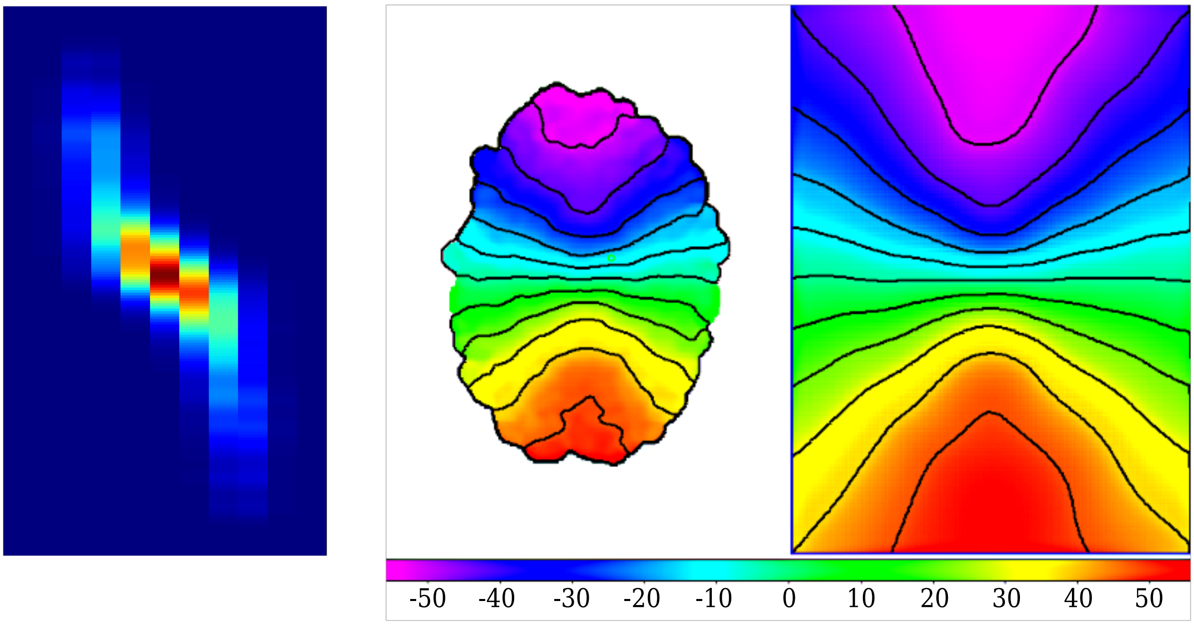

Figure 2.3: Example data products obtained from G0 at 3.0 Gyr, 45° inclination, and 10 Mpc distance. From left to right, we present the optical long-slit spectrum, the H α velocity field, and the H I velocity field. The H I velocity map extends over 7 kpc, reaching a maximum radius of 3.5 kpc into the receeding and the approaching sides, which is roughly the optical radius. The H α map barely reaches ∼3 kpc, corresponding to the region with non-negligible emission. Velocities are colour-coded equally in both maps according to the shown scale. Iso-velocity contours are drawn every 10 km s^{-1}. The long-slit spectrum also extends over 7 kpc. Pixels in the horizontal direction represent the spectral axis, coloured according to the intensity of the emission in each velocity channel.

errors of the fit reported by KINEMETRY. Even though KINEMETRY is in principle able to treat the ellipticity and position angle of the ellipses as free parameters during the fitting, we kept them constant and fixed to their real values in order to avoid one additional source of potential error.

2.3.4.3 H I velocity fields

We also create H I velocity fields following the same prescription. The instrumental parameters are chosen according to the H I survey THINGS (Walter et al., 2008), which, along with LITTLE THINGS (Hunter et al., 2012), represents the best-quality H I data ever used in the cusp-core context. We use a 5.2 km s^{-1} channel separation, a pixel scale of 1.5 arcsec/pixel, and a Gaussian beam of 12 arcsec at FWHM, such that the spatial resolution is $\sim$ 580 pc for galaxies at 10 Mpc. Final rotation curves are determined using KINEMETRY in elliptical rings of 6 arcsec width. We note that the spatial resolution of THINGS is better by a factor of 2 in the velocity maps reduced with the *robust weighting* scheme instead of the *natural weighting* (see Walter et al., 2008, for details). This fact is exploited to emphasize the advantages of using THINGS velocity maps for cusp-core studies, although it is sometimes not properly stated. For example, Oh et al. (2011b) mentioned the higher spatial resolution in their introduction, but then the poorer resolution ($\sim$12 arcsec) was actually used. This mixup was propagated into Oh et al. (2011), in which a spatial resolution of 6 arcsec was used to construct the mock kinematic observations of the simulated galaxies. On the other hand, the data cubes used in those studies had a spectral resolution of 2.6 km s^{-1} (a factor of 2 better than ours), but most of the velocity maps in a related study by de Blok et al. (2008a) had 5.2 km s^{-1} resolution. Regardless, we have checked that measured rotation curves are insensitive to the assumed spectral resolution as long as the Gaussian emission lines are properly sampled.

2.3.4.4 Hybrid rotation curves

Optical rotation curves have a better spatial resolution than radio observations, but the latter usually cover much larger radii. For this reason, it is very convenient to mix both kinds of data when they are available for the same object, using the H α measurements in the inner region and appending the H I velocities in the outer part. In this manner, one minimizes concerns about beam smearing while hopefully reaching the flat part of the rotation curve with a high enough number of points in order to put meaningful constraints on the overall shape of the DM halo using rotation curve fitting methods (Sec. 2.3.5).

We create hybrid rotation curves by joining the H I data to both the long-slit and the KINEMETRY H α rotation curves. Given that H I rotation curves are clearly affected by beam smearing in their inner parts, we implemented an automatic algorithm to discard the first H I data points, as needed to get a continuous rotation curve with a positive, monotonically decreasing radial derivative at the H α/H I interface. The hybrid rotation curves are truncated at $\sim$2 times the optical radius, which is approximated as $\sim$3.2 times the scale-length of the stellar disc (Persic and Salucci, 1995), thus yielding radial extents between 5 and 19 kpc, which are representative of real observations.

2.3.5 Differentiating cusps from cores via rotation curve fitting

When there is kinematic information available beyond the rising part of the rotation curve, the typical method to differentiate cusps from cores is fitting different analytic models to the dataset and choosing the best one on the basis of the minimum χ^2_ν of the fits. Among the variants presented in the literature, the most common models are the cuspy NFW model (see equations 2.6 and 2.7), for which $\rho_{\rm inner} \sim r^{-1}$, and the cored pseudo-isothermal sphere (hereafter ISO), for which $\rho_{\rm inner} \sim r^0$ and the full profile is given by

$$\rho_{\rm ISO}(r) = \frac{\rho_0}{1 + (r/R_c)^2}, \tag{2.22}$$

$$V_{\rm ISO}(r) = \sqrt{\frac{4\pi G \rho_0 R_c^3}{r}\left[\frac{r}{R_c} - \tan^{-1}\left(\frac{r}{R_c}\right)\right]}, \tag{2.23}$$

where ρ_0 represents the central DM density and R_c the core radius.

We note that regarding the structure of DM haloes, another criticism of ΛCDM simulations is that the few acceptable NFW fits to observations tend to violate the tight cosmological relation between the free parameters (c, V_{200}) predicted by the simulations themselves. Some authors explicitly use the cosmological mass-concentration relation as a constraint for the NFW fits in order to highlight this additional facet of the cusp-core problem (Kuzio de Naray et al., 2008b). We do not impose such a restriction. Instead, we let both parameters vary freely and later investigate the range of values covered by the fits.

When we fit the models to the theoretical velocity profiles $V_{\rm dm}$, $V_{\rm tot}$, and $V_{\rm cir}$, we first re-sample these curves to the same positions at which the mock hybrid rotation curves are measured so that we can properly compare the results and interpret the differences. These radial positions depend on the spatial resolution and the extents of the H α/H I components of each galaxy. Note that at 10 Mpc, the inner theoretical velocity profiles are oversampled because they were created in steps of ~100 pc, whereas the mock H α rotation curves are defined every ~50 pc (2 points per seeing). However, this is not a concern because we find the results at 10 and 20 Mpc to be essentially identical, as we will show in Sec. 2.4.3 and Sec. 2.5.2. We assume constant error bars of 1 km s^{-1} when fitting the theoretical curves.

We recall that this work is focused on the minimum disc approximation; thus, we do not attempt to explicitly account for the baryonic contribution to the rotation curves. In other words, we fit the different analytic models proposed for the DM halo directly to the *observed* data or to the theoretical circular velocity profiles. To avoid spurious results, we do not try fits to rotation curves with less than 8 points, which in practice only filters out the velocity profiles from the Dwarf1 and G0 simulations at 80 Mpc.

2.4 Results

Here, we describe the theoretical velocity profiles of our simulated galaxies, their mock kinematic observations, and some statistics regarding the fits with the NFW and the ISO analytic models. We give special attention to the differences amongst the various velocity profiles and to the effects of spatial resolution and inclination. When reporting on general trends based on observations at all inclinations, we use the term V_{kin} to refer to hybrid rotation curves where the H α part was extracted with KINEMETRY from the velocity maps, and V_{ls} to refer to those hybrids where the H α portion uses the mock *long-slit* data.

2.4.1 Density profiles

In Fig. 2.4, we present a compilation of the real DM density profiles in our simulations. Remarkably, we see that our DM haloes remain basically unchanged[2], even in the case of G1, which develops a relatively strong bar. The simulated galaxies' DM profiles can be accurately represented with the NFW formula, and there is no ambiguity about their cuspy nature. We emphasize this point by including in each panel an inclined straight line with a slope of -1 to facilitate a visual comparison, recalling that a core would appear here as a horizontal line.

---

[2] This is likely the case because our simulations use the Springel and Hernquist (2003) effective equation of state to model the effects of supernova feedback and do not include explicit feedback-driven outflows; as a result, the simulated galaxies form stars steadily, in contrast with the very bursty star formation exhibited by simulations that explicitly include multi-channel stellar feedback (e.g. Hopkins et al., 2014; Sparre et al., 2015). As detailed in Sec. 2.1, strong bursts of star formation and the associated supernova feedback-driven outflows may be able to transform cusps into cores. Thus, it is desirable *not* to include this still-uncertain effect in our simulations because we wish to test whether cusps can be mistaken for cores, not whether cusps can be transformed into cores via baryonic processes.

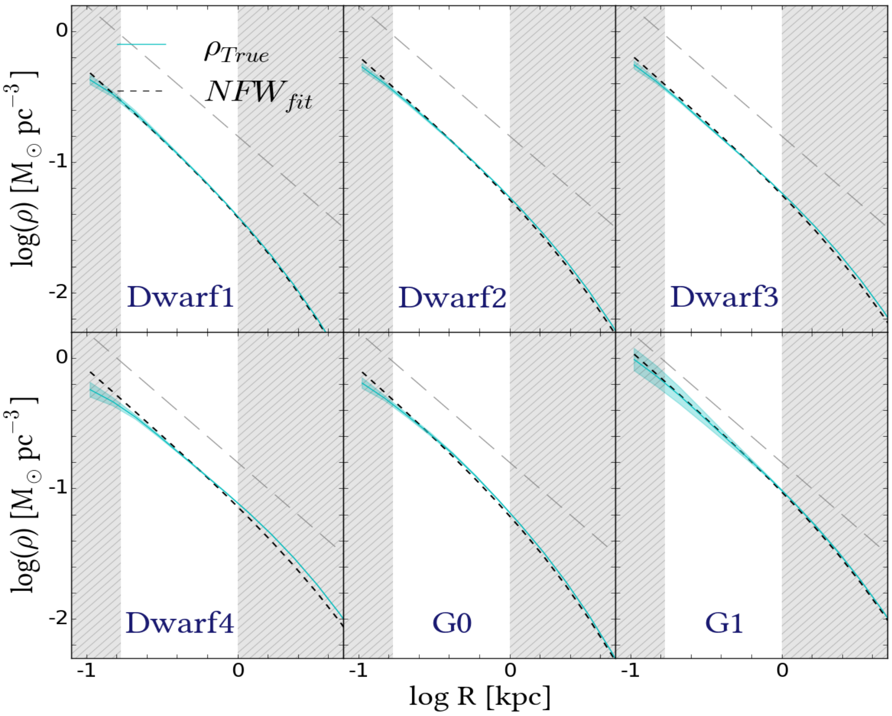

Figure 2.4: Real DM density profiles in the simulations. The solid cyan lines represent the mean of all the snapshots, and the shaded cyan regions denote the 1-σ scatter. In each panel, the short dashed black line is the mean of the best NFW fits to the real density profiles. The hatched, grey shaded regions indicate the central region between 0.17 kpc (the position of our first velocity measurement) and 1 kpc, where the core-cusp discrepancy has been more debated. Straight diagonal lines (long dashed) with a slope of -1 (i.e. the cusp profile expected for an NFW profile) are shown for comparison. All of the simulated galaxies clearly retain central DM cusps throughout their evolution.

2.4.2 Rotation curves

In Fig. 2.5, we present a compilation of the theoretical velocity profiles for all galaxies and snapshots. Recall that $V_{\rm gas}$, $V_\star$, and $V_{\rm dm}$ represent the circular velocity profiles generated by the gravitational potential of the individual components, $V_{\rm tot}$ is their sum in quadrature, and $V_{\rm cir}$ is the actual circular speed of the gas in the disc. The negligible scatter demonstrates that our target configurations remain highly stable for all galaxies but G1. Apparently the formation of the bar induces time evolution in the azimuthally averaged velocity profiles, even if the DM structure does not change much. A visual inspection of the face-on stellar maps confirms a smooth, stable morphology without substructures for galaxies D1 to D4. Some minor distortions in the central part of G0 are observed, but they are not a concern because the initial potential-velocity structure remains the same. In the following, we present results for the whole sample, excluding G1 at first, and we then comment on this system afterwards.

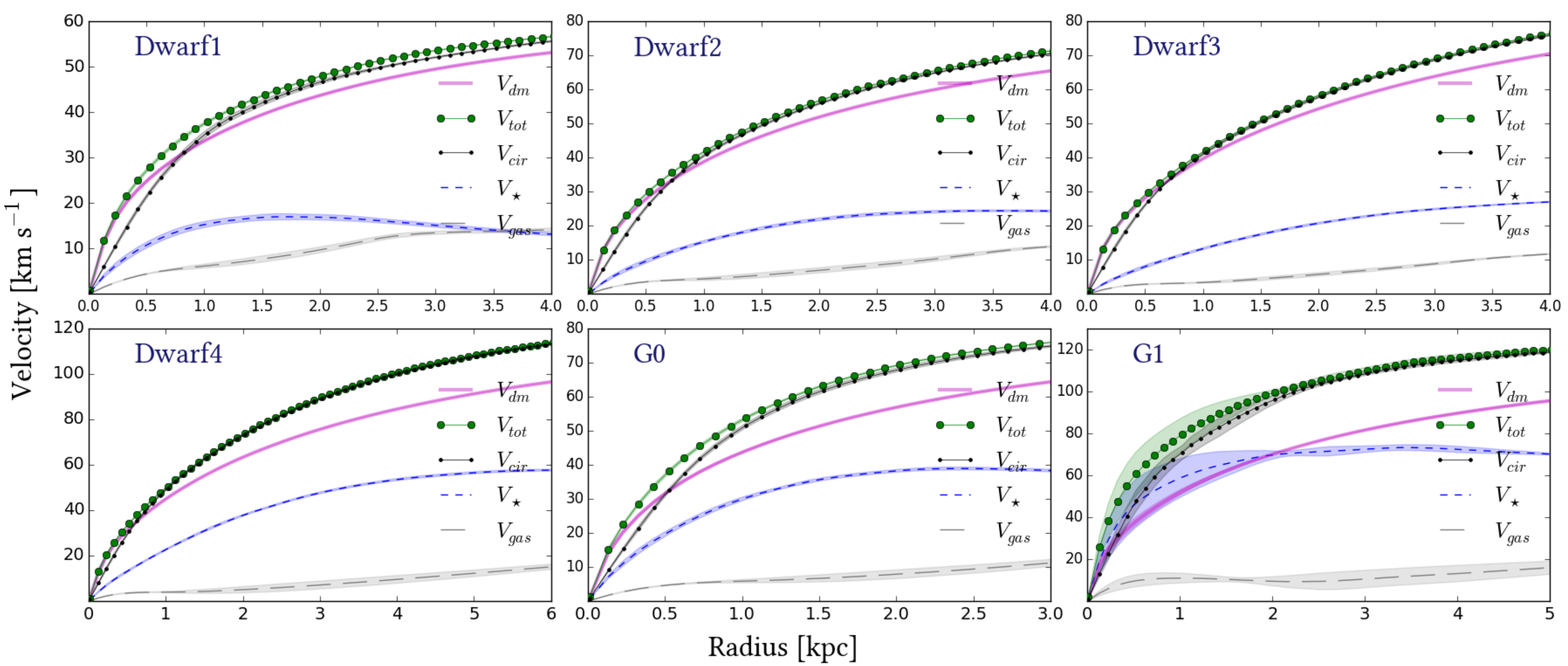

Figure 2.5: Inner parts of the theoretical rotation curves as defined in Sec. 2.3. The thick magenta line represents V_{dm}, solid green line with circles is V_{tot}, solid black line with dots is V_{cir}, the short-dashed blue line is $V_\star$, and long-dashed gray line is for V_{gas}. In each case the main line is the mean curve from all snapshots, and the shaded regions indicate the 1-σ scatter. Except for G1, the simulated galaxies are DM-dominated at all radii. The differences between V_{tot} and V_{cir} in the central ~ 1 kpc, which are typically $\sim 4-5$ km s^{-1}, are due to pressure support; below, we shall see that this difference can have important consequences for the DM profile shape inferred from the rotation curves.

Fig. 2.5 shows that baryons are dynamically sub-dominant in all cases. Inside the first kiloparsec, $V_{\rm tot}$ exceeds $V_{\rm dm}$ by less than 6 km s^{-1} for galaxies D1 to D4 and less than 10 km s^{-1} for G0. The mean difference $\langle V_{\rm tot} - V_{\rm dm} \rangle$ is less than 3 km s^{-1} in this inner region. Beyond the first kiloparsec, the baryonic contribution to $V_{\rm tot}$ is ~10 per cent in galaxies D1, D2, and D3 and ~20 per cent in D4 and G0. It is also apparent in Fig. 2.5 that $V_{\rm cir}$ closely follows $V_{\rm tot}$ in the outer region, but it is slightly less than $V_{\rm tot}$ in the center. The general agreement demonstrates that our systems are in a rotational equilibrium that is mainly sustained by gravity. Nevertheless, as the rotational speed of the gas nearly coincides with the expectation from its radial acceleration (see Sec. 2.5.1), the small differences in the centres of the galaxies imply that the radial acceleration experienced by the gas component is smaller than that expected from the gravitational potential, which can be interpreted as evidence for pressure support. The residual $(V_{\rm tot} - V_{\rm cir})$ peaks between 6 and 8 km s^{-1} at 0.17 kpc and linearly decreases to ~1-2 km s^{-1} at 1 kpc, which implies a mean pressure support correction of ~ 4-5 km s^{-1} to be added to $V_{\rm cir}$ over this radial range. The importance of this small difference in the cusp-core scenario will become clear in the next sections.

In Fig. 2.6, we present some of the rotation curves and the non-circular motion profiles extracted from the mock H α and H I velocity maps using KINEMETRY for the simulated galaxies placed at 10 and 80 Mpc and viewed at an inclination of 45°. We also show the theoretical $V_{\rm cir}$ to facilitate the comparison. It is clear from the figure that our galaxies are completely dominated by rotational motions, with the non-circular component being less than 5 km s^{-1} at all radii (except for G1). Fig. 2.7 shows the mean (taken over all simulations and snapshots) $\langle V_{\rm cir} - V_{\rm kin} \rangle$ residual as a function of spatial resolution for the simulated galaxies viewed from multiple inclinations, considering only the inner region with H α emission. These figures demonstrate that H α observations of the simulated galaxies at a 100-pc spatial resolution (placed at a distance of ~10 Mpc) almost perfectly trace the actual circular motions of the gas ($\langle V_{\rm cir} - V_{\rm kin} \rangle < 2$ km s^{-1}). The residual increases as the spatial resolution diminishes and reaches as much as ~ 5 km s^{-1} for a 800-pc resolution (~80 Mpc distance) and inclination of 75°. The H I rotation curves (the red lines in Fig. 2.6) underestimate the true rotational velocities in the central few kiloparsecs of the galaxies (even when the galaxies are placed at 10 Mpc) but are in agreement with $V_{\rm cir}$ at larger radii. The effect of beam smearing is stronger with distance, but because we

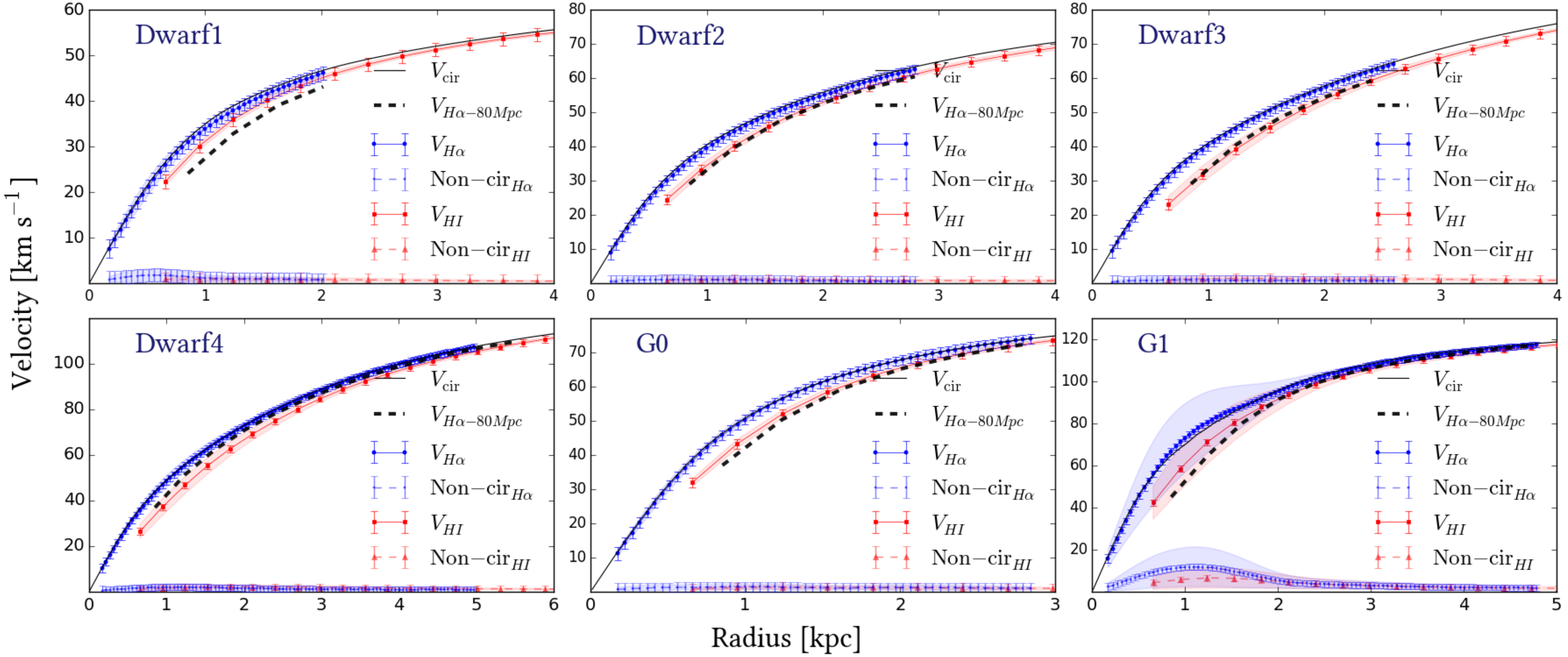

Figure 2.6: Inner parts of the mock observed rotation curves and net amount of non-circular motion as inferred by KINEMETRY for the simulated galaxies placed at 10 Mpc and viewed at an inclination of 45°. H α observations appear in blue and H I in red. In each case, the rotation curve is represented with a solid line and the non-circular motion profile with a dashed line. For each of the above, the plotted curve represents the mean curve from all snapshots, the shaded region indicates the 1-σ scatter, and the error bars represent the typical error bar at each radius on individual rotation curves. The theoretical $V_{\rm cir}$ is also shown. The thick black dashed line in each panel is the H α rotation curve at 80 Mpc. The rotation curves are dominated by circular motion at all radii. The H α rotation curves almost perfectly trace the true circular motions of the gas for galaxies placed at 10 Mpc but underestimate them by as much as ~ 5 km s^{-1} when the galaxies are placed at 80 Mpc (and even more so for G1 because of the non-negligible amount of non-circular motion in the central 2 kpc). The H I rotation curves underestimate the true circular velocity in the central few kiloparsecs because of beam smearing.

use the H I data only to extend the optical rotation curves into the flat part, this is not a primary concern for our discussion.

G1 qualitatively differs from the other simulations. In this simulation, the stellar component dominates the gravitational potential within the first 2 kpc. As a result, $V_{\rm tot}$ exceeds $V_{\rm dm}$ by 27 ± 5 km s^{-1} at 1 kpc (see Fig. 2.6), which represents a discrepancy of $\sim$50 per cent. In the outer region, this excess is about 30-40 per cent. The residual $(V_{\rm tot} - V_{\rm cir})$ is 15 ± 5 km s^{-1} at 0.17 kpc, 8 ± 5 km s^{-1} at 1 kpc, and 2 km s^{-1} at $\sim$ 2.5 kpc. However, in this case, the difference is not simply attributable to the effect of pressure support because of the presence of the bar and its associated non-circular motions, which invalidate the axisymmetric approximation. We emphasize that G1 resembles classical dwarf galaxies and LSBs in terms of several properties, such as the maximum circular velocity and stellar mass; for this reason, we keep it in our sample even though it is not close to the ideal case. Modelling the complex kinematics of barred potentials is far from simple and beyond the scope of this work.

The mock H α rotation curves obtained from the 2D velocity maps underestimate the circular motions of the gas more severely in less-inclined (i.e. more face-on) galaxies. Despite the differences being small, they are systematic, as shown in Fig. 2.7. On a case-by-case basis, some scatter and random small-scale fluctuations are visible. In particular, the rotation curves for galaxies viewed at an inclination of 15° often exhibit prominent shape distortions that are not seen at other inclinations.

We find the same trend with spatial resolution but not with inclination in the mock long-slit data. In this case, the rotation curves of galaxies viewed at an inclination of 75° exhibit the most underestimated circular velocities, followed by galaxies at 15°; for other inclinations, the long-slit rotation curves are effectively independent of inclination (see Fig. 2.7). The long-slit rotation curves are a bit noisy and exhibit more scatter than those from the 2D velocity maps, mainly at low inclinations and high spatial samplings (small distances). Nevertheless, the average difference $\langle V_{\rm cir} - V_{\rm ls} \rangle$ is comparable to the previous case. The only exception is G1 viewed at an inclination of 75°, for which the average velocity underestimation at 80 Mpc increases to $\sim$ 11 km s^{-1} because of the galaxy's lack of symmetry during the second half of the simulation.

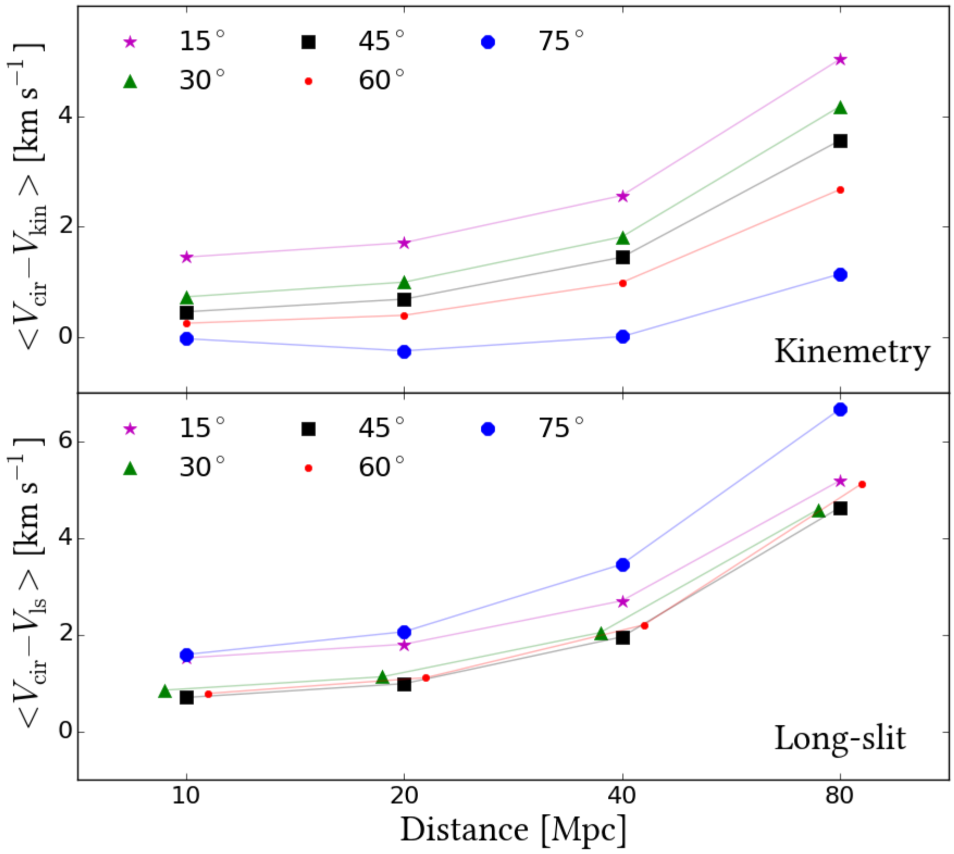

Figure 2.7: Mean H α velocity residuals $\langle V_{\rm cir} - V_{\rm kin}\rangle$ (top), and $\langle V_{\rm cir} - V_{\rm ls}\rangle$ (bottom) as a function of distance (spatial resolution) and inclination for all galaxies and snapshots. The mean is taken over all galaxies and snapshots. Some markers are slightly shifted horizontally to make the plot more readable. The residual increases as the spatial sampling gets coarser, reaching as much as $\sim$5 km s^{-1}. The rotation curves from the KINEMETRY analysis exhibit larger residuals because the galaxies are viewed more face-on. In the long-slit case, the largest residual occurs in discs inclined at 75°.

2.4.3 Rotation curve fitting

In Fig. 2.8, we compare the reduced χ^2_ν of the best-fitting NFW and ISO models for the various types of rotation curves for the D2 simulation placed at 10 Mpc. This is a good example of the general trends in the whole sample, so we use it to introduce our main findings before going into a more detailed analysis.

Points that lie below the one-to-one line in Fig. 2.8, represent better agreement of the data with the NFW model, and points above the diagonal indicate that the ISO model provides a better description of the data. We see that the NFW profile fits the theoretical $V_{\rm dm}$ and $V_{\rm tot}$ curves much better, as expected because by construction the central potential of the galaxy is dominated by the DM, which obeys an NFW profile. The results from fitting $V_{\rm tot}$ are somewhat closer to the line of equality between models than those from $V_{\rm dm}$

because of the effect of the baryonic contribution to the rotation curve. Surprisingly, $V_{\rm cir}$ is better fit by the ISO model than the NFW model. The fits to the mock rotation curves tend to favour the ISO model, especially when the galaxies are viewed at high inclinations.

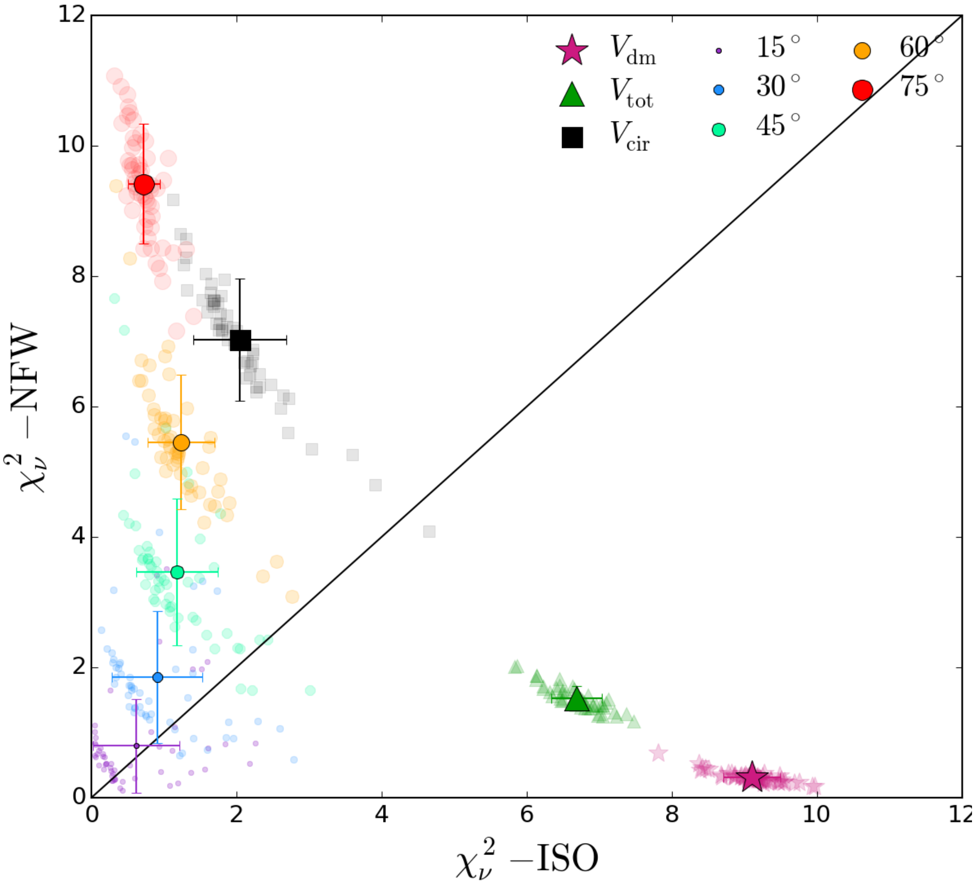

Figure 2.8: Distribution of χ^2_ν obtained by fitting the NFW and ISO models to the various types of rotation curves for the Dwarf2 simulation placed at 10 Mpc. The shapes, colours, and sizes of the markers are coded according to the specific rotation curve used, as detailed in the legend. Background semi-transparent symbols correspond to the results for individual snapshots, the solid symbols in the front denote the centroids of the corresponding clouds of points, and the error bars represent the 1-σ scatter in the horizontal and vertical directions. The black diagonal line represents equality between the goodness of the fits. For this simulation, the theoretical rotation curves $V_{\rm dm}$ and $V_{\rm tot}$ are better fit by the cuspy NFW model. However, the theoretical rotation curve $V_{\rm cir}$ is better fit by the ISO model because pressure support causes $V_{\rm cir}$ to be less than $V_{\rm tot}$ in the central ~ 1 kpc. The mock rotation curves obtained using KINEMETRY are generally better fit with the ISO model, especially when the galaxies are viewed at inclinations of 45° or greater. These results demonstrate that rotation curve fitting can indicate the presence of a core when the true DM profile is cuspy.

We now discuss the results for all of the galaxies and snapshots. In Fig. 2.9 and Table 2.2, we show the fraction of cases in which one of the models is preferred over the other for each type of circular velocity profile.[3] We estimate a lower limit on these fractions by demanding one χ^2_ν to be at least 1.5 times smaller than its counterpart and stating that both models are equally good otherwise. For this reason, the sum of the NFW and ISO fractions is not always unity. Upper limits are obtained by relaxing our threshold on the χ^2_ν's ratio from 1.5 to 1.1. We find 100 per cent of the $V_{\rm dm}$ rotation curves to be better represented by the cuspy NFW model for all the tested spatial samplings ($\leq$ 400 pc for $D \leq 80$ Mpc) in perfect agreement with the underlying DM distributions in the simulations.

Using $V_{\rm tot}$, we find that between 52 and 61 per cent of the rotation curves are better fit with the NFW profile, whereas between 35 and 39 per cent of the cases are better fit by the ISO model. This means that the signature of the NFW haloes is still detectable, although the inclusion of the baryonic contribution to the potential without an explicit correction included in the fit introduces considerable errors. In particular, we note that the NFW model is always better for D1, D2, and D3, but it is disfavoured for D4 and G0. In the case of G1, both models provide comparable fits to $V_{\rm tot}$. Strikingly, the $V_{\rm cir}$ rotation curves for simulated galaxies viewed at $D \leq 40$ Mpc, i.e. whose inner parts are sampled every $\leq$ 200 pc, are better fit with the ISO model for 74-95 per cent of the sample. Such a result would be typically interpreted as proof of the ubiquitous presence of cores in the central region of galactic haloes, but because there are no cores in our simulations, this conclusion would be incorrect. This fact is particularly shocking because $V_{\rm cir}$ is a perfect theoretical measurement of the gas rotational velocity, and it occurs even when the galaxies are viewed at 10 Mpc (i.e. the spatial resolution is optimal). When viewed at 80 Mpc, the difference between models decreases, although the illusion of DM cores does not vanish entirely; the NFW profile is preferred in 25-44 per cent of the cases, and the ISO model provides a better fit in 42-49 per cent of the cases.

Regarding the mock observations and considering all distances and inclinations, the ISO model provides a better fit to $V_{\rm kin}$ for 73-90 per cent of the sample, and the NFW

---

[3] We remind the reader that the theoretical rotation curves ($V_{\rm dm}$, $V_{\rm tot}$, and $V_{\rm cir}$) are resampled to the same positions of the mock observations; consequently, the results depend on the assumed distance. Also recall that we *observe* the curves at a rate of two points per seeing. So, at a distance of 80 Mpc, the spatial resolution of the mock observations is $\sim$800 pc, but they are sampled at a rate of $\sim$1/400 pc^{-1}, and this is what matters for the theoretical velocity profiles.

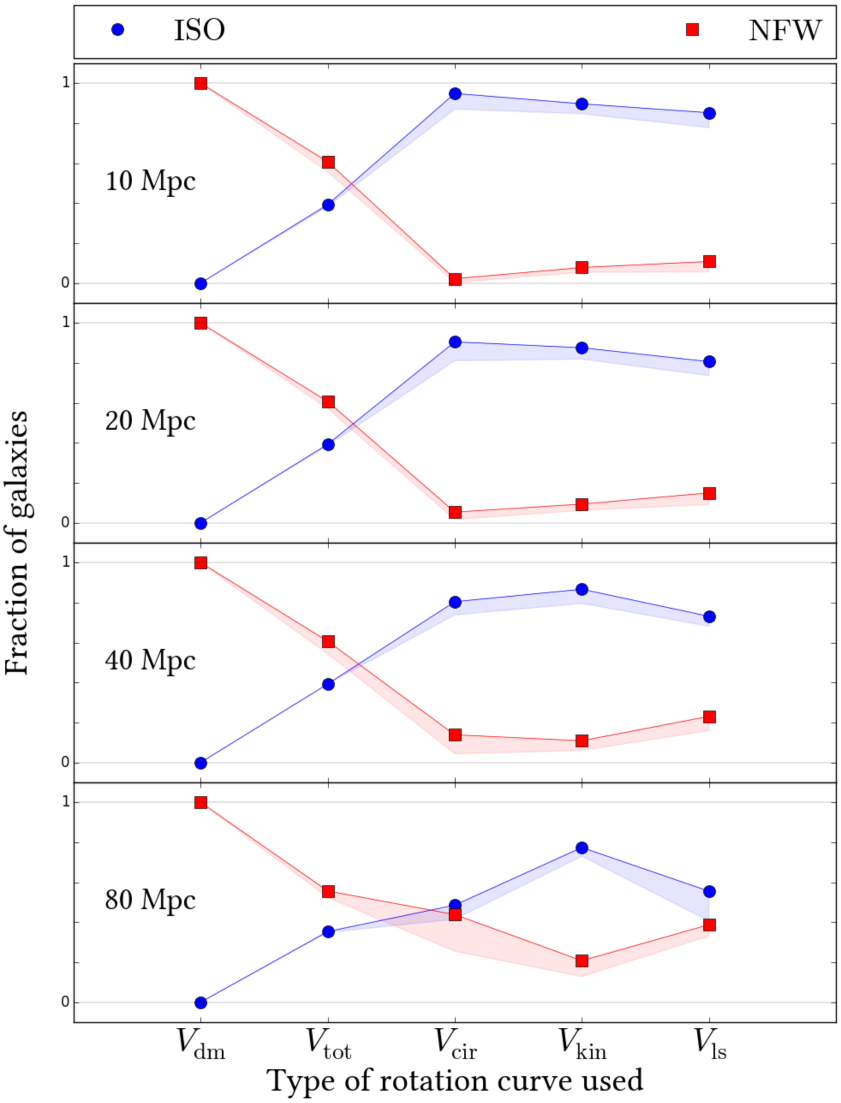

Figure 2.9: Fraction of galaxies that are better represented by the NFW or ISO models based on the best-fit χ^2_ν values. Solid lines are established by demanding that one of χ^2_ν values is at least 1.5 times bigger than the other one. The upper limit of the shaded regions represents the upper limits on the NFW/ISO fractions, which were obtained using a threshold of 1.1 instead of 1.5. $V_{\rm dm}$ is always better fit by the NFW model, as expected because the DM profiles of the simulations obey an NFW profile. In contrast, $V_{\rm tot}$ is sometimes better fit by the ISO model because of the baryonic contribution to the potential. In the vast majority of cases, the cored ISO model provides a better fit to the theoretical circular velocity profile $V_{\rm cir}$ and the mock rotation curves, despite the simulations containing cuspy dark matter profiles by construction.

model is preferred for only 5-21 per cent of the sample. Thus, this type of analysis applied to our *observed* rotation curves would provide *strong evidence* of the widespread existence of cores in the DM haloes of dwarf galaxies and LSBs, which is in tension with the cuspy nature of the DM haloes in our simulations. This effect is more misleading for more nearby

Table 2.2 - Percentages of rotation curves that are better represented by the NFW or ISO models according to the type of rotation curve fit and the spatial resolution (assumed distance).

H α PSF (pc)		∼100	∼200	∼400	∼800
D (Mpc)		10	20	40	80
V_{dm}	NFW	100 (100)	100 (100)	100 (100)	100 (100)
	P-iso	0 (0)	0 (0)	0 (0)	0 (0)
	Both	0 (0)	0 (0)	0 (0)	0 (0)
V_{tot}	NFW	56 (61)	57 (61)	54 (61)	52 (56)
	P-iso	38 (39)	39 (39)	39 (39)	35 (35)
	Both	6 (0)	4 (0)	6 (0)	13 (9)
V_{cir}	NFW	0 (2)	2 (5)	4 (14)	25 (44)
	P-iso	87 (95)	81 (91)	74 (81)	42 (49)
	Both	13 (3)	17 (4)	22 (6)	33 (8)
V_{KIN}[a]	NFW	5 (8)	6 (9)	6 (11)	13 (21)
	P-iso	85 (90)	82 (88)	80 (87)	73 (77)
	Both	10 (2)	12 (3)	14 (2)	14 (2)
V_{LS}	NFW	6 (11)	9 (15)	16 (23)	33 (39)
	P-iso	78 (85)	74 (81)	68 (73)	41 (56)
	Both	16 (4)	17 (4)	16 (4)	26 (6)

Note: The fiducial NFW/ISO fractions are estimated by demanding that one of the χ^2_ν values to be at least 1.5 times smaller than the other one. Values in parentheses require a minimum ratio of 1.1 between the χ^2_ν values. The rows labeled 'Both' correspond to cases for which the χ^2_ν values of the NFW and ISO fits differ by less than a factor of 1.5 (1.1).
[a] The values for $V_{\rm kin}$ and $V_{\rm ls}$ are for the mock rotation curves at all inclinations.

galaxies. It is worth emphasizing that whatever the reason for the ISO model being a better fit to the mock observations, the effect is already evident when we analyse the theoretical circular motions of the gas, $V_{\rm cir}$. We note the same trend in the results from long-slit data as for the 2D velocity maps. The only difference occurs at 80 Mpc, where the ISO model is preferred by a much smaller margin and the number of unresolved cases is larger when the long-slit rotation curves are used.

In Fig. 2.10 and Table 2.3, we categorize the results from the 2D mock observations according to the inner spatial resolution and inclination. We see that the NFW profile is virtually never preferred when the galaxies are viewed at an inclination of 75°. Considering specific combinations of distance and inclination, we see that the NFW model sometimes provides better fits, but these are limited to a maximum of 24 per cent of the sample, whereas the ISO profile fits the data better in 65-99 per cent of the cases. In Fig. 2.10, note that the blue (ISO) and red (NFW) regions never overlap, reflecting the fact that the fraction of rotation curves that are better fit with the ISO model is always greater than the fraction better fit with the NFW model. The difference between the two fractions increases with inclination. Finally, we note that the gap between the coloured stripes becomes narrower at 80 Mpc, as the samplig gets poorer.

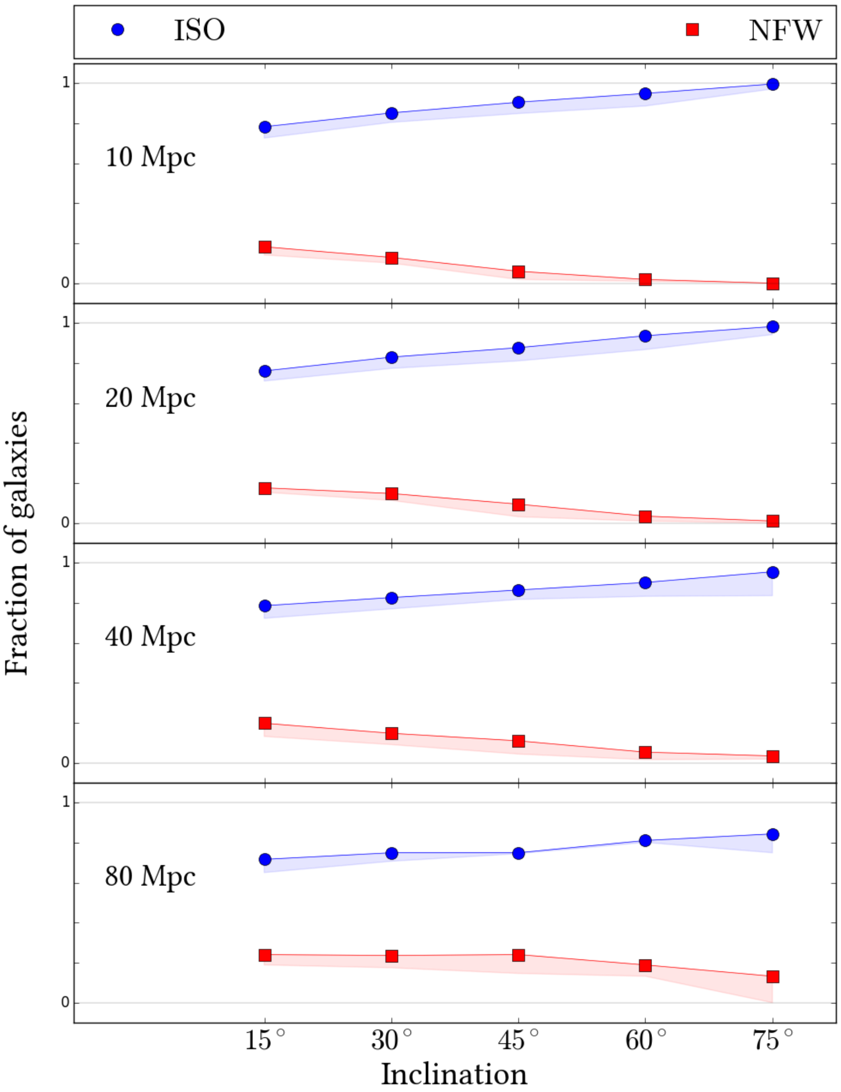

Figure 2.10: Fraction of mock rotation curves that are better described by the NFW/ISO models as a function inclination for the mock 2D observations analysed with KINEMETRY. The different rows correspond to different assumed distances (from top to bottom: 10, 20, 40, and 80 Mpc). The symbols and colours are the same as in Fig. 2.9. Independent of inclination and distance, the rotation curves derived from the 2D velocity maps are always better fit by the cored ISO model than the cuspy NFW model.

Table 2.3 - Similar to Table 2.2, but for the rotation curves obtained by analysing the mock 2D velocity maps with KINEMETRY ($V_{\rm kin}$) and classified according to the assumed distance and inclination.

H α PSF (pc)		∼100	∼200	∼400	∼800
D (Mpc)		10	20	40	80
15°	NFW	14 (18)	15 (18)	13 (20)	19 (24)
	P-iso	73 (78)	71 (76)	72 (79)	65 (72)
	Both	13 (3)	14 (6)	14 (2)	16 (4)
30°	NFW	10 (13)	11 (15)	9 (15)	17 (24)
	P-iso	81 (85)	77 (83)	77 (83)	71 (75)
	Both	9 (2)	11 (2)	14 (3)	12 (1)
45°	NFW	2 (6)	3 (9)	4 (11)	15 (24)
	P-iso	85 (91)	81 (88)	82 (86)	75 (75)
	Both	13 (3)	16 (3)	14 (3)	11 (1)
60°	NFW	1 (2)	1 (3)	2 (5)	13 (19)
	P-iso	89 (95)	87 (94)	83 (90)	80 (81)
	Both	10 (3)	12 (3)	15 (4)	7 (0)
75°	NFW	0 (0)	0 (1)	2 (3)	0 (13)
	P-iso	97 (100)	94 (98)	84 (96)	75 (84)
	Both	3 (0)	6 (1)	14 (1)	25 (2)

In Fig. 2.11 and Table 2.4, we repeat the exercise for the long-slit data. At 10 Mpc (∼100 pc inner spatial resolution), we see the same trend with inclination as before, i.e. more-inclined galaxies appear more cored. This tendency becomes weaker at 20 Mpc, and it does not hold beyond that. Regarding the trend with distance, the ambiguity between models increases more rapidly compared with when the 2D velocity maps were used. In particular, when the galaxies are placed at 80 Mpc, of order half the sample appears to contain cores and a major fraction of the other half appears to contain cusps. Finally, it is worth noting that these general results are not biased by the inclusion of G1, i.e. they do not change substantially if we exclude this simulation.

2.5 *Discussion*

So far we have presented strong evidence that rotation curve fitting can yield qualitatively incorrect conclusions regarding the inner curvature of the density profiles of galactic DM haloes. Here, we discuss the origin of the errors based on the differences amongst

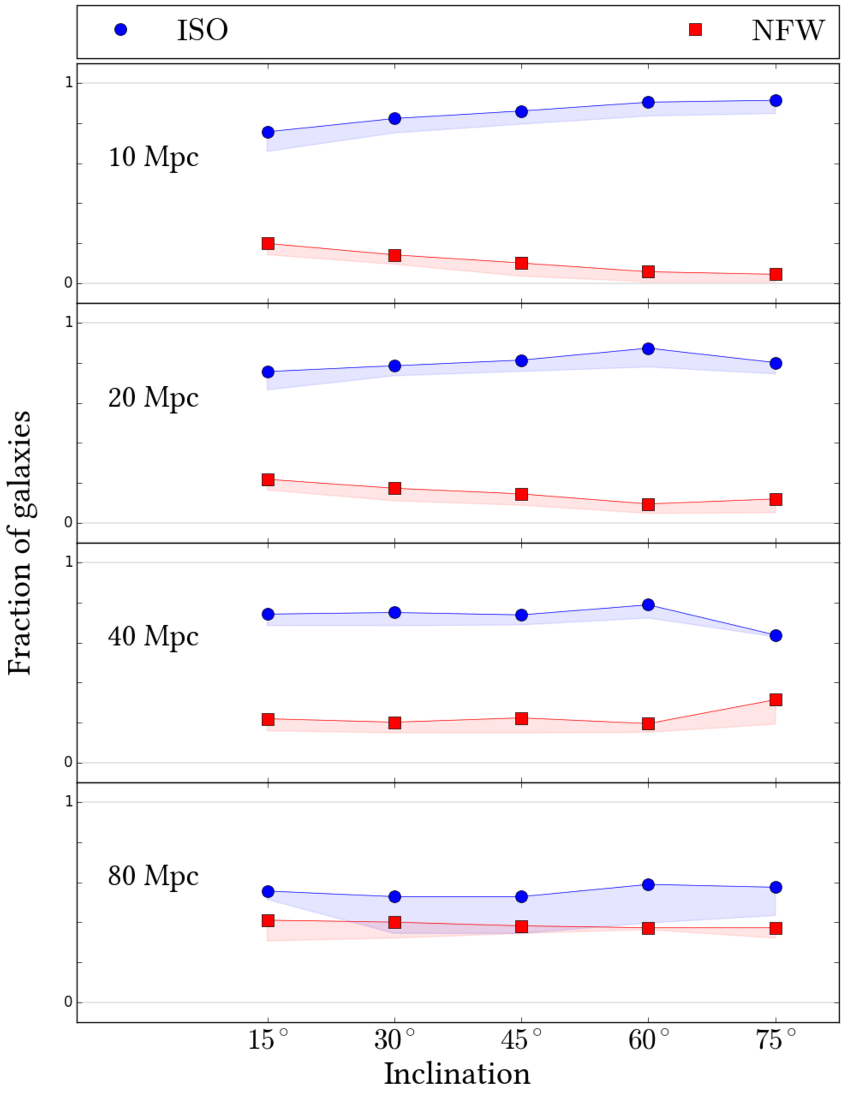

Figure 2.11: Fraction of mock rotation curves that are better described by the NFW/ISO models as a function of distance and inclination for the hybrid RCs using mock H α long-slit data. The symbols and colours are the same as in Fig. 2.9. Except for an assumed distance of 80 Mpc, the ISO model is incorrectly preferred in the majority of cases. For 80 Mpc, of order half of the rotation curves are better fit with the cored ISO model despite the galaxies having cuspy profiles.

the theoretical velocity profiles, check the dependence of the results on the radial range covered by the rotation curves, and compare the coefficients of our best fits to a collection of results from the literature to demonstrate that our mock observed rotation curves are in fact representative of real galaxies. We also compare our main findings against other works which analysed synthetic observations from numerical simulations in the core-cusp context.

Table 2.4 - Similar to Table 2.2 but for $V_{\rm ls}$, the hybrid rotation curves using the mock H α long-slit data, classified according to the assumed distance and inclination.

H α PSF (pc)		$\sim$100	$\sim$200	$\sim$400	$\sim$800
D (Mpc)		10	20	40	80
15°	NFW	14 (20)	16 (22)	16 (22)	31 (41)
	P-iso	66 (76)	67 (76)	69 (74)	51 (56)
	Both	20 (4)	17 (3)	16 (4)	18 (3)
30°	NFW	9 (14)	11 (17)	15 (20)	32 (40)
	P-iso	75 (82)	74 (79)	68 (75)	34 (53)
	Both	15 (3)	15 (4)	17 (5)	33 (7)
45°	NFW	3 (10)	9 (14)	15 (22)	34 (38)
	P-iso	80 (86)	76 (81)	69 (74)	34 (53)
	Both	17 (4)	15 (4)	16 (4)	31 (9)
60°	NFW	1 (6)	5 (9)	15 (19)	36 (37)
	P-iso	84 (91)	78 (87)	72 (79)	40 (59)
	Both	16 (4)	17 (3)	13 (2)	24 (4)
75°	NFW	1 (4)	5 (12)	19 (31)	32 (37)
	P-iso	85 (92)	75 (80)	63 (64)	43 (58)
	Both	14 (4)	20 (8)	18 (5)	25 (5)

2.5.1 *Unraveling the illusion of DM cores*

First, we focus on the real shapes of the different velocity profiles, i.e. we refer to rotation curves of simulated galaxies placed at 10 Mpc, for which the spatial resolution is high ($\sim$ 100 pc). The explicit effect of poorer spatial resolution is commented on in Sec. 2.5.2. We recall that 100 per cent of the $V_{\rm dm}$ profiles are better described by the NFW model. Consequently, in principle, rotation curve fitting can recognise a cuspy DM distribution from its true circular velocity profile given sufficient spatial sampling ($\leq$ 400 pc).

As for $V_{\rm tot}$, we have seen that NFW profiles are more favoured in the sample as a whole, although the ISO model fits the velocity profiles from D4 and G0 better, and for G1, the two models provide superior fits for similar fractions of the rotation curves. Additionally, for D1, D2, and D3, the confidence with which the rotation curve fitting detects the cuspy haloes, as judged based on the χ^2_ν values of the fits to $V_{\rm tot}$, is somewhat reduced compared with $V_{\rm dm}$. These results challenge the widespread assumption that the contribution of baryons to the potential will tend to make the DM profile inferred under the minimum disc assumption cuspier than the true DM profile.[4] These results also imply that the minimum disc approximation is unacceptable for some dwarf galaxies. To better understand this result, in Fig. 2.12 we plot the inner velocity profiles expressed as fractions of $V_{\rm tot}$. Noting that the circular velocity profile of a spherical halo is given by the enclosed mass as a function of radius, which can be estimated from the density profile by integration, it can be shown that $\rho \propto r^0$ cores result in linear inner circular velocity profiles, $V_{\rm inner} \propto r^1$, whereas $\rho \propto r^{-1}$ NFW cusps lead to $V_{\rm inner} \propto r^{0.5}$. In other words, cuspier density profiles produce more curved velocity profiles characterized by smaller exponents, but always inside the interval $[0.5, 1]$ for the limits we are considering. Because the fraction $V_{\rm dm}/V_{\rm tot}$ systematically decreases with radius, this quotient has a negative exponent when expressed as a power law, which implies that the exponent of $V_{\rm tot}$ is larger (closer to 1) than that of $V_{\rm dm}$. Consequently, the dark matter distributions inferred from $V_{\rm tot}$ are less cuspy than those inferred from $V_{\rm dm}$. In other words, the contribution of baryons to the potential tends to make the circular velocity profile flatter rather than cuspier. This result may not hold for all galaxies, but the salient point is that there is no justification to claim an universal ability of the minimum disc approximation to make the inferred dark matter density profiles appear cuspier than they truly are. More likely, the resulting cuspiness of $V_{\rm tot}$ will depend on the relative curvatures and normalizations of the dark and luminous components. Also note that in Fig. 2.12, the inner, negative slope of the $V_{\rm dm}/V_{\rm tot}$ profile is shallower in D1, D2, and D3 than in the other simulations, and these simulated galaxies have the smallest baryonic-to-DM ratios amongst our sample. Consequently, the inner curvatures of $V_{\rm dm}$ and $V_{\rm tot}$ must differ the less in these galaxies.

In the case of $V_{\rm cir}$, the rotation curve fitting analysis is completely misleading because the cored ISO model provides better fits to most of the rotation curves. Thus, the core-like shape that we infer from the mock rotation curves is already imprinted in $V_{\rm cir}$ and is therefore not (only) a consequence of observational errors (e.g. projection effects). Fig. 2.12 provides insight into this issue. We see that in all galaxies, $V_{\rm cir}$ is approximately ~ 50 per cent of $V_{\rm tot}$ in the very center and progressively increases until it reaches a fractional contribution of order unity just outside the first kiloparsec. This systematic trend is

---

[4] This is usually expressed in other words, i.e. stating that the minimum disc approximation puts an upper limit on the steepness of the DM halo density profile (e.g. de Blok et al., 2001).

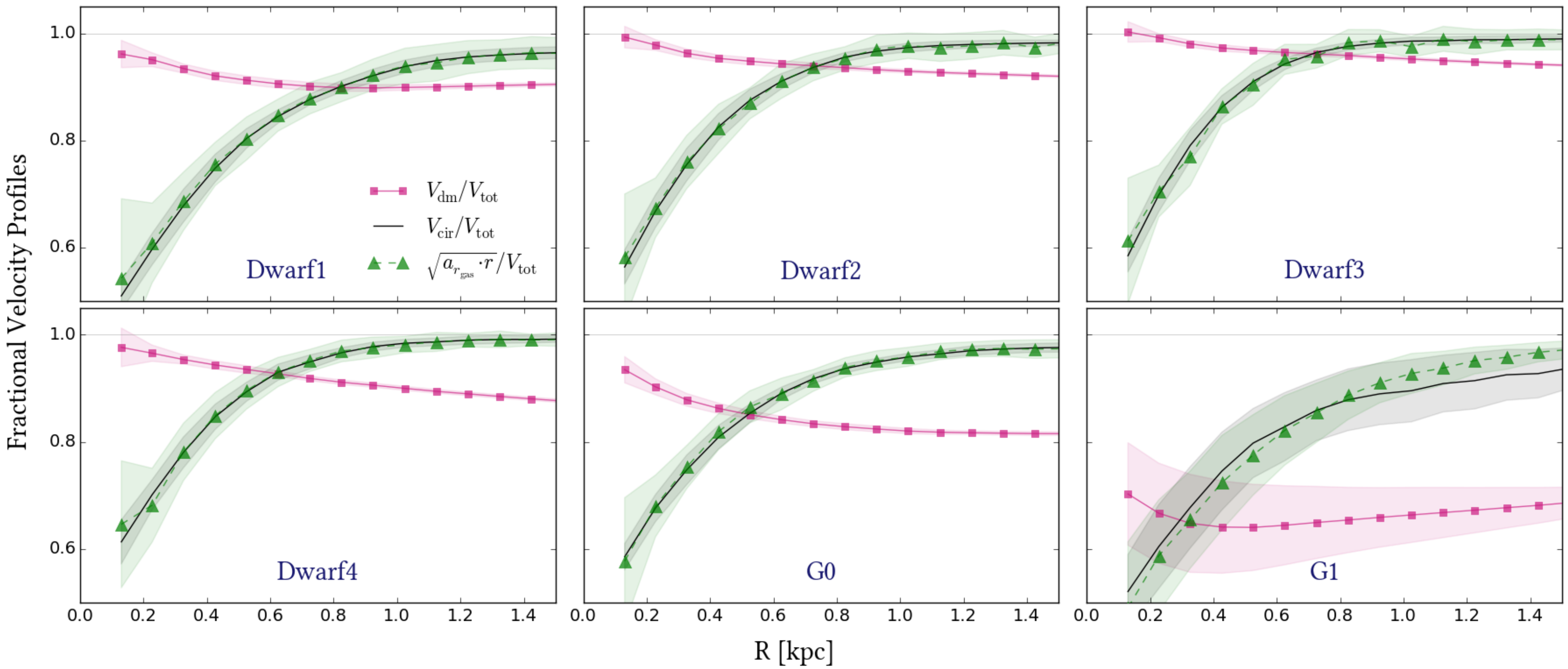

Figure 2.12: Theoretical velocity profiles within the central 1.5 kpc expressed as a fraction of V_{tot}. Black solid line is for V_{cir} and magenta solid line with square markers for V_{dm}. In addition, we show with green triangles joined by a dashed line the velocity profiles inferred from the radial acceleration of the gaseous particles in our simulations, i.e. $\sqrt{a_{r_{\mathrm{gas}}}\, r}$. Each line represents the mean taken over all snapshots, and the shaded regions represent the 1-σ scatter amongst snapshots. The fact that $V_{\mathrm{dm}}/V_{\mathrm{tot}}$ decreases with radius implies that the DM profile is cuspier than the total mass profile and thus the minimum disc assumption does not place an upper limit on the cuspiness of the DM profile. Moreover, both V_{cir} and the circular velocity corresponding to the radial acceleration experienced by the gas component, which are almost identical, are generally less than V_{tot} because of pressure support, and the fractional difference is greater at smaller radii. This systematic beaviour implies that the matter distribution inferred from v_{cir} will look flatter than that inferred from V_{tot}.

opposite to the one that we found in the case of $V_{\rm dm}$ and necessarily implies that the inner curvature of $V_{\rm cir}$ is much less pronounced than that of $V_{\rm tot}$ (i.e. the mass distribution inferred from $V_{\rm cir}$ is less cuspy than the true mass distribution).

Why is $V_{\rm cir}$ typically less than $V_{\rm tot}$, especially at small radii? Our tests indicate that it is the result of pressure support, i.e. an effective decrease in the radial acceleration because of an outward force of the gas on itself, which is the result of a negative radial pressure gradient. To illustrate this point, we include in Fig. 2.12 the circular velocity corresponding to the radial acceleration experienced by the gas component, i.e. $\sqrt{a_{r_{\rm gas}} r}$, which closely corresponds to the actual circular velocity of the gas, $V_{\rm cir}$. This correspondence demonstrates that the gas component is in rotational equilibrium but also shows that within the first kiloparsec, the radial acceleration experienced by the gas particles is less than that experienced by the stellar ones (which is used to define $V_{\rm tot}$). Because the overall gravitational potential is the same for gas and stars, the only physical phenomenon we identify that is capable of causing the difference is pressure support associated with the high gas density in the galactic centres and the injection of thermal energy from stars into the interstellar medium (ISM).

Regarding the mock observations, we know that for galaxies placed at 10 Mpc, the mock rotation curves perfectly follow the theoretical $V_{\rm cir}$ curve (Fig. 2.6); thus, their cored shapes simply reflect the curvature of the true circular motions of the gas, as determined by the full hydrodynamics and not only by gravity. Moreover, careful inspection of Fig. 2.9 reveals that the gap between the ISO and NFW fractions is less for $V_{\rm ls}$ than for $V_{\rm kin}$. After a thorough review of the fitting procedure, we concluded that this difference is a result of the size of the error bars, which are larger for the long-slit observations than for the rotation curves obtained from the 2D velocity maps with KINEMETRY. Consequently, the individual points of the mock H α long-slit rotation curves, which determine the inner curvature of the profiles, have a smaller weight during the fits than the outer points from the mock H I rotation curves, thus reducing the significance of the core detections.

2.5.2 Dependence on spatial resolution and inclination: beam-smearing and projection effects

Recalling that our theoretical rotation curves for galaxies at $D > 10$ Mpc are simply re-sampled versions of the 10-Mpc curves and noting that the NFW model fits better all the V_{dm} profiles independent of distance, we conclude that rotation curve fitting methods can distinguish the signature of an ideal cuspy NFW profile even at a sampling rate of $\sim$400 pc in the rising part (1 arcsec at 80 Mpc) with the first measurement at ~ 0.9 kpc, at least for the (c, V_{200}) parameter space covered by our models.

The situation is a bit different for cores. We know from the former sections that the intrinsic shape of V_{cir} is close to the ISO profile, which is favoured in more than 80 per cent of the fits for galaxies placed at 10. However, the fraction of cores steadily declines as the galaxies are placed further away, with a simultaneous increase in the number of preferred NFW fits and ambiguous cases. At 80 Mpc, the number of galaxies catalogued as cusps is comparable to the number of galaxies catalogued as cores. This is partially explained by the small sizes of the fake cores ($\sim$1 kpc), whose signature is progressively washed out as the sampling gets poorer and the first measured point moves to larger radii. Yet we note that this is only true for D2, D3, and mildly for G1. Fits to V_{cir} in the other galaxies favour the ISO model at all distances, showing that the outcome of the fits depends on more subtleties than just the sampling rate.

It is important to note that undersampling the curves is not sufficient to fully model the impact of spatial resolution. Beam smearing, i.e. the smoothing of the velocity gradients in the rising part of the rotation curves caused by averaging over large PSF/beam areas, is also a resolution effect. The measured velocities are further lowered by projection effects related to the fact that, in inclined discs of finite thickness, any line of sight targeting an inner position mixes information from tracers at larger radii, whose line-of-sight velocity component is very small because of the inherent geometry of the rotating disc (Rhee et al., 2004). Note that the volume of gas crossed by a single telescope pointing increases as the spatial resolution becomes coarser and as the galaxy inclination and disc thickness are increased; thus, in order to assess these entangled effects properly, we must confront our mock kinematic observations with the theoretical velocity profiles.

Comparing the results from V_{kin} with those from V_{cir} (Fig. 2.9), we see that they are very similar at $D \leq 40$ Mpc, i.e. the effect of beam smearing and projection effects is mild for inner spatial resolutions ≤ 400 pc, though they effectively introduce the dependence with inclination discussed in Sec. 2.4.3. At 80 Mpc, in contrast, beam-smearing and projection effects cause a significant difference between the results from V_{kin} and V_{cir}, as a large fraction of the mock observations are better explained by a cored profile. In this case, the signature of the fake core does not vanish with the poor sampling in any case because the additional effects considerably lower the inner measured velocities, thereby reinforcing the illusion of a DM core (Fig. 2.6).

As can be seen in Fig. 2.10 and Table 2.3, the effect of distance on $V_{\rm ls}$ is to progressively reduce the fraction of cases that are better fit by the ISO model, while augmenting those which are better fit by the NFW profile. The increasing ambiguity, which is more noticeable than in the case of $V_{\rm kin}$, results from the larger size of the H α long-slit error bars in comparison to the H I error bars reported by kinemetry and illustrates the sensibility of the rotation curve fitting analyses to the specific details in the treatment of the data. Using $V_{\rm ls}$, we only observe systematic effects with inclination at 10 and 20 Mpc; we suspect they are strongly dependent on the existence of inner measurements and their relative weights during the fits.

2.5.3 Dependence on the extent of the rotation curve

In Fig. 2.13, we show the average value of the ratio $\chi^2_{\nu_{\rm ISO}}/\chi^2_{\nu_{\rm NFW}}$ after truncating the 10-Mpc theoretical velocity profiles at different radii and repeating the fits. We quantify the extent of a curve by the number of points inside the truncation radius, $N_{\rm points}$, which we vary from 10 to approximately 3.3 times the optical radius, roughly corresponding to 65 points in Dwarf1 and to 182 points in Dwarf4, the most extended galaxy in our sample. According to Fig. 2.13, $V_{\rm dm}$ is always better represented by the NFW formula independently of the truncation point. $V_{\rm tot}$ is also better represented by the NFW profile but still marginally consistent with the ISO model. In contrast, $V_{\rm cir}$ is better fit by the ISO profile for any truncation radius, although for small values of $N_{\rm points}$, the difference between models is more extreme because the fake inner core dominates the fits. We do not plot equivalent profiles for the mock observations to avoid overcrowding the figure, but we note that they behave in the same manner as $V_{\rm cir}$. Thus, the underestimation of the first points of the rotation curves determines the outcome of the rotation curve fitting analysis (i.e. the detection of spurious DM cores), regardless of the extent of the kinematic observations. Consequently, our specific choice to truncate the velocity profiles at approximately two times the optical radius does not affect the main conclusions of this work. At larger distances, we observe exactly the same qualitative results and the same shape for the $\chi^2_{\nu_{\rm ISO}}/\chi^2_{\nu_{\rm NFW}}$ radial profiles.

We remade the main plots presented in Sec. 2.4 but with the truncation radii of all the curves varying between ∼1 and ∼3 times the optical radius, and we observed only minor differences in the results. In particular, we noted that when using more extended rotation curves, the fits to $V_{\rm ls}$ less often preferred the ISO model than when the fiducial truncation radius was used. Once again, this is due to the fact that in the long-slit case, the H α error bars are larger than the H I error bars, such that the effect of the inner core on the fit is progressively diminished as more outer points are used in the χ^2_ν calculation.

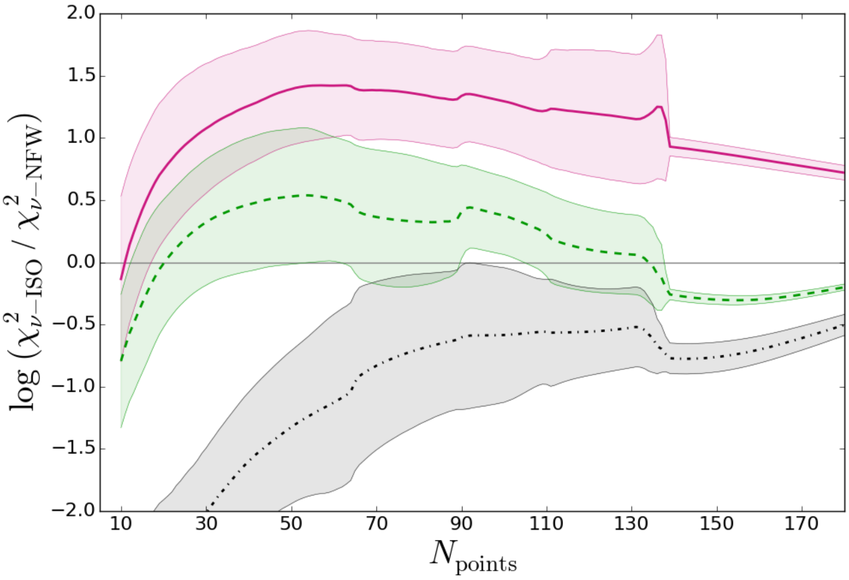

Figure 2.13: Dependence of the χ^2_ν ratio on the extent of the rotation curves. $N_{\rm points}$ represents the number of points considered for the fit. The horizontal line represents equality between the models. We show the results for $V_{\rm dm}$ (magenta, solid line), $V_{\rm tot}$ (green, dashed line), and $V_{\rm cir}$ (black, dot-dashed line) for galaxies placed at 10 Mpc (∼100 pc inner resolution). The reported lines denote the mean trends from all galaxies (or those reaching a given radial extent), whereas the shaded regions represent the 1-σ scatter. Beyond 134 points the only contributor is D4, which is why the scatter is much smaller than at smaller radii. This plot demonstrates that the conclusion that $V_{\rm dm}$ and $V_{\rm tot}$ are better fit with the NFW model (in the sample as a whole), whereas $V_{\rm cir}$ (and the mock observed rotation curves, which are not shown) is better fit with the ISO model, is effectively independent of the truncation radius employed.

2.5.4 Comparison with the literature

2.5.4.1 Comparison with observational results

In Fig. 2.14 (left), we present the coefficients (c, V_{200}) of the best NFW fit obtained for each velocity profile in our study, along with a collection of observational results from the literature based on high-resolution rotation curves. We fit our rotation curves trying all possible extents from 1 to 3 times the optical radius (typical of observations) in order to approximate the stochasticity of real data. This is equivalent to maximum extents of between 2.6 and 29 kpc and $N_{\rm points}$ between 42 and 180, depending on the size of the galaxy.

We note that the coefficients c and V_{200} from the fits appear correlated both in our simulations and in the observational data and, more importantly, that our fits are very consistent with the parameter space spanned by observations. Strikingly, this is only true when our results consider different truncation radii and different distances together, as the fits to our fiducial mock data (truncated at 2 times the optical radius) at 10 Mpc cover just a narrow subset of the whole parameter space, roughly $\log(V_{200}) \leq 2$ and $\log(c) \geq 0.8$, as indicated with the shaded gray region in the plot. The agreement between observations and the fits to our mock data is enhanced by the inclusion of fits to less-extended versions of our rotation curves, probably because many observational studies use only H α information, and they often do not reach the same radial extent as our fiducial mock dataset. This is related to another facet of the core-cusp problem pointed out by observational studies, according to which the few reasonable NFW fits to real galaxies prefer large values of V_{200} and very low concentrations, which are not compatible with the mass-concentration relation predicted by cosmological simulations. As our results illustrate, this might originate in the large dependence of the observational analyses on subtle details and thus may not represent a genuine discrepancy between ΛCDM cosmological simulations and observations.

We repeat the same experiment with the ISO model and present the results and a comparison with the literature in Fig. 2.14 (right). The shaded region encloses the subset of the parameter space covered by the fits to galaxies at 10 Mpc using the fiducial extent of the rotation curves ($2\times R_{\rm opt}$). The full set of results includes fits to the mock rotation curves truncated at different radii, ranging from 1 to 3 times $R_{\rm opt}$. Our fits populate a region of the ρ_0-R_c parameter space that is consistent with the observational works, although they do not fully cover the low ρ_0-high R_c end of the observed relation. This time the disagreement is only slightly alleviated by the use of different distances and truncation radii, i.e., despite the fact that the effects we discuss in this work offer a plausible explanation for the cusp-core discrepancy in terms of logarithmic density slopes, they are not sufficient to explain the largest cores inferred from ISO fits to real galaxies, associated with the large diversity of dwarf galaxy rotation curves, as discussed by Oman et al. (2015). It is also interesting to note that our fits naturally produce a correlation between ρ_o and R_c that agrees extremely

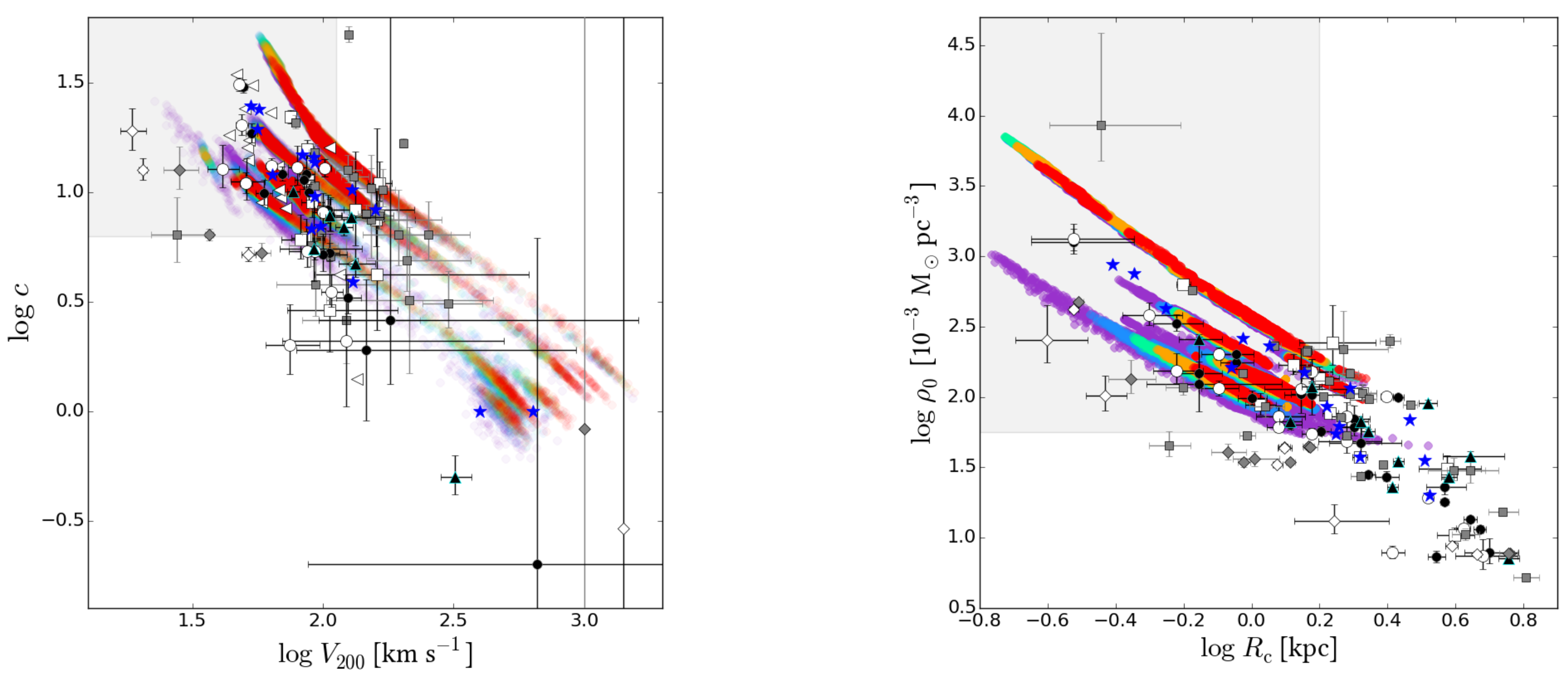

Figure 2.14: Coefficients of the best fits to our mock rotation curves (NFW models on the left, ISO models on the right) compared with observational results from the literature. We used different extents for the mock rotations curves, ranging from 1 to 3 times the optical radius. Results are colour-coded by inclination as in Fig. 2.8. The following background markers represent observational results from the literature: circles (de Blok and Bosma, 2002), triangles (Kuzio de Naray et al., 2006), stars (Swaters et al., 2003), squares (de Blok et al., 2001), left-pointed triangles (van den Bosch and Swaters, 2001), and diamonds (Oh et al., 2011b). White symbols represent fits for which the gas contribution was subtracted from the observed rotation curve before the fitting (but a mass-to-light ratio of zero was still assumed for the stellar component). We include error bars whenever they are reported. Note that de Blok et al. (2001); de Blok and Bosma (2002); Oh et al. (2011b) estimated (c,V_{200}) in alternative ways for some galaxies when the best-fit c value was negative or too close to zero; we do not include those galaxies in our comparisons. The positions of the simulated galaxies in the (c, V_{200}) plane depend on the distance to the galaxy and the radial extent of the mock data. At 10 Mpc, NFW fits to curves with fiducial extent ($2 \times R_{\rm opt}$) lie in a subset of the parameter space spanned by observations, roughly $\log(V_{200}) \leq 2$ and $\log(c) \geq 0.8$, as indicated with by gray square in the plot. Only when a larger diversity of extents and distances is allowed do we see the NFW fits almost covering the full parameter space that observations do. A similar trend occurs for the ISO model, though it appears less dramatic. At 10 Mpc, fits to curves with the fiducial extent lie on the shaded gray region, and slightly larger, less-dense cores are only recovered when we try different extents and distances. Nevertheless, none of the fits to our mock data is able to reproduce the largest, least dense cores observed in some galaxies. Interestingly, as the ISO fits to our simulated data represent illusory cores, and they reproduce the correlation between ρ_0 and R_c that has been obtained for real galaxies, this may be an artefact of the fitting process rather than a physical relation obeyed by real DM haloes.

well with that evident from observations. More specifically, both "free" parameters lie on a straight line with a slope close to -1, which corresponds to a relation of inverse proportionality (the product $\rho_o \times R_C$ is approximately constant). This observation has been used to argue that DM haloes are cored and exhibit a constant inner surface density as some sort of universal property (see Spano et al., 2008; Kormendy and Freeman, 2016, and references therein); however, the physical meaning of this conclusion is clearly put into question by our results[5].

2.5.4.2 Comparison with simulation works employing similar methodologies

We now put our work into context by means of a brief comparison with other studies that have investigated how well the inner shape of DM profiles can be extracted from synthetic observations of simulated galaxies[6]. We start with the pioneering work of Rhee et al. (2004), which found that bars, small bulges, and projection effects induce underestimates of the inner circular velocities that can prevent the detection of cuspy DM haloes, making them look cored. The authors mention that the individual effects lead to velocity errors of only a few km s^{-1}, but their cumulative effect can result in qualitatively incorrect conclusions.

This result is consistent with our study, but we note that the reason for this agreement is not straightforward because Rhee et al. (2004) did not simulate the gaseous phase. The velocity underestimation they observe is partially due to the dynamics of the stellar component (the so-called asymmetric drift effect)and to projection effects. Fig. 19 of Rhee et al. (2004) suggests that in axisymmetric systems, the inferred DM density profile slightly flattens, although it does not present a strong core. In contrast, in the presence of small bulges and bars, the combination of the former effects and non-circular motions makes the inferred density profiles artificially cored.

---

[5] Note that Spano et al. (2008) and Kormendy and Freeman (2016) did not use the pseudo-isothermal sphere model but a variant known as the non-singular isothermal sphere, but Kormendy and Freeman (2016) found the core radius and the central surface density estimated from one model to be proportional to the corresponding quantities in the other model, so, our discussion regarding the alleged ∼constancy of $\rho_0 \times R_c$ is straightforward.

[6] Here we refer to N-body numerical simulations, not to synthetic observations generated via analytic models. The advantage of the former is that they are more suitable for studying the three-dimensional dynamical evolution of galactic systems in a self-consistent way.

Interestingly, Rhee et al. (2004) show with convincing observational evidence that stars and ionized gas rotate similarly in the inner region, contrary to the general belief that the gas rotates faster because it is a dynamically colder component. The authors list possible explanations for this behaviour that have been suggested in the literature, including pressure support. In our simulations, the rotational velocities of the stellar and the gaseous particles inside the first kiloparsec are indeed similar, but not identical. In general we find the gaseous rotation curves to be more lowered in the very centre, whereas beyond $\sim 0.5 - 1$ kpc, the stellar component rotates more slowly. This means that the matter distribution recovered from the gaseous $V_{\rm cir}$ will tend to be flatter, explaining why we infer the presence of spurious cores even in systems without bulges or bars.

Valenzuela et al. (2007) further investigated the impact of systematic effects and presented detailed mass modelling of the dwarf galaxies NGC 3109 and NGC 6822. They compared collisionless N-body simulations and full hydrodynamical runs with and without star formation and stellar feedback and found that without feedback, the gas rotational speed is similar to the true circular velocity of the gravitational potential. In contrast, once injection of thermal energy from stellar processes into the ISM is included, the gaseous phase rotates considerably more slowly as a result of pressure support. This effect creates a notable flattening of the inferred density profile, which is further accentuated by the presence of a small bar and projection effects. Valenzuela et al. (2007) clearly illustrated how non-circular motions related to small asymmetries in the baryonic matter distribution, which might be easily overlooked, can bias the measured rotational velocities towards core-like profiles. An exhaustive analysis of asymmetric drift and pressure support corrections is also presented; Valenzuela et al. (2007) conclude that it is possible to recover the true circular velocity from the observed gaseous rotation curve in their models, but this requires very careful, detailed corrections for numerous systematic effects, even for axisymmetric discs. They also emphasize that observing low-rms velocity dispersions ($\sim$10 km s^{-1}) in a galaxy does not mean that such corrections can be safely neglected. Overall, we find our results to be in very good agreement with those of Valenzuela et al. (2007) and Rhee et al. (2004).

Kuzio de Naray and Kaufmann (2011) analysed mock observations of simulated galaxies embedded in cuspy, cored, and triaxial DM haloes. They generated realistic mock observations by choosing the spatial resolution, spatial coverage, and inclination according to the observational sample studied in Kuzio de Naray et al. (2006) and Kuzio de Naray et al. (2008b). Kuzio de Naray and Kaufmann (2011) found that typical rotation curve analyses are able to efficiently recognise the cuspiness of a DM halo and that it should be possible to observe the characteristic signature of a DM cusp in velocity maps. Particularly, in cored spherical haloes, the iso-velocity contours appear parallel in the center of the galaxy, whereas in spherically symmetric cuspy DM haloes, the central velocity contours are "pinched". The authors present examples of mock velocity fields in which such features are evident. They also found that stellar feedback had little effect on the mock velocity fields and observed RCs.

Why these results are so different from those referenced earlier is difficult to understand, especially noting that Kuzio de Naray and Kaufmann (2011) used the same code as Valenzuela et al. (2007). In the latter, stellar feedback was proven to be an efficient source of pressure support; thus, we speculate that the specific feedback implementation might have been different in Kuzio de Naray and Kaufmann (2011), leading to weaker pressurisation of the ISM. Alternatively, the simulations of Kuzio de Naray and Kaufmann (2011), which were initially composed only of gas and DM, might not have formed a sufficient number of stars for stellar feedback to pressurize the ISM significantly. We highlight the fact that using a different code with an independent stellar feedback implementation, our own simulations, which represent real galaxy populations in terms of the amount of gas and stars in the disc, reproduce the previous findings of Valenzuela et al. (2007) regarding the role of pressure support. We also note that our velocity fields are not pinched in the centre; instead the iso-velocity contours appear parallel there (see Fig. 2.3).

Oh et al. (2011) analysed mock velocity fields and images of two dwarf galaxies formed in cosmological simulations in the same manner as a sample of dwarfs previously studied in Oh et al. (2011b). The authors did not use the minimum disc approximation but rather attempted to subtract the contributions of gas and stars from the mock rotation curve. They were able to approximately recover the true DM density distribution from the mock observations using typical tilted-ring modelling, and they state that pressure support effects and non-circular motions did not hamper this recovery. Nevertheless, one of their two recovered DM density profiles underestimated the true density by a factor of 3 in the central region, but they associated this to errors in the estimation of the gravitational potential of the gas. Oh et al. (2011) found good agreement between their simulation results and observations. They concluded that DM cores likely exist in the sample of real galaxies and that the mechanisms which transform DM cusps into cores in their cosmological simulations (i.e. violent outflows of gas caused by repetitive, intense starburst episodes) are plausible. However, an important cautionary note is that Oh et al. (2011) only analysed mock observables when the DM haloes were already cored; therefore, this work does not lend insight into the possibility of identifying DM cusps via the same type of analysis. Regardless of whether it is possible to infer the presence of cores via rotation curve fitting, our results (and others mentioned above) suggest that cusps may be mistaken for cores and thus the cusp-core problem may be an illusion.

2.6 Conclusions

Our results demonstrate that pressure support effects can easily make DM cusps appear as cores in kinematic observations. Small errors of ~ 5 km s^{-1} within the central kiloparsec are sufficient to completely remove the signature of a DM cusp if they coherently decrease the measured velocity. Thus, not correcting for pressure support can be catastrophic in the cusp-core context, even for high-resolution data generated from perfectly symmetric rotating discs. We highlight the fragility of this type of rotation curve analysis: small errors can lead to qualitatively incorrect conclusions regarding the shape of the inner DM profile. Because multiple sources of errors (e.g. beam-smearing, non-circular motions, small bulges, and projection effects) act in a similar manner as pressure support (i.e. they tend to cause the observed circular velocity to underestimate the true circular velocity), even if the amount of pressure support present in our simulations differs in detail from reality, our main conclusion would still hold.

Strikingly, increasing the spatial resolution does not lead to more reliable conclusions. Instead, the ISO model is preferred more often when the simulated galaxies are placed at smaller distances because the signature of the fake core is better sampled. We also note that the coefficients of the best-fitting NFW profile strongly depend on the spatial extent of the rotation curve. Best fits to data that do not extend into the flat part of the rotation curve (which is often the case for H α-only data) tend to prefer larger V_{200} values and lower concentrations. Our data are very consistent with the literature once we account for the different rotation curve truncation radii employed; this agreement pre-empts criticism regarding possible inconsistency between the coefficients of the NFW fits of real galaxies and the ΛCDM mass-concentration relation predicted by N-body simulations.

Our best ISO fits also lie in the region of parameter space spanned by the results of observational studies and naturally reproduce the observed inverse proportionality between ρ_0 and R_c. This result suggests that this correlation may be an artefact of the fitting process rather than a real physical property of DM haloes. It is interesting to note that beam-smearing can dramatically impact H α rotation curves of galaxies at ~80 Mpc. This is not a surprise because *linear* resolution depends not only on the *angular* resolution but also on the distance at which a galaxy is located. Nonetheless, this result must be emphasized because the high angular resolution of optical data is often interpreted as providing sufficient protection against beam-smearing. This is evidenced by the large amount of galaxies more distant than 50 and even 100 Mpc that have been employed in some cusp-core studies. Projection effects also play an important role, making false detections of cores more likely in galaxies at high inclinations, especially at larger distances.

Our model galaxies do not support the widely accepted claim that the minimum disc approximation yields an upper limit on the true steepness of a dark matter halo density profile. In all our galaxies, whose properties are carefully modeled after observations of real dwarf galaxies in the local Universe, the addition of baryons to the gravitational potential of the dark matter haloes makes the true circular velocity profiles flatter rather than cuspier. Thus, the minimum disc approximation would cause one to infer that the dark matter profile is flatter than it actually is.

The analysis presented here has highlighted the difficulties involved in reliably inferring the central dark matter structure in a rotation curve analysis of observational data. In particular, we have shown that it is comparatively easy to mistake a DM cusp for a DM core, even with high-quality data. This certainly suggests that previous observational claims of core detections need to be taken with a grain of salt and should be followed-up further.

Our simulations have limitations, of course, the most important ones being that they are idealised compound galaxy models that lack a self-consistent cosmological context and that they do not include explicit supernova ‘blast wave’ feedback, which some simulations have suggested can transform cusps into cores. It would thus be interesting to repeat a similar analysis with galaxies extracted from full cosmological hydrodynamic simulations of galaxy formation, which now have sufficiently high resolution to study the cusp-core problem (e.g. Vogelsberger et al., 2014; Marinacci et al., 2014; Hopkins et al., 2014; Oñorbe et al., 2015; Chan et al., 2015; Schaye et al., 2015b; Sawala et al., 2016). Such models could then also account for perturbations in the circular motions of the gas due to central black holes, galaxy encounters, and cosmological torques. However, we stress that the idealised nature of our simulations (which contain strong, unperturbed NFW cusps by construction and, with the exception of G1, are highly axisymmetric) should make it *easier* to detect cusps than would be the case if fully cosmological simulations with explicit stellar feedback were employed. For this reason, in reality, it may actually be *more difficult* to observationally identify cusps via rotation curve fitting than suggested by our work.

Chapter 3

Additional remarks on the cusp-core problem

Regarding the cusp-core problem, in the former chapter I demonstrated that rotation curve fitting methods may be not completely robust in the presence of physical or instrumental effects that systematically modify the curvature of the very inner velocity profiles. In the set of simulations studied here, pressure support effects inducing an average velocity underestimation of 4$\sim$5 km s^{-1} in the first kiloparsec were able to completely mask the signatures of the dark matter cuspies, making them appear as cores.

In this chapter I exploit the same set of simulations, theoretical density/velocity profiles, and mock observations, to explore further the cusp-core controversy, addressing some additional questions of high interest. First, I test the performance of several rotation curve inversion methods from the literature, which make use of the Poisson's equation to directly approximate a dark matter density profile from the inversion of the observed rotation curve. Afterwards I present some theoretical analyses to demonstrate that at least two out of the three methods considered are affected by systematic biases that make them unsuitable for cusp-core studies. Finally, an entire section is dedicated to explore the question of whether or not pressure support effects as those observed in the simulations considered here may be corrected from observationally accessible information.

3.1 The halo steepness as seen by rotation curve inversion

As discussed in Sec. 1.4.3.2, in the minimum disc limit one can invoke Poisson's equation to approximate the halo density profile from the observed rotation curve using equation (1.18), which I reproduce here to facilitate the discussion,

$$4\pi G\rho_{\mathrm{dm}} \approx 2\,\frac{V_{\mathrm{c}}}{r}\,\frac{\mathrm{d}}{\mathrm{d}r}\,(V_{\mathrm{c}}) + \left(\frac{V_{\mathrm{c}}}{r}\right)^2. \tag{3.1}$$

By performing this rotation curve inversion, several studies observe a “break radius” in the resulting $\log(\rho) - \log(r)$ plane, separating a shallow inner density profile from a steep outer region (e.g. de Blok et al., 2001; de Blok and Bosma, 2002; Spekkens et al., 2005; Kuzio de Naray et al., 2008b; Oh et al., 2011b). A linear fit inside the break radius then provides a rough measurement of the inner logarithmic density slope that is the matter of discussion in the cusp-core problem, which is equivalent to using a power law approximation of the form,

$$\rho_{\mathrm{inner}} \sim r^{-\alpha}, \tag{3.2}$$

where α close to 0 implies a dark matter density core while α equal to 1 recovers the original cuspy shape of the NFW profile.

3.1.1 *Three different methods from the literature*

Note that, because of the derivative, the implementation of equation (3.1) is not trivial, and for that reason several approximations have been tried in the literature. In order to make a comprehensive study of the performance of the rotation curve inversion methods, I mimic three different solutions applied in influencial reported investigations of the cusp-core problem. Two of this methods explicitly assess the density profile from equation (3.1). In the first one I calculate the velocity derivative using a forward-difference scheme, roughly,

$$\frac{\mathrm{d}v}{\mathrm{d}r}(r_{\mathrm{n}}) = \frac{v_{\mathrm{n+1}} - v_{\mathrm{n}}}{r_{\mathrm{n+1}} - r_{\mathrm{n}}}. \tag{3.3}$$

Applying this procedure to the publicly available smoothed rotation curves from de Blok and Bosma (2002) I closely recover their published density profiles, so I think this is a good approximation to their original method [1]. Note that de Blok and Bosma first replace the observed velocity points with a smooth analytical function to minimize the impact of the scatter and small-scale noise, but this is not necessary in the case studied here because all the rotation curves are already smooth. From now on I refer to this method as *finit-diff*.

---

[1] The detail about the estimation of the derivative is not explicitly mentioned in the paper.

The second alternative that I will explore is the one proposed by Spekkens et al. (2005). They fit the data with a smooth empirical formula they call the *polyex* function,

$$V_{\rm pe}(r) = V_{\rm o}(1 - e^{-r/r_{\rm pe}})(1 + \beta r/r_{\rm pe}), \tag{3.4}$$

which thereafter they use to calculate the velocity, its derivative, and the corresponding density at every point analytically. I will refer to this method as *polyex*.

Once a dark matter density profile is determined by means of the *finit-diff* or the *polyex* methods, the quoted authors amongst others (e.g. Oh et al., 2011b), identify the break radius by eye in the $\log(\rho) - \log(r)$ space, and they fit a straight line to the inner points to determine the logarithmic slope α. Additional straight lines are fit to the same set of points plus/minus one point, and the error is defined as the mean difference between their slopes and the fiducial one. Hereafter I will refer to the number of points inside the break radius as $N_{\rm break}$, or simply to the number of points used in the linear fit in those cases when a sharp break is not detected. Typically the inner slope is reported as a function of the position of the first measurement in the rotation curve, which I will identify as $R_{\rm inner}$ in the text.

Measuring α without inversion

As an interesting third case I want to bring attention to the method introduced in Bolatto et al. (2002); Simon et al. (2003b, 2005). As these authors highlight, a power-law matter distribution generates a power-law circular velocity profile, so they fit power-law models to their whole optical rotation curves to estimate α without performing the inversion, exploiting the equivalence relation,

$$\rho \propto r^{-\alpha} \Longleftrightarrow V_{\rm c} \propto r^{(2-\alpha)/2}, \tag{3.5}$$

which can be easily computed from equations (1.14) and (1.15). I will refer to this method as *power-law* throughout the text.

3.1.2 *Steepness of the real density profiles*

After computing the spherically-averaged dark matter density profiles in the simulations as described in Sec. 2.3.2, I define their logarithmic slopes at a given radius through a central-difference scheme,

$$\alpha(r_{\rm n}) = -\frac{{\rm d}\log(\rho)}{{\rm d}\log(r)} \approx -\frac{\log(\rho_{\rm n+1}) - \log(\rho_{\rm n-1})}{2\,\Delta\log(r)}, \tag{3.6}$$

where the radial logarithmic step is the same employed in the determination of $\rho(r)$, namely $\Delta\log(r) = 0.15$, where r is in kpc. An appropriate selection of this parameter is crucial, as smaller values of $\Delta\log(r)$ may produce undesirable fluctuations in the resulting α profiles. I illustrate this with an example in Fig. 3.1 (top). Additionally, in order to minimize the uncertainty from the discretization process I perform a sanity check using the circular velocity of the halo as estimated from the enclosed-mass profile (equation (1.14)) computed in the same radial bins from which the theoretical density profile and its slope are being determined. I invert this circular velocity profile into a density profile using the *finit-diff* method, and I compute its steepness as a function of radius from equation (3.6). To check for self-consistency, in Fig. 3.1 (bottom) I plot the difference between the slope α calculated in this way and the fiducial one, for different values of $\Delta\log(r)$. The residuals are mostly consistent with zero, as they should, but notice the steep increment in the inner region when the bin is too large ($\Delta\log(r) \geq 0.2$). In order to minimize systematic errors, as well as the spurious fluctuations observed for $\Delta\log(r) \leq 0.1$, I adopt $\Delta\log(r) = 0.15$ as the fiducial value and I report a conservative error of ± 0.1 in $\alpha_{\rm true}$ to account for the remainning uncertainty in the numerical scheme.

3.1.3 Inferred logarithmic slopes and errors

In Fig. 3.2 I compare the true dark matter density profiles with those obtained by the inversion of $V_{\rm dm}$, $V_{\rm tot}$, and $V_{\rm cir}$ by means of the *finit-diff* method. In Fig. 3.3 I compare the true dark matter density profiles with those obtained using the *polyex* method. Regarding the *finit-diff* method, it can be seen that the density profiles computed from $V_{\rm dm}$ closely follow the true dark matter density profiles. The density profiles obtained by the inversion of $V_{\rm tot}$ in some cases exceed those from $V_{\rm dm}$ because of the addition of baryons (as expected), albeit a visual inspection of Fig. 3.2 indicates that the inner steepness does not change much. This confirms that in idealized circumstances a discretized implementation of equation (1.18) is handy for catching the inner slope of the halo density profile, that a sampling of ∼100 pc is acceptable, and that the simulated galaxies are suitable for the minimum disk approximation. What is much more stunning in Fig. 3.2 is that the inversion

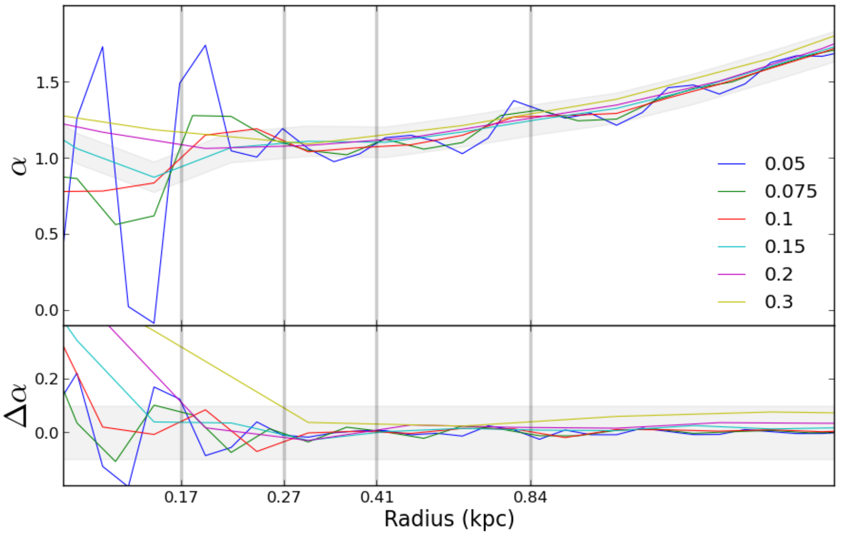

Figure 3.1: Top: theoretical α slope as a function of radius from the dark matter density profiles calculated using different logarithmic shell widths in equation (3.6). Different colours represent different values of $\Delta \log(r)$ as specified in the labels in the right-hand side. They refer to r values expressed in kpc. The shaded region represents ± 0.1 around the estimation made with the fiducial value, $\Delta \log(r) = 0.15$. Bottom: $\Delta\alpha$ residual between estimations from the density profiles obtained in slightly different ways (see main text). The shaded region encloses ± 0.1 around 0. This example is for galaxy Dwarf1 at 4.3 Gyr simulation time. The vertical lines indicate the position of the first measured point in the mock observed rotation curves traced at different spatial resolutions (i.e. viewed at different distances), namely $R_{\rm inner} = 0.17, 0.27, 0.41, 0.84$ kpc.

of $V_{\rm cir}$ leads to the illusion of a dark matter core in all galaxies, which is in contrast with the cuspy haloes in the simulations. This is a further confirmation of the main result of Chapter 2, i.e. that the intrinsic curvature of $V_{\rm cir}$ has been modified with respect to $V_{\rm dm}$, masking the true nature of the dark matter haloes in the simulations. Results from the *polyex* method look similar to those of *finit-diff* in the outer parts of the galaxies. In the inner part, however, the profiles calculated by the inversion of $V_{\rm dm}$ and $V_{\rm tot}$ are somehow flattened. They also exhibit clear artificial cores for $V_{\rm cir}$.

In order to estimate the inner logarithmic slope of the density profiles using the *finit-diff* or the *polyex* methods one needs to define a break radius, and then perform the linear fits described in Sec. 1.4.3.2. At this point is important to mention that the rotation curve inversion methods have been often used to study dwarf galaxies or LSBs using long-slit observations, which a tipical radial sampling of 1 point per spatial resolution element, instead of 2, as it is commonly the case for the tilted-ring analysis of velocity maps. For consistency with this large fraction of the literature I followed the same prescription, sampling the rotation curves at a spatial rate of 1 point every 2 arcsec. This is likely not causing

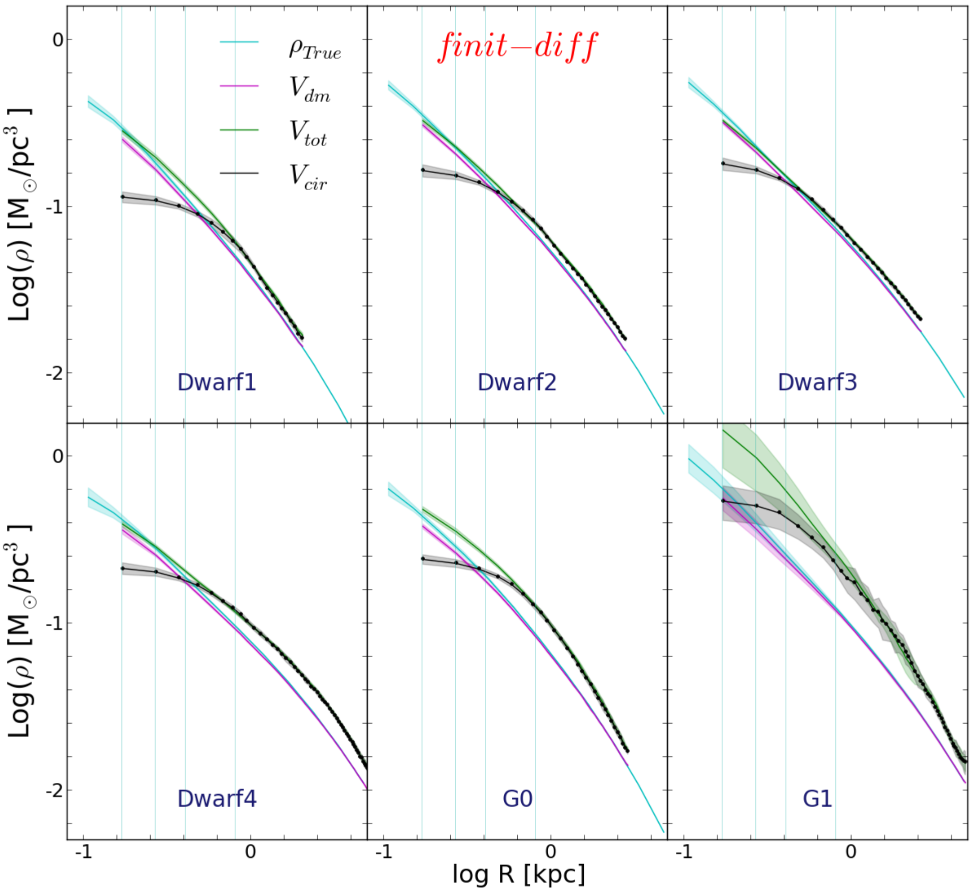

Figure 3.2: Dark matter density profiles obtained by the inversion of the theoretical velocity profiles using the *finit-diff* method. The results from all snapshots are stacked together. Solid lines represent the mean density profiles, and shaded regions their 1-σ dispersion. The true density profile appears in cyan. The density profiles obtained by the inversion of $V_{\rm dm}$ are shown in magenta, those from $V_{\rm tot}$ in green, and the ones from $V_{\rm cir}$ in black.

any difference in the main conclusions, which depend on trends that are clearly visible for galaxies at 10 Mpc, where the spatial sampling is quite good (∼100 pc). Nevertheless, even though the motivation for this choice came from long-slit data, all the results of this section were obtained from rotation curves extracted using KINEMETRY , as they are more regular and allow a better assessment of the intrinsic biases of the methods that I will introduce later in this chapter.

As there are no strong core-like features in the density profiles corresponding to $V_{\rm dm}$ and $V_{\rm tot}$, for these I adopt $N_{\rm break} = 2$ at all distances. To study the density profiles derived from $V_{\rm cir}$ and from the mock H α observations at 10 Mpc I choose $N_{\rm break} = 4$ after examining the profiles, as all of them exhibit shallow inner regions extending over 2∼7 points, but $N_{\rm break} = 4$ is the most common case. Additionally, I note that in those cases where the fake core looks more extended, the slope inferred with $N_{\rm break} = 4$ is often the same as

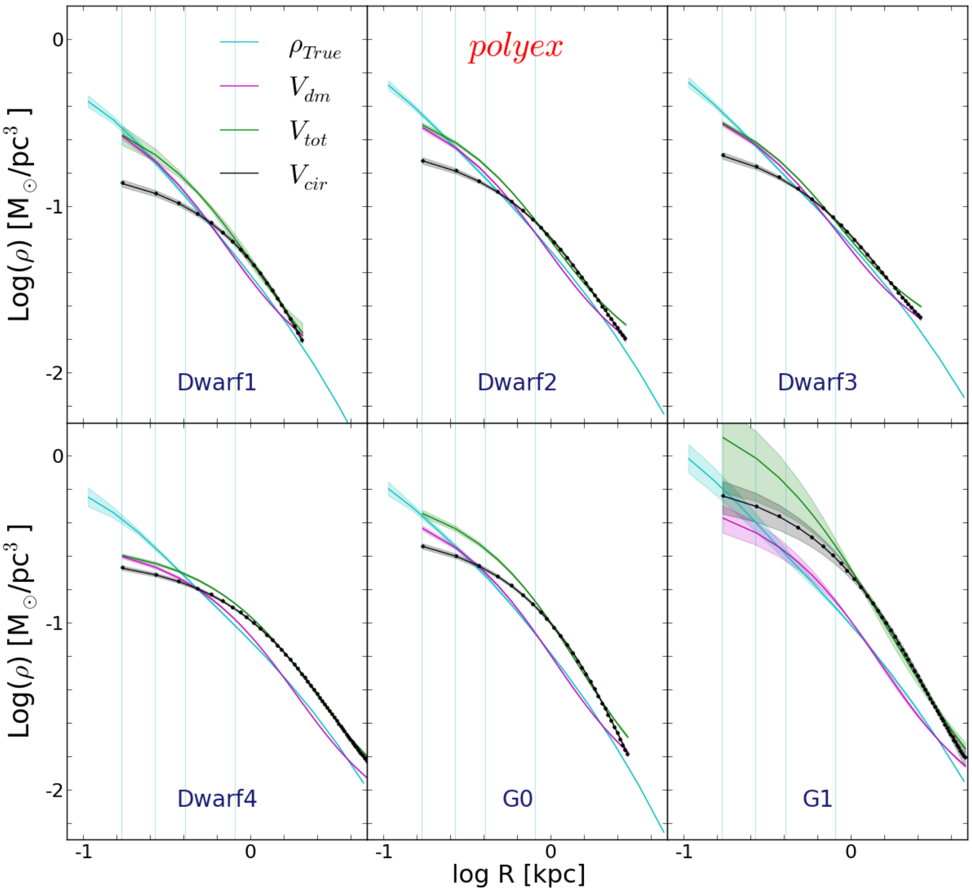

Figure 3.3: Dark matter density profiles obtained by the inversion of the theoretical velocity profiles using the *polyex* method. The results from all snapshots are stacked together. Colours and symbols are the same as in Fig. 3.2

using the entire core size, and in those cases where $N_{\rm break} = 2, 3$ is a better description of the data, $N_{\rm break} = 4$ leads to a conservative estimation of the error, as including points ouside the *core* makes the linear fits get steeper, partially compensating for the artificial flattening of the inner density profile. A similar analysis supports $N_{\rm break} = 3$ at 20 Mpc. At 40 and 80 Mpc the only acceptable choice is $N_{\rm break} = 2$ as the signature of the fake core dilutes, because it is undersampled by the comparatively low spatial resolution (∼400/800 pc).

Now I introduce the compiled α inferences yielded by the different methods. First I present a qualitative overview of the results, and then I quantify the overall performance and typical errors. In Fig. 3.4 I show the probability distribution function (PDF) of α as inferred from each combination of circular velocity profile, method, distance, and inclination. To create the total PDFs I combine the results from all simulations and snapshots. From each individual measurement I draw a gaussian centered at $\alpha_{\rm measured}$,

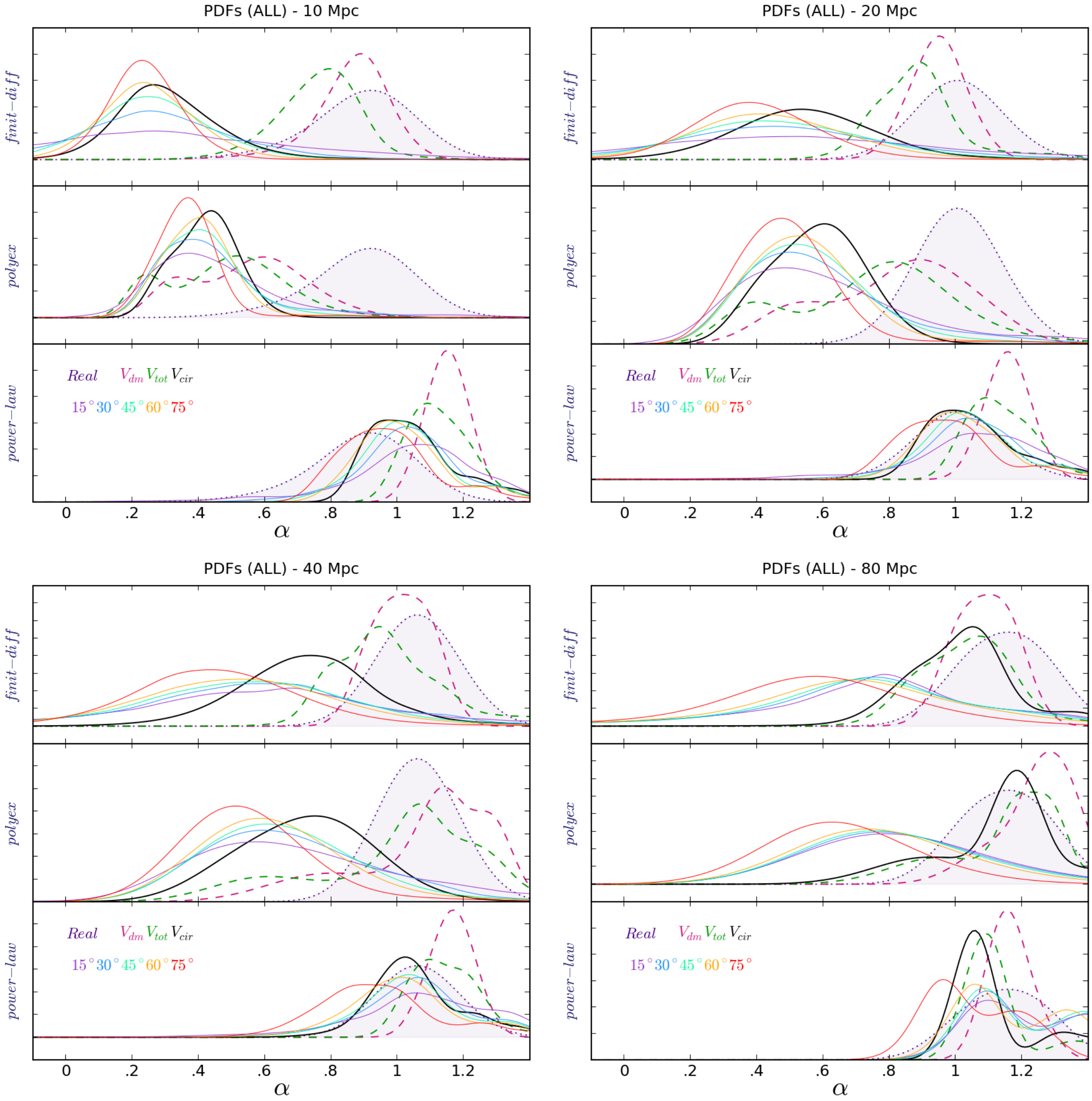

Figure 3.4: Probability distribution function of α from the different circular velocity profiles. Each panel is for a different distance and subplots are for the different methods. Purple dotted line (and shaded area below it) represents the real distribution of slopes in the simulations, measured at the same position of the first point in the mock H α rotation curves. Inferences from theoretical $V_{\rm dm}$ and $V_{\rm tot}$ appear as dashed lines in magenta and green respectively. Slopes inferred from theoretical $V_{\rm cir}$ are represented by the black solid line, and from the mock observed rotation curves by the solid thin lines colour-coded by inclination.

with a standard deviation given by its error, and then I add them up all together. To avoid unrealistically small uncertainties I impose a minimum error of 0.05 to individual values of $\alpha_{\rm measured}$.

In Fig. 3.4 it can be seen that the probability distribution function of the true slopes is cuspy, and perfectly consistent with the target NFW profiles of the haloes in the simulations. It also shows that, independently of the distance, the application of *finit-diff* method to $V_{\rm dm}$recovers a set of slopes that is very consistent with the true distribution of slopes in the simulation The same method slightly underestimates α when it is applied to $V_{\rm tot}$. Strikingly, when $V_{\rm cir}$ is inverted using *finit-diff* at 10 Mpc, a severe underestimation of α occurs, creating the strong illusion of dark matter cores that was formerly observed from the analysis of the rotation curve fitting methods in Chapter 2. The error diminishes with distance until it becomes unimportant at 80 Mpc. The results from the mock observed rotation curves are similar to those from $V_{\rm cir}$, except for two facts. First, the α PDFs are more extended, i.e., the spread of the slopes inferred from the mock observations is larger. Second, even though the slope underestimation also declines with distance, this time it is notorious even at 80 Mpc.

According to Fig. 3.4, at 10 Mpc the *polyex* method underestimates the true halo density slopes in all cases, regardless of the circular velocity profile being inverted. Yet the errors appear to decrease with distance. Surprisingly, the inferences from $V_{\rm dm}$ only partially agree with the true distribution of slopes at D$\leq$20 Mpc, a fact that can not be explained by any of the effects that I have discussed to this point so far, and that seriously put into question the ability of the *polyex* method to accomplish the task for which it was designed. The *polyex* inversion of $V_{\rm tot}$ produces a distribution of slopes very similar to those from $V_{\rm dm}$, but always a bit flatter. The slopes inferred from these curves with *polyex* are flatter than the true ones at D$\leq$20 Mpc, but slightly overestimate $\alpha_{\rm true}$ at D$\geq$40 Mpc. The inversion of $V_{\rm cir}$ yields flatter slopes than $V_{\rm dm}$and $V_{\rm tot}$at all distances, underestimating $\alpha_{\rm true}$ at all distances except for 80 Mpc. From the mock observations at 10 Mpc the *polyex* method got very similar results to those from $V_{\rm cir}$, but more underestimated slopes at larger distances, being the only case for which there is a considerable error even at 80 Mpc.

The results from the *power-law* method look quite different from the former two methods discussed. The steepness inferred from all the velocity profiles slightly overestimates the true distribution of α's at 10 Mpc, and progressively gets to an stunning agreement at larger distances. The results from $V_{\rm cir}$ and from the mock observations overlap the true α PDF already at 20 Mpc. Despite this remarkable success in recovering the α slopes, these results look suspicious, as a large body of evidence shows that the inner curvature of the velocity profiles is not the same for all of them.

I quantify the net committed error in α estimation through the difference $\Delta\alpha = \alpha_{\rm true} -$

$\alpha_{\rm measured}$, and the uncertainty in this quantity as the quadratic sum of both uncertainties. Drawing individual gaussians and suming them up one can compute the PDF of $\Delta\alpha$, which serves to report a characteristic error for each combination of circular velocity profile, method, and distance. In Fig. 3.5 and in Table 3.1 I report the mean error $< \alpha_{\rm true} - \alpha_{\rm measured} >$ as the first moment of the $\Delta\alpha$ distribution, with an uncertainty that I define as the radius around the mean error enclosing 67% of the PDF area.

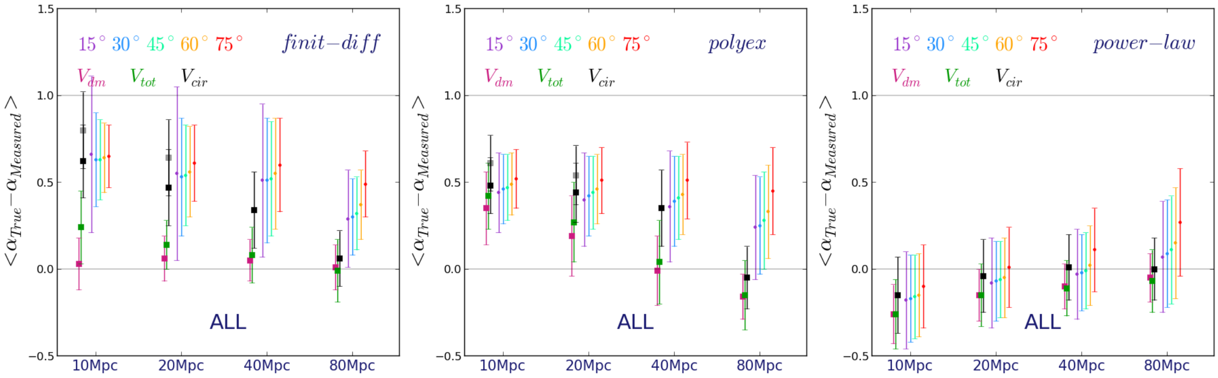

Figure 3.5: Net error in the estimation of the logarithmic slope α. Each panel is for a different method. Squared markers are for theoretical rotation curves and dots for the mock observations. Colours are the same as in Fig. 3.4. Small horizontal shifts between data points are used to facilitate the visualization.

Fig. 3.5 and Table 3.1 confirm the previous qualitative analysis. Method *finit-diff* in combination with $V_{\rm dm}$ successfully recovers the dark matter slopes at all distances. The same method applied to $V_{\rm tot}$ somewhat underestimates α at 10 Mpc by 0.24±0.21, but errors get steadily more consistent with 0. The inversion of $V_{\rm cir}$ leads to severe underestimations of α at all distances but 80 Mpc. Errors are more pronounced for closer galaxies, reaching 0.62±0.21 at 10 Mpc. Applying *finit-diff* on $V_{\rm kin}$ errors are larger than those from $V_{\rm cir}$ at D$\geq$ 20 Mpc. Interestingly, note that at no distance the combination of *finit-diff* and $V_{\rm kin}$ recognizes the cuspy nature of the haloes in the simulations, with underestimations diminishing with distance from 0.64±0.25 to 0.35±0.24.

At 10 Mpc, the *polyex* method applied to any of the circular velocity profiles underestimates the true value of α, though errors systematically decrease as a function of distance. Strikingly, inverting $V_{\rm dm}$ at 10 Mpc the density slope is underestimated by 0.35±0.21; agreement is good only at D$\geq$40 Mpc, and at 80 Mpc the value of α is actually overestimated by 0.16±0.13. In comparison to $V_{\rm dm}$, the errors that occur when the *polyex* method is used slightly increase for $V_{\rm tot}$ (by less than 0.1), but they grow considerably for $V_{\rm cir}$,

Table 3.1 - Mean error $< \alpha_{\mathrm{true}} - \alpha_{\mathrm{measured}} >$ committed by the different methods.

D (Mpc)	V_{dm}	V_{tot}	V_{cir}	V_{kin} [a]
		finit-diff		
10	0.03 ± 0.15	0.24 ± 0.21	0.62 ± 0.21	0.64 ± 0.25
20	0.06±0.13	0.14±0.14	0.47±0.22	0.56±0.31
40	0.05±0.12	0.08±0.16	0.34±0.22	0.54±0.34
80	0.01±0.13	-0.01±0.18	0.06±0.16	0.35±0.24
		polyex		
10	0.35±0.21	0.42±0.19	0.48±0.16	0.48±0.19
20	0.19±0.23	0.27±0.23	0.44±0.17	0.45±0.22
40	-0.01±0.2	0.04±0.24	0.35±0.22	0.42±0.26
80	-0.16±0.13	-0.15±0.2	-0.05±0.18	0.31±0.28
		power-law		
10	-0.26±0.17	-0.26±0.2	-0.15±0.22	-0.15±0.25
20	-0.15±0.15	-0.15±0.18	-0.04±0.21	-0.05±0.24
40	-0.1±0.13	-0.11±0.16	0.01±0.19	0.01±0.24
80	-0.05±0.14	-0.07±0.18	0.0±0.18	0.14±0.32

Note: [a] Results in the last column are obtained taking mock 2D observations at all inclinations together.

reaching between 0.46±0.16 and 0.32±0.22 at D≤40 Mpc, and suddenly drop to ∼0 at 80 Mpc. Results from V_{kin} systematically underestimate α at all distances, producing errors between 0.48±0.19 and 0.31±0.18.

As for the *power-law* method, it overestimates the logarithmic slope by 0.26±0.17 when applied to V_{dm} or V_{tot} at 10 Mpc, but the excess diminishes with distance and gets progressively more consistent with 0. V_{cir} allows a slightly better job; it overestimates α by 0.15±0.22 at 10 Mpc, but get errors that are fairly consistent with 0 at D≥ 20 Mpc. As for the mock observations, note that the α PDFs overestimate the real slopes at 10 Mpc by 0.15±0.25, to match them at 20,40 Mpc, and to underestimate them at 80 Mpc by 0.14±0.32.

I find a tendency for more inclined galaxies to mimic flatter density profiles with all the methods. The effect is mild at 10 Mpc but it gets more pronounced with distance. At 80 Mpc the difference between errors at 15° and 75° is up to 0.2, although measurements at all inclinations still agree within error bars.

3.2 Successes, drawbacks, and possible biases

3.2.1 The intrinsic curvature of the theoretical velocity profiles

To better understand the meaning of the results described up to here, I investigate the intrinsic curvature of the inner velocity profiles at 10 Mpc through their logarithmic versions, presented in Fig. 3.6. I only consider the first 5 points of each profile, in order to determine the inner slope without mixing information from the outer parts.

I also include a linear fit to each dataset, and two red lines representing the cuspy NFW profile ($\alpha = 1$) and the cored pseudo-isothermal sphere (ISO) model ($\alpha = 0$) for comparison. Every curve is shifted in the horizontal and vertical directions as to place the first measurement at the origin. This is possible because the degree of curvature of a velocity profile is given solely by the slope of its linear fit in the logarithmic space, which I designate as β;

$$V \sim r^{\beta} \Longleftrightarrow \log(V) \sim \beta \log(r). \tag{3.7}$$

Recalling the velocity-density equivalence of equation (3.5), one can estimate the logarithmic density slope from the linear fit to the logarithmic velocity as,

$$\alpha = 2(1 - \beta). \tag{3.8}$$

Note that higher values of β correspond to lower α density slopes. This equation shows clearly that cored dark matter haloes ($\alpha = 0$) exhibit solid-body circular velocity profiles ($\beta = 1$), while the canonical NFW cusps ($\alpha = 1$) display curved inner velocity profiles ($\beta = 1/2$).

The values of α computed in this way from each circular velocity profile are quoted in Fig. 3.6. It is immediate that the curvature of $V_{\rm dm}$ reflects the target NFW density profiles, as the estimated α ranges from 0.85 to 0.94. The intrinsic curvature of $V_{\rm tot}$ slightly deviates towards a flatter density profile, lowering the inferred α's by $\sim$0.1. As for $V_{\rm cir}$, I find its inner curvature to be much better represented by the cored ISO model, with α's between 0.16 and 0.35. Therefore I can say that the main trends observed in Sec. (2.4), regarding the *finit-diff* method, are actually imprinted in the velocity profiles themselves. $V_{\rm dm}$ in

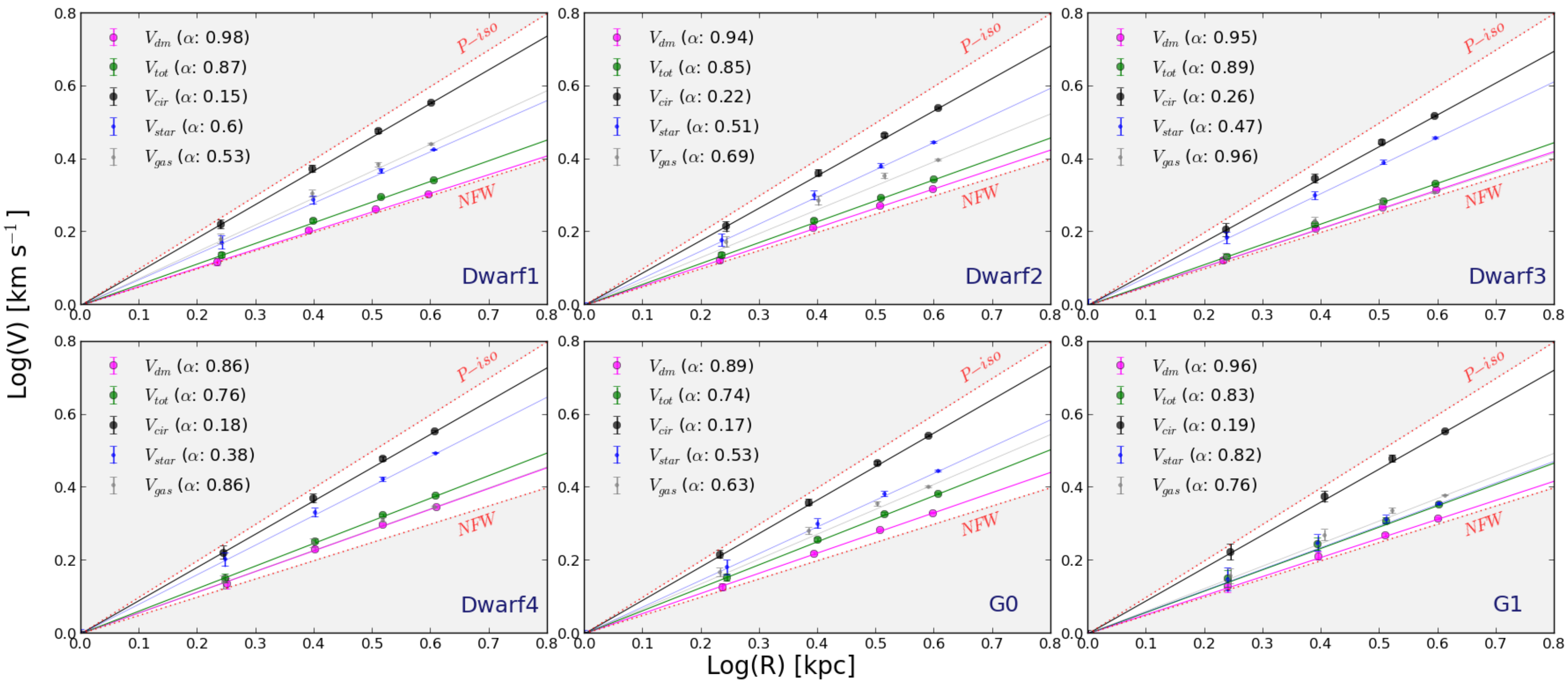

Figure 3.6: Logarithmic version of the inner theoretical velocity profiles. Data points are the mean values from all the snapshots, and error bars represent the $1-\sigma$ scatter (smaller than the markers wherever they are not visible). The slope of the linear fits, β, can be associated with an equivalent density slope $\alpha = 2(1-\beta)$. For comparison I include in each plot the expectation from the analytical NFW ($\beta = 0.5$) and ISO models ($\beta = 1$). All datasets are shifted vertically and horizontally to put the first measurement at the origin.

fact looks “cuspy”[2], $V_{\rm tot}$ is a bit “flatter”, and $V_{\rm cir}$ looks “cored”. This is an important verification of the different inner curvatures amongst the profiles.

In the case of $V_{\rm tot}$, I find the addition of baryons to lower the inferred value of α in comparison to the dark matter-only velocity profiles. As can be seen in Fig. 3.6, the intrinsic curvature of $V_{\rm star}$ and $V_{\rm gas}$ is characterized by higher β slopes than that of $V_{\rm dm}$, which will result in $\beta_{\rm tot} > \beta_{\rm dm}$ when the quadratic sum is performed. This implies that the density profiles inferred from $V_{\rm tot}$ will look flatter than those inferred from $V_{\rm dm}$ (i.e. $\alpha_{\rm tot} < \alpha_{\rm dm}$). Nonetheless, the difference is small because the dark matter component is largely dominant in the simulated galaxies, even at the very centre. Let me stress that the baryonic spatial distribution in the simulations was carefully tuned to follow widely accepted models based on observations, so, either this effect may be present in real galaxies as well, or simple models such as perfect exponential discs are excessively idealized for cusp-core studies. I explore this result further in Sec. 3.2.2.

In Chapter 2, I presented evidence pointing at pressure support as the origin of the lowering of $V_{\rm cir}$ with respect to $V_{\rm tot}$ in the inner part, characterized by mean residuals $< V_{\rm tot} - V_{\rm cir} >$ of 4∼5 km $\rm s^{-1}$ in the first kiloparsec for all galaxies but G1. Such a correction is typically considered small, given the size of the velocity error bars, and it is often ignored because of that. Strikingly, I find it to play a major role in the determination of the halo density slopes, creating the illusion of inexistent dark matter matter cores. The reason why such small errors can impact the curvature of the velocity profiles is that they are not stochastic, but systematic. In the galaxies simulated here I find the difference in the velocities driven by pressure support, $(V_{\rm tot} - V_{\rm cir})$, to monotonically decrease as a function of radius. Dividing that difference by $V_{\rm tot}$, which grows with radius, it follows that the term $(1 - \frac{V_{\rm cir}}{V_{\rm tot}})$ diminishes monotonically as a function of radius, which implies that the fraction $\frac{V_{\rm cir}}{V_{\rm tot}}$, on the contrary, must increase (see Fig. 2.12). If one approximates both velocity profiles as power laws, $V_{\rm cir} \sim r^{\beta_{\rm cir}}$, $V_{\rm tot} \sim r^{\beta_{\rm tot}}$, this necessarily implies $\beta_{\rm cir} > \beta_{\rm tot}$. Combining this result with the former one leads to $\alpha_{\rm dm} > \alpha_{\rm tot} > \alpha_{\rm cir}$, which explains why the sequence $V_{\rm dm} \rightarrow V_{\rm tot} \rightarrow V_{\rm cir}$ moves away from the NFW model towards the ISO one in Fig. 3.6.

---

[2] i.e. the intrinsic curvature of the velocity profile is consistent with that expected for a cuspy dark matter density profile.

3.2.2 How reliable is the minimum disc approximation?

The fact that $V_{\rm tot}$ leads one to infer density profiles that look flatter than those inferred from $V_{\rm dm}$ is in open contradiction with the bottom-line of the widely accepted minimum disc approximation. Even though the difference is not so large ($\sim$0.1), it is a result that deserves further consideration, because it appears systematically in all the simulations, and because the combination of small errors can easily add up and conduct the cusp-core traditional analyses to misleading results (e.g. Rhee et al., 2004).

Let me start by mentioning that the expectation of the observed rotation curves being suitable to put an upper limit to the dark matter density slope does not lie on the basis of first principles, but it is the consequence of some empirical comparisons between fits with and without baryons. This result was originally obtained by de Blok and Bosma (2002) and it has been mistaken as a granted property from then on. It is clear that neglecting the baryons during the inversion of the rotation curve will lead to an overestimation of the true dark matter content at all radii, as $V_{\rm tot}$ is always larger than $V_{\rm dm}$. In my opinion, it seems that a loose interpretation of this fact has caused the erroneous general impression that the minimum disc approach also serves to place an upper limit to the steepness of the inferred density profiles, which is not necessarily true. As a dummy illustrative example, note that in the radial range $[0.2, 1.8]$ both of the following inequalities are true,

$$2\,r^{1/2} > r^{1} \quad ; \quad r^{1/2} < 3\,r^{1}, \tag{3.9}$$

which demonstrates that the relative amplitude of two functions does not depends solely on their steepness, but also on their individual normalizations and on the radial range where the comparison is performed.

It is worth mentioning that different authors than de Blok and Bosma have also found steeper slopes from the minimum disc approximation than the slopes they found after explicitly discounting the contribution of baryons to the rotation curves(e.g. Simon et al., 2005), but this is no more than a necessary cross check that has to be done in every new study, and it ought to be considered circumstantial evidence rather than a universal property of disc galaxies. In spite of that fact, several cusp-core works quote this “property” of the minimum disc approximation to justify the use of this approach without a thorough verification.

Besides that, recall that the difference between $V_{\rm tot}$ and $V_{\rm dm}$ is basically a reflection of the baryonic density profiles, which in the simulations studied here are modelled after the typical exponential discs observed in many late-type galaxies, and experience very small transformations along the simulated time. All this evidence suggests that either exponential discs are not an appropriate description of the baryonic density profiles all the way up to centre, or that the observational analyses may be offering misleading evidence as a result of an incorrect shape of the central part of the velocity profiles or of the surface brightness profiles. If ideal exponential discs are to be blamed for this unexpected result in the simulations of this work, then it would be a double-edge sword, as this model is largely exploited in observational analyses of rotation curves. A third possibility is that dark matter haloes were actually cored, and because of that the addition of baryons would make the profiles appear cuspier. In that case, the comparison of fits with and without baryons would be providing further evidence of the existence of cores, but then one has to be absolutely sure of being tracing the circular velocity related to the gravitational potential, which seems to be a much harder task than previously assumed according to the evidence presented in Chapter 2. In conclusion, I can not establish the exact origin of the discrepancy at this stage, but I want to emphasize that rotation curve studies in the cusp-core context seem to be extremely sensitive to the details in the inner part of the galaxies, which poses serious concerns to the reliability of their conclusions.

As an instructive exercise I revisit the case of a thin disc with an exponential surface density profile of scale-length h, whose circular velocity profile has a well-known analytic solution (see Binney and Tremaine, 1987) that can be written in logarithmic form as,

$$\begin{aligned} \log(V) &\propto \log(r) \\ &+ \frac{1}{2}\log[I_0(r/2h)K_0(r/2h) - I_1(r/2h)K_1(r/2h)], \end{aligned} \tag{3.10}$$

where the functions I_0, K_0, I_1, K_1 are the Bessel functions of first and second kinds. Fitting straight lines to this analytic expression over 1 kpc I find the slope β to lie between 0.65 and 0.86 for scale-lengths between 0.5 and 9 kpc, respectively. That is equivalent to α slopes between 0.7 and 0.27, and therefore it means that the combination of a NFW dark matter halo and a thin exponential disc will necessarily exhibit a lower steepness than that of a perfect NFW profile.

3.2.3 The intrinsic bias of the polyex method

In Sec. 3.1.3 I showed that the *polyex* method fails to recover the true cuspyness of the haloes from the inversion of $V_{\rm dm}$at its highest spatial resolution. This is an enormous concern regarding the suitability of this proposed solution to study the cusp-core problem. Recalling that in this case the inner quantities depend on the fit of the entire velocity profile to a *polyex* model, I decided to explore the mathematical properties of this function to determine the origin of the observed bias in the inferred slopes. To probe the intrinsic shape of the *polyex* family of curves I combined equations (3.1), (3.6), and (3.4) to derive an exact analytical expression for the α slope as a function of radius,

$$\alpha = -\frac{r}{\rho}\frac{{\rm d}\rho}{{\rm d}r} = \alpha(r, R_{\rm pe}, \beta). \tag{3.11}$$

Note that, for the intrinsic logarithmic nature of this derivative, the dependence with the amplitude coefficient $V_{\rm o}$ vanishes. To have a feeling of the relevant space of parameters covered by $(R_{\rm pe}, \beta)$ in a realistic scenario, note that at a radius of 2∼3 times $R_{\rm pe}$ the rotation curve must be turning flat, because the negative exponential goes to zero in equation (3.4). Therefore a reasonable value of this parameter should be between a fraction of a kiloparsec and a few kiloparsecs. Secondly, note that for $r \gg R_{\rm pe}$ the polyex model tends to a linear relation

$$V_{\rm pe}(r) \approx V_{\rm o} + \left(\frac{\beta V_{\rm o}}{R_{\rm pe}}\right) r. \tag{3.12}$$

If the velocity profile extends beyond the rising part, this means that $V_{\rm o}$ must be representative of $V_{\rm flat}$, and the slope $\beta V_{\rm o}/R_{\rm pe}$ must be close to zero. Using limiting values for $V_{\rm o}$ and $R_{\rm pe}$ I estimated an extreme upper limit at $|\beta| < 2$. As a matter of fact, all the *polyex* fits to my circular velocity profiles, and also those found by Spekkens et al. (2005) to their observed rotation curves lie in a narrower subset of the parameter space, namely $|\beta| \leq 0.5$.

In Fig. 3.7 I present a contour plot of the intrinsic slope α associated to the *polyex* formula at 20 Mpc (i.e. evaluated at $R_{\rm inner} = 0.27$) as a function of the coefficients $(R_{\rm pe}, \beta)$. I also include the set of parameters $(\beta, R_{\rm pe})$ obtained from the *polyex* fits to all my theoretical velocity profiles, and to the mock observations truncated at different positions. Here I consider not only the H α data, but also the hybrid H α + H I rotation curves. I did this to verify how the *polyex* parameters behave in those cases where the flat part of the rotation curves is effectively reached with a considerable number of points. I also overplot a subset of the fits to the observed rotation curves published by Spekkens et al. (2005), filtering out those galaxies beyond 100 Mpc or excessively inclined (> 80°).

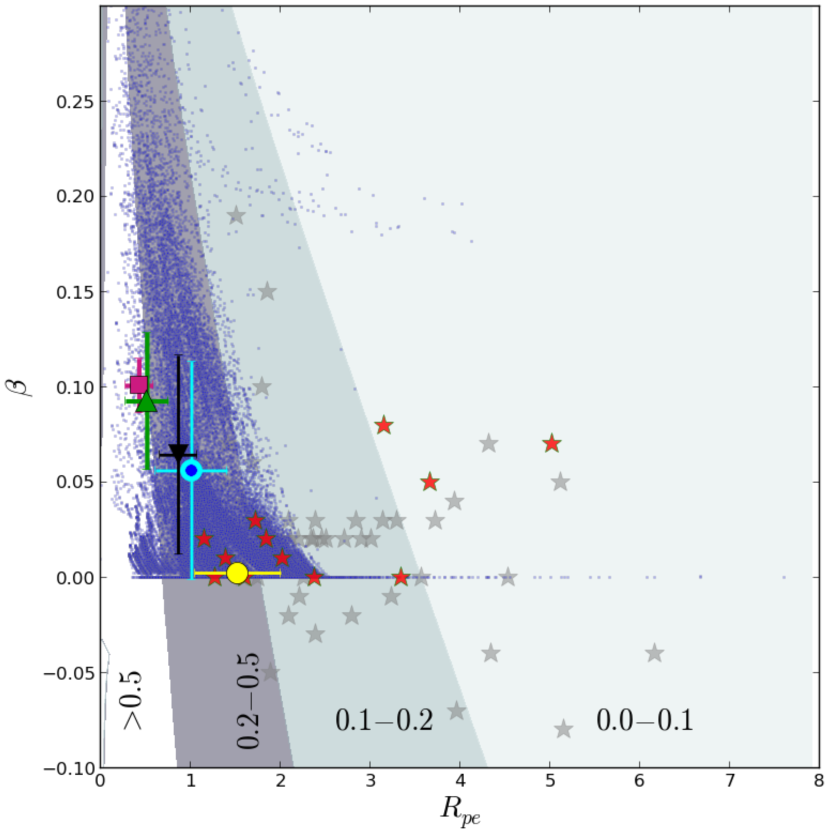

Figure 3.7: Shaded areas in the background show the intrinsic slope α as a function of $(R_{\rm pe}, \beta)$ at 20 Mpc using the *polyex* method. I include individual results from the *polyex* fits to high-resolution H α rotation curves of Spekkens et al. (2005) closer than 100 Mpc and with inclinations below 80°, differentiating galaxies at ∼20 Mpc (red stars) from the rest (grey stars). I show the mean result and the 1-σ scatter for the theoretical $V_{\rm dm}$ (magenta square), $V_{\rm tot}$ (green triangle), and $V_{\rm cir}$ (black down-pointing triangle). Small blue dots correspond to *polyex* fits to the mock observed rotation curves trying different truncations, from 10 points to the whole hybrid rotation curve. The mean and the 1-σ scatter of the fits to the entire H α rotation curves is shown as a cyan circle with a blue dot in the centre. The same quantity for the hybrid H α + H I case is shown as a yellow circle.

The main *take-away* from Fig. 3.7 is that, for any plausible combination of β and $R_{\rm pe}$, the *polyex* function intrinsically imposses a flattened slope $\alpha \leq 0.5$. Even for $V_{\rm dm}$ and $V_{\rm tot}$ the *polyex* method biases the slope α towards flatter values than the true ones. The only way to get steeper slopes than 0.5 is by forcing $R_{\rm pe}$ to stay below 0.5 kpc, but this means that the corresponding rotation curve must have completed the rising part and should have turned a steady linear profile before reaching 2 kpc, which can by no means be reconciled with the large diversity of observed rotation curve shapes. Virtually all the fits to the mock rotations curves lie in regions of the parameter space with intrinsic α slopes flatter than

0.5. The results from the entire H α rotation curves are quite similar to those from $V_{\rm cir}$, but not very consistent with the sample from Spekkens et al. (2005). The agreement is better if I consider the whole hybrid rotation curves. This is probably explained by the fact that the H α emission in the galaxies observed by of Spekkens et al. (2005) reached the flat part of the rotation curves in many cases, while my fiducial mock H α-only observations do not. At 10 Mpc the situation is more delicate as the contours slightly shift towards the left, making it more difficult to get steep α's. This explains why the *polyex* method fails to recover the real distribution of dark matter density slopes at 10 and 20 Mpc in my simulations, even from $V_{\rm dm}$. At larger distances the α contours move to the right, so this method is able to recover the steepness of the dark matter density slopes from $V_{\rm dm}$ and $V_{\rm tot}$, but never from the mock observed rotation curves. At such large distances the fits do also shift slightly to the right, towards larger values of $R_{\rm pe}$, but the shift just improves the agreement with the fits found by Spekkens et al. slightly. It is worth performing further analyses to determine exactly the cause of the differences, and to find out if the results from Spekkens et al. are in fact affected by the bias demonstrated in Fig. 3.7 or not.

3.2.4 Dependence of the inferred α slope on the assumed distance

A striking result from Fig. 3.5 is that, in those cases where a fake core is inferred at 10 Mpc, the agreement between the true and the inferred α slopes improves as the galaxies are placed farther away. I investigate this effect using the theoretical velocity profiles, through a comparison of the recovered density profiles as a function of distance. In the case of *polyex* the inverted density profiles, which can be estimated analytically from the ($V_{\rm o}$, $R_{\rm pe}$, β) coefficients of the *polyex* fit to the rotation curve, overlap. There are no changes to the inferred densities, except for a poorer sampling of the profiles at larger distances.

In the case of the *finit-diff* method, one can only evaluate the density at the positions where the velocity profiles were measured. By overplotting all the densities inferred by inversion of the velocities at the different distances, I see the most inner points to slightly shift as a function of distance, but this effect by itself seeems unimportant regarding the steepness of the density profiles.

The former discussion implies that the sampling rate of the velocity profiles does not alter considerably the shape of the inverted density profiles. I find the primary cause of the trend with distance to be in the radius at which α is measured and reported ($R_{\rm inner}$), which systematically moves out of the artificial cores in farther galaxies, as the spatial resolution of the associated mock observations gets poorer. Additionally, the undersampling of the inverted density profiles artificially steppens the slopes inferred from the linear fit to the data points inside the break radius, with respect to the steepness that would be inferred from an ideal measurement of the derivative at the same position, if one had a continuous profile instead of discrete and sparse points. I illustrate this in Fig. 3.8. There it can be seen that the slopes inferred from the linear fit inside the break radius artificially get steeper with distance; the linear fits systematically move from the ISO model towards the NFW one for the reasons described.

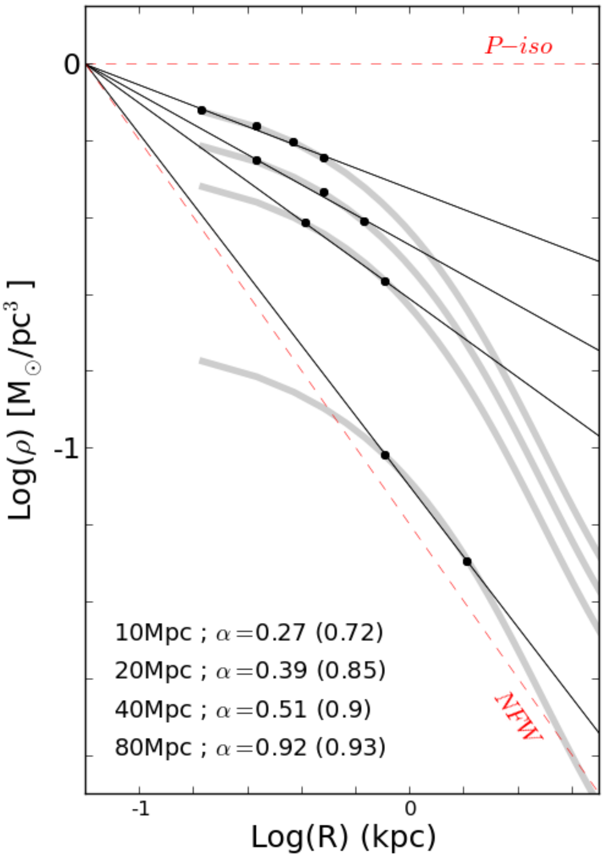

Figure 3.8: Effect of the distance in the determination of α. Thick grey lines represent the mean density profile obtained by the inversion of $V_{\rm cir}$ in galaxy Dwarf4 using the *polyex* method, which has exactly the same shape independent of the distance. I plot the same density profile four times, identifying each one to a distance from 10 Mpc (top) to 80 Mpc (bottom), in order to clearly show the effects introduced by the corresponding sampling in each case. Black dots mark the measurements used to perform the linear fit at different distances. Every set has been shifted vertically to make all linear fits coincident. ISO and NFW characteristic slopes are also shown for comparison. In the legend I indicate the slope α inferred from the straight line fit, and in parentheses I show the true slope of the dark matter density profile at the position of the first measurement, as evaluated analytically using the polyex formula.

3.2.5 Dependence with $N_{\rm break}$ and a comment on the power-law *method*

In order to test the robustness of the results, in Fig. 3.9 I present the dependence of the compiled average error, $< \alpha_{\rm true} - \alpha_{\rm measured} >$, as a function of a variable definition of the break radius, determined by the number of points in the linear fit to $log(\rho) - log(r)$, $N_{\rm break}$, for methods *finit-diff* (top) and *polyex* (middle) at 10 Mpc. The main conclusions do not change substantially if I increase $N_{\rm break}$ by one point. The inferred slopes are raised by 0.15 or less if one uses $N_{\rm break} = 3$ for $V_{\rm dm}$ and $V_{\rm tot}$, and $N_{\rm break} = 5$ for $V_{\rm cir}$ and $V_{\rm kin}$. Those profiles that were already identified as cusps or cores, remain on the same side of this bimodal categories, including the soft cores, oddly estimated from $V_{\rm dm}$ and $V_{\rm tot}$ by *polyex*. Increasing $N_{\rm break}$ further would be incompatible with the shape of the inverted density profiles, as one would be adding points that are definitively outside of any reasonable definition of the break radius, as can be seen in Figs. 3.2 and 3.3, or in Fig 3.8. Particularly, if one wants to make the *polyex* or the *finit-diff* methods to recover the correct steep slopes from the simulations, from the inversion of $V_{\rm cir}$or $V_{\rm kin}$, this would require to use $N_{\rm break} \geq 10$, which is completely at odds with the data.

In Fig. 3.9 I show the results from the *power-law* method, after truncating the velocity profiles at different positions that I identify by the number of points included in the fit, $N_{\rm points}$. There it can be seen that the α slopes inferred from the fits to the velocity profiles exhibit the same qualitative behaviour than the slopes obtained by means of the *finit-diff* method (top panel). For a small number of points, the error committed from $V_{\rm dm}$is consistent with 0, the error committed from $V_{\rm tot}$is small ($\sim$0.2), and the α error from $V_{\rm cir}$and $V_{\rm kin}$peaks at $\sim$0.8, making the cusps in the simulations to be mistaken by cores. As the number of points being fit increases, the errors from $V_{\rm dm}$and $V_{\rm tot}$turn slightly negative, indicating a small overestimation of the true distribution of slopes, and the error from $V_{\rm cir}$and $V_{\rm kin}$diminishes, making the inferred slopes progressively more consistent with the real ones. The main difference is that, by estimating α from the inverted density profile as done by *finit-diff* , an error consistent with 0 is reached for $N_{\rm break}$ $\sim$10, while $N_{\rm points}$ $\sim$15 is necessary to achieve the same result from the *power-law* method. This roughly means that, in this regime, the α estimation from the *finit-diff* method is always a bit steeper (by $\sim$ 0.1) than that from *power-law* , though this difference by itself would not be able to mask a cusp into a core, neither the other way around.

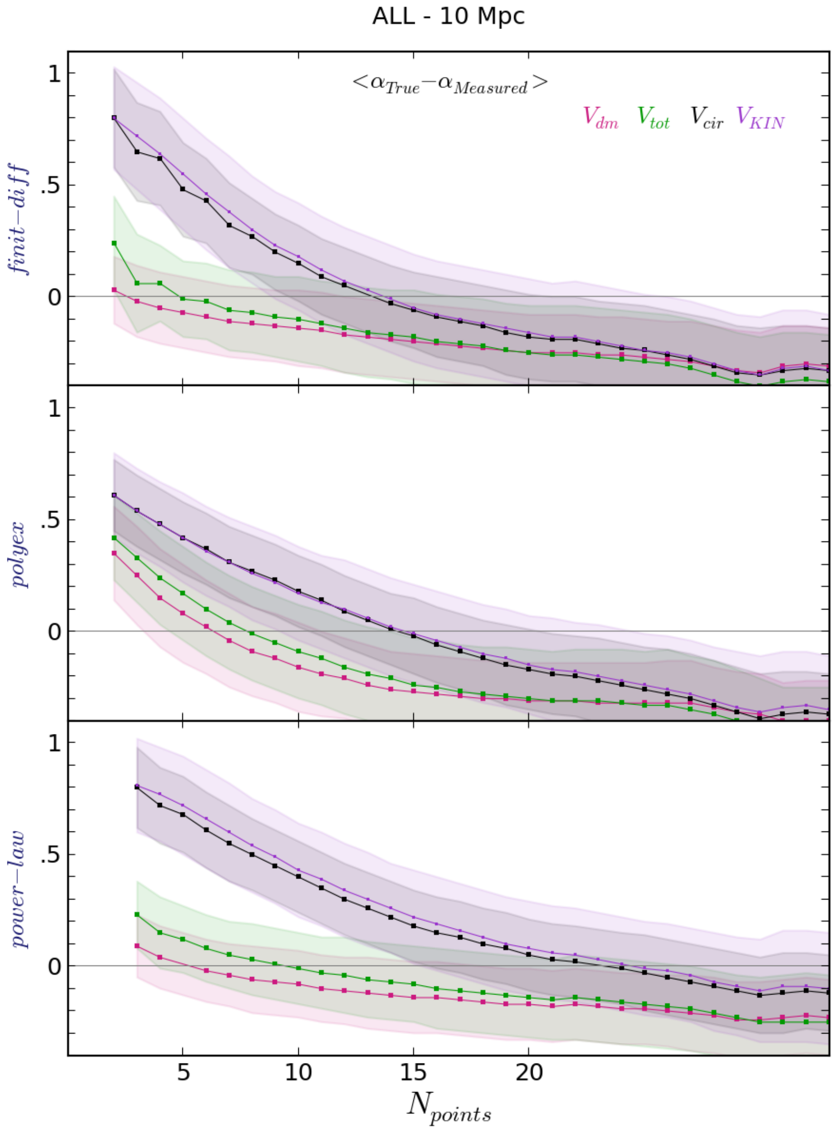

Figure 3.9: Mean errors in the estimation of α as a function of the number of points considered in the fits. Each panel is for a different method. Top: *finit-diff* , centre: *polyex* , bottom:*power-law* . In the first 2 cases the number of points refers to N_{break}, and the fit is performed in the $\log(\rho) - \log(r)$ space. In the *power-law* method the nomber of points refers to N_{points}, which is the number of points of the velocity profiles to be directly fit with the *power-law* model without performing the inversion. These results are a compilation from all galaxies and snapshots at 10 Mpc. Solid lines with points represent the mean error for each value of N_{break} or N_{points}, and shaded regions denote the 1-σ dispersion.

Therefore, at least for small radii for which the single power-law approximation is best suited, the equivalence expressed by equation 3.5 is verified in practice at a first approximation, as it was already mentioned in Sec 3.2.1 from the linear fits to the logarithmic velocity profiles. In other words, if the inner density profile is to be modelled as a single power-law, the result may be directly obtained from a power-law fit the corresponding velocity profile, which may be seen as a linear fit in logarithmic space. I suggest that the latter, which is an easier implementation, is less prone to errors introduced during the inversion of the velocity profile, as those evidenced in the intrinsic bias of the *polyex* function, or others more subtle related to the specific numerical implementation of the velocity derivative (specially for poor samplings) or the propagation of the error bars, which may be the origin of the small systematic bias of ∼0.1 comented in the former paragraph. Still the visualization of the logarithmic density profile remains a very important tool of analysis for determining the possible presence of a break radius, but the fit itself may be more straightforward in the $\log(v) - \log(r)$ plane than in the density space.

The bottom panel of Fig. 3.9 also shows that, as one allows larger numbers of points in the fit, the α slopes estimated from $V_{\rm cir}$and $V_{\rm kin}$using the *power-law* method grow quickly (i.e. the error in α decrease), until they reach and eventually exceed the true values of the distribution of slopes in the simulations. Considering that the fiducial results from the *power-law* method were obtained from fits to the whole extension of the H α velocity profiles, which have of the order of 20∼40 points, this explains the results observed in Figs. 3.4, 3.5, i.e. that the *power-law* method somehow overestimates the true α distribution from all the velocity profiles, although the error is less noticeable from $V_{\rm cir}$and $V_{\rm kin}$, from which it is partially consistent with 0. Nevertheless, note that this would be equivalent to make a fit to the inverted density profile using a large number of points, i.e. including a lot of data from outside the break radius, which will make the inferred slope necessarily steep, but will not tell us anything about the very inner structure of the velocity/density profiles. Therefore, even though the results from *power-law* look promising in Fig. 3.9 and Table 3.1, the reason is completely misleading.

3.2.6 Comparison with the literature

Finally, I compare the results obtained from the mock observations to some influential observational studies from the literature, which also relied on the minimum disc approximation to estimate α. In Fig. 3.10 I plot the inferred α slope as a function of the position of the first velocity measurement ($R_{\rm inner}$), along with the expectations from some typical NFW and ISO models employed in the literature to differentiate between cusps and cores (e.g. de Blok and Bosma, 2002), and the true values of α as a function of radius of the target NFW configurations of the simulated haloes. This plot clearly shows that the results from the simulated galaxies are very consistent with observational findings discussed in the literature. Typically, the analysis of Fig. 3.10 would lead to the wrong conclusion that the *observed* galaxies live inside cored dark matter halos, whose density profiles are more consistent with the ISO profile than with the NFW model.

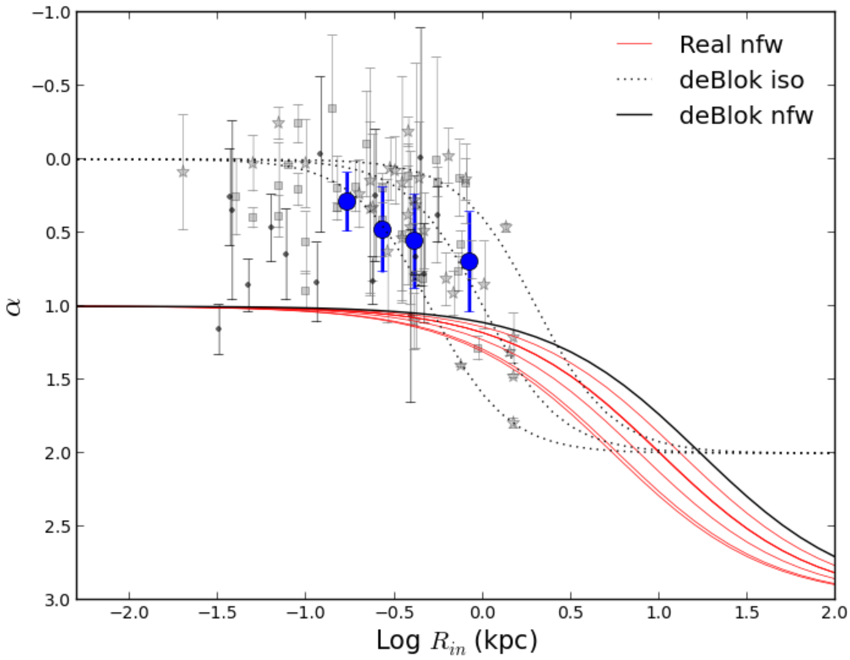

Figure 3.10: Measurements of α as a function of the position of the first velocity measurement. All grey symbols come from the literature (dots: Swaters et al. (2003), squares: de Blok and Bosma (2002), stars: de Blok et al. (2001)). Blue circles represent the mean results from the mock rotation curves and error bars indicate the interval enclosing 67% of the area of the α PDF. I also show the ISO and NFW models used by de Blok et al. (2001) to discriminate cusps from cores in the original formulation of this plot, as well as the target NFW models chosen for the galaxies simulated here.

For a more detailed comparison, in Fig. 3.11 I plot an histogram of a subset of the α slopes collected from the literature, to compare it against the results obtained from the mock rotation curves studied here. To make the comparison meaningful, I only consider observations with $0.1 \leq R_{\rm inner} \leq 1$ kpc, and inclinations between $10°$ and $80°$. Additionally, I count the number of galaxies having $R_{\rm inner}$ in different radial bins, namely between 0.1 and 0.22 kpc, between 0.22 and 0.34 kpc, between 0.34 and 0.62 kpc, and between 0.62 and 1 kpc. Then I randomly extract some of the results from mock observations, demanding that the number of galaxies at 10, 20, 40, and 80 Mpc, conversely with $R_{\rm inner}$ at 0.17, 0.27, 0.41, and 0.84 kpc, is proportional to the number of observations in the radial bins mentioned before, and I calculate the correspoding α PDF. I repeat this 100 times and I take the mean PDF for the comparison, shown in red in Fig. 3.11. The similarity of both

α distributions is remarkable, the more notable difference being a secondary peak at $\alpha = 0.85$ from observations that is not reproduced by the PDF of the slopes I *observed* from the simulations. Nevertheless, notice that this comparison should not be taken literally for all the details, because there are still many possible sources of differences. In particular, note that the observational histogram might be affected by low-number statistics, specially given the fact that the simulated galaxies are perfectly-symmetric discs, which is not the case of real systems for which a considerable random scatter is likely affecting the shape of the histogram.

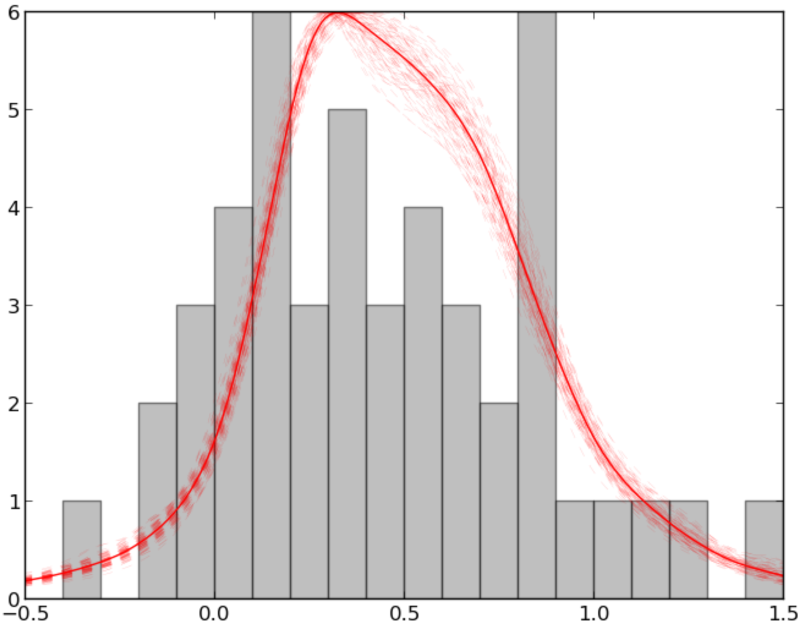

Figure 3.11: Compilation of slopes α from the literature. The histogram considers galaxies with $\mathrm{R}_{\mathrm{inner}}$ between 100 pc and 1 kpc and inclinations between 10° and 80°. The red line represents the total PDF of a sub-sample of the results ontained in this work, selected to match the distribution of R_{in} of the observed galaxies; the thick line is the mean PDF from 100 realizations (thin lines).

3.3 Can pressure support effects be corrected?

Now that we have demonstrated the crucial role of pressure support in cusp-core studies, we address the matter of whether its effect may be corrected using observationally accessible information. Please note that this section is also part of the paper presented in the former chapter (Pineda et al., 2016), and that is the reason for the small differences in the style of the text with respect to the rest of the thesis.

3.3.1 Pressure support vs. asymmetric drift

First, we would like to clarify the theoretical concepts related to the physics of pressure support, as there is some ambiguity in the literature. Our main concern is the use of the terms *pressure support* and *asymmetric drift* as interchangeable expressions despite the fact that they represent different physical properties. This common mix up was recently pointed out by Dalcanton and Stilp (2010), but it still deserves further attention, as we will demonstrate below.

One can start by stating what pressure support truly means and its proper formulation. Consider the Euler momentum conservation equation for a gas element in an external gravitational field,

$$\frac{\mathrm{d}\boldsymbol{V}}{\mathrm{d}t} = \boldsymbol{a}_{\mathrm{grav}} - \frac{1}{\rho}\boldsymbol{\nabla} P. \tag{3.13}$$

If this gas element moves on a circular orbit in the midplane of a system with axial and vertical symmetries, the three terms of equation (3.13) are aligned in the radial direction, leading to the scalar relation

$$\frac{v_\phi^2}{r} = \frac{v_c^2}{r} + \frac{1}{\rho}\frac{\mathrm{d}P}{\mathrm{d}r}, \tag{3.14}$$

where v_ϕ represents the rotational speed of the gas; v_c is the expected circular velocity from the gravitational potential; and the second term on the right is the radial acceleration due to pressure gradients, ρ being the gas density and P its pressure. The sign inversion on the right hand side is because centripetal accelerations point inwards, i.e. in the negative $\boldsymbol{r}$ direction. Note that if pressure falls off as a function of radius (as it is often the case in galactic discs), the gradient becomes negative, making $v_\phi < v_c$; this is pressure support. Also note that equation (3.14) is valid in the equatorial plane for any combination of spherical and disc-like components, so the approximation of a spherical potential ($a_{r_{\mathrm{grav}}} \approx \frac{GM(<r)}{r^2}$) used by Dalcanton and Stilp (2010) is not necessary.

The sources of pressure typically mentioned (if any) in the cusp-core literature are thermal pressure and turbulence. Other possible sources, such as magnetic fields or cosmic rays, are rarely mentioned, although they may be important for the dynamics of the ISM (Boulares and Cox 1990; Ferrière 2001; but cf. ?). Dalcanton and Stilp (2010) highlight that turbulence dominates the random motions of the gas and for that reason the pressure relates to the 1-dimensional velocity dispersion as

$$P = \rho\sigma^2. \tag{3.15}$$

Substituting equation (3.15) into equation (3.14), rearranging terms, and expressing the velocities in our notation, the pressure support correction can be written as

$$V_{\text{tot}}^2 = V_{\text{cir}}^2 - \sigma^2 \frac{\mathrm{d}\log\left(\rho\sigma^2\right)}{\mathrm{d}\log r}. \tag{3.16}$$

Furthermore, assuming that the vertical structure of the disc does not depend on radius, one can express the logarithmic derivative in terms of the mass surface density of the gas Σ, which is the observable quantity

$$V_{\text{tot}}^2 = V_{\text{cir}}^2 - \sigma^2 \frac{\mathrm{d}\log\left(\Sigma\sigma^2\right)}{\mathrm{d}\log r}. \tag{3.17}$$

This is equivalent to equation (11) of Dalcanton and Stilp (2010). We have omitted the subindex r in the velocity dispersion to emphasize that turbulence is classically treated as an isotropic source of pressure[3]. Dalcanton and Stilp (2010) argue that the distinctive boundary conditions in the vertical direction and in the equatorial plane likely invalidate the assumption of isotropy in the velocity dispersion, which is indeed a relevant concern for the macroscopic scales probed by observations. Nevertheless, in practice, σ is in general treated as isotropic, mostly due to the difficulty of disentagling its radial component from the observed projection along the line of sight.

Asymmetric drift, on the other hand, is a phenomenon experienced by collisionless particles. Its origin is succinctly presented in Binney and Tremaine (2008), to which we refer the reader for details. In brief, the Jeans equations for a stellar population rotating in the equatorial plane of a smooth potential with axial and vertical symmetries yield

$$v_{\mathrm{c}}^2 - \overline{v_\phi}^2 = \sigma_\phi^2 - \overline{v_r^2} - \frac{r}{\nu}\frac{\partial(\nu\overline{v_r^2})}{\partial r} - r\frac{\partial(\overline{v_r v_z})}{\partial z}, \tag{3.18}$$

---

[3] This seems to be a good approximation when the dominant contribution comes from microturbulence at much smaller scales than the size of the region being considered (Mac Low and Klessen 2004; but cf. Elmegreen and Scalo 2004)

where v_c represents the circular velocity associated with the gravitational potential, v_r, v_ϕ, and v_z are the three components of the actual stellar velocity, σ_ϕ is the azimuthal velocity dispersion, and ν is the probability of finding a star at a certain position. The last quantity is proportional to the mass density of the tracers and can be replaced by the mass surface density Σ if the vertical structure of the stellar distribution does not vary with radius. Assuming no net radial motions ($\overline{v_r^2} = \sigma_r^2$) and using our notation, equation (3.18) becomes

$$V_\mathrm{tot}^2 = V_\mathrm{cir}^2 + \sigma_\phi^2 - \sigma_r^2 - \sigma_r^2 \frac{\mathrm{d}\log\left(\Sigma\sigma_r^2\right)}{\mathrm{d}\log r} - r\frac{\partial(\overline{v_r v_z})}{\partial z}. \tag{3.19}$$

The similarity of equations (3.19) and (3.17) is remarkable, but further assumptions are needed if one wants to make them look identical. These are (1) that there are no tilts in the velocity ellipsoid, so the last term of equation (3.19) vanishes, and (2) that the velocity dispersion of the stars is isotropic. Neither of these assumptions is straightforward, so, in spite of the fact that the Euler and the Jeans equations can be obtained from the Boltzmann equation in similar fashions, they are not physically equivalent.

Some authors explicitly suggest that ionized gas might actually experience the effects of asymmetric drift if it is clustered into individual clouds which dynamically behave like collisionless particles (e.g. Cinzano et al., 1999; Verdoes Kleijn et al., 2000; Weijmans et al., 2008). Invariably, all the studies addressing this hypothesis are focused on early-type galaxies which are dynamically hot, exhibiting internal velocity dispersions of hundreds of km s^{-1} that are hard to reconcile with thermal agitation and small-scale turbulence. On the other hand, late-type galaxies such as those regularly studied in the cusp-core literature are comparatively cold systems, with reported H I velocity dispersions of the order of $\sim$12 km s^{-1}. These small velocity dispersions can be naturally explained by thermal and turbulent pressures. Therefore, there is no need to invoke alternative scenarios. Note also that a large fraction of the 21-cm emission comes from the warm (6000$-$10000°K) neutral gas in the disc, which, in contrast with the clumpy, cold (100°K) H I phase, is a diffuse medium with a large spatial extent (Ferrière, 2001). The same applies for the warm ($\sim$8000°K) ionized medium responsible for the diffuse H α emission outside of H II regions (Cox, 2005). In light of these facts, it seems more likely that the dominant source of non-centrifugal support in gaseous discs of late-type galaxies is pressure support, not asymmetric drift. Incidentally, we note that equation (3.17), which describes pressure support, is the universal recipe employed to correct gaseous rotation curves affected by random motions in cusp-core studies, but it is often improperly named "*the asymmetric drift correction*". Sometimes equation (3.19) is invoked, but then the precise supplementary approximations to reduce it to (3.17) are invariably assumed.

The trouble with conflating pressure support and asymmetric drift is that this may lead to an erroneous assessment of the magnitude of the correction. Note that in equation (3.19), all the quantities refer exclusively to the stellar population that is being traced, while in equation (3.17), they refer to the gaseous medium as a whole. One may argue that according to the classic pictures of the ISM (Field et al., 1969; McKee and Ostriker, 1977), the different phases are expected to coexist in thermal pressure equilibrium; if so, tracing a single phase (for instance, the warm H I) provides information about the global thermal state of the ISM. Nevertheless, this scenario is an oversimplification, and thermal pressure imbalances have been observed even in the local ISM (Bowyer et al., 1995; Berghöfer et al., 1998). This implies either that pressure equilibrium must include non-thermal sources that are dynamically important, such as turbulence, magnetic fields, and cosmic rays (Ferrière, 2001; Cox, 2005), or that pressure imbalances may exist locally as a result of complex events such as recent supernova explosions, for instance. Therefore, a comprehensive assessment of the dynamical state of the gas through multiple observational tracers is highly desirable.

Some authors have expressed concerns about the estimation of the gas velocity dispersion and the gas surface density profiles from a single tracer, as this may bias the measurements in regions with significant fractions of other ISM components (e.g. Simon et al., 2003b; Dalcanton and Stilp, 2010). Regrettably, these biases are most often simply overlooked, and the majority of the cusp-core literature considering pressure support only vaguely states that random motions may provide support to the gas when they are comparable to the rotation velocity. A fraction of this subset of studies argues that pressure support corrections are known to be unimportant, increasing the magnitudes of rotation curves by only a few km s^{-1}, and do not attempt any sort of correction. The remaining fraction applies equation (3.17) to the data at hand, normally from only a single tracer, often without considering the uncertainties in this correction. As we will demonstrate below, effective corrections for pressure support effects may be much more challenging than has been traditionally assumed.

3.3.2 Ideal and realistic pressure support corrections

We here study the feasibility of pressure support corrections in our models, first based on ideal theoretical measurements and then using observationally accessible information, i.e. the surface density profiles (Σ) and the velocity dispersion profiles (σ), obtained from the corresponding mock maps by taking azimuthal averages along the same elliptical rings used to analyse the velocity maps.

We start by checking the validity of equation (3.16) directly in the simulations. We measure σ and ρ from all gas particles in the equatorial plane using the same radial bins as for the theoretical velocity profiles. The velocity dispersion is calculated using equation (2.13), recalling that the code indirectly models the effect of the turbulence induced by stellar and supernova feedback by employing an effective equation of state that is stiffer than isothermal, thereby enhancing the pressure and thus temperature in high-density, star-forming gas. By means of equation (3.16), we find exceptional agreement between $V_{\rm tot}$ and the corrected version of $V_{\rm cir}$ for all galaxies, as we illustrate with an example in Fig. 3.12. Moreover, the results of the NFW/ISO fits to the corrected version of $V_{\rm cir}$ are in stunning agreement with those of $V_{\rm tot}$, as we report in Table 3.2. The correction is performed using the theoretical profiles in radial bins of 100-pc width. The fits reported at distances $D = 20$ Mpc in Table 3.2 are done after resampling the corrected curves to the corresponding poorer spatial resolution.

Notwithstanding, even though the pressure corrections work properly in the ideal case, a number of difficulties prevent effective correction of the mock observations. After applying equation (3.17) to our mock rotation curves using the *observed* Σ, σ profiles, the cuspy dark matter haloes still appear disguised as cores to the rotation curve fitting method, as we also show in Table 3.2. To understand this result, we need to discuss in detail several aspects of the implementation of equation (3.17).

The first difficulty in correcting for pressure support based on observed quantities is that virtually all the cusp-core studies considering this effect use H I data alone, with very few exceptions that use kinematic data from the ionized gas but then lack the H I extension (Simon et al., 2003b; Chemin et al., 2016). Extrapolating a sort of "standard" observational correction for our case, we correct the inner H α velocities using the $\sigma_{\rm H\alpha}$ velocity dispersion and the outer H I velocities using $\sigma_{\rm HI}$. For the gas surface density profile, we take $\Sigma_{\rm HI}$ at

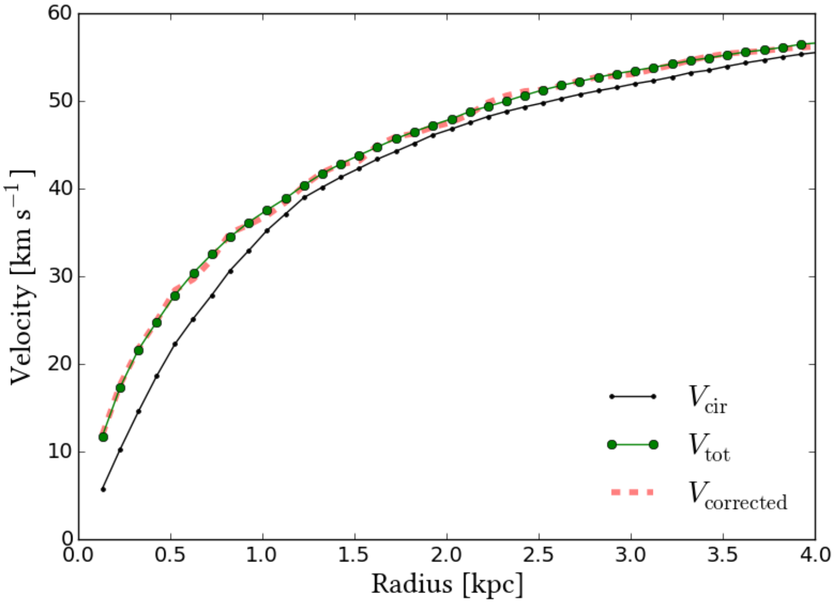

Figure 3.12: Theoretical verification of the pressure support effect in galaxy Dwarf1 at half the simulation time. The solid green line with circles represents $V_{\rm tot}$, the black solid line with points represents $V_{\rm cir}$, and the long-dashed red thick line in the background is the corrected version of $V_{\rm cir}$ after adding the term on the right-hand side of equation (3.16). The correction exactly recovers $V_{\rm tot}$ from $V_{\rm cir}$, confirming pressure support as the cause of their difference.

Table 3.2 - Percentages of corrected rotation curves that are better represented by the NFW or ISO models. For comparison, we include the results from $V_{\rm tot}$, which were already presented in Table 2.2. We do not correct the mock observations at 40 or 80 Mpc because the H I spatial resolution is too low.

H α PSF (pc)		∼100	∼200
D (Mpc)		10	20
V_{tot}	NFW	56 (61)	57 (61)
	P-iso	38 (39)	39 (39)
	Both	6 (0)	4 (0)
$V_{\rm cir}$ (corrected)	NFW	57 (61)	58 (60)
	P-iso	37 (39)	36 (38)
	Both	6 (0)	6 (2)
V_{KIN} (corrected)	NFW	15 (21)	13 (20)
	P-iso	67 (74)	69 (77)
	Both	18 (5)	17 (4)

all radii. Because the H I spatial resolution is coarser than that of the H α observations, it is necessary to extrapolate the $\Sigma_{\rm HI}$ profile in the center. We achieve this by fitting a polynomial-plus-gaussian function to the first 10 kpc of $\Sigma_{\rm HI}$, checking that it follows the data well and that it exhibits reasonable asymptotic behaviour in the inner region. Then, we calculate the pressure support correction at each point of the rotation curves by evaluating the derivatives in equation (3.17) with a finite-difference scheme. In Figs. 3.13 and 3.14, we present an example of the mass surface density profile and of the velocity dispersion profile as traced by different gas phases, along with the true quantities from all the gas in the equatorial plane of the simulations. Because our mock H I observations use all the gas particles regardless of their physical state, we also show for comparison the profiles extracted from the cold gas ($T < 10^4$ °K) alone, which may be a better proxy for real H I observations. We note that unlike the H I case, our mock H α emission is not only proportional to the mass but also the star formation rate of the emitting particles, making the conversion factor between the intensity maps and the gaseous mass uncertain. For this reason, we plot the mock H α luminosity profile in Fig. 3.13, rescaled as necessary to facilitate the comparison with the surface mass density profiles. These plots are for a specific *observed* galaxy, but similar trends are observed for the rest of the sample.

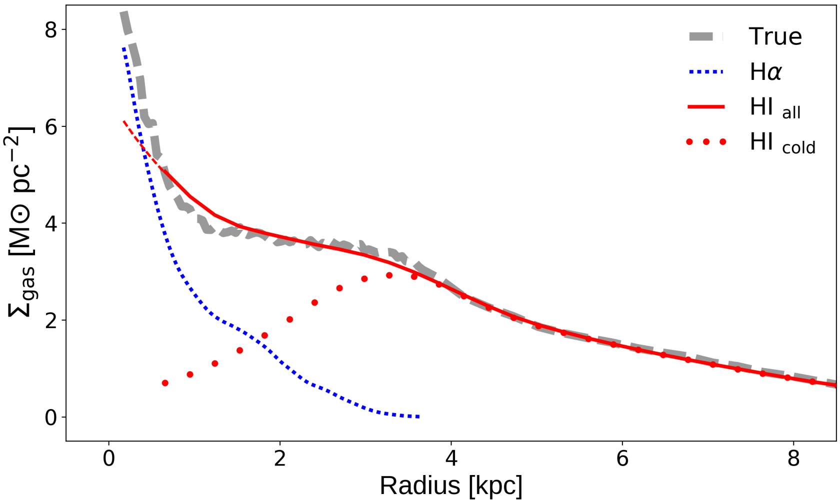

Figure 3.13: Gas surface density profiles for G0 at 3 Gyr, 45° inclination, and a distance of 10 Mpc. The thick dashed gray line represents the true mass surface density profile as measured from the simulation. The dotted blue line is the H α surface brightness profile, re-scaled to have a central amplitude similar to that of the true mass profile. The solid red line shows our fiducial $\Sigma_{\rm HI}$ mass surface density profile, extrapolated in the very center with an analytical function represented by a thin dashed line. The red dots represent the alternative observation from the cold gas alone, $\Sigma_{\rm HI-cold}$. The low spatial resolution smoothes the $\Sigma_{\rm HI}$ profile and leads to an underestimation of the central gas concentration. Observations from the cold H I phase would be more strongly biased in the center, where most of the gas in our simulations is hot and forming stars.

Recalling that our mock H α emission traces only the star-forming gas, a joint analysis of Figs. 3.13 and 3.14 reveals that there are three different regimes in the disc. In the very

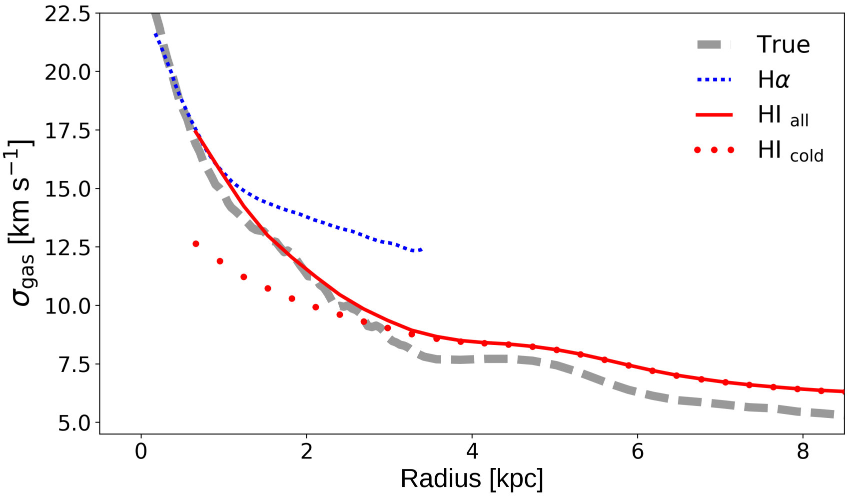

Figure 3.14: Velocity dispersion profiles for G0 at 3 Gyr, 45° inclination, and a distance of 10 Mpc. Colours and symbols are the same as in Fig. 3.13, identifying the true profile in the simulation and those inferred from our mock H α, H I, and H I$_{\rm cold}$ observations. This plot shows that in areas where hot and cold gas coexist, measurements based on a single tracer differ from the true values.

inner region, within ∼0.6 kpc, virtually all of the gas is forming stars, and both the $\Sigma_{\rm H\alpha}$ and $\sigma_{\rm H\alpha}$ profiles follow well the true theoretical quantities. At intermediate radii (between ∼0.6 and ∼3.5 kpc), there is a mix of star-forming and non star-forming gas, with the H α emission steeply going to zero while the cold gas density steadily grows. Taking into account that the star-forming gas is systematically hotter than average, this explains why in this intermediate regime, $\sigma_{\rm H\alpha}$ increasingly overestimates the true global velocity dispersion, while $\sigma_{\rm HI\text{-}cold}$ stays below the true σ profile but systematically approaches it as the fraction of cold, non-star forming gas starts to dominate. We also note that in this intermediate region, the slope of $\sigma_{\rm H\alpha}$, which will influence the pressure correction term, is shallower than that of the true total velocity dispersion profile. Beyond ∼3.5 kpc, virtually all the gas in the simulation is cold and passive, there is no mock H α emission and the measurements from the cold gas phase coincide with our fiducial H I observations. In general the fiducial mock H I observations follow the true theoretical quantities well, though the low resolution makes the *observed* profiles appear smoother and σ slightly overestimated. This smoothing propagates and introduces a bias during the extrapolation of $\Sigma_{\rm HI}$ to the very center, leading to an underestimation of the true total surface density and also of its steepness.

We have shown that there are biases in both the amplitude and the slope of the observationally inferred Σ and σ profiles at different radial ranges and from different tracers. Regarding posterior cusp-core analyses, in which direction will these biases act? The answer depends largely on the logarithmic slope of the product $\Sigma\sigma^2$, i.e. on its curvature, which can not be simply inferred from our qualitative analysis. After evaluating equations (3.16) and (3.17) we found that, for our particular experiment and for the choices we made, the observational correction exhibits the right radial profile but it falls behind the theoretical expected value. We show this in Fig. 3.15, where we present the net difference between the corrected velocity profiles and the original ones, ΔV, as a function of radius and inclination. The mean difference between the theoretical and the observational corrections is never larger than 4 km s^{-1}, falling between 1 and 2 km s^{-1} over most of the first kiloparsec. However, this small difference is enough for the intended observational correction to fail because the curvature of the "corrected" rotation curves is still more compatible with the ISO model in at least 67% of the sample (see Table 3.2). In spite of the fact that the tension is slightly less critical than before the correction, the inferences from the rotation curve fitting continue to be misleading compared with those from $V_{\rm tot}$, largely overestimating the fraction of "observed" cores because of the inaccurate pressure support corrections.

Fig. 3.15 and Table 3.3 also demonstrate that the magnitude of the pressure support is more underestimated, i.e. the correction is less effective, in more inclined discs. This is as a result of projection effects and the low spatial resolution, which make the Σ and σ profiles flatter, thus lowering the inferred logarithmic slope of the product $\Sigma\sigma^2$. We do not correct the mock observations at 40 or 80 Mpc because the observables are extremely biased by the effect of the spatial resolution. Particularly, note that at 40 Mpc, the first $\Sigma_{\rm HI}$ data point lies at 2.4 kpc, ruling out any possibility of performing an accurate correction inside the first kiloparsec.

It is very interesting to note that the observationally inferred ΔV values peak at ∼3.5 km s^{-1} and quickly drop to ∼1 km s^{-1}, in agreement with typical corrections estimated from observations, which are sometimes interpreted as a reflection of the insignificant role of pressure support. This conviction is often supported by the observed low velocity dispersions, typically ∼10 km s^{-1}. However, note that this estimate regularly comes from H I data alone, and that in general, the ionized gas is expected to have a larger velocity dispersion, one of the reasons why it tends to form thicker discs than the neutral gas (Fathi et al., 2007). Fig 3.14 reveals that the cold dynamical component in our simulations looks similar to many H I observations in this regard, peaking at ∼13 km s^{-1} and exhibiting a

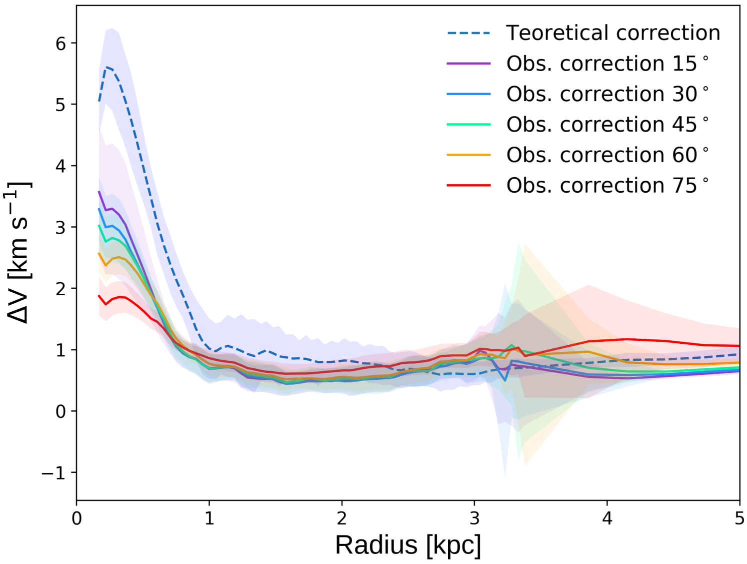

Figure 3.15: Theoretical and observational pressure support corrections for galaxy Dwarf2 viewed at 10 Mpc. We plot the net velocity excess ΔV to be added to the observed rotation curves (or to V_{cir}) to get their corrected versions. Solid lines represent the mean correction as a function of radius, and the shaded regions enclose the 1-σ scatter of the profiles. The observational corrections are colour-coded by inclination as indicated in the legend. This plot shows that observational corrections underestimate the theoretical correction as a result of biased estimates for Σ and σ; even though the difference seems small, it prevents faithful recovery of the inner curvature of the *observed* rotation curves, which still appear more compatible with the ISO model after the attempted correction.

smooth radial gradient; however, we know that this tracer is extremely biased relative to the full velocity dispersion of the whole gas, which is the necessary quantity for accurate pressure support corrections[4]. The true value of σ in our simulations peaks at $\sim$25 km s^{-1} and steeply decreases, dropping to $\sim$10 km s^{-1} at $\sim$2 kpc. This is compatible with the few reported H α observations we could find in cusp-core works. For example, Simon et al. (2003b) observed a linewidth of 34 km s^{-1} for the dwarf spiral NGC 2976, Epinat et al. (2010) mentions an average velocity dispersion of 24 km s^{-1} for a local sample of 153 nearby disc galaxies of mixed morphological types extracted from the GHASP survey (Epinat et al., 2008,?), and Chemin et al. (2016) found a velocity dispersion profile peaking at 25 km s^{-1} and dropping to $\sim$19 km s^{-1} at 2 kpc for the grand-design spiral M99.

Note also that according to Fig. 3.13, the cold gas strongly underestimates the true gas density in the center. Moreover, the inferred $\Sigma_{\mathrm{HI-cold}}$ profile has a positive slope there, which would partially reverse the sign of the pressure support correction term if it were

---

[4] Interestingly, at inclinations $\leq 30°$, the $\sigma_{\text{HI-cold}}$ profile is even flatter and stays below 10 km s^{-1}.

Table 3.3 - Percentages of rotation curves extracted from the 2D maps that are better represented by the NFW or ISO models after the observational pressure support corrections.

H α PSF (pc)		~100	~200
D (Mpc)		10	20
15°	NFW	22 (31)	19 (28)
	P-iso	55 (63)	57 (66)
	Both	22 (6)	24 (6)
30°	NFW	24 (31)	20 (28)
	P-iso	57 (64)	61 (69)
	Both	19 (5)	19 (3)
45°	NFW	19 (26)	17 (24)
	P-iso	61 (70)	63 (71)
	Both	20 (4)	20 (5)
60°	NFW	8 (15)	8 (14)
	P-iso	70 (78)	74 (82)
	Both	22 (7)	18 (4)
75°	NFW	1 (3)	0 (0)
	P-iso	93 (96)	98 (99)
	Both	6 (1)	2 (1)

inserted in equation (3.17). Even though this modelling may be too simplistic to explain the complexity of real H I observations, it is interesting to note that central "holes" in the $\Sigma_{\rm HI}$ profiles are not rare, and they are treated in different ways when performing pressure support corrections; some authors use $\Sigma_{\rm HI}$ as is, while others extrapolate the external exponential disc behaviour to the center to try to compensate for the ionized and molecular hydrogen mass contributions, which are very difficult to assess.

It is not absolutely clear if the gas in our simulations may be over-pressurized compared with real systems, but we consider that the very good agreement between our mock data and real observations, as well as the agreement in the best-fit coefficients presented in Figure 2.14, should motivate further scientific discussion and careful review of some observational results. Independent of the possible differences between our models and real dwarf irregulars and LSBs, the exercise performed here suffices to demonstrate the intrinsic difficulties in properly assessing the effect of pressure support (amongst others), and it underlines the sensitivity of rotation curve fitting methods to very small errors or biases in the central parts of galaxies.

3.4 Summary and discussion

The study of the rotation curve inversion methods performed in this chapter has further confirmed that pressure support is able to erase the signatures of cusps in our models. The fit of straight lines to the logarithmic version of $V_{\rm cir}$ shows that its inner curvature is indeed more alike with an ISO dark matter core than with a cuspy NFW model in the simulations. I have also found that the intrinsic curvature of the velocity profile associated to a exponential disc is somewhere in the middle of the two extreme cases discussed here (NFW/ISO). Because of that, its quadratic addition to a cored $V_{\rm dm}$ will make this profile become "cuspier", but it would also make a cuspy $V_{\rm dm}$ appear more "cored". This result seriously question the traditional interpretation of the minimum disc approximation as a safe way to impose an upper limit to the cuspyness of the haloes.

Two out of the three methods tested here to measure the cuspiness of the halos from the cuspiness (curvature) of the inner velocity profiles were proven to be affected by intrinsic biases, which prevent them to report reliable logarithmic density slopes. The third method, which resorts to a simple evaluation of the velocity derivatives using a finite difference scheme, is able to recover the true logarithmic velocity density at a good approximation, proven that sufficient spatial resolution is given and that the velocity profile is smooth.

I also studied in detail the amount of pressure support in the simulations and the possibility of correcting for it using observationally accessible information. The evidence suggests that, even using observations typically considered of high-quality for cusp-core studies, it is very unlikely that pressure support effects can be properly estimated and corrected. This is partially due to spatial resolution issues and to projection effects, but also at a large extent because a proper prescription of the pressure state of the gas would require a detail assessment of the state of the different phases (e.g., neutral, ionized, molecular) and their interplay.

Chapter 4

Simulations part II: Estimating dark and baryonic matter in spiral galaxies

In this chapter I present an early version of a second set of controlled experiments with numerical simulations. Its ultimate goal is to test the suitability of surface photometry analyses to calibrate mass models of the stellar component in spiral galaxies. As extensively commented in Chapter 1.4, this step is mandatory in cusp-core studies of galaxies for which the minimum disc approximation is not admissible

In this chapter I introduce additional simulations to those formerly analysed in Chapters 2 and 3, modelling larger galaxies with more massive discs for which I mimic realistic photometric observations using the multiwavelenght radiative transfer code SUNRISE . Then I analyse the mock images in the very same manner as it is typically done for observations of late-type galaxies, i.e. fitting elliptical isophotal contours. The final goal of this work is to compare the inferred stellar matter distributions with the real ones as measured directly from the simulations, as a function of different physical and observational parameters. In this thesis I will introduce the general framework and the results from some initial experiments, that may be hopefully completed in future work.

4.1 Radiative transfer in simulated galaxies with SUNRISE

I have used the multiwavelength radiative transfer code SUNRISE (Jonsson et al., 2006, 2010) to model the spectral energy distribution of the light that would be observed with a telescope/camera from the simulated galaxies. SUNRISE has proved to be able to produce realistic results concerning morphologies, dust extinction, spectral lines, and integrated magnitudes and colours of late-type simulated galaxies, showing itself useful to study simulations of galactic systems both in mergers as well as in isolation (Rocha et al., 2008; Jonsson et al., 2010; Snyder et al., 2011). In the following, I will briefly summarize the principal methods and models implemented in the current version of SUNRISE . For a more detailed description of the code and its capabilities, please refer to the quoted references.

Basically, SUNRISE performs the calculation of the resulting SED coming out from the galaxy, and reaching a virtual telescope/camera, in three steps.

First step: *The source SED of stellar particles including HII and PDR regions.*

In the first step, the code assigns to each stellar particle, depending on its age and metallicity, a given SED from a library of single stellar populations. As young stars are expected to be surrounded by thick envelopes of gas and dust associated to their parenting clouds, their light will experience a differential, large extinction, as a sizable fraction of its energy in the optical and the UV will be consumed in the photoionization of the hydrogen atoms and the heating of dust. The resulting HII regions and photodissociation regiosn (PDR), are also known to be responsible for a large number of narrow emission lines, but all these processes related to the physics of the star-forming regions are normally occuring at spatial scales below the spatial resolution of galaxy simulations. To deal with this, SUNRISE resorts to the MAPPINGS III code (Groves et al., 2004), specifically developed to calculate the radiative transfer trough HII regions and PDRs (Dopita et al., 2005; Groves et al., 2008). At the end of the first step, SUNRISE has calculated the SED of the bare stellar population as well as its modified version, replacing the light from young stellar particles by the SED of the MAPPINGS III models. The latter version is the one that will be actually used as input for the next stage.

Second step: *Absorption and scatter of the stellar light*

In the second step SUNRISE initiates the radiative transfer calculations, estimating the expected amount of spectral energy absorbed and scattered in different directions, according to the spatial geometry of the gaseous material in the simulation and to the assumed composition of the ISM. Roughly, from the gaseous density field SUNRISE creates a three-dimensional grid, locally refined to enhance the spatial resolution in high-density regions. The amount of interestelar dust is assumed as a constant fraction of the metals in the gaseous phase, and the distribution of silicates and carbonates grain sizes, which determines the cross section of interactions with the radiation field at different wavelengths, is modelled to follow observations of the Milky way and of the large and small magellanic clouds, including polycyclic aromatic hydrocarbon molecules (PAH) (Weingartner and Draine, 2001; Draine and Li, 2007). From these models and the dust masses, a characteristic opacity and albedo can be attributed to each cell, and finally translated into optical depths which will determine the probability of radiation-dust interactions.

Then SUNRISE employs a multi-wavelenght, ray-traced montecarlo technique, and a so-called *forced scattering* approach. In brief, SUNRISE draws a large number of individual rays from the stellar sources in random directions, in order to sample the global stellar radiation field, and it follows the journey of these rays through the interstellar medium, tracking the interactions (absorption, scattering) with the galactic dust and updating the spatially-resolved radiation field accordingly.

The forced scattered approach refers to the fact that, instead of actually reproducing the whole "brownian" path of every ray (which may be scattered several times and, in most occasions, leave the galactic system in a different direction than that of the virtual observer), SUNRISE will "force" the radiation-dust interactions to happen (in a statistical sense), in order to reproduce the correct probability distribution function of photons reaching the camera in an efficient way. It works in the following manner.

In first place, after choosing the sourcing position for a new ray, SUNRISE computes the probability that it goes towards the camera ($1/4\pi$ for isotropic distributions), and what would be the intensity this ray had if it reached the camera without being neither absorbed nor scattered, but just attenuated by the optical length of the material in its way. This virtual direct contribution is effectively recorded in the camera. Then a random direction is selected for the "true" journey of the ray, and SUNRISE computes in each cell along this path what is the probability that the ray would interact there. The sum of these probabilities serves to estimate the overall chance that the ray would interact with ISM or that it would escape without interacting at all. Then the forced scattered is applied, actually splitting the ray into two rays, a escaping one and an interacting one, with relative intensities given by the probabilities determined before. The interacting ray is forced to scatter at a random point, using the cumulative optical depth to define the probability distribution of this event as a function of the travelled distance. Then the albedo of the corresponding grid cell is used to determine the fraction of the ray energy that would be absorbed, which is recorded in the "memory" of the cell, in order to self-consistently calculate the dust temperature later on. The remaining fraction of the energy in the ray would be scattered in an arbitrary direction given by the scatter phase function. Yet, before picking an angle SUNRISE estimates the probability that the new ray goes towards the camera, and the contribution of this hypothetical ray, dimmed by the probability of having that direction and by the optical length it would have to cross to reach the camera, is effectively recorded as a detection there. After tracking this first-order scattered contribution, the "true" scattered ray may be indeed drawn in a random direction, repeating the whole process until a given number of high-order forced scatterings is reached. In the end, by using a large enough number of rays, this algorithm effectively reconstructs the true distribution function of the photons reaching the telescope, and also the spatially-resolved photoheating of the dust in the grid cells in an optimized way.

Contrary to former, simpler implementations, the rays traced by SUNRISE are not monochromatic but carry information of the whole espectral range at once. This means than, instead of having a scalar intensity value, each ray has an associated vector of intensities related to the different wavelengths. Yet there is a reference wavelength which is used to calculate the probability of interactions at a given cell of the grid. As this probability is not uniform, but wavelength-dependent according to the distribution of sizes of the dust grains, SUNRISE modulates each element in the vector of intensities, after an interaction occurs, according to the ratio between probability of interaction of every wavelength and the probability of interaction of the reference wavelength. This so-called *bias* scheme is fully correct from a statistical point of view, and it allows an enormous gain in computation time. This is one of the major improvements of SUNRISE in comparison with other radiative transfer codes, which allow it to make a fully panchromatic treatment of the radiative transfer problem in a single run.

Third step: *Thermal dust emission*

In the third step, the temperature of the dust in each grid cell is computed out of the total energy absorbed from the stellar radiation field. This allows the estimation of the corresponding thermal dust emission, modifying the interestelar radiation field in the infrared part of the spectrum. This excess of radiation induces a further heating of the dust due to self-absorption, therefore driving a new update of the radiation field, and so on. This computation is iterated until the dust temperature converges to a state of thermal equilibrium, and the total contribution of this thermal emission to the SED that would reach the camera is additioned.

Finally, having determined the SED at every pixel of the camera, dimmed according to the assumed distance, SUNRISE creates the images by performing a spectral convolution with the user-defined filters, which may belong to any desired photometric system ranging from the ultraviolet to the submillimetre.

4.2 Simulations

The experiments presented in this chapter are relevant for the dynamical analyses of galaxies with relatively massive discs, for which the minimum disc approximation is not suitable. Therefore, a different sample of galaxies than the one studied in Chapters 2 and 3 is necessary. I found an optimal solution in re-simulating some of the galaxy models presented by Cox (2004), and further studied in other works (e.g. Cox et al., 2006; Jonsson et al., 2006; Lotz et al., 2008; Rocha et al., 2008). This set of simulations spans a wide range of masses, sizes, and morphologies, as it was modelled after the main structural properties of a large sample of local observed late-type galaxies. This was already mentioned in Sec. 2.2.1 where the galaxy models G0 and G1 were introduced, as they actually belong to the sample of Cox (2004). Another reason to work with these galaxy models is that they have been previously imaged using SUNRISE , which served to demonstrate that their integrated magnitudes and colours as estimated from the model SEDs effectively match several scaling relations from observations of galaxies in the local universe (Jonsson et al., 2010).

As galaxies G0 and G1 represent a well-suited low-mass and low-size end of a monotonic sequence with the rest of the sample that I extracted from Cox (2004), and given that the physical models regarding the stellar ages and metallicites required by SUNRISE have been already proposed for these systems (Rocha et al., 2008; Jonsson et al., 2010), these are the only two galaxies from the sample of dwarfs that I will retain in this chapter. Amongst the other galaxies in this sample, there are two normal massive spirals, labeled as G2 and G3, and two giant Sbc-type spirals, labeled Sbc- and Sbc. The sample of (Cox, 2004) was designed to reproduce several properties of galaxies in the local Universe, being disc size, dynamical mass, and gas fraction, the most important parameters. The smaller systems, marked as “G”, are based on median properties of galaxies observed by the SDSS and correspond to spiral galaxies with gas contents between 20 per cent and 40 per cent of the total baryonic mass, exhibiting bars and moderate bulges. Disc scale lengths and gas fractions as a function of the stellar mass were obtained from Shen et al. (2003) and Bell et al. (2003). The Sbc's systems correspond to gas-rich late-type spiral galaxies bigger than the “G” systems, forming much smaller bulges, prominent spiral arms, and no bars. Sbc was modeled using median properties of the sample of Sbc galaxies from Roberts and Haynes (1994). Sbc- follows the lower quartile of the parameters distribution of parameters. All the models studied here follow basically the same prescriptions already discussed for the sample of dwarfs in Sec. 2.2.1, i.e. they are composed by a NFW dark matter halo and an exponential disc of stars and gas, and they are simulated in isolation using GADGET and very similar numerical parameters. This sample was simulated two times, as I will describe in the following.

4.2.1 First run

The first run of simulations presented in this chapter used a hybrid mix of softening lengths, namely 25 pc for stellar and gaseous particles, and 100 pc for the dark matter particles. Note that a lower resolution of the dark halo allows the use of more massive particles. In these simulations each dark matter particle has 1.25×10^5 $M_\odot$, compared to $2 \sim 5 \times 10^4$ $M_\odot$ that was used for the sample of dwarfs, where the softening length was 25 pc for all species. Using a coarser resolution for the dark component is a common practice because the haloes encompass, by far, the largest mass fraction in galactic systems, and this choice was justified for these simulations because they were used for preliminar tests and to analyse the correspondence between mass and light in the disc, i.e. in a scale of one to several kiloparsecs, for which the details of the dynamics of the dark matter inside the first ∼300 pc (3 times the softening length, roughly the expected spatial resolution) should not be a concern. In this first run the galaxies were simulated including a bulge component, as it was the case in the original models of Cox (2004). They were characterized through a Hernquist profile of the form:

$$\rho_{\rm b} = \frac{M_{\rm b}\, a}{2\pi r(r+a)^3}, \tag{4.1}$$

where M represents the total mass in the bulge, and a is its scale length. The original sample of Cox (2004) and posterior analyses of the same models (e.g. Jonsson et al., 2006) have resorted to the Hernquist model, so I use the same for consistency. In any case, as I am not intending to study specific properties of real bulges, this choice is fair enough for the purposes of this work.

The principal structural properties of the galaxies simulated in the first run are reported in Table 4.1, and an example of the mock images created with SUNRISE appear in Figs. 4.1 and 4.2.

After some early experiments with the set of simulations just described I concluded that, for a comprehensive analysis of the systematics in mass modelling studies, one should start by using simpler models, in order to be able to disentangle the individual effects before mixing them all up. For that reason the bulge components where excluded in the initial conditions of the second run of simulations. Incidentally, this was also the motivation to make up the sample of dwarf galaxies later on, and to perform the analyses of the minimum disc approximation presented in Chapters 2 and 3, which are free of the uncertainties related to the mass modelling of the baryonic components.

Table 4.1 - Properties of the models in the initial run, with a lower resolution of the dark matter halo (softening length = 100 pc) and containing bulges.

Model	$M_{\rm halo}$[a] (M$_\odot$)	$N_{\rm halo}$[b] ($\times10^6$)	c[c]	$M_\star$[d] (M$_\odot$)	$N_\star$[e] ($\times10^6$)	h_0[f] (kpc)	z_0[g] (kpc)	$M_{\rm b}$[h] (M$_\odot$)	$N_{\rm b}$[i] ($\times10^3$)	$a_{\rm b}$[j] (kpc)	$M_{\rm gas}$[k] (M$_\odot$)	$N_{\rm gas}$[l] ($\times10^6$)	$h_{\rm gas}$[m] (kpc)	f_g[n]	$V_{\rm flat}$[o] (km s^{-1})
G0	5.1×10^{10}	0.4	14	1.0×10^{9}	0.06	1.1	0.22	1.6×10^{7}	2	0.15	6.1×10^{8}	0.04	3.3	0.38	67
G1	2.0×10^{11}	1.6	12	4.7×10^{9}	0.3	1.5	0.3	2.8×10^{8}	18	0.20	2.0×10^{9}	0.1	4.5	0.29	103
G2	5.1×10^{11}	4.0	9	1.4×10^{10}	0.9	1.9	0.38	1.6×10^{9}	100	0.26	4.6×10^{9}	0.3	5.7	0.76	139
G3	1.2×10^{12}	8.8	6	4.1×10^{10}	2.6	2.8	0.56	8.7×10^{9}	550	0.37	1.2×10^{10}	0.8	8.4	0.23	192
Sbc-	3.6×10^{11}	2.5	8	1.9×10^{10}	1.2	4.0	0.2	5.0×10^{9}	320	0.40	2.6×10^{10}	1.6	12	0.25	155
Sbc	8.1×10^{11}	5.7	8	3.9×10^{10}	2.5	5.5	0.28	1.0×10^{10}	650	0.45.	5.4×10^{10}	3.4	16.5	0.25	195

Note: [a]Halo mass; [b]Number of particles in DM halo; [c]Halo concentration; [d]Stellar mass; [e]Number of stellar particles; [f]Stellar disc scale length; [g]Stellar disc scale height; [h]Bulge mass; [i]Number of bulge particles; [j]Bulge scale length [k]Gas mass; [l]Number of gas particles; [m]Gaseous disc scale length; [n]Gas fraction relative to baryonic mass; [o]Maximum rotation velocity.

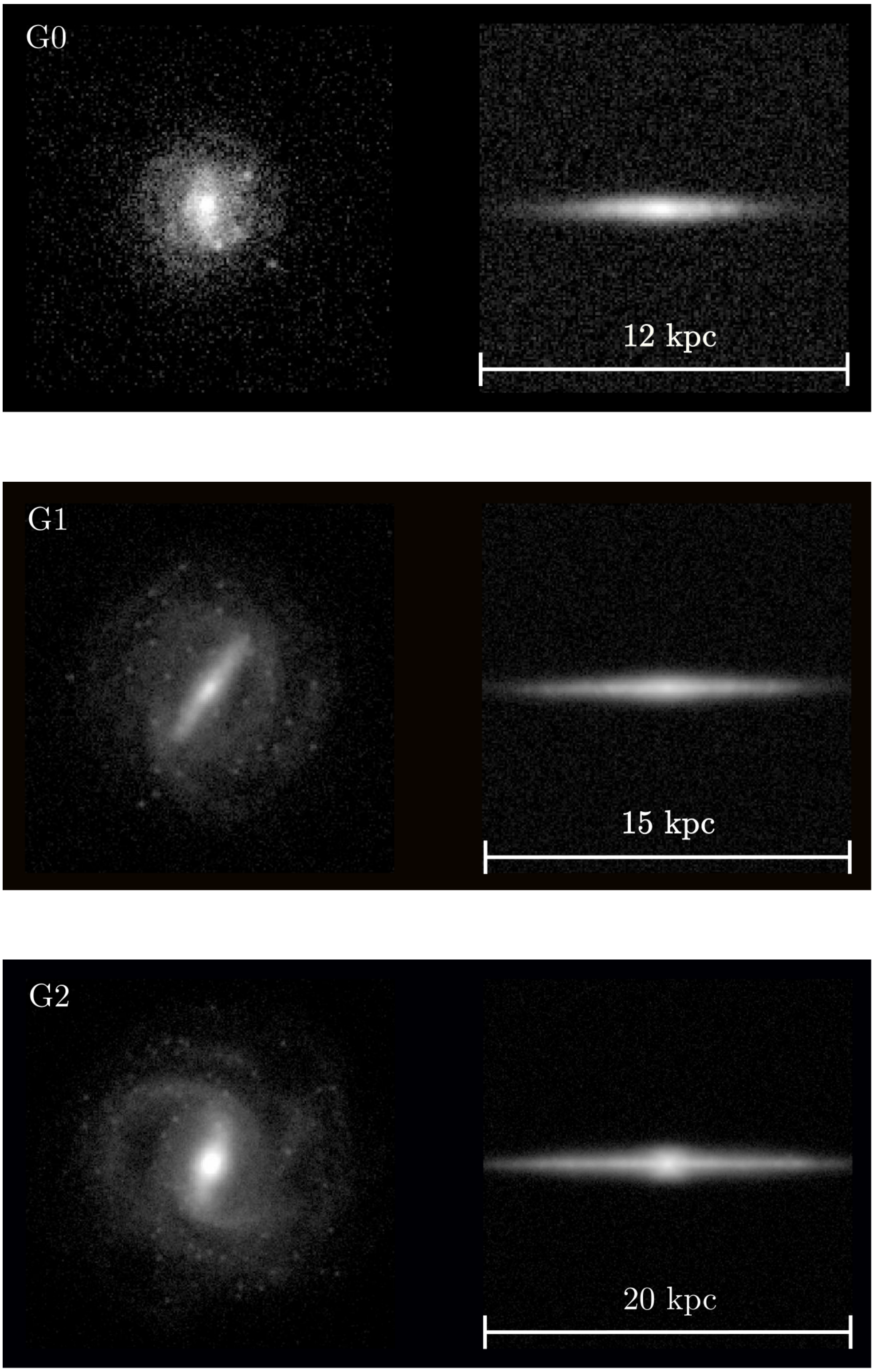

Figure 4.1: Example of the mock images created with SUNRISE for the simulated galaxies. These images correspond to face-on (left) and edge-on (right), for galaxies G0, G1 and G2 of the first simulation run at 3 Gyr. These images mimic the *r* band from SDSS, assuming a distance of 40 Mpc. The spatial scale is indicated for each system.

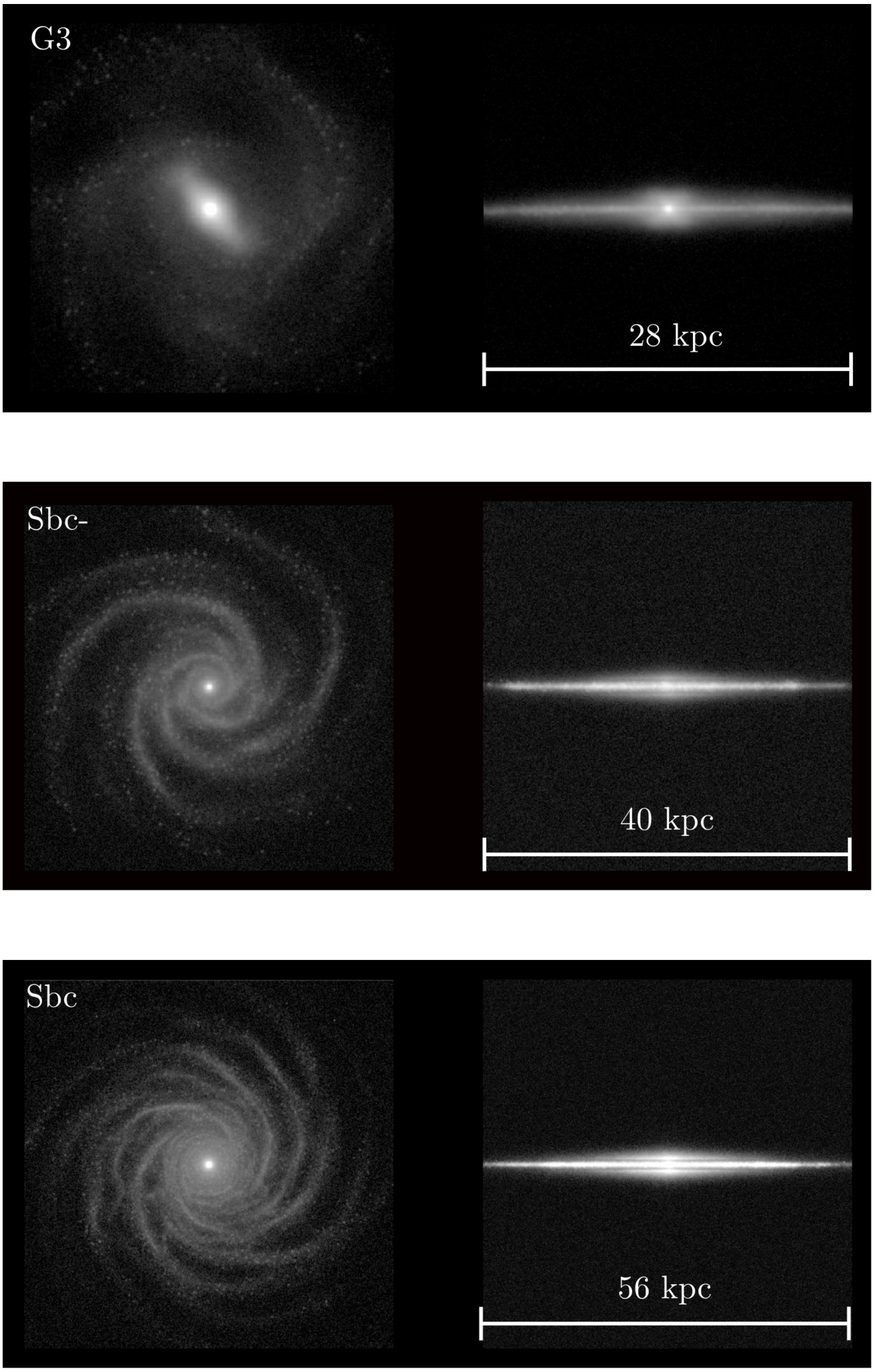

Figure 4.2: Same as Fig 4.1 for galaxies G3, Sbc- and Scb.

4.2.2 Second run

Two differences were introduced in the second run of simulations. First, the galaxies were simulated without bulges, but redistributing the mass in the bulge fo the former simulations into the stellar discs, i.e. preserving the total mass of the stellar component unchanged in order to minimize deviations from the target scaling relations defined by Cox (2004). Second, I increased the resolution of the dark matter halo by using a 25-pc softening length, i.e., the same of the stellar particles, and resorting to particle masses of $2 \sim 5 \times 10^4$ M$_\odot$. Having a high spatial resolution of the halo is very important if the data is intended to be used for cusp-core studies.

The properties of the simulations on this second run principal structural properties of the sample of galaxies employed in this chapter can be found in Table 4.2. Some examples of the SUNRISE mock images are shown in Figs. 4.3 and 4.4. The main simulations were run with the same spatial resolution of the former sample of dwarf galaxies, i.e. approximately at 50$\sim$75 pc, according to the chosen softening length of 25 pc for baryonic end dark matter particles. This high spatial resolution will allow the use of these models and the results obtained from them in further studies of the cusp-core problem beyond the minimum disc limit. For technical reasons G3 was not resimulated, as it requieres a long computation time for the desired resolution and higher demands in storage and post-processing. Additionally, G3 develops a very massive bar and is the system which deviates the most from the simple picture of an underlying axysimmetric disc, being therefore not well-suited for the kind of study developed here.

Table 4.2 - Properties of the models in the second simulation run. Galaxies did not contain bulges, and the spatial resolution of the halo was increased (softening length = 25 pc).

Model	$M_{\rm halo}$[a] (M$_\odot$)	$N_{\rm halo}$[b] ($\times 10^6$)	c[c]	$M_\star$[d] (M$_\odot$)	$N_\star$[e] ($\times 10^6$)	h_0[f] (kpc)	z_0[g] (kpc)	$M_{\rm gas}$[h] (M$_\odot$)	$N_{\rm gas}$[i] ($\times 10^6$)	$h_{\rm gas}$[j] (kpc)	f_g[k]	$V_{\rm flat}$[l] (km s^{-1})
G0	5.1×10^{10}	1.3	14	1.0×10^{9}	0.2	1.1	0.22	6.1×10^{8}	0.1	3.3	0.38	67
G1	2.0×10^{11}	5.0	12	5.0×10^{9}	0.3	1.5	0.3	2.0×10^{9}	0.1	4.5	0.29	103
G2	5.1×10^{11}	12.8	9	1.5×10^{10}	1.0	1.9	0.38	4.6×10^{9}	0.3	5.7	0.76	139
Sbc-	3.6×10^{11}	14.4	8	2.4×10^{10}	1.5	4.0	0.2	2.6×10^{10}	1.6	12	0.25	155
Sbc	8.1×10^{11}	16.2	8	4.9×10^{10}	3.1	5.5	0.28	5.4×10^{10}	3.4	16.5	0.25	195

Note: [a]Halo mass; [b]Number of particles in DM halo; [c]Halo concentration; [d]Stellar mass; [e]Number of stellar particles; [f]Stellar disc scale length; [g]Stellar disc scale height; [h]Gas mass; [i]Number of gas particles; [j]Gaseous disc scale length; [k]Gas fraction relative to baryonic mass; [l]Maximum rotation velocity.

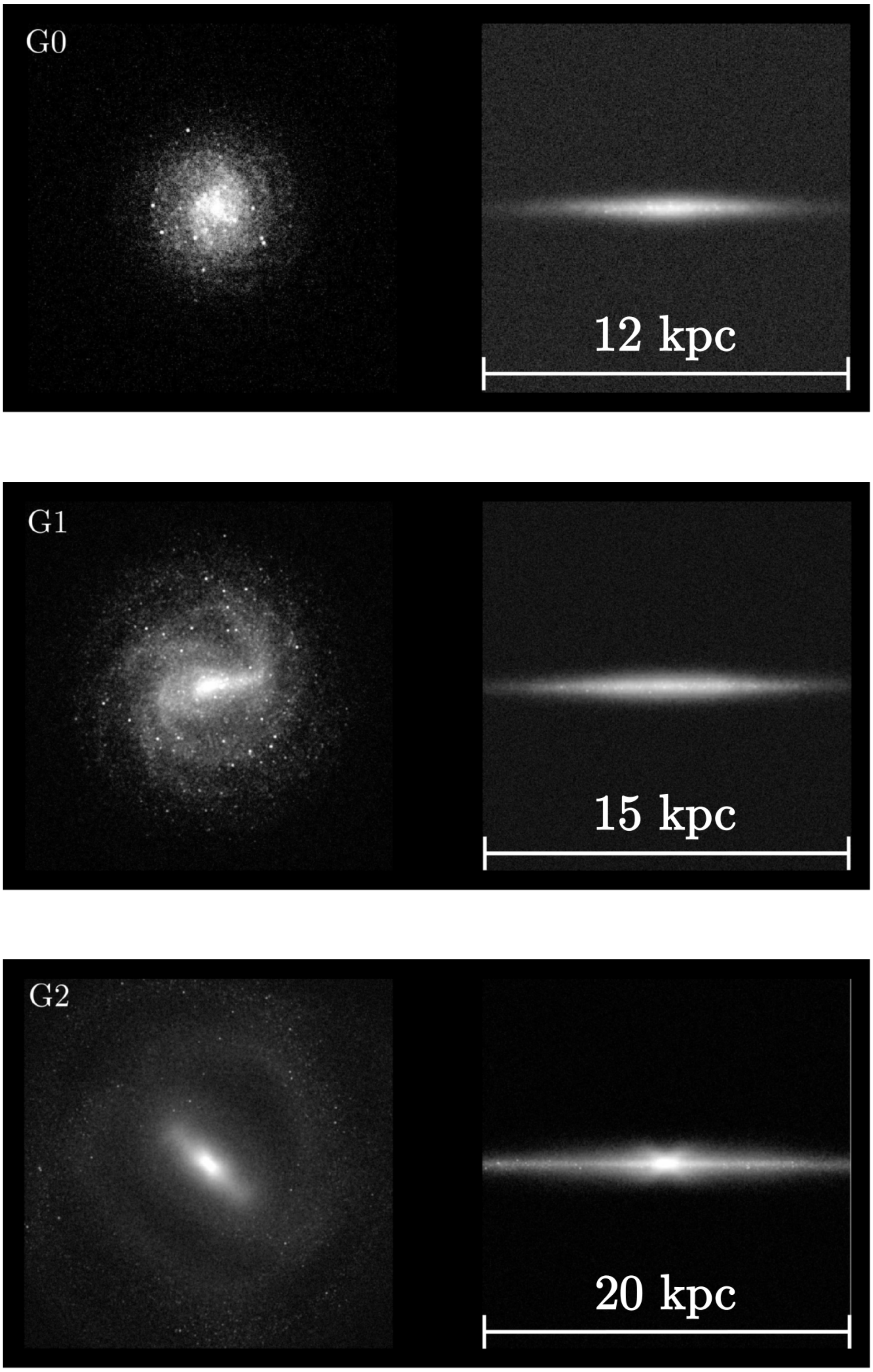

Figure 4.3: Example of the SUNRISE images for the second simulation run. G0, G1, and G2, are shown face-on (left) and edge-on (right), assuming a distance of 10 Mpc, after 3 Gyr of simulation time.

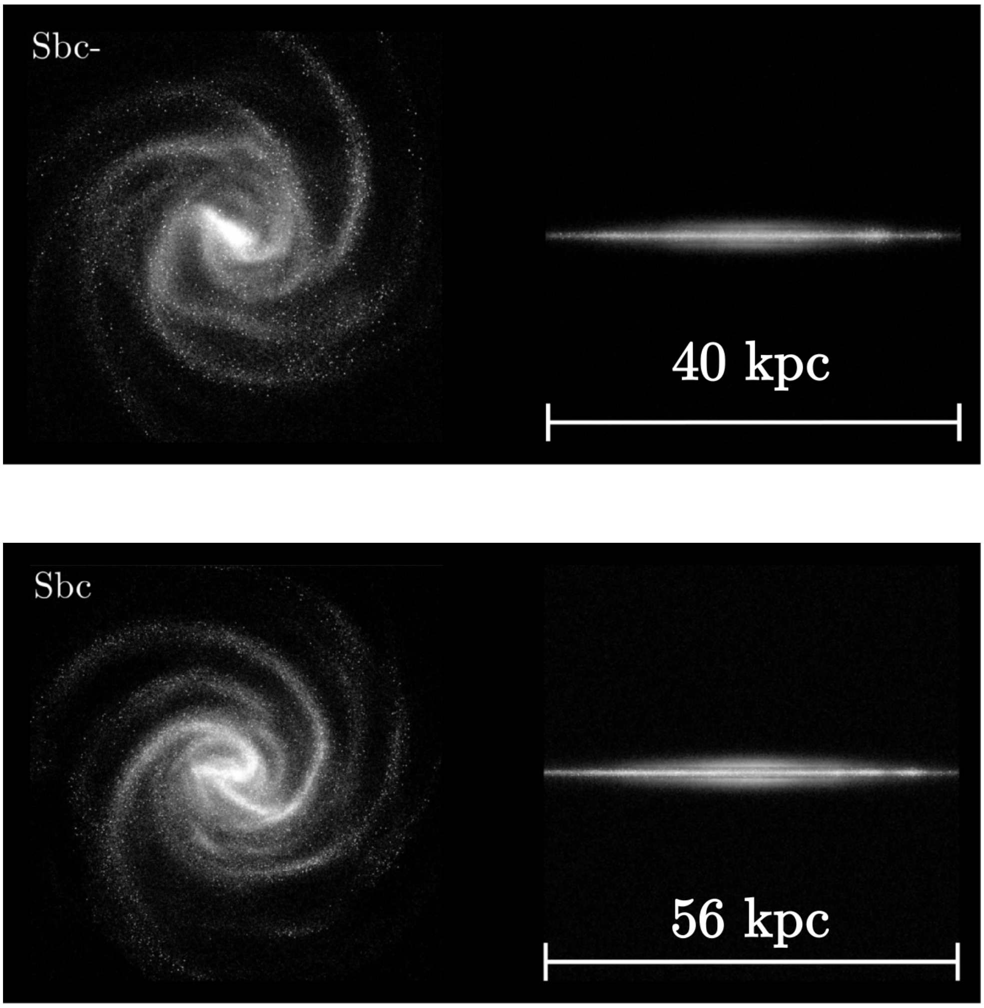

Figure 4.4: Same as Fig. 4.3 for galaxies Sbc- and Sbc.

4.3 *Mock photometry*

I create mock images in the *gri* bands from the Sloan Digital Sky Survey (SDSS) and the 3.6-micrometer band of the SPITZER telescope using SUNRISE . In addition to determine the spatially-resolved spectral energy distribution of the light coming out of the galaxy, SUNRISE may perform the spectral convolution with provided filters to generate idealized images, which then I modify to simulate some relevant instrumental effects, namely: a spatial convolution with a model PSF and the addition of random sky fluctuations. The necessary parameters to model these effects were chosen after the characteristics of a sample of actual SDSS observations. I keep the noise level to a conservative estimation in order to not introduce numerical artifacts or systematic effects. For some experiments, I create, for each combination of galaxy and photometric band, images at different distances and inclinations of the galaxy in the sky, ranging from face-on (0°) to edge-on (90°).

As mentioned in section 2, infrared photometry is preferred over its optical counterpart because the obscuration of stellar light by the interestellar dust is minimal. Recently, the 3.6 μm SPITZER band has become very popular because dust extinction is virtually null, even though a small contamination from the emission of PAHs is still possible. In spite of this fact, the 3.6 μm band is considered nowadays the best proxy to trace the stellar mass, and so, it is commonly used in the recent literature of the cusp-core problem (e.g. de Blok et al., 2008b; Elson et al., 2010; Oh et al., 2011). The K-band from 2MASS is also considered a good choice for similar reasons, but as this band largely overlaps the spectral range covered by the quoted SPITZER band, one shall not expect notable differences between the resulting surface brightness profiles. Therefore I only simulated the 3.6 μm photometry in the infrared.

I imaged the simulated galaxies in the SDSS optical bands for two reasons. In first place, to check whether the use of optical or infrared photometry induces sensible differences in the results. Secondly, because at the time the cusp-core controversy was put forward, the SPITZER telescope did not exist, and the researchers in this field had to rely on results from images in other bands including Sloan, though the most common sources of data were the I and R bands. The red end of the optical espectrum was usually preferred because it traces mainly the old stellar populations, which are the major contributors to the galaxy mass. Together with the lower extinction at longer wavelenghts, these facts derive into a smaller uncertainty in the mass-to-light relations from Bell and de Jong (2001); Bell et al. (2003) for redder bands. Noting that the I/R bands basically overlap the same range of wavelengths as the Sloan *riz*, one is allowed to use the SDSS set of filters expecting only small differences in the inferred stellar density distribution. More than that, I favour the use of SDSS data because this makes this work much more standard and reproducible, given that the instrumental parameters are well characterized and publicly available. This is not the case for the I/R bands in the literature of the cusp-core problem, where the instrumental setup is quite different in each case. Signal-to-noise ratio (SNR) is also not a concern because I will use a lower-limit noise contribution for the Sloan mock observations, as it is described in the following. Yet I imaged only the *gri* bands, dropping the u, z bands which have the lowest SNR. Finally, let me mention that the even though the SDSS photometric system is not the most popular, it has actually been used in some papers in the context of this work (e.g. Kassin et al., 2006).

For the mock images in the SDSS bands I modeled a plate scale of 0.4 arcsec/pixel and a typical psf of ~ 3.2 arcsec at FWHM (modelled as a gaussian). A gaussian noise component representing sky fluctuations was added, with $\sigma = 5$ ADU in the gr bands and $\sigma = 7$ ADU in the i band. These values correspond to a lower limit, as I have directly confirmed from the set of one hundred SDSS images of galaxies used by Barbosa et al. (2015b), against which I expect to make meaningful comparisons in future work. To convert the physical units returned by SUNRISE into ADUs I followed the dr7 SDSS documentation, and I used the average instrumental parameters from the headers of the images in the same reference sample. In Appendix B I provide some examples of the instrumental parameters from the whole SDSS sample of Barbosa et al. (2015b), including those related to noise characteristics and the PSF of each observation. The filter transfer functions were those reported in Doi et al. (2010), which are representative of the survey as a whole. In the case of the SPITZER images I used a plate scale of 1.2 arcsec/pixel, a gaussian noise component with $\sigma = 0.03$ MJy sr^{-1} following Kennicutt et al. (2003), and the filter transfer function and PSF reported in the SPITZER handbook.

4.3.1 models of metallicity and age

To determine the stellar radiation field, SUNRISE attributes to each stellar particle a emerging SED from a stellar population library depending on age and metallicity. These informations are not self-consistently determined from the simulations I presented here because these are not fully cosmological runs; yet the age and metallicity profiles of the simulated galaxies have been already modelled after typical properties of late-type galaxies by Rocha et al. (2008) resulting in very realistic photometric properties (Jonsson et al., 2010), so, I used exactly the same prescription. Basically, a central metallicity and a radial metallicity gradient are put by hand following observational measurements (see Rocha et al., 2008, for details). As for the ages, it is assumed that the stars were formed following an exponential star formation rate from the past to the time of the first snapshot, while it is assumed that all stars in the bulge were born at the same time and exhibit a characteristic age at the beginning of the simulation. Then SUNRISE can pick up an age-metallicity pair for each stellar particle from a probability distribution function determined by the parameters mentioned above. In Fig. 4.5 I present some of the mock images obtained in the different bands for G3 and Sbc- at 2 different inclinations.

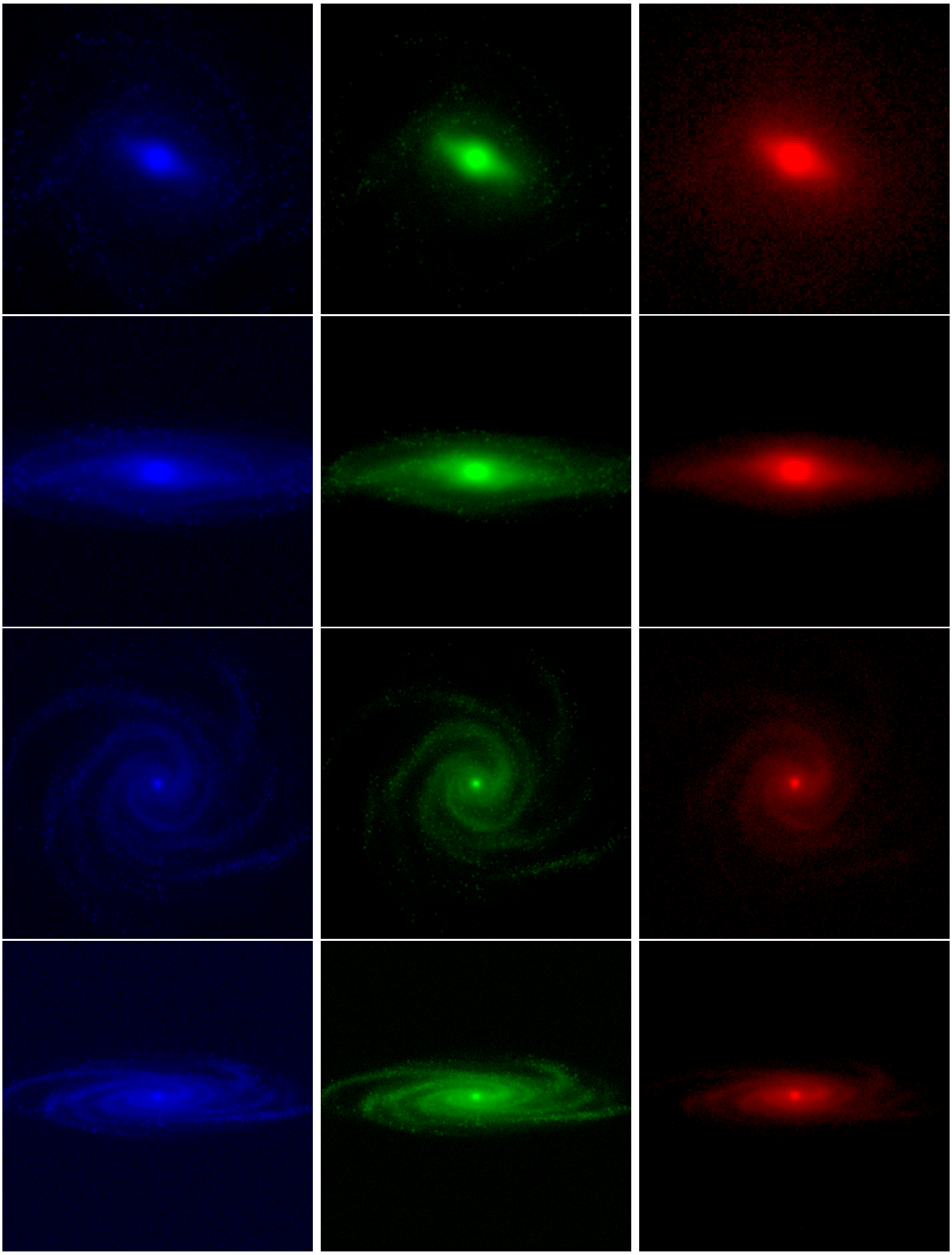

Figure 4.5: Mock SUNRISE images in different bands. First two rows correspond to galaxy Sbcm, face-on and inclined at 75°. Next two rows are the equivalent for G3. I present images in the following bands: g (blue), r (green), and 3.6 μm from Spitzer (red).

4.4 *Photometric analysis with* ELLIPSE

I used the IRAF task ELLIPSE to create Surface Brightness Profiles for each image in the mock catalog. ELLIPSE fits elliptic isophotal contours on an image using a χ^2 minimization technique optimized for this purpose. Each isophotal contour is defined by an intensity value and a set of geometrical parameters, i.e, ellipticity, position angle (P.A), and the coordinates of the center. ELLIPSE is capable to optimize each parameter from ring to ring, or can be also run with fixed values.

As it was mentioned in Sec. 1.4.2.2, it is more meaningful to choose a fixed, constant value of the geometrical parameters of the galaxies rather than letting them vary from radius to radius. I consider that it is the fairest approach from the point of view of rotation curve decompositions, because those methods implicitely assume that a galaxy can be decomposed as a sum of simple geometrical mass components exhibiting axyal symmetry and sharing the same center and orientation. So, the first question I addressed using the mock images is whether the true single values of the geometrical parameters can be recovered from typical photometric analyses based in the fit of elliptical isophotes.

In order to perform elliptical isophotal analyses and to build Surface Brightness Profiles, first it is necessary to determine the center of the images. The most common approaches in the literature are to fix the center to the brigthtest pixel (e.g. Kassin et al., 2006), or to run ELLIPSE with the center as a free parameter, then choosing the mean value to which the inner isophotes are converging to (e.g. Simon et al., 2005). I tried both approaches and compared the results, finding that they tend to the same position inside the errors (i.e., the size of the seeing).

Nevertheless, even though both estimatives agreed well, this does not mean that they are actually showing the central position of the whole gravitational potential, which is the center around which the disk material should rotate. So, I calculated the center of the gravitational potentials in order to compare with the photometric center, and I found that both centers are in good agreement inside the expected resolution of these simulations ($\sim$ 100 pc). In figure (4.6) there is an example of the histogram of errors between the brightest pixel and the real center of the potential. It shows that the typical error is about

2 pixels, i.e, less than 1 arcsec which is really good compared to the PSF. Then I decided to keep the centers fix to their real positions in the subsequent analyses for simplicity.

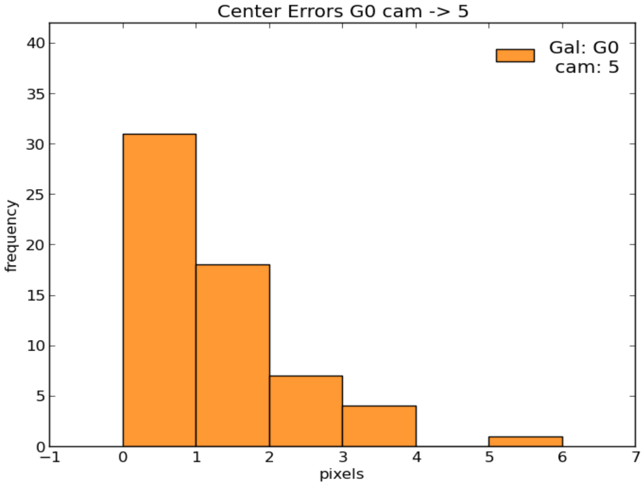

Figure 4.6: Example histogram of the errors commited calculating the center of the galaxies. Here I present the error committed by the "brightest-pixel" method with respect to the true center of the gravitational potential. This is for galaxy Sbcm- of the first simulation run, considering all the snapshots viewed at 75° in the r band.

These results also suggest that miss-centers can be ruled out as a source of problematics in this case. Nevertheless, it is worth remembering that the galaxies simulated here are the best possible case; they are born in dynamical equilibrium and perfect symmetry, without mimicking any perturbation from their formation history or from closeby encounters with other galaxies, and they do not experience any asymmetrical force from the cosmic web. Whether miscenters can still be present in real systems remains as a question to be further explored.

After fixing the center I tried to determine the mean position angle and inclination (ellipticity) of the simulated galaxies using an iterative method similar to that of Simon et al. (2003b). The whole process is done for each image independently. Basically, after fitting the center I run ELLIPSE with the position angle and inclination free to vary as a function of radii. From an inspection of the best position angle adopted for the "outer" isophotes (i.e. those excluding the bulge, reaching the exponentical disc, but extending only over regions with enough SNR), I fix this parameter to its average value. Please note that I only accept a value for these parameter if it converges in the outer isophotes. If it otherwise exhibits a dispersion larger than 15° in individual isophotes, then the galaxy is rejected, in an attempt to keep in the mock sample only those galaxies that probably observers would not exclude from a photometric inspection. An additional run of ELLIPSE is done to try to determine the average inclination of the galactic disc, following exactly the same criteria.

In Fig. 4.7 I show the error in the *photometrically* estimated geometrical parameters with respect to their real values in the simulations, as a function of inclination. Different colors represent different galaxies. For every galaxy and inclination I am plotting the mean value of the error over all the snapshots, with error bars representing the 1-σdispersion over all snapshots. It is apparent in Fig. 4.7 that the automatic algorithm explored in this experiment is able to properly recover the real values of the geometrical parameters, producing errors smaller than 10°, which is normally considered a good estimation in observations. That figure also shows that the error in position angle strongly diminishes at larger inclinations, and that the algorithm often fails for low-inclined galaxies (close to face-on), as it is harder for the fitting routine to converge to a single value of the position angle. It can be seen that for 15° inclinations, the failure rate is extremely high ($\sim 80\%$) Errors in inclination show a systematic trend with inclination itself, reaching an optimum point at 45°. For lower inclinations there is a tendency to overestimate the real value, while the opposite happens for higher inclinations.

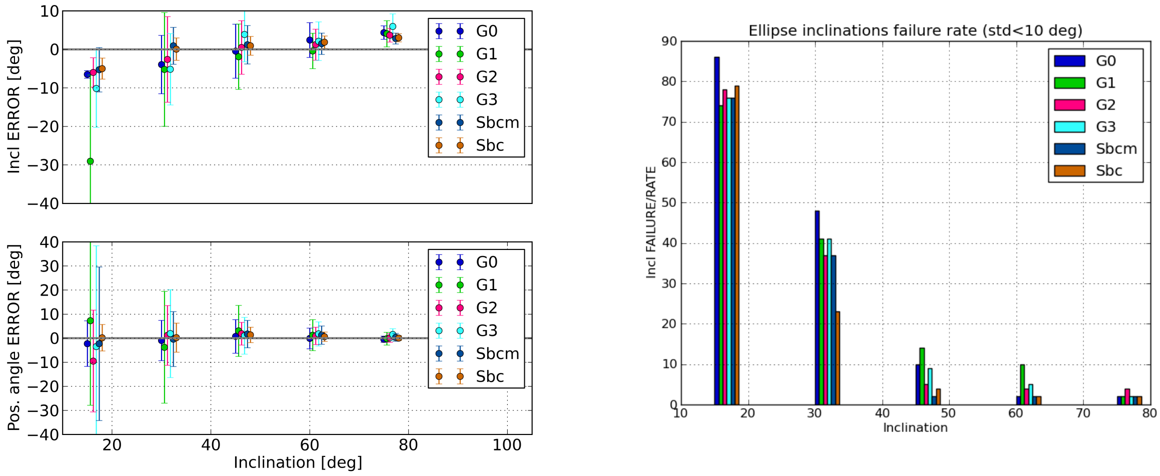

Figure 4.7: Results from the photometric analyses of the mock images using ELLIPSE to try to recover the true position angle and inclination in an iterative automatic way. On the left I show the typical errors commited from the isophotal analysis; the symbols represent the average error and error bars the 1-σ dispersion over all snapshots using the r-band images. On the right I represent the failure rate of the algorithm as a function of galaxy and inclination, i.e., the fraction of images for which the automatic algorithm was not able to converge towards a definite value of P.A or inclination.

4.5 Concluding remark

In this chapter I have presented some early experiments intended to offer a whole new way of testing the ability of typical surface-photometry analyses to accuratly trace the stellar mass distribution in late-type discs.

It was shown that isophotal analysis allows a reasonable determination of the average geometrical parameters in well-behaved discs. In future work it should be tested whether the resulting surface brightness profiles indeed follow the radial profiles of the stellar mass surface density, and whether the mass-to-light ratios from Bell and de Jong (2001) among others are consistent with the models employed by SUNRISE , or what are the possible physical resons for any observed difference.

Those future experiments will be better performed with the second sample of simulated galaxies, which do not exhibit bulges, and furthermore have the necessary spatial resolution in the baryonic and dark matter components as to allow the use of the mock photometric data in cusp-core experiments going beyond the minimum disc approximation.

Chapter 5

Conclusions and perspectives

In this thesis, I have investigated the ability of typical observational methods that try to differentiate cusps from cores in the dark matter distribution of late-type dwarfs and low surface brightness galaxies. For this, a set of specific purpose experiments were designed using up to date numerical simulations of isolated galaxies. In addition to that, mock realistic observations of the photometry and the kinematics of the simulated galaxies were introduced, and a whole framework to perform thorough theoretical analyses of the different dynamical components in the simulations was established, which may be further exploited in future works.

As it has been extensively discussed, there are a large number of potential sources of systematics affectting observational studies, and that is the reason for the necessity of further and improved controlled experiments with simulations. In order to afford a comprehensive study, which allows the disentangling of the numerous possible effects, I started from the scenario that is less affected by systematic errors, i.e. by modelling late-type dwarfs and low surface brightness galaxies in isolation, modelled after idealized axisymmetric discs in pure rotation, without bulges or notorious sub-structures. Strikingly, this study shows that even in such idealized scenario different sources of small errors exist which can modify the intrinsic curvature of a velocity profile, potentially making a whole population of cuspy dark matter haloes appear cored.

Among such errors I found pressure support –due to the injection of thermal and turbulent energy from the stars into the ISM– to be the most important, systematically lowering the inner rotation velocities of the gas component and effectively changing the curvature of the profile, creating the illusion of ubiquitous cores that are very well described by the typical parameters inferred from observations. Surprisingly, the average velocity underestimation responsible for such a dramatic change in the results from rotation curve analyses is just of 4∼5 km s^{-1} in the first kiloparsec. These results suggest that the overall body of evidence for the existence of dark matter cores should be revisited in detail. It is not absolutely clear if the gas phase in the simulations may be over-pressurized in comparison to real galaxies, but the very good agreement between the mock data and real observations should motivate further scientific discussions and a careful revision of several observational results.

Overall, independently of the possible differences between the physical models in the simulations and the real nature of the ISM in dwarf irregulars ans LSBs, the exercise developed through these pages suffices to demonstrate the intrinsic difficulties in properly assessing the effects of pressure support (amongst others effects) and, more than that, it evidences the fragility of rotation curve fitting methods to return faithful information about the presence of cusps or cores in face of very small errors in the central part of galaxies, which may efficiently -and catastrophically- alter the curvature of a rotation curve by inducing errors of a few km s^{-1}.

Thinking of the future scientific work, the methodology established here opens up the possibility of extending these kind of analyses to more generalized models. Testing different codes and different physical implementations of the interestelar medium and the stellar feedback is worthy, as it is going beyond the perfect axisymmetric case. Re-simulating galaxies formed in a cosmological context with high-enough resolution has become feasible in the last few years, and it is a perfect chance to explore more realistic scenarios than the idealized discs in isolation presented here.

Additionally, the preliminary experiments that were carried out with the radiative transfer models delimite a very promising way for testing the potential systematic errors in the determination of stellar mass models based on surface photometry, which may impact several areas of research in astrophysics beyond the cusp-core problem.

Bibliography

Adams J. J., Simon J. D., Fabricius M. H., van den Bosch R. C. E., Barentine J. C., Bender R., Gebhardt K., Hill G. J., Murphy J. D., Swaters R. A., Thomas J., van de Ven G., Dwarf Galaxy Dark Matter Density Profiles Inferred from Stellar and Gas Kinematics, ApJ, 2014, vol. 789, p. 63

Agertz O., Moore B., Stadel J., Potter D., Miniati F., Read J., Mayer L., Gawryszczak A., Kravtsov A., Nordlund Å., Pearce F., Quilis V., Rudd D., Springel V., Stone J., Tasker E., Teyssier R., Wadsley J., Walder R., Fundamental differences between SPH and grid methods, MNRAS, 2007, vol. 380, p. 963

Alpher R. A., Bethe H., Gamow G., The Origin of Chemical Elements, Phys. Rev., 1948, vol. 73, p. 803

Alpher R. A., Herman R. C., On the Relative Abundance of the Elements, Physical Review, 1948, vol. 74, p. 1737

Angulo R. E., Springel V., White S. D. M., Jenkins A., Baugh C. M., Frenk C. S., Scaling relations for galaxy clusters in the Millennium-XXL simulation, MNRAS, 2012, vol. 426, p. 2046

Barbosa C. E., Kinematics and stellar populations of galaxies in the local universe, University of São Paulo, 2016, Ph.D. Thesis

Barbosa C. E., Mendes de Oliveira C., Amram P., Ferrari F., Russeil D., Epinat B., Perret V., Adami C., Marcelin M., GHASP: an Hα kinematic survey of spiral galaxies - X. Surface photometry, decompositions and the Tully-Fisher relation in the R$_c$ band, MNRAS, 2015a, vol. 453, p. 2965

Barbosa C. E., Mendes de Oliveira C., Amram P., Ferrari F., Russeil D., Epinat B., Perret V., Adami C., Marcelin M., GHASP: an Hα kinematic survey of spiral galaxies - X. Surface photometry, decompositions and the Tully-Fisher relation in the R_c band, MNRAS, 2015b, vol. 453, p. 2965

Barnes E. I., Sellwood J. A., Kosowsky A., Mass Models for Spiral Galaxies from Two-dimensional Velocity Maps, AJ, 2004, vol. 128, p. 2724

Begum A., Chengalur J. N., Karachentsev I. D., Sharina M. E., Kaisin S. S., FIGGS: Faint Irregular Galaxies GMRT Survey - overview, observations and first results, MNRAS, 2008, vol. 386, p. 1667

Bell E. F., de Jong R. S., Stellar Mass-to-Light Ratios and the Tully-Fisher Relation, ApJ, 2001, vol. 550, p. 212

Bell E. F., McIntosh D. H., Katz N., Weinberg M. D., A First Estimate of the Baryonic Mass Function of Galaxies, ApJ, 2003, vol. 585, p. L117

Berghöfer T. W., Bowyer S., Lieu R., Knude J., The Thermal Pressure of the Hot Interstellar Medium Derived from Cloud Shadows in the Extreme Ultraviolet, ApJ, 1998, vol. 500, p. 838

Bershady M. A., Verheijen M. A. W., Swaters R. A., Andersen D. R., Westfall K. B., Martinsson T., The DiskMass Survey. I. Overview, ApJ, 2010, vol. 716, p. 198

Betoule M., Kessler R., Guy J., Mosher J., Hardin D., Bet al. Improved cosmological constraints from a joint analysis of the SDSS-II and SNLS supernova samples, A&A, 2014, vol. 568, p. A22

Binney J., Tremaine S., Galactic dynamics, 1987

Binney J., Tremaine S., Galactic Dynamics: Second Edition. Princeton University Press, 2008

Blais-Ouellette S., Amram P., Carignan C., Accurate Determination of the Mass Distribution in Spiral Galaxies. II. Testing the Shape of Dark Halos, AJ, 2001, vol. 121, p. 1952

Blais-Ouellette S., Carignan C., Amram P., Côté S., Accurate Parameters of the Mass Distribution in Spiral Galaxies. I. Fabry-Perot Observations of NGC 5585, AJ, 1999, vol. 118, p. 2123

Blake C., Davis T., Poole G. B., Parkinson D., et al. The WiggleZ Dark Energy Survey: testing the cosmological model with baryon acoustic oscillations at z= 0.6, MNRAS, 2011, vol. 415, p. 2892

Bolatto A. D., Simon J. D., Leroy A., Blitz L., The Density Profile of the Dark Matter Halo of NGC 4605, ApJ, 2002, vol. 565, p. 238

Bouché N., Carfantan H., Schroetter I., Michel-Dansac L., Contini T., GalPak^{3D}: A Bayesian Parametric Tool for Extracting Morphokinematics of Galaxies from 3D Data, AJ, 2015, vol. 150, p. 92

Boulares A., Cox D. P., Galactic hydrostatic equilibrium with magnetic tension and cosmic-ray diffusion, ApJ, 1990, vol. 365, p. 544

Bowyer S., Lieu R., Sidher S. D., Lampton M., Knude J., Evidence for a large thermal pressure imbalance in the local interstellar medium, Nature, 1995, vol. 375, p. 212

Boylan-Kolchin M., Springel V., White S. D. M., Jenkins A., Lemson G., Resolving cosmic structure formation with the Millennium-II Simulation, MNRAS, 2009, vol. 398, p. 1150

Bradač B. Bullet Cluster Collaboration Shedding Light on Dark Matter:. Seeing the Invisible with the Bullet Cluster 1E0657-56. In Dark Matter in Astroparticle and Particle Physics , 2008, p. 254

Broeils A. H., van Woerden H., A search for spiral galaxies with extended HI disks., A&AS, 1994, vol. 107, p. 129

Carignan C., Freeman K. C., Basic parameters of dark halos in late-type spirals, ApJ, 1985a, vol. 294, p. 494

Carignan C., Freeman K. C., Basic parameters of dark halos in late-type spirals, ApJ, 1985b, vol. 294, p. 494

Ceverino D., Klypin A., The Role of Stellar Feedback in the Formation of Galaxies, ApJ, 2009, vol. 695, p. 292

Chabrier G., Galactic Stellar and Substellar Initial Mass Function, PASP, 2003, vol. 115, p. 763

Chan T. K., Kereš D., Oñorbe J., Hopkins P. F., Muratov A. L., Faucher-Giguère C.-A., Quataert E., The impact of baryonic physics on the structure of dark matter haloes: the view from the FIRE cosmological simulations, MNRAS, 2015, vol. 454, p. 2981

Chemin L., Huré J.-M., Soubiran C., Zibetti S., Charlot S., Kawata D., Asymmetric mass models of disk galaxies. I. Messier 99, A&A, 2016, vol. 588, p. A48

Cinzano P., Rix H.-W., Sarzi M., Corsini E. M., Zeilinger W. W., Bertola F., The kinematics and the origin of the ionized gas in NGC 4036, MNRAS, 1999, vol. 307, p. 433

Conroy C., Gunn J. E., The Propagation of Uncertainties in Stellar Population Synthesis Modeling. III. Model Calibration, Comparison, and Evaluation, ApJ, 2010, vol. 712, p. 833

Côté S., Carignan C., Freeman K. C., The Various Kinematics of Dwarf Irregular Galaxies in Nearby Groups and Their Dark Matter Distributions, AJ, 2000, vol. 120, p. 3027

Cox D. P., The Three-Phase Interstellar Medium Revisited, ARA&A, 2005, vol. 43, p. 337

Cox T. J., Star formation and feedback in simulations of interacting galaxies, University of California, nta Cruz, California, USA, 2004, Ph.D. Thesis

Cox T. J., Jonsson P., Primack J. R., Somerville R. S., Feedback in simulations of disc-galaxy major mergers, MNRAS, 2006, vol. 373, p. 1013

Dalcanton J. J., Stilp A. M., Pressure Support in Galaxy Disks: Impact on Rotation Curves and Dark Matter Density Profiles, ApJ, 2010, vol. 721, p. 547

Davis M., Efstathiou G., Frenk C. S., White S. D. M., The evolution of large-scale structure in a universe dominated by cold dark matter, ApJ, 1985, vol. 292, p. 371

de Blok W. J. G., The Core-Cusp Problem, Advances in Astronomy, 2010, vol. 2010, p. 5

de Blok W. J. G., Bosma A., High-resolution rotation curves of low surface brightness galaxies, A&A, 2002, vol. 385, p. 816

de Blok W. J. G., Bosma A., McGaugh S., Simulating observations of dark matter dominated galaxies: towards the optimal halo profile, MNRAS, 2003, vol. 340, p. 657

de Blok W. J. G., McGaugh S. S., The dark and visible matter content of low surface brightness disc galaxies, MNRAS, 1997, vol. 290, p. 533

de Blok W. J. G., McGaugh S. S., Bosma A., Rubin V. C., Mass Density Profiles of Low Surface Brightness Galaxies, ApJ, 2001, vol. 552, p. L23

de Blok W. J. G., McGaugh S. S., Rubin V. C., High-Resolution Rotation Curves of Low Surface Brightness Galaxies. II. Mass Models, AJ, 2001, vol. 122, p. 2396

de Blok W. J. G., McGaugh S. S., van der Hulst J. M., HI observations of low surface brightness galaxies: probing low-density galaxies, MNRAS, 1996, vol. 283, p. 18

de Blok W. J. G., van der Hulst J. M., Bothun G. D., Surface photometry of low surface brightness galaxies, MNRAS, 1995, vol. 274, p. 235

de Blok W. J. G., Walter F., Brinks E., Trachternach C., Oh S.-H., Kennicutt Jr. R. C., High-Resolution Rotation Curves and Galaxy Mass Models from THINGS, AJ, 2008a, vol. 136, p. 2648

de Blok W. J. G., Walter F., Brinks E., Trachternach C., Oh S.-H., Kennicutt Jr. R. C., High-Resolution Rotation Curves and Galaxy Mass Models from THINGS, AJ, 2008b, vol. 136, p. 2648

de Jong R. S., Bell E. F., Comparing Dynamical and Stellar Population Mass-To-Light Ratio Estimates, Astrophysics and Space Science Proceedings, 2007, vol. 3, p. 107

Di Teodoro E. M., Fraternali F., ^{3D} BAROLO: a new 3D algorithm to derive rotation curves of galaxies, MNRAS, 2015, vol. 451, p. 3021

Diemand J., Zemp M., Moore B., Stadel J., Carollo C. M., Cusps in cold dark matter haloes, MNRAS, 2005, vol. 364, p. 665

Doi M., Tanaka M., Fukugita M., Gunn J. E., Yasuda N., Ivezić Ž., Brinkmann J., de Haars E., Kleinman S. J., Krzesinski J., French Leger R., Photometric Response Functions of the Sloan Digital Sky Survey Imager, AJ, 2010, vol. 139, p. 1628

Dopita M. A., Groves B. A., Fischera J., Sutherland R. S., Tuffs R. J., Popescu C. C., Kewley L. J., Reuland M., Leitherer C., Modeling the Pan-Spectral Energy Distribution of Starburst Galaxies. I. The Role of ISM Pressure and the Molecular Cloud Dissipation Timescale, ApJ, 2005, vol. 619, p. 755

Draine B. T., Li A., Infrared Emission from Interstellar Dust. IV. The Silicate-Graphite-PAH Model in the Post-Spitzer Era, ApJ, 2007, vol. 657, p. 810

Du W., Wu H., Lam M. I., Zhu Y., Lei F., Zhou Z., Low Surface Brightness Galaxies Selected from the 40% Sky Area of the ALFALFA H I Survey. I. Sample and Statistical Properties, AJ, 2015, vol. 149, p. 199

Dutton A. A., Courteau S., de Jong R., Carignan C., Mass Modeling of Disk Galaxies: Degeneracies, Constraints, and Adiabatic Contraction, ApJ, 2005, vol. 619, p. 218

Edvardsson B., Andersen J., Gustafsson B., Lambert D. L., Nissen P. E., Tomkin J., The Chemical Evolution of the Galactic Disk - Part One - Analysis and Results, A&A, 1993, vol. 275, p. 101

Elmegreen B. G., Scalo J., Interstellar Turbulence I: Observations and Processes, ARA&A, 2004, vol. 42, p. 211

Elson E. C., de Blok W. J. G., Kraan-Korteweg R. C., The dark matter content of the blue compact dwarf NGC 2915, MNRAS, 2010, vol. 404, p. 2061

Epinat B., Amram P., Balkowski C., Marcelin M., Evidence for strong dynamical evolution in disc galaxies through the last 11 Gyr. GHASP VIII - a local reference sample of rotating disc galaxies for high-redshift studies, MNRAS, 2010, vol. 401, p. 2113

Epinat B., Amram P., Marcelin M., GHASP: an Hα kinematic survey of 203 spiral and irregular galaxies - VII. Revisiting the analysis of Hα data cubes for 97 galaxies, MNRAS, 2008, vol. 390, p. 466

Epinat B., Amram P., Marcelin M., Balkowski C., Daigle O., Hernandez O., Chemin L., Carignan C., Gach J.-L., Balard P., GHASP: an Hα kinematic survey of spiral and irregular galaxies - VI. New Hα data cubes for 108 galaxies, MNRAS, 2008, vol. 388, p. 500

Fathi K., Beckman J. E., Zurita A., Relaño M., Knapen J. H., Daigle O., Hernandez O., Carignan C., Evolution of structure in late-type spiral galaxies. I. Ionized gas kinematics in NGC 628, A&A, 2007, vol. 466, p. 905

Ferreras I., Sakellariadou M., Yusaf M. F., Necessity of Dark Matter in Modified Newtonian Dynamics within Galactic Scales, Physical Review Letters, 2008, vol. 100, p. 031302

Ferrière K. M., The interstellar environment of our galaxy, Reviews of Modern Physics, 2001, vol. 73, p. 1031

Field G. B., Goldsmith D. W., Habing H. J., Cosmic-Ray Heating of the Interstellar Gas, ApJ, 1969, vol. 155, p. L149

Flores R. A., Primack J. R., Observational and theoretical constraints on singular dark matter halos, ApJ, 1994, vol. 427, p. L1

Garrido O., Marcelin M., Amram P., Boulesteix J., GHASP: An Hα kinematic survey of spiral and irregular galaxies. I. Velocity fields and rotation curves of 23 galaxies, A&A, 2002, vol. 387, p. 821

Garrison-Kimmel S., Rocha M., Boylan-Kolchin M., Bullock J. S., Lally J., Can feedback solve the too-big-to-fail problem?, MNRAS, 2013, vol. 433, p. 3539

Gelato S., Sommer-Larsen J., On DDO 154 and cold dark matter halo profiles, MNRAS, 1999, vol. 303, p. 321

Gentile G., Salucci P., Klein U., Vergani D., Kalberla P., The cored distribution of dark matter in spiral galaxies, MNRAS, 2004, vol. 351, p. 903

Gnedin O. Y., Zhao H., Maximum feedback and dark matter profiles of dwarf galaxies, MNRAS, 2002, vol. 333, p. 299

Governato F., Brook C., Mayer L., Brooks A., Rhee G., Wadsley J., Jonsson P., Willman B., Stinson G., Quinn T., Madau P., Bulgeless dwarf galaxies and dark matter cores from supernova-driven outflows, Nature, 2010a, vol. 463, p. 203

Governato F., Brook C., Mayer L., Brooks A., Rhee G., Wadsley J., Jonsson P., Willman B., Stinson G., Quinn T., Madau P., Bulgeless dwarf galaxies and dark matter cores from supernova-driven outflows, Nature, 2010b, vol. 463, p. 203

Governato F., Zolotov A., Pontzen A., Christensen C., Oh S. H., Brooks A. M., Quinn T., Shen S., Wadsley J., Cuspy no more: how outflows affect the central dark matter and baryon distribution in Λ cold dark matter galaxies, MNRAS, 2012, vol. 422, p. 1231

Groves B., Dopita M. A., Sutherland R. S., Kewley L. J., Fischera J., Leitherer C., Brandl B., van Breugel W., Modeling the Pan-Spectral Energy Distribution of Starburst Galaxies. IV. The Controlling Parameters of the Starburst SED, ApJS, 2008, vol. 176, p. 438

Groves B. A., Dopita M. A., Sutherland R. S., Dusty, Radiation Pressure-Dominated Photoionization. I. Model Description, Structure, and Grids, ApJS, 2004, vol. 153, p. 9

Guo Q., White S., Li C., Boylan-Kolchin M., How do galaxies populate dark matter haloes?, MNRAS, 2010, vol. 404, p. 1111

Guth A. H., Inflationary universe: A possible solution to the horizon and flatness problems, Phys. Rev. D, 1981, vol. 23, p. 347

Hayashi E., Navarro J. F., Springel V., The shape of the gravitational potential in cold dark matter haloes, MNRAS, 2007, vol. 377, p. 50

Hayward C. C., Torrey P., Springel V., Hernquist L., Vogelsberger M., Galaxy mergers on a moving mesh: a comparison with smoothed particle hydrodynamics, MNRAS, 2014, vol. 442, p. 1992

Hopkins P. F., Kereš D., Oñorbe J., Faucher-Giguère C.-A., Quataert E., Murray N., Bullock J. S., Galaxies on FIRE (Feedback In Realistic Environments): stellar feedback explains cosmologically inefficient star formation, MNRAS, 2014, vol. 445, p. 581

Hubble E., A Relation between Distance and Radial Velocity among Extra-Galactic Nebulae, Proceedings of the National Academy of Science, 1929, vol. 15, p. 168

Hunter D. A., Ficut-Vicas D., Ashley T., Brinks E., Cigan P., Elmegreen B. G., Heesen V., Herrmann K. A., Johnson M., Oh S.-H., Rupen M. P., Schruba A., Simpson C. E., Walter F., Westpfahl D. J., Young L. M., Zhang H.-X., Little Things, AJ, 2012, vol. 144, p. 134

Impey C., Bothun G., Low Surface Brightness Galaxies, ARA&A, 1997, vol. 35, p. 267

Jedrzejewski R. I., CCD surface photometry of elliptical galaxies. I - Observations, reduction and results, MNRAS, 1987, vol. 226, p. 747

Jonsson P., Cox T. J., Primack J. R., Somerville R. S., Simulations of Dust in Interacting Galaxies. I. Dust Attenuation, ApJ, 2006, vol. 637, p. 255

Jonsson P., Groves B. A., Cox T. J., High-resolution panchromatic spectral models of galaxies including photoionization and dust, MNRAS, 2010, vol. 403, p. 17

Kamphuis P., Józsa G. I. G., Oh S.-. H., Spekkens K., Urbancic N., Serra P., Koribalski B. S., Dettmar R.-J., Automated kinematic modelling of warped galaxy discs in large H I surveys: 3D tilted-ring fitting of H I emission cubes, MNRAS, 2015, vol. 452, p. 3139

Kassin S. A., de Jong R. S., Pogge R. W., Dark and Baryonic Matter in Bright Spiral Galaxies. I. Near-Infrared and Optical Broadband Surface Photometry of 30 Galaxies, ApJS, 2006, vol. 162, p. 80

Kassin S. A., de Jong R. S., Weiner B. J., Dark and Baryonic Matter in Bright Spiral Galaxies. II. Radial Distributions for 34 Galaxies, ApJ, 2006, vol. 643, p. 804

Kazantzidis S., Abadi M. G., Navarro J. F., The Sphericalization of Dark Matter Halos by Galaxy Disks, ApJ, 2010, vol. 720, p. L62

Kennicutt Jr. R. C., Armus L., Bendo G., Calzetti D., Dale D. A., Draine B. T., Engelbracht C. W., Gordon K. D., Grauer A. D., Helou G., Hollenbach D. J., SINGS: The SIRTF Nearby Galaxies Survey, PASP, 2003, vol. 115, p. 928

Klypin A., Kravtsov A. V., Bullock J. S., Primack J. R., Resolving the Structure of Cold Dark Matter Halos, ApJ, 2001, vol. 554, p. 903

Klypin A., Yepes G., Gottlober S., Prada F., Hess S., MultiDark simulations: the story of dark matter halo concentrations and density profiles, ArXiv e-prints, 2014

Komatsu E., Smith K. M., Dunkley J., Bennett Seven-year Wilkinson Microwave Anisotropy Probe (WMAP) Observations: Cosmological Interpretation, ApJS, 2011, vol. 192, p. 18

Kormendy J., Freeman K. C., Scaling Laws for Dark Matter Halos in Late-type and Dwarf Spheroidal Galaxies, ApJ, 2016, vol. 817, p. 84

Krajnović D., Cappellari M., de Zeeuw P. T., Copin Y., Kinemetry: a generalization of photometry to the higher moments of the line-of-sight velocity distribution, MNRAS, 2006, vol. 366, p. 787

Kuzio de Naray R., Kaufmann T., Recovering cores and cusps in dark matter haloes using mock velocity field observations, MNRAS, 2011, vol. 414, p. 3617

Kuzio de Naray R., McGaugh S. S., de Blok W. J. G., Mass Models for Low Surface Brightness Galaxies with High-Resolution Optical Velocity Fields, ApJ, 2008a, vol. 676, p. 920

Kuzio de Naray R., McGaugh S. S., de Blok W. J. G., Mass Models for Low Surface Brightness Galaxies with High-Resolution Optical Velocity Fields, ApJ, 2008b, vol. 676, p. 920

Kuzio de Naray R., McGaugh S. S., de Blok W. J. G., Bosma A., High-Resolution Optical Velocity Fields of 11 Low Surface Brightness Galaxies, ApJS, 2006, vol. 165, p. 461

Kuzio de Naray R., McGaugh S. S., Mihos J. C., Constraining the NFW Potential with Observations and Modeling of Low Surface Brightness Galaxy Velocity Fields, ApJ, 2009a, vol. 692, p. 1321

Kuzio de Naray R., McGaugh S. S., Mihos J. C., Constraining the NFW Potential with Observations and Modeling of Low Surface Brightness Galaxy Velocity Fields, ApJ, 2009b, vol. 692, p. 1321

Lia C., Carraro G., Salucci P., The dark and luminous matter coupling in the formation of spheroids: a SPH investigation, A&A, 2000, vol. 360, p. 76

Lotz J. M., Jonsson P., Cox T. J., Primack J. R., Galaxy merger morphologies and time-scales from simulations of equal-mass gas-rich disc mergers, MNRAS, 2008, vol. 391, p. 1137

Ludlow A. D., Navarro J. F., Angulo R. E., Boylan-Kolchin M., Springel V., Frenk C., White S. D. M., The mass-concentration-redshift relation of cold dark matter haloes, MNRAS, 2014, vol. 441, p. 378

Mac Low M.-M., Klessen R. S., Control of star formation by supersonic turbulence, Reviews of Modern Physics, 2004, vol. 76, p. 125

Madau P., Shen S., Governato F., Dark Matter Heating and Early Core Formation in Dwarf Galaxies, ApJ, 2014, vol. 789, p. L17

Maraston C., Strömbäck G., Stellar population models at high spectral resolution, MNRAS, 2011, vol. 418, p. 2785

Marchesini D., D'Onghia E., Chincarini G., Firmani C., Conconi P., Molinari E., Zacchei A., Hα Rotation Curves: The Soft Core Question, ApJ, 2002, vol. 575, p. 801

Marinacci F., Pakmor R., Springel V., The formation of disc galaxies in high-resolution moving-mesh cosmological simulations, MNRAS, 2014, vol. 437, p. 1750

Martinsson T. P. K., Verheijen M. A. W., Westfall K. B., Bershady M. A., Andersen D. R., Swaters R. A., The DiskMass Survey. VII. The distribution of luminous and dark matter in spiral galaxies, A&A, 2013, vol. 557, p. A131

Mashchenko S., Wadsley J., Couchman H. M. P., Stellar Feedback in Dwarf Galaxy Formation, Science, 2008, vol. 319, p. 174

Mathewson D. S., Ford V. L., Buchhorn M., A southern sky survey of the peculiar velocities of 1355 spiral galaxies, ApJS, 1992, vol. 81, p. 413

McGaugh S. S., Oxygen abundances in low surface brightness disk galaxies, ApJ, 1994, vol. 426, p. 135

McGaugh S. S., Bothun G. D., Structural characteristics and stellar composition of low surface brightness disk galaxies, AJ, 1994, vol. 107, p. 530

McGaugh S. S., de Blok W. J. G., Schombert J. M., Kuzio de Naray R., Kim J. H., The Rotation Velocity Attributable to Dark Matter at Intermediate Radii in Disk Galaxies, ApJ, 2007, vol. 659, p. 149

McGaugh S. S., Schombert J. M., Color-Mass-to-light-ratio Relations for Disk Galaxies, AJ, 2014, vol. 148, p. 77

McKee C. F., Ostriker J. P., A theory of the interstellar medium - Three components regulated by supernova explosions in an inhomogeneous substrate, ApJ, 1977, vol. 218, p. 148

Meidt S. E., Schinnerer E., van de Ven G., Zaritsky D., Peletier R., Knapen J. H., Sheth K., Regan M., Querejeta M., Muñoz-Mateos J.-C., Mizusawa T., Reconstructing the Stellar Mass Distributions of Galaxies Using S^4G IRAC 3.6 and 4.5 μm Images. II. The Conversion from Light to Mass, ApJ, 2014, vol. 788, p. 144

Milgrom M., A modification of the Newtonian dynamics as a possible alternative to the hidden mass hypothesis, ApJ, 1983, vol. 270, p. 365

Moore B., Evidence against dissipation-less dark matter from observations of galaxy haloes, Nature, 1994, vol. 370, p. 629

Moore B., Quinn T., Governato F., Stadel J., Lake G., Cold collapse and the core catastrophe, MNRAS, 1999, vol. 310, p. 1147

Navarro J. F., Eke V. R., Frenk C. S., The cores of dwarf galaxy haloes, MNRAS, 1996a, vol. 283, p. L72

Navarro J. F., Eke V. R., Frenk C. S., The cores of dwarf galaxy haloes, MNRAS, 1996b, vol. 283, p. L72

Navarro J. F., Frenk C. S., White S. D. M., The Structure of Cold Dark Matter Halos, ApJ, 1996a, vol. 462, p. 563

Navarro J. F., Frenk C. S., White S. D. M., The Structure of Cold Dark Matter Halos, ApJ, 1996b, vol. 462, p. 563

Navarro J. F., Frenk C. S., White S. D. M., A Universal Density Profile from Hierarchical Clustering, ApJ, 1997, vol. 490, p. 493

Navarro J. F., Hayashi E., Power C., Jenkins A. R., Frenk C. S., White S. D. M., Springel V., Stadel J., Quinn T. R., The inner structure of ΛCDM haloes - III. Universality and asymptotic slopes, MNRAS, 2004, vol. 349, p. 1039

Noll S., Burgarella D., Giovannoli E., Buat V., Marcillac D., Muñoz-Mateos J. C., Analysis of galaxy spectral energy distributions from far-UV to far-IR with CIGALE: studying a SINGS test sample, A&A, 2009, vol. 507, p. 1793

Oñorbe J., Boylan-Kolchin M., Bullock J. S., Hopkins P. F., Kerĕs D., Faucher-Giguère C.-A., Quataert E., Murray N., Forged in FIRE: cusps, cores, and baryons in low-mass dwarf galaxies, ArXiv e-prints, 2015

Oh S.-H., Brook C., Governato F., Brinks E., Mayer L., de Blok W. J. G., Brooks A., Walter F., The Central Slope of Dark Matter Cores in Dwarf Galaxies: Simulations versus THINGS, AJ, 2011, vol. 142, p. 24

Oh S.-H., de Blok W. J. G., Brinks E., Walter F., Kennicutt Jr. R. C., Dark and Luminous Matter in THINGS Dwarf Galaxies, AJ, 2011a, vol. 141, p. 193

Oh S.-H., de Blok W. J. G., Brinks E., Walter F., Kennicutt Jr. R. C., Dark and Luminous Matter in THINGS Dwarf Galaxies, AJ, 2011b, vol. 141, p. 193

Oh S.-H., de Blok W. J. G., Walter F., Brinks E., Kennicutt Jr. R. C., High-Resolution Dark Matter Density Profiles of THINGS Dwarf Galaxies: Correcting for Noncircular Motions, AJ, 2008a, vol. 136, p. 2761

Oh S.-H., de Blok W. J. G., Walter F., Brinks E., Kennicutt Jr. R. C., High-Resolution Dark Matter Density Profiles of THINGS Dwarf Galaxies: Correcting for Noncircular Motions, AJ, 2008b, vol. 136, p. 2761

Oh S.-H., Hunter D. A., Brinks E., Elmegreen B. G., Schruba A., Walter F., Rupen M. P., Young L. M., Simpson C. E., Johnson M. C., Herrmann K. A., Ficut-Vicas D., Cigan P., Heesen V., Ashley T., Zhang H.-X., High-resolution Mass Models of Dwarf Galaxies from LITTLE THINGS, AJ, 2015, vol. 149, p. 180

Oman K. A., Navarro J. F., Fattahi A., Frenk C. S., Sawala T., White S. D. M., Bower R., Crain R. A., Furlong M., Schaller M., Schaye J., Theuns T., The unexpected diversity of dwarf galaxy rotation curves, ArXiv e-prints, 2015

Ott J., Stilp A. M., Warren S. R., Skillman E. D., Dalcanton J. J., Walter F., de Blok W. J. G., Koribalski B., West A. A., VLA-ANGST: A High-resolution H I Survey of Nearby Dwarf Galaxies, AJ, 2012, vol. 144, p. 123

Penzias A. A., Wilson R. W., A Measurement of Excess Antenna Temperature at 4080 Mc/s., ApJ, 1965, vol. 142, p. 419

Perlmutter S., Aldering G., Goldhaber G., Knop R. A., et al. Measurements of Ω and Λ from 42 High-Redshift Supernovae, ApJ, 1999, vol. 517, p. 565

Perlmutter S., Aldering G., Goldhaber G., Knop R. A., Nugent P., Castro P. G., Deustua S., Fabbro S., Goobar A. e. a., The Supernova Cosmology Project Measurements of Omega and Lambda from 42 High-Redshift Supernovae, ApJ, 1999, vol. 517, p. 565

Persic M., Salucci P., Rotation Curves of 967 Spiral Galaxies, ApJS, 1995, vol. 99, p. 501

Pineda J. C., Hayward C. C., Springel V., Mendes de Oliveira C., Rotation curve fitting and its fatal attraction to cores in realistically simulated galaxy observations, Monthly Notices of the Royal Astronomical Society, 2016

Planck Collaboration Adam R., Ade P. A. R., Aghanim N., Akrami Y., Alves M. I. R., Arnaud M., Arroja F., Aumont J., Baccigalupi C., et al. Planck 2015 results. I. Overview of products and scientific results, ArXiv e-prints, 2015

Planck Collaboration Ade P. A. R., Aghanim N., Alves M. I. R., Armitage-Caplan C., Arnaud M., Ashdown M., Atrio-Barandela F., Aumont J., Aussel H., et al. Planck 2013 results. I. Overview of products and scientific results, A&A, 2014, vol. 571, p. A1

Planck Collaboration Ade P. A. R., Aghanim N., Arnaud M., et al. Planck 2015 results. XIII. Cosmological parameters, ArXiv e-prints, 2015

Pontzen A., Governato F., How supernova feedback turns dark matter cusps into cores, MNRAS, 2012, vol. 421, p. 3464

Pontzen A., Governato F., Cold dark matter heats up, Nature, 2014, vol. 506, p. 171

Power C., Navarro J. F., Jenkins A., Frenk C. S., White S. D. M., Springel V., Stadel J., Quinn T., The inner structure of ΛCDM haloes - I. A numerical convergence study, MNRAS, 2003, vol. 338, p. 14

Read J. I., Gilmore G., Mass loss from dwarf spheroidal galaxies: the origins of shallow dark matter cores and exponential surface brightness profiles, MNRAS, 2005, vol. 356, p. 107

Read J. I., Iorio G., Agertz O., Fraternali F., Understanding the shape and diversity of dwarf galaxy rotation curves in LCDM, ArXiv e-prints, 2016

Rhee G., Valenzuela O., Klypin A., Holtzman J., Moorthy B., The Rotation Curves of Dwarf Galaxies: A Problem for Cold Dark Matter?, ApJ, 2004, vol. 617, p. 1059

Riess A. G., Filippenko A. V., Challis P., Clocchiatti A., et al. Observational Evidence from Supernovae for an Accelerating Universe and a Cosmological Constant, AJ, 1998, vol. 116, p. 1009

Roberts M. S., Haynes M. P., Physical Parameters along the Hubble Sequence, ARA&A, 1994, vol. 32, p. 115

Roberts M. S., Whitehurst R. N., The rotation curve and geometry of M31 at large galactocentric distances., ApJ, 1975, vol. 201, p. 327

Rocha M., Jonsson P., Primack J. R., Cox T. J., Dust attenuation in hydrodynamic simulations of spiral galaxies, MNRAS, 2008, vol. 383, p. 1281

Rubin V. C., Thonnard N., Ford Jr. W. K., Extended rotation curves of high-luminosity spiral galaxies. IV - Systematic dynamical properties, SA through SC, ApJ, 1978, vol. 225, p. L107

Salpeter E. E., The Luminosity Function and Stellar Evolution., ApJ, 1955, vol. 121, p. 161

Salucci P., The constant-density region of the dark haloes of spiral galaxies, MNRAS, 2001, vol. 320, p. L1

Salucci P., Burkert A., Dark Matter Scaling Relations, ApJ, 2000, vol. 537, p. L9

Sawala T., Frenk C. S., Fattahi A., Navarro J. F., Bower R. G., Crain R. A., Dalla Vecchia C., White S. D. M., The APOSTLE simulations: solutions to the Local Group's cosmic puzzles, MNRAS, 2016, vol. 457, p. 1931

Sawala T., Scannapieco C., Maio U., White S., Formation of isolated dwarf galaxies with feedback, MNRAS, 2010, vol. 402, p. 1599

Schaller M., Frenk C. S., Bower R. G., Theuns T., Jenkins A., Schaye J., Crain R. A., Furlong M., Dalla Vecchia C., McCarthy I. G., Baryon effects on the internal structure of ΛCDM haloes in the EAGLE simulations, MNRAS, 2015, vol. 451, p. 1247

Schaye J., Crain R. A., Bower R. G., Furlong M., Schaller M., Theuns T., Dalla Vecchia C., Trayford J., The EAGLE project: simulating the evolution and assembly of galaxies and their environments, MNRAS, 2015a, vol. 446, p. 521

Schaye J., Crain R. A., Bower R. G., Furlong M., Schaller M., Theuns T., Dalla Vecchia C., Trayford J., The EAGLE project: simulating the evolution and assembly of galaxies and their environments, MNRAS, 2015b, vol. 446, p. 521

Schombert J. M., Bothun G. D., Schneider S. E., McGaugh S. S., A catalog of low surface brightness galaxies - List II, AJ, 1992, vol. 103, p. 1107

Schombert J. M., McGaugh S. S., Eder J. A., Gas Mass Fractions and the Evolution of Low Surface Brightness Dwarf Galaxies, AJ, 2001, vol. 121, p. 2420

Sersic J. L., Atlas de galaxias australes, 1968

Shen S., Mo H. J., White S. D. M., Blanton M. R., Kauffmann G., Voges W., Brinkmann J., Csabai I., The size distribution of galaxies in the Sloan Digital Sky Survey, MNRAS, 2003, vol. 343, p. 978

Simon J. D., Bolatto A. D., Leroy A., Blitz L., High-Resolution Measurements of the Dark Matter Halo of NGC 2976: Evidence for a Shallow Density Profile, ApJ, 2003a, vol. 596, p. 957

Simon J. D., Bolatto A. D., Leroy A., Blitz L., High-Resolution Measurements of the Dark Matter Halo of NGC 2976: Evidence for a Shallow Density Profile, ApJ, 2003b, vol. 596, p. 957

Simon J. D., Bolatto A. D., Leroy A., Blitz L., Gates E. L., High-Resolution Measurements of the Halos of Four Dark Matter-Dominated Galaxies: Deviations from a Universal Density Profile, ApJ, 2005, vol. 621, p. 757

Snyder G. F., Cox T. J., Hayward C. C., Hernquist L., Jonsson P., K+A Galaxies as the Aftermath of Gas-rich Mergers: Simulating the Evolution of Galaxies as Seen by Spectroscopic Surveys, ApJ, 2011, vol. 741, p. 77

Sofue Y., Rubin V., Rotation Curves of Spiral Galaxies, ARA&A, 2001, vol. 39, p. 137

Spano M., Marcelin M., Amram P., Carignan C., Epinat B., Hernandez O., GHASP: an Hα kinematic survey of spiral and irregular galaxies - V. Dark matter distribution in 36 nearby spiral galaxies, MNRAS, 2008, vol. 383, p. 297

Sparre M., Hayward C. C., Feldmann R., Faucher-Giguère C.-A., Muratov A. L., Kereš D., Hopkins P. F., (Star)bursts of FIRE: observational signatures of bursty star formation in galaxies, ArXiv e-prints, 2015

Spekkens K., Giovanelli R., Haynes M. P., The Cusp/Core Problem in Galactic Halos: Long-Slit Spectra for a Large Dwarf Galaxy Sample, AJ, 2005, vol. 129, p. 2119

Springel V., The cosmological simulation code GADGET-2, MNRAS, 2005, vol. 364, p. 1105

Springel V., E pur si muove: Galilean-invariant cosmological hydrodynamical simulations on a moving mesh, MNRAS, 2010, vol. 401, p. 791

Springel V., Hernquist L., Cosmological smoothed particle hydrodynamics simulations: a hybrid multiphase model for star formation, MNRAS, 2003, vol. 339, p. 289

Springel V., White S. D. M., Jenkins A., Frenk C. S., Yoshida N., Gao L., Navarro J., Thacker R., Croton D., Helly J., Peacock J. A., Cole S., Thomas P., Couchman H., Evrard A., Colberg J., Pearce F., Simulations of the formation, evolution and clustering of galaxies and quasars, Nature, 2005, vol. 435, p. 629

Stadel J., Potter D., Moore B., Diemand J., Madau P., Zemp M., Kuhlen M., Quilis V., Quantifying the heart of darkness with GHALO - a multibillion particle simulation of a galactic halo, MNRAS, 2009, vol. 398, p. L21

Stark D. V., McGaugh S. S., Swaters R. A., A First Attempt to Calibrate the Baryonic Tully-Fisher Relation with Gas-Dominated Galaxies, AJ, 2009, vol. 138, p. 392

Swaters R. A., Madore B. F., Trewhella M., High-Resolution Rotation Curves of Low Surface Brightness Galaxies, ApJ, 2000, vol. 531, p. L107

Swaters R. A., Madore B. F., van den Bosch F. C., Balcells M., The Central Mass Distribution in Dwarf and Low Surface Brightness Galaxies, ApJ, 2003, vol. 583, p. 732

Trachternach C., de Blok W. J. G., Walter F., Brinks E., Kennicutt Jr. R. C., Dynamical Centers and Noncircular Motions in THINGS Galaxies: Implications for Dark Matter Halos, AJ, 2008, vol. 136, p. 2720

Valenzuela O., Rhee G., Klypin A., Governato F., Stinson G., Quinn T., Wadsley J., Is There Evidence for Flat Cores in the Halos of Dwarf Galaxies? The Case of NGC 3109 and NGC 6822, ApJ, 2007, vol. 657, p. 773

van Albada T. S., Bahcall J. N., Begeman K., Sancisi R., Distribution of dark matter in the spiral galaxy NGC 3198, ApJ, 1985a, vol. 295, p. 305

van Albada T. S., Bahcall J. N., Begeman K., Sancisi R., Distribution of dark matter in the spiral galaxy NGC 3198, ApJ, 1985b, vol. 295, p. 305

van Albada T. S., Sancisi R., Dark matter in spiral galaxies, Philosophical Transactions of the Royal Society of London Series A, 1986, vol. 320, p. 447

van den Bosch F. C., Robertson B. E., Dalcanton J. J., de Blok W. J. G., Constraints on the Structure of Dark Matter Halos from the Rotation Curves of Low Surface Brightness Galaxies, AJ, 2000, vol. 119, p. 1579

van den Bosch F. C., Swaters R. A., Dwarf galaxy rotation curves and the core problem of dark matter haloes, MNRAS, 2001, vol. 325, p. 1017

van der Kruit P. C., Freeman K. C., Galaxy Disks, ARA&A, 2011, vol. 49, p. 301

van der Kruit P. C., Searle L., Surface photometry of edge-on spiral galaxies. I - A model for the three-dimensional distribution of light in galactic disks., A&A, 1981, vol. 95, p. 105

Verdoes Kleijn G. A., van der Marel R. P., Carollo C. M., de Zeeuw P. T., The Black Hole in IC 1459 from Hubble Space Telescope Observations of the Ionized Gas Disk, AJ, 2000, vol. 120, p. 1221

Vogelsberger M., Genel S., Sijacki D., Torrey P., Springel V., Hernquist L., A model for cosmological simulations of galaxy formation physics, MNRAS, 2013, vol. 436, p. 3031

Vogelsberger M., Genel S., Springel V., Torrey P., Sijacki D., Xu D., Snyder G., Bird S., Nelson D., Hernquist L., Properties of galaxies reproduced by a hydrodynamic simulation, Nature, 2014, vol. 509, p. 177

Vogelsberger M., Genel S., Springel V., Torrey P., Sijacki D., Xu D., Snyder G., Nelson D., Hernquist L., Introducing the Illustris Project: simulating the coevolution of dark and visible matter in the Universe, MNRAS, 2014, vol. 444, p. 1518

Vogelsberger M., Zavala J., Simpson C., Jenkins A., Dwarf galaxies in CDM and SIDM with baryons: observational probes of the nature of dark matter, MNRAS, 2014, vol. 444, p. 3684

Walker M. G., Peñarrubia J., A Method for Measuring (Slopes of) the Mass Profiles of Dwarf Spheroidal Galaxies, ApJ, 2011, vol. 742, p. 20

Walter F., Brinks E., de Blok W. J. G., Bigiel F., Kennicutt Jr. R. C., Thornley M. D., Leroy A., THINGS: The H I Nearby Galaxy Survey, AJ, 2008, vol. 136, p. 2563

Walter F., Cannon J. M., Roussel H., Bendo G. J., Calzetti D., et al. Dust and Atomic Gas in Dwarf Irregular Galaxies of the M81 Group: The SINGS and THINGS View, ApJ, 2007, vol. 661, p. 102

Weijmans A.-M., Krajnović D., van de Ven G., Oosterloo T. A., Morganti R., de Zeeuw P. T., The shape of the dark matter halo in the early-type galaxy NGC 2974, MNRAS, 2008, vol. 383, p. 1343

Weingartner J. C., Draine B. T., Dust Grain-Size Distributions and Extinction in the Milky Way, Large Magellanic Cloud, and Small Magellanic Cloud, ApJ, 2001, vol. 548, p. 296

Zwicky F., Die Rotverschiebung von extragalaktischen Nebeln, Helvetica Physica Acta, 1933, vol. 6, p. 110

Appendix

Appendix A

Initial experiments

The short article presented in the following pages correspond to some preliminar work developed at the early stages of this thesis, which was published in the proceedings of the *VIII International Workshop on the Dark Side of the Universe*, Buzios, Brasil, 2012.

PROCEEDINGS OF SCIENCE

The CUSP/CORE problem from a 2D view

Juan Carlos Basto-Pineda*, **Claudia Mendes de Oliveira, Carlos Eduardo Barbosa**
Instituto de Astronomia, Geofísica e Ciências Atmosféricas, Universidade de São Paulo
Rua do Matão 1226, São Paulo SP, Brazil
E-mail: `basto-pineda@usp.br`, `oliveira@astro.iag.usp.br`,
`carlos.barbosa@usp.br`

Philippe Amram, Valentin Perret
Aix Marseille Université, CNRS, LAM (Laboratoire d'Astrophysique de Marseille)
UMR 7326, 13388, Marseille, France
E-mail: `philippe.amram@oamp.fr`, `valentin.perret@oamp.fr`

It has been claimed for a long time that the shapes of galactic dark matter haloes in numerical simulations are not consistent with those of real galaxies, as inferred from observations. While the former may have a steep density profiles in the center, the latter may reveal nearly flat central dark matter distributions, and that is why this controversy is known as the "cusp/core problem". Nevertheless, it is important to highlight that most of the comparisons have been made using results from dark-matter-only simulations, e.g, ignoring the real effects of baryonic feedback at galactic scales. On the other hand, many observational works rely on the assumption that galactic disks are highly symmetric rotating structures, which is rarely the case either for light distributions or for velocity fields.

In this work we use high-resolution Hα velocity fields to make a comparison between the results obtained when perfectly rotating disks are assumed, against the results obtained using a harmonic decomposition to effectively separate non-circular motions from the pure circular component, which may be a better tracer of the underlying potential. We have selected a sample of galaxies analyzed and published by different authors. These have been considered good candidates for mass modeling, and have, therefore, played a role into the cusp/core controversy.

Following a classical approach to create mass models of rotating galaxies we show that conclusions about the cuspiness of the DM halo could be affected by the way the data are treated, and that there is a general trend towards higher mass-to-light ratios of baryonic components when the "pure rotation" assumption is considered.

VIII International Workshop on the Dark Side of the Universe
June 10-15, 2012
Búzios, Rio de Janeiro, Brasil

---

[*] Speaker.

© Copyright owned by the author(s) under the terms of the Creative Commons Attribution-NonCommercial-ShareAlike Licence.

1. Introduction

It has been claimed for a long time that there is a mismatch between the shape of dark matter galactic haloes predicted by ΛCDM cosmological simulations of structure formation, and the shape inferred from observations of late type rotating spiral galaxies. The former approach suggests a density profile becoming extremely sharp towards the center (cusp) (e.g Dubinski & Carlberg 1991; Navarro et al. 1996b, 1997), while the latter indicates a flat density profile (core) in the central region (e.g. Athanassoula et al. 1987; e.g., Begeman et al. 1991). This apparent contradiction is known as the cusp/core problem and it is considered as one of the greatest challenges for current numerical cosmology (for an up-to-date review see de Blok, 2010).

Nevertheless, some important facts should be noticed before considering this contradiction a problem for the ΛCDM cosmological paradigm. First, we should keep in mind that this problem was noticed using dark-matter-only numerical simulations; it means that the effect of baryons during the galaxy assembly process was completely neglected. Today it is widely accepted that in some cases baryonic feedback in the form of star formation, supernovae explosions, and galactic winds, for instance, could play a significant role in modeling the potential well and density profiles of the different components of a galactic system (e.g. Navarro et al. 1996a), even transforming cusps into cores (Governato 2012).

On the other hand, the analysis of observational data has some inherent uncertainties which are not always properly taken into account. For example, most of the works fitting rotation curves of disk galaxies implicitly consider that late-type spiral galaxies are fully-rotating systems, even though many of these systems exhibit non-negligible random motions. Most typical approaches assume axial symmetry as well, although this is not the case in general, spiral arms and bars being the most evident counter-examples. Thus, it is possible to say that the cusp/core controversy has not been definitively solved yet, and that there are still several facts which could be influencing the possible scenarios.

In this paper we revisit the cusp/core controversy using the galaxies and data from the GHASP survey. The main focus is the comparison between the results obtained when velocity fields are treated in two different ways: considering that all velocities are circular, or disentangling non-circular motions via a harmonic decomposition.

2. Mass models of galaxies

In order to derive the shape and concentration of dark matter haloes of real spiral galaxies, the typical approach is to assume that rotation curves/velocity fields are fair tracers of the underlying potential, so that $v_c(r) = \sqrt{-\nabla\phi \cdot r}$ holds. This method implicitly assumes that deviations from axial symmetry in mass and velocity distributions are low, and that the whole system is in a state of dynamical equilibrium. Then one creates a mass model of the galaxy using building blocks representing the real observed components (a stellar bulge, a stellar disk, or a gas disk, for instance, as given by the photometry), and possibly a model for the unseen dark matter halo. Given the linearity of the gravitational potential and the gradient operator, then it follows that velocity components can be added in quadrature $v_c^2(r) = V_{Disk}^2 + V_{Bulge}^2 + V_{Gas}^2 + V_{Halo}^2 + V_{...}^2 \cdots$.

name		D	Spatial Resol.	Incl.	P.A	Vsys	Type	Ref.
		Mpc	pc	deg	deg	km s^{-1}		
ugc3876	-	14.5	∼239	59±5	178±3	854±2	SA(s)d	Sp08
ugc5842	ngc3346	15.2	∼258	47±9	112±2	1245±1	SB(rs)cd	Sp08
ugc7045	ngc4026	11.4	∼116	68±2	99±2	758±1	SA(s)c	Sp08
ugc7876	ngc4365	14.5	∼211	53±9	944±1	164±3	SAB(s)d	Sp08
ugc8334	ngc5055	9.8	∼109	66±1	100±1	484±1	Sbc	dB08
ugc9866	ngc5949	7.4	∼248	56±6	148±2	430±1	SBc	dP12/S05
ugc11300	ngc6689	8.4	∼151	70±3	168±2	482±1	SABc	dP12/S05

Table 1: Sample information. Spatial resolution is measured from the average psf of the observatory. The last column lists at least one article where the galaxy was published in the context of the cusp/core problem. *References*: Sp08 = Spano et al. 2008, dB08 = de Blok et al. 2008, dP12 = del Popolo 2012, S05 = Simon et al. 2005.

3. Observations and data reduction

3.1 The GHASP Survey

The data used in this work comes from the GHASP (Gassendi Hα survey of SPirals) project, a compilation of Hα data cubes obtained with a scanning Fabry-Perot mounted on the 1.93 m telescope at the *Observatoire de Haute-Provence*, for a large sample of nearby spiral and irregular galaxies (http://fabryperot.oamp.fr/PerotFabry/). From these data cubes, the GHASP team has derived Hα maps, velocity fields, position-velocity diagrams, rotation curves and kinematical parameters as reported in (Epinat et al. 2008). The accuracy is about 5 km s^{-1} on average in velocity and 2 arcsec in spatial resolution (limited by seeing) (Garrido et al. 2003).

Additionally, images in the Rc band were obtained for a sub-sample of galaxies including those analyzed here, using a 1.2 m telescope at the same observatory between 2002 and 2009. Data are described elsewhere (Barbosa et al. 2013, in preparation).

3.2 Sample selection

For this comparison we have chosen a sample of 7 spiral galaxies published by other authors in the context of the cusp/core problem (i.e. considered as suitable for mass modeling procedure). These galaxies are close enough as to allow probing the first inner kiloparsec of the rotation curve, where the cusp/core discrepancy is more severe. Additionally, we require that the galaxies have moderate inclinations $70^\circ > i > 30^\circ$ and high-quality velocity maps. The source for the distance measurement to each galaxy and morphological type can be found in Epinat et al. (2008). The geometrical parameters are those determined from the kinematics by the GHASP team and reported in the same paper. Basic information is summarized in table 1.

3.3 Stellar Rotation Curves

Images in the Rc band of our galaxies were used in order to determine the stellar contributions to the rotation curve. After applying the instrumental zero point calibration, sky subtraction, and galactic extinction corrections, surface brightness profiles were drawn using the task ELLIPSE within the IRAF package. Then we run a typical decomposition of the profiles into a Sérsic bulge and an exponential disk, even though our images suggest the existence of more or different components in some cases. We insist in doing it in this way for simplicity, and because we are just interested in the impact on the results owed to the way the velocity field is treated. Thus, some of the bulge/disk decompositions presented here could be a poor physical description, fact that will be further explored in a forthcoming paper using 2D image decompositions instead of 1D surface brightness profiles.

Once we had the bulge/disk decompositions we created generic rotation curves for each component assuming mass-to-light ratios γ equal to one (in $M_{\odot}/L_{\odot}$), assuming spherical symmetry for the Sérsic component, and a thick stellar disk with a vertical structure governed by a $\mathrm{sech}^2\left(\frac{z}{2z_0}\right)$ model. To take into account other values of γ different from one we simply need to multiply the velocity amplitudes by $\sqrt{\gamma}$.

4. Methodology

4.1 From Velocity Maps to Rotation Curves

In the past, rotation curves were built using long-slit spectroscopy along the major axis. Even though these points have the lowest velocity uncertainties, the lack of two-dimensional information rules out the possibility of measuring and correcting for non-circular motions. Additionally, slits used to be placed along the photometric major axis which does not necessarily match the kinematical one. For these reasons, several authors now use high resolution velocity fields (e.g. Spano et al. 2008; Kuzio de Naray et al. 2009), which is also the case for this work.

Here we propose to build the final rotation curve in two different ways. The first one consists in assuming perfect circular velocities in a thin disk, so the inferred circular velocity and the line-of-sight measured component would be simply related by

$$v_{los}(r) = v_{sys} + v_c(r)\frac{\sin(i)\cos(\Psi)}{\sqrt{\cos^2(\psi) + \frac{\sin^2(\psi)}{\cos^2(i)}}}$$

where v_{los} represents line-of-sight velocity component, v_c the interpreted circular velocity, v_{sys} is the systemic velocity of the galaxy as a whole, i holds for inclination and Ψ is the polar angle from the major axis in the plane of the sky. This method will be referred everywhere in this work as the "pure rotation" assumption, and could be considered as the natural extension of the long-slit spectroscopy technique, except for the fact that now we include in the fit a much higher number of velocity points and misalignment uncertainties disappear. We have defined the final uncertainty as

$$\sigma_{V\,rot} = \frac{\sigma_{V\,los}}{\cos(\theta)\sin(i)}$$

where θ holds for the polar angle in the plane of the disk. We have excluded an angular region of 22.5° around the minor axis due to large errors when θ is large. We end up not with a rotation curve but a cloud of velocity points as those showed in blue in Figure 1 for ugc8334. We avoided to bin this cloud because this would introduce an uncertainty in the radius, and it is not necessary for the fitting procedure.

On the other hand, we will define our alternative rotation curve by means of a harmonic decomposition of the whole velocity field based on the Kinemetry package by Krajnović (2006), which allows us to separate non-circular motions from the pure rotating component using

$$V_{los} = a_0 + \sum_i a_i \sin(i\psi) + b_i \cos(i\psi)$$

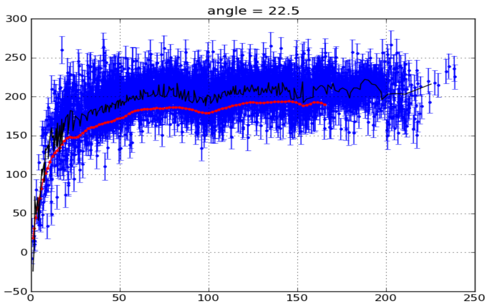

Figure 1: Kinemetry rotation curve for ugc8334 (red). “Pure rotation” velocity cloud (blue) and its binned version (black). Velocities are in km s^{-1}.

In this equation, the a_0 coefficient will be related to V_{sys} and to coherent motions out of the galactic plane, b_1 to the circular velocity, a_1 to the coherent expansion velocity, and all other coefficients will absorb the effect of random motions.

In this case we will define the uncertainty in a different way, adding in quadrature the statistical uncertainty from the kinemetry fitting procedure and the systematic uncertainty due to the uncertainty in the geometrical parameters, because it seems that the statistical uncertainties alone are unrealistically low as pointed out by Simon et al. (2005). In fact, they are much lower than the uncertainties defined for the “pure rotation” velocity cloud, so this is an attempt to make them comparable. Nonetheless, it should be noted that reduced χ^2’s found later on for both rotation curves can not be compared directly in a statistical sense, given that uncertainties have been defined in these different ways.

To calculate the systematic uncertainty we follow Simon et al. (2005), drawing a Gaussian probability distribution function for each geometrical parameter, picking 1000 combinations and drawing the resulting 1000 rotation curves. Then we take their mean as the final RC and their standard deviation as the systematic uncertainty. The final kinemetry rotation curve for our canonical example is shown in red in Figure 1. The black line represents a binned version of the blue velocity cloud, just to give an impression of its global behavior. Note that the black line is systematically offset to higher velocities than the red one, which is expected from the fact that in the former case we are overestimating the real pure circular velocity component.

4.2 Rotation Curves Fitting and DM Halo Density Profiles

We will just consider the stellar disks and bulges described above, and two different models for the dark matter halo: a Navarro-Frenk-White profile (NFW) and an Isothermal Sphere model (ISO). The first one is a good description of dark matter haloes in numerical simulations (Navarro, 1996b), and it grows as steep as $\rho \propto r^{-1}$ towards the center. The second is flat in the central region ($\rho \propto r^0$) and has been successfully used in the literature to fit real data (e.g. Athanassoula et al. 1987). Both of them are characterized by two parameters, a central density ρ_0 and a characteristic radius R_0.

We run two very simple tests. The first one is known as the *zero disk* fit, and consists in fitting the rotation curve using the DM halo alone, i.e. neglecting the contribution of stellar components, therefore giving an upper limit on the concentration of the halo density.

The second test is known as the *maximal disk* fitting, and consists in allowing the maximum contribution of baryons to the rotation curve before fitting the mass model, in order to put a lower limit on the concentration of the DM halo. In our case we have included a bulge component, so we call this approach the *maximal stars fitting* instead of *maximal disk*. To make the following procedures comparable for the kinemetry RC and the “pure rotation” velocity cloud, the latter was binned at the same radii where its kinemetry counterpart is defined, and a smoothing was applied in order to avoid spurious fluctuations, specially in the inner part where the number of pixels per bin is small. To determine the maximum stars contribution we followed a modified version of the method described in Simon et al. (2005), looking for the values of γ_{disk} and γ_{bulge} that minimize the χ^2_ν without overpassing any point of the rotation curve. The very first point of each rotation curve was excluded because it may strongly affect the results and its uncertainty is large.

5. Results

5.1 Zero Stars

In table 2 we present the results of the *zero disk* test using the isothermal sphere model for the DM halo. We see that parameters ρ_0 and R_0 were similar for each galaxy for both RCs, but never remain the same. In order to check whether or not this change is statistically significant we should compute χ^2_ν in a grid of values around this best solution, but this analysis is still in progress. Same comments apply to the case of NFW profiles whose results are not shown.

Zero Stars ISO						
	’Pure Rotation’			’Kinemetry’		
	ρ_0 $10^{-3}M\odot/pc^3$	R_0 kpc	χ^2_ν	ρ_0 $10^{-3}M\odot/pc^3$	R_0 kpc	χ^2_ν
ugc3876	202	1.9	3.05	182	1.57	1.83
ugc5842	92	2.9	4.22	63.7	2.5	0.74
ugc7045	422	1.9	3.13	570	1.41	7.56
ugc7876	159	1.9	2.23	107	1.7	2.36
ugc8334	1764	1.3	4.93	1808	1.12	44.7
ugc9866	924	0.96	1.56	854.4	0.72	1.21
ugc11300	229	1.7	3.56	247.2	1.38	5.15

Table 2: Comparison of best isothermal halo parameters obtained for each galaxy using both rotation curves.

More interesting results are those shown in table 3. It compares the quality of the fit for the ISO and NFW model. Those values of χ^2_ν highlighted in green indicate the best model for each galaxy and rotation curve. If no model is highlighted in green, it means that both of them are equally good. In the case of the Kinemetry RC there is a favorite model for each galaxy, and one would conclude that there are 4 cuspy haloes and 3 flat haloes in our sample. On the other hand, results obtained using the “pure rotation” velocity cloud hardly allowed us to select a best option between the models. Only in two cases the NFW DM halo fits the RC much better than the Isothermal sphere, while the opposite never happens.

5.2 Maximal disk

Concerning the *Maximal disk* test, we present in table 4 the maximum values of γ_{bulge} and γ_{disk} allowed by each rotation curve. As can be seen, this time there is a big difference between the

χ^2_ν Zero Stars - Best Model				
	Pure Rotation		Kinemetry	
	ISO	NFW	ISO	NFW
ugc3876	3.05	2.99	1.83	0.8
ugc5842	4.22	4.32	0.74	11.85
ugc7045	3.13	2.64	7.56	2.26
ugc7876	2.23	2.32	2.36	7.05
ugc8334	4.93	3.2	44.7	4.75
ugc9866	1.56	1.52	1.21	3.24
ugc11300	3.56	3.31	5.15	0.85

Table 3: Zero Stars - Best Model.

values obtained using kinemetry or "pure rotation". For instance, in the case of ugc7045 the "pure rotation" case allows the existence of a massive bulge in the center while kinemetry produces a very light central component, and even a smaller γ_{disk} which means a much smaller overall baryonic mass content. As a general trend we notice that all γ_{disk} are higher in the "pure rotation" case than in the kinemetry one, ugc8334 showing the biggest difference between them. Maximum bulges allowed tend to be more massive when one uses kinemetry, but the differences are less strong in general, so it seems that an overall higher baryonic content is allowed for the "pure rotation" RC. This fact is not really unexpected, given that the "pure rotation" RC tends to reach higher velocities than the kinemetry, by definition.

Maximal stars comparison				
	'Pure Rotation'		'Kinemetry'	
	γ_{disk}	γ_{bulge}	γ_{disk}	γ_{bulge}
ugc3876	7.19 ±0.67	0.00+1.60	5.31±0.82	0.32±1.06
ugc5842	1.86±0.61	0.00±0.00	0.74±0.30	0.00±0.00
ugc7045	3.32±0.01	4.45±0.88	2.93±0.50	0.23±0.39
ugc7876	1.81±0.83	0.00±0.00	0.41±0.56	0.00±0.00
ugc8334	2.55±0.18	0.18±0.15	0.80±0.13	1.54±0.29
ugc9866	3.29±0.06	0.06±0.28	2.14±0.47	0.00+0.50
ugc11300	2.01±0.34	0.17±0.36	1.98±0.12	0.52±0.41

Table 4: Comparison of mass-to-light ratios obtained when a maximal contribution from stars is allowed, in the "pure rotation" and kinemetry cases. All the values are expressed in $M \odot /L_{\odot}$

6. Summary and Conclusions

Mass models of galaxies combining photometry and kinematics is currently the main way of probing galactic dark matter haloes. Here we present simplified mass models for a sample of seven galaxies previously studied in the context of the cusp/core problem, using their high-resolution velocity maps in two different ways. Our tests suggest that assuming pure rotation or effectively correcting for non-circular motions strongly affect the conclusions about the cuspiness of the DM halo and about the maximum baryonic content allowed by the data. Thus it is very important to study in more detail at which extent it is possible to recover true information about the shape of DM haloes from velocity fields, and what is the best way of using the data for this purpose.

Acknowledgments

JCBP and CMdO would like to thank FAPESP for support (PhD fellowship 2011/21678-0 and thematic grant 2006/56213-9). We also want to acknowledge the VIII International Workshop on the Dark Side of the Universe organizers for financial support which allowed JCBP to participate in this conference.

References

[1] E. Athanassoula, A. Bosma, & S. Papaioannou, *Halo parameters of spiral galaxies*, A&A, 1987, 179, 23.

[2] K. G. Begeman, A. H. Broeils, & R.H. Sanders, *Extended rotation curves of spiral galaxies - Dark haloes and modified dynamics*, MNRAS, 1991, 249, 523.

[3] W. J. G. de Blok, F. Walter, E. Brinks, C. Trachternach, S.H. Oh, & R. C. Kennicutt, *High-resolution rotation curves and galaxy mass models from THINGS*, AJ, 2008, 136, 2648.

[4] W. J. G. de Blok, *The Core-Cusp Problem*, Advances in Astronomy, 2010.

[5] A. del Popolo, *Statistical properties of the dark matter haloes of dwarf galaxies and correlations with the environment*, MNRAS, 2012, 419, 971.

[6] J. Dubinski, & R. G. Carlberg, *The structure of cold dark matter halos* ApJ, 1991, 378, 496.

[7] B. Epinat, P. Amram, M. Marcelin, C. Balkowski, O. Daigle, O. Hernandez, L. Chemin, C. Carignan, J.L. Gach, P. Balard, *GHASP: an Hα kinematic survey of spiral and irregular galaxies - VI. New Hα data cubes for 108 galaxies*, MNRAS, 2008, 388, 500.

[8] O. Garrido, M. Marcelin, P. Amram, O. Boissin, *GHASP: An Hα kinematic survey of spiral and irregular galaxies. II. Velocity fields and rotation curves of 15 galaxies*, A&A, 2003, 399, 51.

[9] F. Governato, A. Zolotov, A. Pontzen, C. Christensen, S.H. Oh, A. M. Brooks, T. Quinn, S. Shen, J. Wadsley, *Cuspy no more: how outflows affect the central dark matter and baryon distribution in Λ cold dark matter galaxies*, MNRAS, 2012, 422, 1231.

[10] D. Krajnović, M. Cappellari, P.T. de Zeeuw, Y. Copin, *Kinemetry: a generalization of photometry to the higher moments of the line-of-sight velocity distribution* , MNRAS, 2006, 366, 787.

[11] R. Kuzio de Naray, S. S. McGaugh, & J. C. Mihos, *Constraining the NFW potential with observations and modeling of low surface brightness galaxy velocity fields*, ApJ, 2009, 692, 1321.

[12] J. F. Navarro, V. R. Eke, & C. S. Frenk, *The cores of dwarf galaxy haloes*, MNRAS, 1996a, 283, L72.

[13] J. F. Navarro, C. S. Frenk, & S. D. M. White, *The Structure of Cold Dark Matter Halos*, ApJ, 1996b, 462, 563.

[14] J. D. Simon, A. D. Bolatto, A. Leroy, L. Blitz, & E. L. Gates, *High-resolution measurements of the halos of four dark matter-dominated galaxies: deviations from a universal density profile*, ApJ, 2005, 621, 757.

[15] M. Spano, M. Marcelin, P. Amram, C. Carignan, B. Epinat, O. Hernandez, *GHASP: an Hα kinematic survey of spiral and irregular galaxies - V. Dark matter distribution in 36 nearby spiral galaxies*, MNRAS, 2008, 383, 297.

Appendix B

Instrumental parameters used to mimic the SDSS photometry

To create the mock images of the simulated galaxies using SUNRISE a set of instrumental parameters need to be set, in order to go from physical fluxes in Jansky to a number of counts in the detector following the prescription given in the SDSS documentation. These parameters include the airmass, the brightness of the sky, typical noise values, the psf, etc. This was done extracting the values reported by the SDSS dr7 from the headers of ∼100 images of galaxies in the local Universe. I assumed as a *typical* value of each parameter its average across the whole sample. In the next plots I show the values measured in the r band, highlighting the mean value of each parameter with a solid line and its 1-σ scatter with a shaded region.

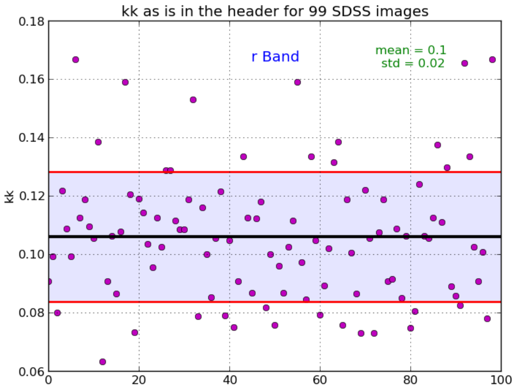

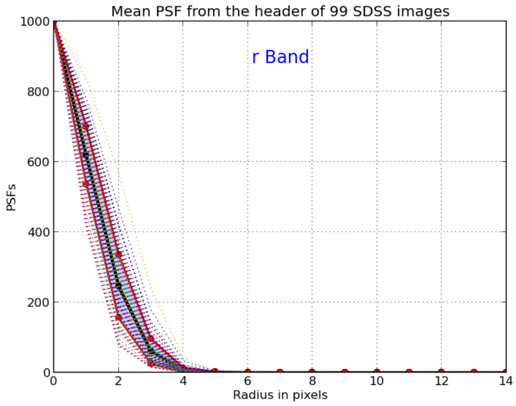

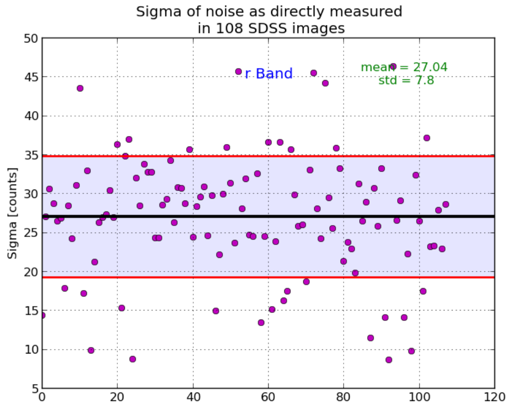
Sigma of noise as directly measured
in 108 SDSS images
r Band
mean = 27.04
std = 7.8
Sigma [counts]
5
10
15
20
25
30
35
40
45
50
0
20
40
60
80
100
120

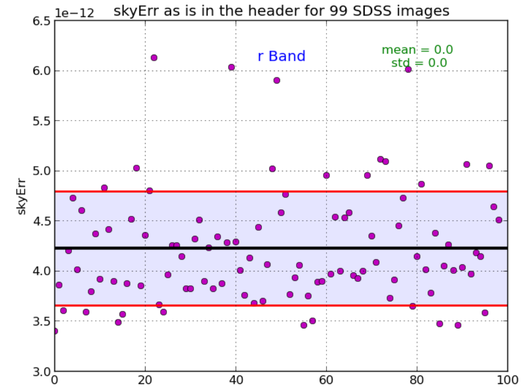
1e−12
skyErr as is in the header for 99 SDSS images
r Band
mean = 0.0
std = 0.0
skyErr
3.0
3.5
4.0
4.5
5.0
5.5
6.0
6.5
0
20
40
60
80
100

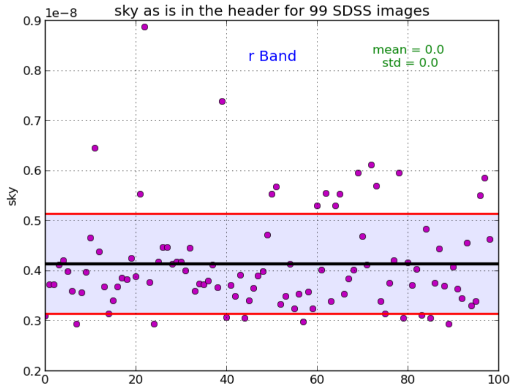
1e−8
sky as is in the header for 99 SDSS images
r Band
mean = 0.0
std = 0.0
sky
0.2
0.3
0.4
0.5
0.6
0.7
0.8
0.9
0
20
40
60
80
100

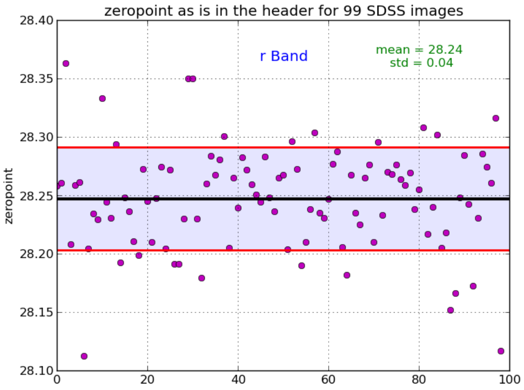
zeropoint as is in the header for 99 SDSS images
r Band
mean = 28.24
std = 0.04
zeropoint
28.10
28.15
28.20
28.25
28.30
28.35
28.40
0
20
40
60
80
100

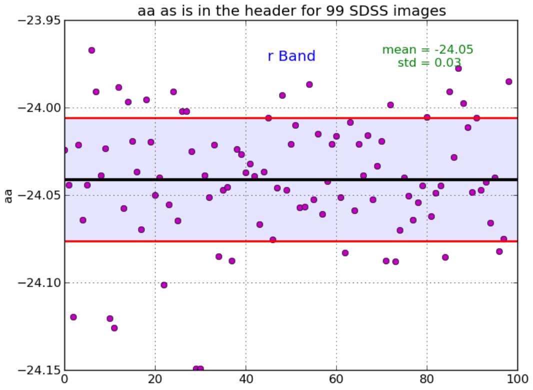
aa as is in the header for 99 SDSS images
r Band
mean = -24.05
std = 0.03
aa
−24.15
−24.10
−24.05
−24.00
−23.95
0
20
40
60
80
100

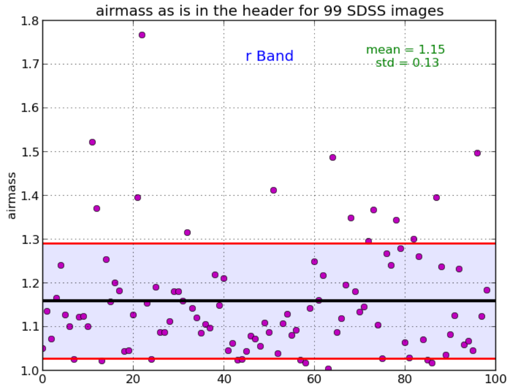
airmass as is in the header for 99 SDSS images
r Band
mean = 1.15
std = 0.13
airmass
1.0
1.1
1.2
1.3
1.4
1.5
1.6
1.7
1.8
0
20
40
60
80
100

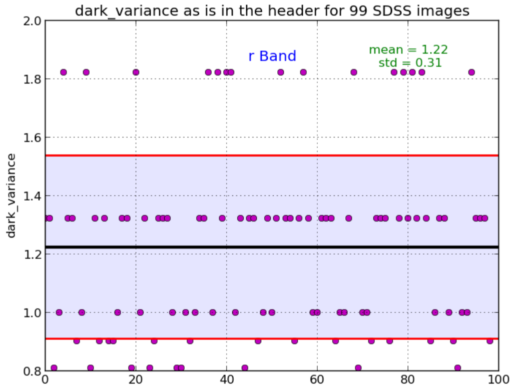
dark_variance as is in the header for 99 SDSS images
r Band
mean = 1.22
std = 0.31
dark_variance
0.8
1.0
1.2
1.4
1.6
1.8
2.0
0
20
40
60
80
100

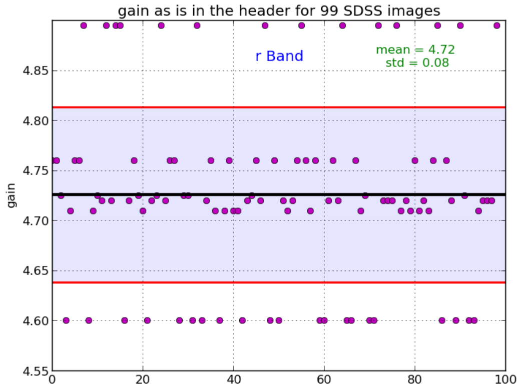
gain as is in the header for 99 SDSS images
r Band
mean = 4.72
std = 0.08
gain
4.55
4.60
4.65
4.70
4.75
4.80
4.85
0
20
40
60
80
100